Geometry and Transport in Development

by

Nicolas François Romeo

B.Sc., École polytechnique (2018)
M.Sc., École polytechnique (2019)

Submitted to the Department of Physics
in partial fulfillment of the requirements for the degree of
Doctor of Philosophy in Physics
at the
MASSACHUSETTS INSTITUTE OF TECHNOLOGY
September 2023

Author . . . .
Department of Physics
July 31, 2023

Certified by . . . .
Jörn Dunkel
Professor of Mathematics
Thesis Supervisor

Certified by . . . .
Mehran Kardar
Professor of Physics
Thesis Supervisor

Accepted by . . . .
Lindley Winslow
Chair, Department Committee on Graduate Theses

Geometry and Transport in Development

by

Nicolas François Romeo

Submitted to the Department of Physics
on July 31, 2023, in partial fulfillment of the
requirements for the degree of
Doctor of Philosophy in Physics

Abstract

Shape changes are some of the most visually striking features of biological development at all scales of living matter. With recent advances in high-resolution microscopy, it becomes possible to track the morphology and motion of systems ranging from organelles to every single cell within specific tissues or even whole organisms. This enables quantitative physical modeling to understand the phenomena driving and controlling the emergence of spatial patterns and organization in development.

In the first half of this thesis, we consider two problems arising in *Drosophila melanogaster* oogenesis. In a small organ known as the egg chamber, we apply ideas from continuum and statistical mechanics to explain the nonlinear dynamics and regulation of nuclear envelope shape and of a cytoplasmic transport event known as 'nurse cell dumping'. In particular, these results show how biological and physical mechanisms can cooperate to enable or regulate developmental processes.

In the second half of this thesis, we consider zebrafish embryogenesis, during which thousands of cells collectively migrate to lay out the organism's body plan. Here, a direct physical modeling approach is hampered by the exploding complexity of a three-dimensional many-body dynamic which obfuscates the identification of relevant degrees of freedom. In this context, we investigate ways to translate cell trajectories into lower-dimensional representations and to capture the essential ordering principles of collective cell organization. By leveraging model inference techniques, the resulting representation of the collective cell dynamics enables a compact characterization of developmental symmetry breaking.

Thesis Supervisor: Jörn Dunkel
Title: Professor of Mathematics

Thesis Supervisor: Mehran Kardar
Title: Professor of Physics

Acknowledgments

I have been fortunate to have been surrounded by exceptional scientists at all stages of their careers. First, thank you Jörn for taking me on as a student and bearing with me through the years. Thank you for making me think deeper and bolder about science; I can only hope to strive to be as creative in my scientific explorations. Mehran Kardar, Nikta Fakhri and Jeff Gore are three of the reasons I got into biophysics, and I am lucky to have such scientists and humans on my thesis committee. Even though he is not on the committee, I am so glad I have been able to collaborate with (and hear Pokémon facts) from Adam Martin and his lab. My most heartfelt thanks go to Jasmin Imran Alsous for introducing me to both biology and the art of David Hockney; it was fun trying to make *a bigger splash* out of every experiment. I am deeply obliged to Alex Mietke for teaching me how to do research on a day-to-day basis, and for being an awesome mentor. Thank you to Jonathan Jackson for all the tea and fun at work. Without you, this thesis would be much thinner; here's to N more years of 'avoiding accidental scientific misconduct'! Thanks to Keaton for teaching me how to make practical code and to ask questions the right way and the hours-long conversations in your office. Thanks to Jan for the endless C++ debugging and laughs. Thanks to Alasdair for being an amazing co-author, friend, officemate and infinite well of numerical algebra knowledge. Thanks to Dom, Jorge, Alex Cohen, George, Shijie and every other members of both the Physical Math and Physics of Living Systems communities over the years for the many lunches and numerous spirited conversations. Thanks to my undergrad mentees Catherine and Allison for bearing with me; I'm looking forward to seeing you do awesome things in grad school.

I would not have been able to produce the work I did without the excellent education I have had the privilege to receive in my undergraduate years. Thanks to my teachers in prépa Dominique Guest, Christian Devanz, Jérôme Degot, Julien Rochet and Jacques Aiache. Far more than just preparing the *Concours*, I owe all my technical skills to their patient hammering of the mathematics gospel down my throat, which I am to this day still processing and likely will forever. I also would not have landed at MIT if I didn't have teachers and mentors such as Étienne Reyssat, Olivier Pinel and Charles Rocques-Carmes at Polytechnique and during my internships.

Finally, I owe most of my pleasant experience in Boston (and sanity) to the friends I made this side of the Atlantic. Thanks Paul for being the best housemate, climbing partner and conference buddy one could hope for; Kathy for infinite adventures; Cole for being the voice of reason; Karina for being the voice of economic rationality; my friends Pierre, Peter, Camille, Taylor, Elise, and all of the MIT Outing Club that I love so much. Thanks to my parents and family for enabling me to do all of this, and the warmest thank you to Elena for being the best partner in all of this that I could hope for.

Contents

List of Figures

List of Tables

Chapter 1

Introduction

Physicists have long speculated on the nature of the mechanisms underlying the formidably complex and robust organization of biological systems. Indeed, as recognized perhaps most famously early on by D'Arcy Thompson in his twentieth-century treatise *On growth and form* and Erwin Schrödinger's *What is Life?* lectures, Biology happens in space and time, and as such the structures of living matter are constrained by physical laws as much as ordinary non-living matter.

That biological matter must follow physical constraints leads to two possible research directions. A first course of action would ask how could Physics help Biology. While over the course of the twentieth century, molecular biology has been able to uncover the molecular and genetic bases of biological function, it is still an open scientific question to understand the mapping between genes and physical organization of biological systems, whether organelles, organs or organisms [5]. Examples of the importance of physical organization abound at all scales of biology: Within cells, the spatial organization of organelles is essential to cell division [6], contributes to cellular sensing [7, 8], and is instrumental for carbon processing in plants [9]. Collective motion of cells is essential for embryo development, wound healing, or tumour progression [10, 11], while mechanical properties of tissues are essential to the immune response [12] or to suppress tumour growth [13, 14].

A second course of action involves finding new Physics in Biology. Indeed, biological systems are a natural playground for exotic physical phenomena emerging from the complexity and scales of the systems involved. At sub-cellular scales, thermal and non-thermal fluctuations are significant with respect to the energy scales involved in the chemical and mechanical processes at play in cells' interior [15, 16]; at larger scales, the ubiquity of low symmetry order or disorder lead to the relevance of exotic order parameters fields that are rarely on the forefront in traditional condensed matter physics [17, 18]; at all scales, phenomena are out of equilibrium and multiple species of discrete objects and fields may interact and couple together through complex, nonlinear or non-reciprocal interactions [19, 20]. The phenomena arising from the resulting dynamics have formed the basis for the field of active matter, a vibrant subject of study in the physics community [21, 22, 23, 24].

Whether one seeks to achieve a quantitative understanding of the ordering principles of Biology or understand the novel physical phenomena that underlie them, it is essential to have means to probe, perturb, and measure biological systems. Indeed, without access to such experimental capacities, D'Arcy Thompson had to admit of his *On growth and form* that "This book of mine has little need of preface, for indeed it is 'all preface' from beginning to end" [25]. To the excitement of the biophysical community, recent advances on the imaging and genetic engineering fronts has enabled direct observations of the dynamics and morphology of systems at scales ranging from ribosomes [26] to every cell in entire fish larvae [3, 27]. With such data, it becomes possible to match theory to experiment, but to do so it also becomes necessary to develop methods to interpret data using the methods of physics.

This thesis considers the use of physical methods to interpret the emergence and dynamics of structure during development. Biological development covers the processes through which multicellular organisms arise, including perhaps the most visually striking feature of biology: morphogenesis - the emergence of shape and form.

That shape and form is connected to function is a well-grounded idea in everyday life, with architecture and design embracing the motto that 'form follows function' [28]. In development, however, the practical consequences of this statement are far from obvious. How does form enable function, and how does form come to be, turning genetic information into tangible structures or flowing materials? To answer these questions in experimentally-relevant settings, we will need to quantify geometry and connect the shape of biological objects to their function, exemplified by their mechanical properties and dynamical transport processes. Conversely, we will also need to understand how transport processes shape the geometry of the developing embryo.

In the first half of this thesis, we consider two problems arising in *Drosophila melanogaster* oogenesis, the events leading to the formation of an unfertilized egg cell known as an oocyte. From insects to mice, oocytes develop alongside nurse-like sister cells within cell clusters known as 'germline cysts', which we study in two joint theoretical and experimental projects with Adam C. Martin's lab.

In chapters 2 and 3, we study geometric nonlinearities in fluctuating elastic membranes, and find that they are essential to describe the surface statistics of cell nuclei. Together with Jonathan Jackson, we build an image processing and spectral shape analysis pipeline to analyze three-dimensional high-resolution data from several hundreds of cell nuclei. This reveals a robust power-law scaling of the radial fluctuation power spectrum as a function of length scale. To explain this power law, we consider a nonlinear surface elasticity model of fluctuating shells, and theoretically show that the experimentally observed exponent is consistent with a regime in which the shell response is dominated by nonlinear contributions [29]. Using pseudo-spectral numerical simulations, we solve the corresponding Langevin equation with hydrodynamic damping, which quantitatively reproduces experimental observations. A scaling argument predicts that osmotic pressure or activity influence the amplitude but only weakly affects the scaling behavior of the wrinkles. This is confirmed by perturbation experiments using osmotic shocks or chemical inhibition of microtubule polymerisation. Together with the theoretical results, this suggests that non-linear surface elasticity effectively sets the response of nuclear envelopes independently of the precise driving forces, providing an example of robust spatial organization through physical constraints. Chapter 2 details the construction and phenomenology of the mechanical model, while chapter 3 is dedicated to its application to nuclear envelope wrinkling. Parts of both chapters have been previously published as a preprint 'Dynamics, scaling behavior and control of nuclear envelope wrinkling', J. A. Jackson,

N. Romeo, A. Mietke, K. J. Burns, J. F. Totz, A. C. Martin, J. Dunkel and J. Imran Alsous. (2023).

Chapter 4, with experiments performed by Jasmin Imran Alsous and Jonathan Jackson, investigates the process known as 'nurse cell dumping' happening in the fruit fly germline cyst: prior to fertilization, the nurse cells' (NC) cytoplasm is transported into the oocyte, which grows as its sister cells regress and die [30]. The cells are connected in a reproducible way by $\sim$10 μm wide channels known as ring canals, allowing for cytoplasm to be exchanged between cells. We discover that, during dumping, most cytoplasm is transported into the oocyte independently of cell surface contractility mediated by the motor protein myosin, before a second phase of transport requires contractility. To explain this observation, we construct a minimal hydraulic network-flow model in which fluid exchange between cells (represented by network nodes) is driven by pressure differences between them. Each cell's pressure is set by a Young–Laplace law involving the effective cell surface tension and inverse cell radius. Long thought to trigger transport through 'squeezing', we fiind that changes in actomyosin contractility are required only once NC volume has become comparable to nuclear volume, in the form of surface contractile waves that drive NC dumping to completion. By showing how development can rely on the physical energy landscape to robustly drive dumping, this work provides an example of biological and physical mechanisms cooperating to enable a critical developmental process that, until now, was thought to be mainly biochemically regulated. The contents of chapter 4 have been in parts previously published as Ref. [30], J. Imran Alsous, N. Romeo, J. A. Jackson, F. M. Mason, J. Dunkel and A. C. Martin, *Proc. Natl. Acad. Sci. U.S.A.* **118** (10) e2019749118 (2021).

In the second half of this thesis, we investigate ways to leverage model inference to capture the essential ordering principles of collective cell organization. As we consider biological systems of larger sizes, the exploding complexity of these many-body systems makes identification of relevant degrees of freedom harder, and hinders traditional modeling approaches. As recent advances in high-resolution live-cell microscopy now enable tracking cellular motions in tissue at the single-cell level [31, 4, 32, 33, 34] or at the organelle level [26, 35], the challenge becomes to translate high-dimensional imaging data into low-dimensional representations that lend themselves to quantitative analysis.

Chapter 5 uses experimental single-cell trajectory data of early zebrafish embryogenesis from [4] as an illustrative example to develop a coarse-graining and inference framework to convert trajectories on a curved surface into coarse-grained hydrodynamic fields and compress the latter further by representing them in terms of suitable harmonic basis functions. By properly accounting for covariance constraints in kernel-based coarse-graining, the resulting low-dimensional representation of the collective cell dynamics enables a compact characterization of developmental symmetry breaking. We are then able to directly infer an interpretable linear hydrodynamic model, which reveals similarities between pan-embryo cell migration and active Brownian particle dynamics on curved surfaces. Chapter 5 and parts of the corresponding appendices B,C have been previously published in Ref. [36], N. Romeo, A. D. Hastewell, A. Mietke and J. Dunkel, Learning developmental mode dynamics from single-cell trajectories, *eLife* 10:e68679 (2021).

Finally, we summarize our results and present possible extension of the ideas developed in this thesis in chapter 6.

Chapter 2

Scaling behavior of fluctuating spherical elastic shells

Parts of this chapter has been previously published as a preprint 'Dynamics, scaling behavior and control of nuclear envelope wrinkling', J. A. Jackson, N. Romeo, A. Mietke, K. J. Burns, J. F. Totz, A. C. Martin, J. Dunkel and J. Imran Alsous. (2023)

Membranes are essential to biological systems: without surfaces defining an inside and an outside, it is impossible to realize the compartments which harbor the machinery of life. Even within a cell, membranes range from very small (60-80 nm) cargo-carrying lipid vesicles [37] to very large complexes surrounding organelles such as the Endoplasmic reticulum or the cell nucleus [38]. The variety of shapes membrane take on inside a cell reflects the diversity of functions they fulfill. To make this idea quantitative, we will see in this chapter that the geometry of a membrane also essentially determines its mechanical response.

Biological membranes such as lipid bilayers are commonly described as fluid membranes which are approximately incompressible but have no shear rigidity [39]. However, composite membranes such as lipid bilayers supported by a network of semiflexible polymers can show an emergent non-zero shear modulus [40]. Those membranes will be the main subjects of interest in this chapter.

At large enough scales that the microscopic details of a molecular description can be safely ignored, one can use the framework of classical elasticity to describe the mechanical properties of these elastic membranes. While elastic theories of plates and shells have a rich history and have been studied since the nineteenth century [41], using those theories at biological scales presents novel challenges. On one hand, with the large deformations allowed by the relative softness of biological materials comes nonlinear behavior and instabilities; understanding and controlling this 'extreme mechanics' regime where membranes snap, buckle or grow has been the source of a renewed interest in elastic theories in recent years [42, 43, 44, 45]. On the other hand, the energy scales associated with deformations of the membranes are of the order of the thermal energy $k_B T$, where k_B is the Boltzmann constant and $T = 300$ K the room temperature. As such, in the cell interior teeming with thousands of molecular motors, fluctuations driven by temperature or the mechanical activity of the cytoplasm are necessary to describe the mechanics of biological surfaces [46]. It is hence essential for sub-cellular biological applications to understand the dynamics of fluctuating nonlinear elasticity.

In this chapter, we build on previous works [46, 47, 29] to provide a theory of fluctuating spherical elastic shells, starting in Sec. 2.1 from shell kinematics to build an effective free energy described in Sec. 2.2 and simulated by methods explained in Sec. 2.3 that will allow us to provide estimates in Sec. 2.4 for the scaling behavior of fluctuating shells. Taken together, those results will be essential to explain experimental observations that will be presented in chapter 3.

2.1 Deformations of surfaces and shallow shell approximation

The starting point of our theory will be to construct the kinematics of deformed surfaces that we will use to describe our elastic shells.

A shell will be represented by a two-dimensional surface $\Gamma \subset \mathbb{R}^3$ with an undeformed reference shape parameterized by $\mathbf{r}(s^1, s^2)$, where s^1, s^2 are curvilinear coordinates. On this surface, tangent and normal vectors are defined by $\mathbf{e}_i = \partial_i \mathbf{X}$

($\partial_i := \partial/\partial s^i$, $i = 1, 2$) and $\mathbf{n} = \mathbf{e}_1 \times \mathbf{e}_2/|\mathbf{e}_1 \times \mathbf{e}_2|$, respectively. The metric tensor and the curvature tensor (also known as the first and second fundamental forms) of the reference surface are given by $g_{ij} = \mathbf{e}_i \cdot \mathbf{e}_j$ and $C_{ij} = \mathbf{n} \cdot \partial_i \partial_j \mathbf{r}$.

When the surface continuously deforms, a point $\mathbf{r}(s^1, s^2)$ moves to a new position $\mathbf{r}' = \mathbf{r}(s^1, s^2) + \boldsymbol{\xi}(s^1, s^2, t)$, where $\boldsymbol{\xi}(s^1, s^2, t)$ describes the displacement and we drop the arguments in the following for brevity. The general strain tensor u_{ij} describing the relative deformations of the surface is defined by $(d\mathbf{r}')^2 - (d\mathbf{r})^2 = 2u_{ij} ds^i ds^j$. Using $d\mathbf{r}' = (\mathbf{e}_i + \partial_i \boldsymbol{\xi}) ds^i$ and $d\mathbf{r}^2 = g_{ij} ds^i ds^j$, the strain tensor takes the form

$$\begin{aligned} u_{ij} =& \frac{1}{2} \left[\mathbf{e}_j \cdot \partial_i \boldsymbol{\xi} + \mathbf{e}_i \cdot \partial_j \boldsymbol{\xi} + (\partial_i \boldsymbol{\xi}) \cdot (\partial_j \boldsymbol{\xi}) \right] \\ =& \frac{1}{2} \left(\nabla_i u_j + \nabla_j u_i \right) - C_{ij} f + \frac{1}{2} (\nabla_i u_k - C_{ik} f)(\nabla_j u^k - C_j^k f) \\ &+ \frac{1}{2} (C_i^k u_k + \partial_i f)(C_j^l u_l + \partial_j f), \end{aligned} \tag{2.1}$$

where we have split the deformation field $\boldsymbol{\xi} = \mathbf{u} + f\mathbf{n}$ into tangential $\mathbf{u} = u^i \mathbf{e}_i$ and normal $f\mathbf{n}$ contributions.

To capture the geometric effects of bending deformations, we additionally discuss how surface deformations $\boldsymbol{\xi}$ change the mean curvature $H = C_i^i$ of an arbitrary surface. The mean curvature H' of a general deformed surface, parameterized on the reference surface with curvature H, is to first order in the deformation field given by [48]:

$$H' = H + \nabla^2 f + C_{ij} C^{ij} f + u^k \nabla_k H + \mathcal{O}(\boldsymbol{\xi}^2), \tag{2.2}$$

where $\nabla^2 f := g^{ij} \nabla_i \nabla_j f$ denotes the Laplace-Beltrami operator on the surface.

The strain tensor in Eq. (2.1) and changes of mean curvature Eq. (2.2) can be further simplified by taking into account the slenderness of the nuclear envelope. First, for envelope thickness h and deformation length scale L, plate and shell theory predict in-plane deformations u_i to be of order $\mathcal{O}(f\frac{h}{L})$ [49]. As a second simplifying assumption, we consider a shell with small and slowly varying curvature, such that $hC_{ij} \ll 1$. Thus, in thin shells with $h/L \ll 1$, in-plane deformations are expected to be significantly smaller than out-of-plane deformations f and all higher order terms involving u_i and/or the curvature C_{ij} in Eq. (2.1) are subdominant. In this shallow-shell approximation, we describe the undeformed reference shape as a spherical surface of radius R, which is oriented such that the normal $\mathbf{n}$ points towards the inside of the sphere. In this case, $C_{ij} = g^{\mathrm{s}}_{ij}/R$, where g^{s}_{ij} denotes the metric tensor on the unit sphere and [49, 47, 50]

$$u_{ij} \approx \frac{1}{2}\left[\nabla_i u_j + \nabla_j u_i + (\partial_i f)(\partial_j f)\right] - g^{\mathrm{s}}_{ij}\frac{f}{R}. \tag{2.3}$$

Similarly, changes in the mean curvature up to linear order in curvature and deformations follow from Eq. (2.2) as

$$H' \approx H + \nabla^2 f. \tag{2.4}$$

For a spherical reference surface of radius R, we have $H = 2/R$.

2.1.1 Spherical harmonic representation of quasi-spherical surfaces

To characterize the deformations of a quasi-spherical surface, in the sense that the surface remains star-convex with respect to the center of the coordinate system, we will throughout this chapter and chapter 3 use a representation of the radial displacement field in spherical harmonics.

The radial displacement field $f(\theta, \phi)$ for quasi-spherical surface is a scalar field on the sphere, and as such under light regularity conditions can be represented as a linear combination of spherical harmonics (Appendix A)

$$f(\theta, \phi) = \sum_{l=0}^{\infty} \sum_{m=-l}^{l} f_{lm} Y_{lm}(\theta, \phi). \tag{2.5}$$

The surface of the shell whose undeformed shape is a sphere of radius R is then located at $R(\theta, \phi) = R + f_{lm}$. The angular number l characterizes the angular size of the deformation such that $L \sim R/l$ is a characteristic lengthscale, while the number m indicates the deformation's orientation. To build a rotation-invariant measure of the intensity of deformations at angular scale l, we will frequently consider the power spectrum

$$P_l = \frac{1}{(2l+1)} \sum_{m=-l}^{l} \left(\frac{f_{lm}}{R} \right)^2 \tag{2.6}$$

which gives the average power per mode of angular number l. P_l, by rotational invariance, is independent of the choice of coordinates used to define the spherical harmonic transform.

2.2 Free energy of shallow elastic shells

Previous work investigating the mechanical properties of nuclear envelopes has demonstrated that their main structural constituents – the double lipid bilayer and the associated lamin filament meshwork – collectively give rise to an effective elasticity and bending rigidity [51, 52]. We thus describe the nuclear envelope in this work as a thin elastic membrane whose elasticity and bending rigidity lead to a resistance against stretching and bending, respectively. Such properties are captured by the free energy

$$F = \int \mathrm{d}\mathbf{r}^2 \left[\frac{\kappa}{2}(H' - H_0)^2 + \frac{1}{2} C_{ijkl}(u^{ij} - {u_0}^{ij})(u^{kl} - {u_0}^{kl}) - pf \right], \tag{2.7}$$

where κ denotes the bending rigidity and we use an elastic modulus tensor $C_{ijkl} = \lambda g_{ij} g_{kl} + \mu(g_{ik} g_{jl} + g_{jk} g_{il})$ with Lamé parameters λ, μ to describe an isotropic elastic response of the surface. For a 2D material, these parameters are related to the 2D Young modulus Y and the Poisson ratio ν by $\lambda = \nu Y/(1+\nu)$ and $2\mu = Y/(1+\nu)$. Additionally, we have introduced a spontaneous curvature H_0. We note that the spontaneous curvature H_0 adds an effective surface tension to the spherical reference surface that vanishes for $H_0 = 2/R$. As we will show below (SI Sec. 2.5) the spectral response of the shell is for sufficiently small curvature variations and mean radius changes equivalently affected by pressure and surface tension. Without loss of generality, we therefore only consider the effects of pressure and set $H_0 = 2/R$ in the free energy Eq. (2.7). The spontaneous strain $(u_0)_{ij}$ in the energy Eq. (2.7) will be specified below. Furthermore, we have introduced in Eq. (2.7) an external normal load that is dimensionally equivalent to a pressure $p(\mathbf{x}, t)$, where $p > 0$ ($p < 0$) correspond to normal forces pointing inwards (outwards). This pressure collects any contribution from thermodynamic and osmotic pressure differences across the surface, as well as from other mechanical interactions with its environment. The effects of a non-zero mean pressure are discussed in Sec. 2.5 below.

We also note that in the case of our application to cells' nuclear envelope, surface area is constantly increasing as development progresses: for our experimental situation [1], we find an area growth rate of about 0.35 to 0.6 percent per minute on average. However, this growth rate is very slow compared to the shape fluctuation timescale, which is on the order of minutes. We therefore consider a quasistatic approximation and neglect area growth.

We additionally allow for material properties that are described by the framework of non-Euclidean shells [53]. Specifically, the effective reference surface, with respect to which the energetic cost of stretching deformations is determined, may not actually be physically realizable in 3D Euclidean space. Such incompatibilities can arise from inelastic effects in the microscopic structure, such as growth, shrinkage or plastic cross-linking [54], but they can also be thought of as a way to effectively account for the presence of metastable states with low energy barriers in the free energy landscape. In this work, we found that an isotropic preferred strain of the form

$$(u_0)_{ij} = g^{\mathrm{s}}_{ij} \left(\frac{1}{R_c} - \frac{1}{R} \right) f, \tag{2.8}$$

is required to explain the experimental observations. The spontaneous strain given in Eq. (2.8) gives rise to incompatibilities, which can be seen as follows: If $R_c = R$, the energetic cost of surface stretching is entirely determined by deformations away from a spherical surface of radius R, compatible with the mean curvature $H_0 = 2/R$. If instead $R_c \neq R$, the effective reference surface for evaluating the energetic cost of out-of-plane deformations becomes instead a spherical surface of radius R with preferred principal curvatures $1/R_c$ everywhere.

With the spontaneous curvature and strain discussed above, and taking into account the shallow shell approximations for strains and curvature changes given in Eqs. (2.3) and (2.4), we arrive at the final free energy. Specifically, Eq. (2.7) becomes

$$F = \int \mathrm{d}\mathbf{r}^2 \left[\frac{\kappa}{2} (\nabla^2 f)^2 + \frac{\lambda}{2} \epsilon_i^{\ i} \epsilon_j^{\ j} + \mu \, \epsilon_{ij} \epsilon^{ij} - pf \right], \tag{2.9}$$

where $\epsilon_{ij} = u_{ij} - (u_0)_{ij}$ denotes the effective strain tensor with components

$$\epsilon_{ij} = \frac{1}{2} \left[\nabla_i u_j + \nabla_j u_i + (\partial_i f)(\partial_j f) \right] - g^{\mathrm{s}}_{ij} \frac{f}{R_c}. \tag{2.10}$$

From the strain given in Eq. (2.10), we see that in the limit of $R_c \to \infty$ the shell equations reduce to the conventional plate theory.

For vanishing pressure $p = 0$, three non-dimensional numbers govern the behavior of a shell described by Eq. (2.9) [47, 29]: the Föppl-von Kármán (FvK) number $\gamma = YR^2/\kappa \approx 10^4 - 10^6$ as discussed in Sec. 3.2.1 [52, 51], the bending rigidity relative to fluctuation intensity κ/kT_{eff}, and the curvature incompatibility R/R_c. If $p \neq 0$, a natural characteristic pressure is the critical buckling pressure $p_c = 4\sqrt{\kappa Y}/R^2$, above which a spherical shell with $R_c = R$ classically buckles; a fourth non-dimensional number p/p_c then becomes relevant to characterize the dynamics of the shell [47].

Finally, we note that by construction, the quality of the small-strain and shallow-shell approximation considered here degrades when used to describe large deformations. Specifically, the geometric approximations made to arrive at Eq. (2.9) will not capture the increasing importance of nonlinear contributions when deviations from the mean radius $\approx |f|/R$, become large. We also note that this free energy does not account for metastable states which commonly arise in shells; we however expect those metastable states to be less relevant when $R_c > R$ and the shell behaves closer to a 'spherical plate'.

2.3 Numerical simulations

To study fluctuating shells into regimes where nonlinear contributions are dominant, we here detail our simulation approach to directly simulate the overdamped stochastic PDE derived from the elastic energy F in Eq. (2.9) using a spherical harmonic variant of Fourier space Brownian dynamics [55]. This method will used for the results shown in Figs. 2-1, 2-2, and in comparison with experimental data in Chapter 3 to generate Fig. 3-5A,B.

In the absence of more detailed noise data, we assume that the fluctuations follow the fluctuation-dissipation theorem, with Gaussian fluctuations at an effective temperature T_{eff}. With this assumption, our results for the steady-state power spectra do not depend on the choice of damping function; to be consistent with the experimental setting of Chapter 3 we consider the shell to be immersed in a viscous fluid, with the fluid free to flow through the membrane. With our quasi-equilibrium assumption, we can authorize ourselves a simplified description of the fluid environment of the nucleus. For simplicity, we assume that both the inner and outer surroundings of the nuclear envelope can be described as a viscous low-Reynolds number fluid [30]. To keep the computational cost feasible, we approximate the corresponding non-local hydrodynamic coupling of the shell with the surrounding. To this end, we neglect radial shape variations and follow Refs. [56, 57] by considering the first order effect of viscous damping experienced by a spherical surface that pushes via a deformation into the surrounding fluid. In harmonic mode space, such a damping is described by [58] $\tilde{\Lambda}_{lm}^{-1} = \eta(2l+1)(2l^2+2l-1+2\delta_{l,0})/[l(l+1)R] \sim \eta l/R$. For simplicity, we additionally assume that the damping of tangential modes is the same as for the normal modes. We then find Langevin equations for the displacement fields $f(\mathbf{r},t)$ and $\mathbf{u}(\mathbf{r},t)$ in terms of the harmonic modes f_{lm} and $\mathbf{u}_{lm} = [u_{lm}^{(1)}, u_{lm}^{(2)}]^\top$ as

$$\partial_t f_{lm}(t) = \tilde{\Lambda}_{lm}\left(-\left[\frac{\delta F}{\delta f}\right]_{lm}(t) + \zeta_{f,lm}(t)\right) \tag{2.11a}$$

$$\partial_t \mathbf{u}_{lm} = \tilde{\Lambda}_{lm}\left(-\left[\frac{\delta F}{\delta \mathbf{u}}\right]_{lm}(t) + \boldsymbol{\zeta}_{u,lm}(t)\right). \tag{2.11b}$$

The Gaussian white noise components $\zeta_{f,lm}(t)$ and $\boldsymbol{\zeta}_{u,lm}(t)$ have zero mean and satisfy $\langle \zeta_{f,lm}(t)\zeta_{f,l'm'}(t')\rangle = 2kT_{\text{eff}}R^{-2}\tilde{\Lambda}_{lm}^{-1}\delta_{mm'}\delta_{ll'}\delta(t-t')$ and $\langle \boldsymbol{\zeta}^{\alpha}_{u,lm}(t)\boldsymbol{\zeta}^{\beta}_{u,l'm'}(t')\rangle = 2kT_{\text{eff}}R^{-2}\tilde{\Lambda}_{lm}^{-1}\delta_{mm'}\delta_{ll'}\delta(t-t')\delta_{\alpha\beta}$, where $\alpha = 1,2$ labels the two tangential components. As noted above, this noise satisfies the fluctuation-dissipation theorem. The functional derivatives of the free energy Eq. (2.9) used in the Langevin Eqs. (2.11a), (2.11b) are given in real space by

$$\begin{aligned}\frac{\delta F}{\delta f} =& \kappa\nabla^2\nabla^2 f - p + 4\frac{\lambda+\mu}{R_c^2}f - \frac{2}{R_c}(\lambda+\mu)\nabla\cdot\mathbf{u} + \frac{1}{R_c}(\lambda+\mu)\left[(\nabla f)^2 + 2f\nabla^2 f\right]\\ &- \mu\nabla\cdot\left([\nabla\mathbf{u}+\nabla\mathbf{u}^{\top}]\cdot\nabla f\right) - \left(\frac{\lambda}{2}+\mu\right)\nabla\cdot[(\nabla f)^2\nabla f] - \lambda\nabla\cdot[(\nabla\cdot\mathbf{u})\nabla f]\end{aligned} \tag{2.12a}$$

$$\begin{aligned}\frac{\delta F}{\delta \mathbf{u}} =& -(\lambda+\mu)\nabla(\nabla\cdot\mathbf{u}) - \mu\nabla^2\mathbf{u} + (\lambda+\mu)\frac{2}{R_c}\nabla f - \frac{\lambda}{2}\nabla[(\nabla f)^2]\\ &- \mu\left[\nabla^2 f\nabla f + \nabla\nabla f\cdot\nabla f\right].\end{aligned} \tag{2.12b}$$

We assume for all simulations that the Poisson modulus is constant with an intermediate value of $\nu = 0.3$, as is typical for isotropic 2D materials. The 2D Lamé parameters are then related to the 2D Young modulus Y by [59]

$$\lambda = \frac{\nu Y}{1-\nu^2} \qquad\qquad \mu = \frac{Y}{2(1+\nu)}. \tag{2.13}$$

All simulations are performed using $\eta = 4\,\text{Pa}\cdot\text{s}$. For simulations with fixed FvK number γ, we set R, R_c and $kT_{\text{eff}} \geq kT_{\text{eq}}$, and vary κ and $Y = \gamma\kappa/R^2$. To stay within reasonable physical regimes ($\kappa \sim 25kT_{\text{eq}} \sim 10^{-19}\,\text{J}$ for lipid bilayers), and $\gamma \sim 10^4 - 10^6$ using $T_{\text{eff}} = 10T_{\text{eq}}$, we vary κ/kT_{eff} in the range $2-20$. In the absence of structural information on the preferred curvature of the nuclear envelope, and motivated by the experimental observation that the qualitative response of the shell does not depend on the size of the nuclei, we choose $R_c = 20R$, such that the crossover lengthscale $L_{\text{el}} = R\gamma^{-1/4}\sqrt{R_c/R}$ where the linear response function 'falls off' into the bending-dominated regime is approximately equal to $R/2$ for $\gamma = 10^4$. This choice both suppresses the appearance of a plateau region in P_l (Sec. 2.4.1, Fig. 2-1), and lowers the energy barrier to larger deformations which, while allowed by the non-convex elastic free energy in finite deformation regimes, are not allowed in our free energy based on a shallow-shell assumption.

We use the pseudo-spectral solver Dedalus 3 [60] to solve the Langevin equation on the surface of the sphere. The equation is spatially discretized with spherical harmonics up to degree $L_{\max} = N - 1$, resolving scales down to $\delta = \pi R/N$ on the surface of the sphere. The nonlinear terms are computed on the Gaussian quadrature grid using a dealiasing factor of 2. The system is temporally integrated using the Euler-Mayurama stochastic integrator. We choose a resolution of $N = 256$ to ensure we sufficiently resolve the elastic scale $L_{\text{el}} = R\gamma^{-1/4}$ for FvK number $\gamma = 10^6$. We rescale all lengths by the radius R and time by $\tau = 4\eta R/Y$, which is the characteristic timescale of the dynamics induced by the cubic terms in the PDEs. The simulations are performed for a duration of 3000τ with time steps of $\Delta t = 10^{-2}\tau$, where each simulation ran on 32 Intel Xeon Platinum 8260 cores on the MIT Supercloud cluster [61], totalling approximately 360 hours of CPU time per simulation for the parameter values considered.

A posteriori checks for convergence are performed by monitoring the dynamics of the mean shell radius. We also verify that the shallow-shell approximation remains valid throughout simulations by monitoring the average norm of the in-plane displacements $\langle|\mathbf{u}|\rangle$. Specifically, we check that in-plane displacements remain small relative to the shell radius and relative to radial deformations, i.e. $\langle|\mathbf{u}|\rangle < 10^{-2}R < \langle|f|\rangle$ for results in Fig. 3-5A,B. We note that the mean radius variation can reach large fractions of the radius for very soft nuclei, limiting the validity of the free energy in Eq. (2.9).

2.4 Scaling behavior of fluctuating elastic shells

In this section we establish a range of linear and nonlinear results that can be obtained from the energy Eq. (2.9) for a fluctuating thin shell. After discussing the basic linear response, we describe how to obtain a free energy written only in terms of the radial displacement, and use this effective free energy to obtain asymptotic scaling behavior results that build on insights from previous renormalization analysis of similar models.

Throughout this section, we consider Gaussian fluctuations with an effective temperature T_{eff} to account for both passive and active fluctuations.

2.4.1 Linear response to fluctuations

We first derive the equilibrium power spectrum P_l of shells described by Eq. (2.9) in the linear response regime by extending a result from reference [47] to the case of $R_c \neq R$. For an external uniform pressure $p = 0$, when shell fluctuations are small enough for the system to be in the linear regime, the free energy Eq. (2.9) is given to quadratic order in the fields by

$$\begin{aligned} F^{\text{lin}} = \frac{1}{2} \int \mathrm{d}^2\mathbf{r} \Bigg[&\kappa(\nabla_{\mathcal{S}}^2 f)^2 + \frac{4(\lambda+\mu)}{R_c^2} f^2 + \lambda(\nabla_{\mathcal{S}} \cdot \mathbf{u})^2 \\ &+ \frac{\mu}{4}\left(\nabla_i u_j + \nabla_j u_i\right)\left(\nabla^i u^j + \nabla^j u^i\right) + \frac{2(\lambda+\mu)}{R_c} f(\nabla_{\mathcal{S}} \cdot \mathbf{u}) \Bigg], \end{aligned} \tag{2.14}$$

where we have introduced the spherical in-plane gradient $\nabla_{\mathcal{S}} = R^{-1}(\mathbf{e}_\theta \partial_\theta + \mathbf{e}_\phi \sin\theta^{-1} \partial_\phi)$. We expand the components f of normal displacements and in-plane displacements $\mathbf{u} = u^i \mathbf{e}_i$ using real scalar and vector spherical harmonics, respectively, such that (Appendix A)

$$f(\mathbf{r}) = \sum_{l=0}^{\infty} \sum_{m=-l}^{m=l} f_{lm} Y_{lm}(\theta, \phi) \tag{2.15a}$$

$$\mathbf{u}(\mathbf{r}) = \sum_{l=1}^{\infty} \sum_{m=-l}^{m=l} \left(u_{lm}^{(1)} \boldsymbol{\Psi}_{lm}(\theta, \phi) + u_{lm}^{(2)} \boldsymbol{\Phi}_{lm}(\theta, \phi) \right), \tag{2.15b}$$

where $\mathbf{\Psi}_{lm} = \nabla_{\mathcal{S}} Y_{lm}$ and $\mathbf{\Phi}_{lm} = \mathbf{e}_r \times \nabla_{\mathcal{S}} Y_{lm}$. Note that with this convention, $u^{(1)}_{lm}$ and $u^{(2)}_{lm}$ have dimensions of (length)^2. Using the identities

$$\int \mathrm{d}^2\mathbf{r} f(\nabla_{\mathcal{S}} \cdot \mathbf{u}) = -\frac{1}{R}\sum_{l,m} l(l+1) u^{(1)}_{lm} f_{lm} \tag{2.16a}$$

$$\int \mathrm{d}^2\mathbf{r} (\nabla_{\mathcal{S}} \cdot \mathbf{u})^2 = \frac{1}{R^2}\sum_{l,m} l^2(l+1)^2 \left(u^{(1)}_{lm}\right)^2 \tag{2.16b}$$

$$\begin{aligned}\frac{1}{4}\int \mathrm{d}^2\mathbf{r} \left(\nabla_i u_j + \nabla_j u_i\right)\left(\nabla^i u^j + \nabla^j u^i\right) &= \frac{1}{R^2}\sum_{l,m} l(l+1)\left(l(l+1)-1\right)\left(u^{(1)}_{lm}\right)^2 \\ &+ \frac{1}{2R^2}\sum_{l,m} l(l+1)\left(l(l+1)-2\right)\left(u^{(2)}_{lm}\right)^2,\end{aligned} \tag{2.16c}$$

which follow from standard properties of scalar and vector-valued spherical harmonics (Appendix A, [62]), we can expand the linearized free energy Eq. (2.14) in terms of the spherical harmonic basis as

$$\begin{aligned}F^{\mathrm{lin}} = \sum_{l,m} &\frac{1}{2}\left[\kappa(l-1)^2(l+2)^2 + 4(\lambda+\mu)\left(\frac{R}{R_c}\right)^2 R^2\right]\left(\frac{f_{lm}}{R}\right)^2 \\ &+ \frac{1}{2} l(l+1)\left[(\lambda+2\mu)l(l+1) - 2\mu\right]\left(u^{(1)}_{lm}\right)^2 + \frac{\mu}{2} l(l+1)\left(l(l+1)-2\right)\left(u^{(2)}_{lm}\right)^2 \\ &- 2\frac{\lambda+\mu}{R_c} R l(l+1) u^{(1)}_{lm} f_{lm}.\end{aligned} \tag{2.17}$$

Within our Gaussian fluctuation assumption, we can functionally integrate out the $u^{(1)}_{lm}$ fields to obtain an effective free energy in terms of f_{lm} only

$$F^{\mathrm{lin}}_{\mathrm{eff}} = \sum_{lm} \frac{1}{2}\left[\kappa(l-1)^2(l+2)^2 + 4(\lambda+\mu)\left(\frac{R}{R_c}\right)^2 R^2\left(1 - \frac{(\lambda+\mu)l(l+1)}{(\lambda+2\mu)l(l+1)-2\mu}\right)\right]\left(\frac{f_{lm}}{R}\right)^2 \tag{2.18}$$

This quadratic free energy then lends itself to the equipartition theorem, and we finally find that the spherical harmonic power spectrum $P_l = (2l+1)^{-1}\sum_m (f_{lm}/R)^2$

follows

$$kT_{\mathrm{eff}}P_l^{-1} = \kappa(l+2)^2(l-1)^2 + 4\mu\left(\frac{R}{R_c}\right)^2 R^2\frac{(\lambda+\mu)(l^2+l-2)}{(\lambda+2\mu)l(l+1)-2\mu}. \tag{2.19}$$

This result agrees with Ref. [47] for $R = R_c$ and serves as a benchmark to validate our numerical simulations (Fig. 2-1A,B, see Sec. 2.3). From Eq. (2.19) it follows that P_l is dominated by the effects of bending at high angular number, where it behaves as $P_l \propto l^{-4}$. At low angular number P_l is dominated by the harmonic 'confining' elastic term and approaches a constant of the order $P_l \sim 1/Y$ with the 2D Young modulus $Y \sim \lambda, \mu$ [59]. The crossover between those two regimes is expected to happen at angular number $l = l_{\mathrm{el}} \equiv \gamma^{1/4}\sqrt{R/R_c}$, where $\gamma = YR^2/\kappa$ is the FvK number.

A criterion that strictly ensures the validity of conclusions drawn from this linear analysis is given by $(kT_{\mathrm{eff}}/\kappa)\sqrt{\gamma} \ll 1$ [47, 29]. For FvK number values of $\gamma > 10^4$ considered here, this criterion then approximately yields the condition $kT_{\mathrm{eff}}/\kappa \ll 10^{-2}$. However, even for a typical lipid bilayer bending rigidity $\kappa \sim 10kT_{\mathrm{eq}}$ with room temperature T_{eq} this condition is not expected to be satisfied. Hence, while this linear analysis provides important insights into the effects of the curvature mismatch R/R_c and helps validate the numerical approach, further analysis presented below is needed the explain the scaling observed in experiments and in numerical simulations for strong fluctuations.

Effective radial free energy

In the next step, we explain how to obtain the scaling form for the free energy presented in Eq. (2.39). Assuming Gaussian fluctuations of an elastic shell described by Eq. (2.9), it is possible to integrate out the in-plane displacements $\mathbf{u} = u^i\mathbf{e}_i$ and the mean radial displacement $f_0 = (4\pi R^2)^{-1}\int \mathrm{d}^2\mathbf{x}\, f$ [63, 46, 47, 29]. This procedure yields an effective free energy written purely in terms of the normal displacements. For convenience, we collect in the following several results distributed across the above references into a single explicit derivation.

We start from the elastic free energy in Eq. (2.9), rewritten in terms of the isotropic elastic tensor $C_{ijkl} = \mu(\delta_{ik}\delta_{jl}+\delta_{il}\delta_{jk})+\lambda\delta_{ij}\delta_{kl}$ and dropping the explicit pressure term for now. We write

$$F = F^{\mathrm{bend}} + F^{\mathrm{stretch}} := \int \mathrm{d}^2\mathbf{x} \left[\frac{\kappa}{2}(\nabla^2 f)^2 + \frac{1}{2}C_{ijkl}\epsilon_{ij}\epsilon_{kl}\right]. \tag{2.20}$$

To use the shallow-shell approach, we consider here a portion of a shallow shell of area A, such that we can use a two-dimensional Cartesian coordinate system and Fourier transforms to describe our fields. As found in Eq. (2.10) by considering in the shallow-shell regime a Cartesian metric $g_{ij} = \delta_{ij}$, the strain tensor is $\epsilon_{ij} = u_{ij} + \frac{1}{2}\partial_i f \partial_j f - \delta_{ij} f/R_c$, where we denote in this section by $u_{ij} = \frac{1}{2}[\partial_i u_j + \partial_j u_i]$ only the *in-plane* contributions of the strain tensor. To simplify the integration procedure, we decompose the symmetric tensor $A_{ij} = \frac{1}{2}\partial_i f \partial_j f$ into a longitudinal and transverse part [63, 46]

$$\frac{1}{2}\partial_i f \partial_j f = \frac{1}{2}[\partial_i v_j + \partial_j v_i] + P^T_{ij} h, \tag{2.21}$$

with a vector field v_i, a scalar field h, and the transverse projection operator $P^T_{ij} = (\delta_{ij} - \partial_i\partial_j/\nabla^2)$. Applying the latter to both sides of this equation, we find $h(\mathbf{x}) = \frac{1}{2}P^T_{ij}\partial_i f \partial_j f$. We will also separate the radial displacement $f(\mathbf{x}) = f_0 + f'(\mathbf{x})$ into its uniform and spatially-dependent parts f_0 and $f'(\mathbf{x})$, respectively.

Here, we use the Fourier convention of the Supplementary Information of Ref. [47], where the direct transform is $f(\mathbf{q}) = (1/A)\int \mathrm{d}^2\mathbf{x}\, f(\mathbf{x})e^{i\mathbf{q}\cdot\mathbf{x}}$ and the inverse is given by $f(\mathbf{x}) = \sum_{\mathbf{q}} f(\mathbf{q})e^{-i\mathbf{q}\cdot\mathbf{x}}$. To keep the notation compact, we use the same symbols for functions in real and Fourier space and indicate their dependence by explicitly writing the argument. Finally, we note that by reality of the displacements fields, each field $f(\mathbf{x})$, $h(\mathbf{x})$ and $\mathbf{u}(\mathbf{x})$ satisfies $f(\mathbf{q}) = f(-\mathbf{q})^*$, with $f(\mathbf{q})^*$ denoting the complex conjugate of $f(\mathbf{q})$.

Fourier representation of the free energy: We can now rewrite the free energy in terms of the displacement fields mode amplitudes. The bending energy can be expressed as $F^{\mathrm{bend}} = (\kappa/2)\sum_{\mathbf{q}} q^4|f(\mathbf{q})|^2$. In the following, we focus on the stretching part $F^{\text{stretch}} = (1/2) \int \mathrm{d}^2\mathbf{x}\, C_{ijkl}\epsilon_{ij}\epsilon_{kl}$ of the free energy. By defining the shifted variable

$$\tilde{u}_i(\mathbf{q}) = u_i(\mathbf{q}) + v_i(\mathbf{q}), \tag{2.22}$$

we can express the contributions from $u_i(\mathbf{q})$ and $v_i(\mathbf{q})$ in terms of the quadratic form $C_{ij}(\mathbf{q}) = \mu q^2(\delta_{ij} - q_i q_j/q^2) + (\lambda + 2\mu) q_i q_j$. We then find a free energy that is quadratic in $\tilde{u}_i(\mathbf{q})$, $h(\mathbf{q})$ and $f(\mathbf{q})$, and given by

$$\begin{aligned} F^{\text{stretch}} = {} & A C_{ijkl}\left(u_{ij}^0 + A_{ij}^0 - \delta_{ij} f_0/R_c\right)\left(u_{kl}^0 + A_{kl}^0 - \delta_{kl} f_0/R_c\right) \\ & + \sum_{\mathbf{q}\neq 0} \tilde{u}_i(\mathbf{q}) C_{ij}(\mathbf{q}) \tilde{u}_j(-\mathbf{q}) + \tilde{u}_i(\mathbf{q}) B_i(-\mathbf{q}) + B_i(\mathbf{q}) \tilde{u}_i(-\mathbf{q}) \\ & + \sum_{\mathbf{q}\neq 0} (\lambda + 2\mu)|h(\mathbf{q})|^2 + 4(\lambda + \mu)\frac{|f(\mathbf{q})|^2}{R_c^2} - \frac{2}{R_c}(\lambda + \mu)\left[f(\mathbf{q})h(-\mathbf{q}) + f(-\mathbf{q})h(\mathbf{q})\right]. \end{aligned} \tag{2.23}$$

Here, we denoted for convenience the uniform modes by

$$u_{ij}^0 := u_{ij}(\mathbf{q} = 0) \quad \text{and} \quad A_{ij}^0 := A_{ij}(\mathbf{q} = 0), \tag{2.24}$$

and introduced $h(\mathbf{q}) = (\delta_{ij} - q_i q_j/q^2) A_{ij}(\mathbf{q})$, as well as

$$B_i(\mathbf{q}) = -i\lambda q_i h(\mathbf{q}) + i\frac{2}{R_c}(\lambda + \mu) q_i f(\mathbf{q}). \tag{2.25}$$

To proceed, we distinguish between the spatially uniform modes ($\mathbf{q} = 0$) and spatially non-uniform modes ($\mathbf{q} \neq 0$).

Spatially non-uniform modes ($\mathbf{q} \neq 0$): We can observe from Eq. (2.23) that spatially non-uniform modes contribute quadratically in $\tilde{\mathbf{u}}(\mathbf{q} \neq 0)$. These modes can therefore be integrated out using the Gaussian Path integral [64]

$$F_{\text{eff}}[f_0, f'] = -kT_{\text{eff}} \ln\left(\int \prod \mathcal{D}u_{ij}^0 \prod_{\mathbf{q}\neq 0} \mathcal{D}\tilde{\mathbf{u}}(\mathbf{q}) \exp\left(-F/(kT_{\text{eff}})\right)\right). \tag{2.26}$$

The contributions from the in-plane degrees of freedom given in the second line of Eq. (2.23), once integrated out, yield a contribution to the effective free energy that is given by

$$\sum_{\mathbf{q}\neq 0} -C_{ij}^{-1}(\mathbf{q}) B_i(\mathbf{q}) B_j(-\mathbf{q}), \tag{2.27}$$

with the inverse of the elastic quadratic form $C_{ij}^{-1}(\mathbf{q}) = \left(\delta_{ij} - q_i q_j/q^2\right)/(\mu q^2) + (\lambda + 2\mu)^{-1}(q_i q_j/q^4)$. Taken together, the spatially non-uniform contributions in the free energy Eq. (2.23) yield an effective free energy

$$\begin{aligned} F_{\text{eff}}^{\text{stretch},\mathbf{q}\neq 0} &= \frac{1}{2}\sum_{\mathbf{q}\neq 0} \frac{1}{\lambda+2\mu}\bigg(-\lambda^2|h(\mathbf{q})|^2 - 4(\lambda+\mu)^2\frac{f^2}{R_c^2} \\ &\qquad + 2\frac{\lambda}{R_c}(\lambda+\mu)\left(f(\mathbf{q})h(-\mathbf{q}) + f(-\mathbf{q})h(\mathbf{q})\right)\bigg) \\ &\quad + (\lambda+2\mu)|h(\mathbf{q})|^2 + 4(\lambda+\mu)\frac{f^2}{R_c^2} - \frac{2}{R_c}(\lambda+\mu)\left(f(\mathbf{q})h(-\mathbf{q}) + f(-\mathbf{q})h(\mathbf{q})\right). \end{aligned}$$

This expression can be simplified using that $h(\mathbf{x})$ and $f(\mathbf{x})$ are real: Defining the 2D Young modulus $Y = 4\mu(\lambda+\mu)/(\lambda+2\mu)$, the contributions from the spatially-varying modes can be written as

$$\begin{aligned} F_{\text{eff}}^{\text{stretch},\mathbf{q}\neq 0} &= \frac{1}{2}\sum_{\mathbf{q}\neq 0} Y|h(\mathbf{q})|^2 + Y\frac{|f(\mathbf{q})|^2}{R_c^2} - \frac{Y}{R_c}\left(f(\mathbf{q})h(-\mathbf{q}) + f(-\mathbf{q})h(\mathbf{q})\right) \\ &= \sum_{\mathbf{q}\neq 0} \frac{Y}{2}\left|h(\mathbf{q}) - \frac{f(\mathbf{q})}{R_c}\right|^2 \\ &= \int \mathrm{d}^2\mathbf{x}\, \frac{Y}{2}\left(\frac{1}{2}P_{ij}^T(\partial_i f \partial_j f) - \frac{f'}{R}\right)^2, \end{aligned} \tag{2.28}$$

where the last line follows from Parseval's theorem. In the case of a flat sheet with $R = \infty$, we recover the classical result presented in Ref. [46]. In particular, one can understand the role of the term $\frac{1}{2}P_{ij}^T(\partial_i f \partial_j f)$ through the geometric identity [46]

$$\nabla^2\left[\frac{1}{2}P_{ij}^T(\partial_i f \partial_j f)\right] = -K(\mathbf{x}), \tag{2.29}$$

where $K(\mathbf{x})$ is the Gaussian curvature of the deformed sheet: In a similar fashion as for the Airy stress function formalism of plate mechanics [49], the integration of in-plane degrees of freedom leads to a situation in which Gaussian curvature acts as a charge density for a stress-generating 'curvature potential' [65].

Spatially uniform modes ($\mathbf{q} = 0$): The zero-wavenumber contributions to the strain tensor, $\epsilon_{ij}^0 := \epsilon_{ij}(\mathbf{q} = 0)$, in Fourier space can be written as

$$\epsilon_{11}^0 = u_{11}^0 + A_{11}^0 - f_0/R_c \tag{2.30a}$$

$$\epsilon_{22}^0 = u_{22}^0 + A_{22}^0 - f_0/R_c \tag{2.30b}$$

$$\epsilon_{12}^0 = u_{12}^0 + A_{12}^0, \tag{2.30c}$$

where we recall that u_{ij}^0 refers to the modes corresponding to uniform in-plane strains. Of the three of these, only two are independent since $u_{11}^0 + u_{22}^0 = 0$, as otherwise this would indicate a uniform stretching of the shell which would lead to a variation in mean radius. We can then define $\Delta u^0 = u_{11}^0 - u_{22}^0$, and write $u_{11}^0 = -u_{22}^0 = \Delta u^0/2$. We can thus rewrite the spatially uniform contributions to the free energy (first line in Eq. (2.23)) as

$$\begin{aligned} F_0^{\text{stretch}} = \frac{A}{2} C_{ijkl} \epsilon_{ij}^0 \epsilon_{kl}^0 =& \frac{A}{2} \Bigg[\lambda \left(A_{11}^0 + A_{22}^0 - 2\frac{f_0}{R_c} \right)^2 + 4\mu \left(u_{12}^0 + A_{12}^0 \right)^2 \\ & + 2\mu \left(\frac{\Delta u^0}{2} + A_{11}^0 - \frac{f_0}{R_c} \right)^2 + 2\mu \left(-\frac{\Delta u^0}{2} + A_{22}^0 - \frac{f_0}{R_c} \right)^2 \Bigg]. \end{aligned} \tag{2.31}$$

We can now directly integrate out the u_{12}^0 field, and by shifting $\Delta u^0 \leftarrow \Delta u^0 + A_{11}^0 + A_{22}^0$ and integrating the field Δu^0, we finally find

$$F_{0,\text{eff}}^{\text{stretch}} = \frac{A}{2} (\lambda + \mu) \left(A_{11}^0 + A_{22}^0 - 2\frac{f_0}{R_c} \right)^2. \tag{2.32}$$

By using $A_{11}^0 + A_{22}^0 = \frac{1}{A} \int \mathrm{d}^2\mathbf{x} |\nabla f|^2$ and including the pressure term, we hence have the final, total effective free energy as

$$\begin{aligned}F_{\text{eff}}[f', f_0] = \int \mathrm{d}^2\mathbf{x} \Bigg[& \frac{\kappa}{2}(\nabla^2 f)^2 + \frac{Y}{2}\left(\frac{1}{2}P^T_{ij}(\partial_i f \partial_j f) - \frac{f'}{R_c}\right)^2 \\ & + \frac{\lambda+\mu}{2}\left(\frac{1}{A}\int \mathrm{d}^2\mathbf{x} |\nabla f|^2 - 2\frac{f_0}{R_c}\right)^2 \Bigg] \\ & - \int \mathrm{d}^2\mathbf{x}\, p(\mathbf{x},t) f(\mathbf{x},t). \end{aligned} \tag{2.33}$$

Effect of pressure: If $p(\mathbf{x},t) = p_0$, then $\int \mathrm{d}^2\mathbf{x}\, p(\mathbf{x},t) f(\mathbf{x},t) = \int \mathrm{d}^2\mathbf{x}\, p_0 f_0$, and after completing the square we can integrate out f_0. We now find

$$F_{\text{eff}}[f'] = \int \mathrm{d}^2\mathbf{x} \left[\frac{\kappa}{2}(\nabla^2 f)^2 - \frac{p_0 R_c}{2}|\nabla f'|^2 + \frac{Y}{2}\left(\frac{1}{2}P^T_{ij}(\partial_i f \partial_j f) - \frac{f'}{R_c}\right)^2 \right]. \tag{2.34}$$

Denoting the spatial average by $\langle . \rangle$, the mean value of f_0 is given by

$$f_0 = \frac{p_0 R_c^2}{4(\lambda+\mu)} + \frac{R_c}{4}\langle |\nabla f'|^2 \rangle. \tag{2.35}$$

If we now consider inhomogeneous contributions to the pressure and write $p(\mathbf{x},t) = p_0 + p'(\mathbf{x},t)$ with $\int \mathrm{d}^2\mathbf{x}\, p'(\mathbf{x},t) = 0$, we find an effective free energy in terms of f' that reads

$$F_{\text{eff}}[f', p'] = \int \mathrm{d}^2\mathbf{x} \left[\frac{\kappa}{2}(\nabla^2 f)^2 - \frac{p_0 R_c}{2}|\nabla f'|^2 + \frac{Y}{2}\left(\frac{1}{2}P^T_{ij}(\partial_i f \partial_j f) - \frac{f'}{R_c}\right)^2 - p' f' \right]. \tag{2.36}$$

After expanding the square, this yields

$$\begin{aligned} F_{\text{eff}} = & \frac{1}{2}\int \mathrm{d}^2\mathbf{r} \left[\kappa(\nabla^2 f)^2 - p_0 R_c (\nabla f)^2 + \frac{Y}{R_c^2} f^2 \right] \\ & + \frac{1}{2}\int \mathrm{d}^2\mathbf{r} \left[\frac{Y}{R_c} f P^T_{ij} \partial_i f \partial_j f \right] \\ & + \int \mathrm{d}^2\mathbf{r} \left[\frac{Y}{8} P^T_{ij} \partial_i f \partial_j f P^T_{kl} \partial_k f \partial_l f - p' f' \right]. \end{aligned} \tag{2.37}$$

Dimensional scaling: If we can assume $p_0 = 0$, we can consider shape variations on a length scale L, and read off from Eq. (2.37) the expected relative contributions of the different terms to the free energy density

$$\delta F_{\text{eff}} \sim \kappa \left(\frac{f}{L^2}\right)^2 + Y\left(\frac{f}{R_c}\right)^2 + \frac{Y}{R_c}\left(\frac{f^3}{L^2}\right) + Y\left(\frac{f}{L}\right)^4 - pf, \qquad (2.38)$$

where $F_{\text{eff}} = \int \mathrm{d}^2\mathbf{r}\, \delta F_{\text{eff}}$. To obtain an analytical prediction for the scaling in the larger-deformation regime $h \sim \sqrt{\kappa/Y} \ll f \ll R < R_c$, we rewrite Eq. (2.38) as

$$\frac{\delta F_{\text{eff}}}{Y} \sim \left(\frac{h}{L}\right)^2\left(\frac{f}{L}\right)^2 + \left(\frac{f}{R_c}\right)^2 + \frac{f}{R_c}\left(\frac{f}{L}\right)^2 + \left(\frac{f}{L}\right)^4 - \frac{pf}{Y}. \qquad (2.39)$$

The first term corresponds to bending, and the second and third terms arise from the non-zero curvature of the undeformed shell. The fourth term describes the non-linear response associated with changes in the Gaussian curvature of the shells. For deformed surfaces with $f \gg h$, the first term can be neglected as it is smaller than the fourth term. Considering deformation amplitudes f_l at the spatial length scale $L \sim R/l$, where l is the angular wave number, the remaining terms can be recast as

$$\frac{\delta F_l}{Y} \sim \left(\frac{f_l}{R_c}\right)^2 + \frac{f_l}{R_c}\left(\frac{f_l}{R}\right)^2 l^2 + \left(\frac{f_l}{R}\right)^4 l^4 - \frac{p}{Y} f_l. \qquad (2.40)$$

Since $R_c > R$, the first two terms will be dominated by the l^4-term implying that, at steady-state, this quartic term and the pressure term must balance out, consistent with a corresponding earlier result for flat plates with $R_c = \infty$ [66]. We thus find $f_l \sim (p/Y)^{1/3}(R/l)^{4/3}$, and hence for the angular power spectrum $P_l \sim (f_l/R)^2$ the scaling law

$$P_l \sim \left(\frac{pR}{Y}\right)^{2/3} l^{-8/3}. \qquad (2.41)$$

In this scaling regime, the surface deformation dynamics is dominated by the shell's resistance to stretching, which causes changes in its Gaussian curvature [67]. The emergence of this regime is observed in our spherical shell simulations for soft shells (Fig. 2-1). If $p_0 \neq 0$, we expect generically from Eq. (2.37) the presence of an additional surface tension term $\sim \nabla^2 f$. However, we find that 'crumpled' shells have vanishing surface tension, under conditions detailed in Sec. 2.5. This scaling analysis thus holds for the rough surfaces we consider in experiments, with p replaced by an effective pressure p_{eff} to accommodate the effects of geometric confinement (Sec. 2.5).

2.4.2 Renormalization of mechanical surface properties and comparison with simulations

We now refine Eq. (2.38) by adapting results from renormalization studies of curved elastic surfaces [47, 29] in order to explain in more detail the observed deviations from linear response in the simulations for soft shells (Fig. 2-1).

Generally, it is expected that thermal fluctuations at length scales $L \sim R/l$ contribute most significantly to the effective mechanical properties of the surface if $L > L_{\text{th}}$, where $L_{\text{th}} = \sqrt{\kappa^2/(kT_{\text{eff}}Y)}$ is the characteristic thermal length scale of the shell. Indeed, it was shown in Refs. [47, 29] that fluctuations in the presence of strong geometrical nonlinearities give rise to length scale-dependent elastic constants and an effective pressure. Specifically, the bending modulus κ, the 2D Young modulus Y, as well as a fluctuation-induced pressure behave in weakly nonlinear regimes as [29]

$$\kappa_R(L) = \kappa(L/L_{\text{th}})^{\eta} \tag{2.42a}$$

$$Y_R(L) = Y(L/L_{\text{th}})^{-\eta_u} \tag{2.42b}$$

$$p_R(L) - p_0 = p_c(L_{\text{th}}/L_{\text{el}})(L/L_{\text{th}})^{2\eta} \tag{2.42c}$$

with exponents set by $\eta \approx 0.8$ and $\eta_u + 2\eta = 2$ and $L_{\text{el}} = (\kappa R^2/Y)^{1/4} = R\gamma^{-1/4}$ is the characteristic elastic length scale beyond which stretching effects dominate over bending for $R = R_c$. Note that except for p_c, all the quantities and scaling exponents in Eqs. (2.42) are independent of the radius R and hence do not depend on the presence of the curvature mismatch $R_c > R$. Far in the bending response-dominated regime at high angular numbers, we then expect from Eqs. (2.42a) and Eq. (2.38) $P_l \sim (kT_{\text{eff}}/\kappa_R)l^{-4} \sim l^{-3.2}$. Thus, as observed in our simulations (Fig. 2-1C), an increasing FvK number γ – corresponding to an increasing significance of nonlinear contributions to the surface mechanics – gradually changes angular number power laws describing the shell response from l^{-4} to $l^{-3.2}$, before reaching a $l^{-8/3}$-scaling [see Eq. (2.41)] in the strongly nonlinear regime.

To better understand the limits of the renormalization approach, it is helpful to remember that the above scaling relations Eq. (2.42) are derived from the integration of the RG flow equations: as contributions from rapidly-varying modes are integrated during the renormalization procedure, the effective scale-dependent elastic parameters are found to satisfy a set of ordinary differential equations in the the parameter $s = \ln(L/a)$ known as the RG flow equations

$$\frac{\mathrm{d}\kappa_R}{\mathrm{d}s} = \beta_\kappa(\kappa_R, p_R, Y_R, R_R, \Lambda) \tag{2.43a}$$

$$\frac{\mathrm{d}p_R}{\mathrm{d}s} = \beta_p(\kappa_R, p_R, Y_R, R_R, \Lambda) \tag{2.43b}$$

$$\frac{\mathrm{d}Y_R}{\mathrm{d}s} = \beta_Y(\kappa_R, p_R, Y_R, R_R, \Lambda) \tag{2.43c}$$

$$\frac{\mathrm{d}R_R}{\mathrm{d}s} = \beta_R(\kappa_R, p_R, Y_R, R_R, \Lambda), \tag{2.43d}$$

where $a = 1/\Lambda \ll R$ is a microscopic lengthscale that does not affect the integration results as long as it is chosen to be small compared to all other lengthscales involved. The integration of these equations from initial conditions (κ, p_0, Y, R) then leads to the scale-dependent parameters $\kappa_R(L), p_R(L), Y_R(L)$, where the lengthscale relates to the wavenumber through $L = \pi/q$ (Fig. 2-2A,C). The precise form of the β-functions is available in Appendix A of Ref. [29].

2.4.3 Power spectrum scaling for large fluctuations

A surprising result from renormalization analysis [29] indicated by Eq. (2.42c) is that fluctuations induce an effective pressure acting on the surface which can cause shells to spontaneously buckle. For the purpose of the following discussion, we consider the renormalized pressure p_R in Eq. (2.42c) at long wavelengths [47]. In this regime, the

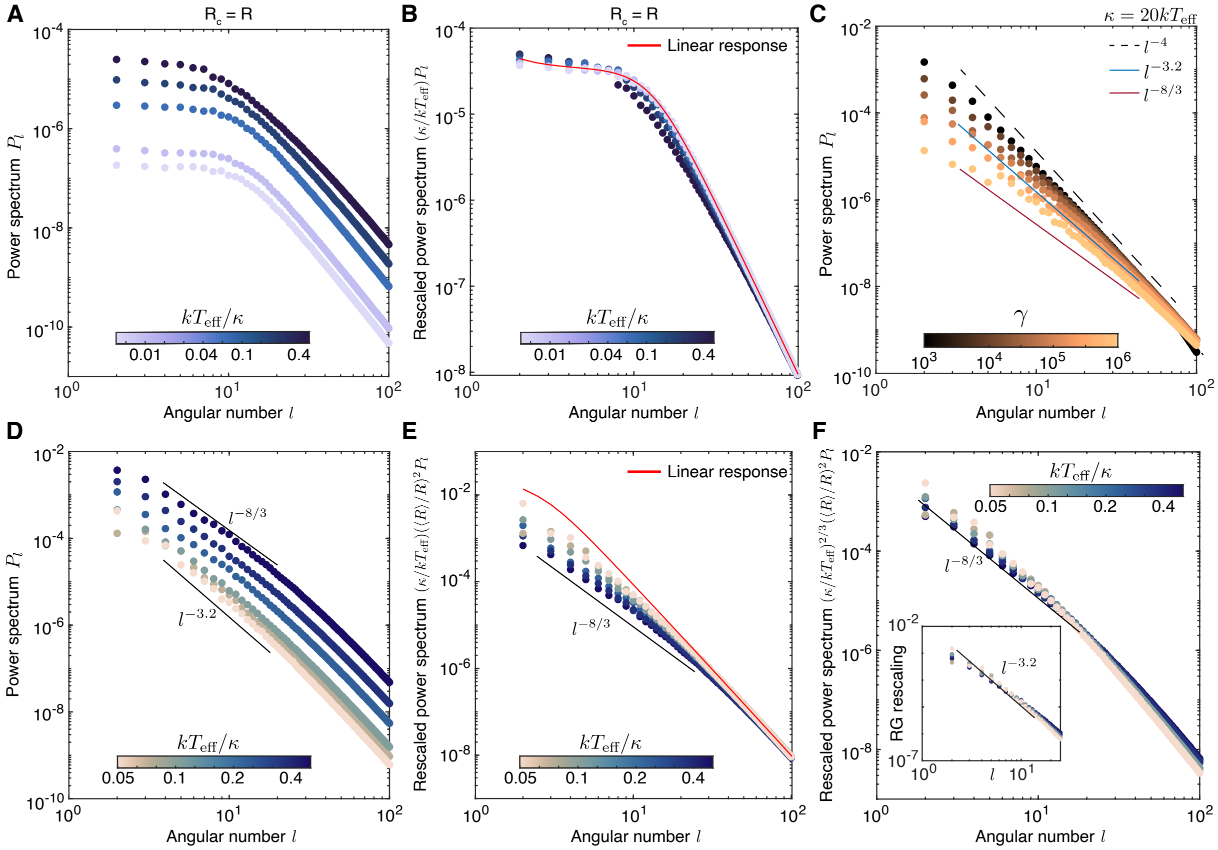

Figure 2-1 : Fluctuating elastic shells. **A,** Fluctuating elastic shell power spectra for $R_c = R$, $\gamma = 3 \times 10^4$ for a variable elastic modulus controlled through kT_{eff}/κ. **B,** Rescaled power spectra from panel **A,** show the validity of the linear regime for stiff shells, and the departure of the shell response from linear response (Eq. (2.19), red solid line) with decreasing rigidity. **C,** Fluctuating elastic shell power spectra for $R_c = 20R$ and variable FvK number γ for constant bending modulus controlled through $\kappa = 20kT_{\text{eff}}$. With increasing γ, nonlinear contributions to the shell elasticity modulate the power spectrum of radial deformations, consistent with predictions from renormalization and scaling arguments. **D,** Full power spectrum for the simulations presented in Fig. 3-5A,B for fixed FvK number $\gamma = 3 \times 10^4$ and $R_c = 20R$. **E,** Rescaling the power spectra from **D** by $(\kappa/kT_{\text{eff}})(\langle R\rangle/R)^2$ shows the departure from linear response Eq. (2.19) **F,** Rescaling the power spectra from **D** by $(\kappa/kT_{\text{eff}})^{2/3}(\langle R\rangle/R)^2$ shows a collapse to a master curve at intermediate wavenumbers, in accordance with the scaling analysis Eq. (2.48). Inset: Rescaling by $(\kappa/kT_{\text{eff}})^{0.6}(\langle R\rangle/R)^2$ as suggested by the RG scaling prediction Eq. (2.49) leads to a similar collapse, confirming the similarity between both viewpoints. All simulations were performed using $T_{\text{eff}} = 10T_{\text{eq}}$ with $T_{\text{eq}} = 300\,\text{K}$.

renormalized pressure is given by

$$p_R \sim p_c \left(\frac{kT_{\text{eff}}}{\kappa}\right)\sqrt{\frac{YR^2}{\kappa}} \sim \frac{Y}{R}\left(\frac{kT_{\text{eff}}}{\kappa}\right), \tag{2.44}$$

where $p_c = 4\sqrt{\kappa Y}/R^2$ is the classical critical buckling pressure determined from a linear stability analysis of an elastic shell [47, 29]. Consequently, the elastic shell is expected to buckle when $p_{\text{eff}} = p_R + p > p_c$. For $p = 0$ and $R_c = R$, Ref. [29] finds from integrating the renormalization group flow that buckling should therefore occur around $p_{\text{eff}}/p_c = (kT_{\text{eff}}/\kappa)\sqrt{\gamma} \gtrapprox 160$. When $R_c > R$, the added tendency for the shell to locally flatten will further modify the buckling pressure, with a new rescaled critical pressure given by $\bar{p}_c = (R/R_c)^2 p_c$. In general, by showing the instability of the ground state of the elastic free energy Eq. (2.37), this signals the breakdown of the validity of the renormalization group analysis from Ref. [29]. However one could expect the scaling form of $p_{\text{eff}} = p_R$ to stay valid in the post-buckling regime of interest to us. Under this assumption, and using the scaling result $P_l \sim (pR/Y)^{2/3} l^{-8/3}$ from the large fluctuation regime with $p \to p_R$, we find

$$P_l \sim \left(\frac{kT_{\text{eff}}}{\kappa}\right)^{2/3} l^{-8/3}, \tag{2.45}$$

independently of the stretching modulus. However, we remark that when the mean radius of the shell $\langle R \rangle = R - \int (4\pi)^{-1} \mathrm{d}\Omega\, f$ deviates from the undeformed radius R (especially when we let $R_c > R$) this scaling has to be corrected as follows.

In the asymptotic regime where we expect the $l^{-8/3}$ scaling to hold, the balance of the nonlinear contribution to surface elasticity with the pressure in Eqs. (2.39) and (2.40) still leads to

$$\frac{Y}{R^4} l^4 f_l^3 \sim p, \tag{2.46}$$

where the spatial length scale $L = R/l$ is related to the undeformed sphere radius R in our simulations. Letting $\langle R \rangle \neq R$, our definition of $P_l \sim (f_l/\langle R \rangle)^2$ in Eq. (3.2) corresponds to a normalization with respect to the *deformed* average shell radius, and we have with Eq. (2.46) that

$$P_l \sim \left(\frac{pR^4}{Y\langle R\rangle^3}\right)^{2/3} l^{-8/3}. \tag{2.47}$$

We then observe that the result of the scaling of the pressure in Eq. (2.44) does not depend on the mean radius $\langle R\rangle$ of the shell, as the outcome of an analysis where the radius of the shell R only plays a role as a material parameter. With this observation, we find from Eq. (2.47)

$$P_l \sim \left(\frac{kT_{\text{eff}}}{\kappa}\right)^{2/3} \left(\frac{R}{\langle R\rangle}\right)^2 l^{-8/3}, \tag{2.48}$$

which is equivalent to Eq. (2.45) for $R/\langle R\rangle \approx 1$.

A similar argument stands for comparisons to theoretical linear regime predictions Eq. (2.19), where a rescaling of P_l by $(\kappa/kT_{\text{eff}})(\langle R\rangle/R)^2$ should lead to a curve collapse even when $R_c > R$ and the mean radius deviates significantly from R. However, we find that for the simulations presented in Fig. 3-5A,B and Fig. 2-1D, a rescaling by $(\kappa/kT_{\text{eff}})(\langle R\rangle/R)^2$ does not lead to a curve collapse, confirming the departure from linear response for those simulation parameters (Fig. 2-1E). Instead, rescaling P_l by $(\kappa/kT)^{2/3}(\langle R\rangle/R)^2$, as suggested by Eq. (2.48), does lead to a collapse of simulation results onto a master curve for corresponding angular numbers l (Fig. 2-1F), further highlighting the importance of contributions from nonlinear surface elasticity for explaining our observations in simulations and experiments.

We note that these scaling results are very similar to RG scaling predictions: in a regime where the shell response is dominated by the renormalized bending rigidity, then

$$P_l \sim \left(\frac{kT_{\text{eff}}}{\kappa}\right)^{1-\eta/2} \gamma^{-\eta/2} \left(\frac{R}{\langle R\rangle}\right)^2 l^{-4+\eta} \approx \left(\frac{kT_{\text{eff}}}{\kappa}\right)^{0.6} \gamma^{-0.4} \left(\frac{R}{\langle R\rangle}\right)^2 l^{-3.2}, \tag{2.49}$$

with $\eta \approx 0.8$. The corresponding curve collapse is shown in the inset of Fig. 2-1F. This result serves as confirmation that both approaches, either using perturbative corrections to the linear response or using dimensional arguments to obtain a scaling form for the nonlinear response, lead to reasonable predictions [68].

2.5 Effects of non-zero uniform pressure

Our results above assumed that the system is in an environment where $p_0 = 0$. Here, we revisit this assumption on the basis of RG predictions and simulations, and provide justification for an experimentally-relevant regime in which the effective surface tension of the shell is 0. Integrating out the mean radial dynamics in Eq. (2.33) leads to an effective surface tension in Eq. (2.36) with value $\sigma_{\text{eff}} = -p_0 R$. The physical effects due to this tension strongly depend on the sign of p_0:

When the pressure is oriented outwards ($p_0 < 0$) it tends to stabilize the shell, akin to an inflated rubber balloon. Consequently, fluctuations are suppressed, leading to the power spectrum scaling as l^{-2} due to the gradient-squared term in the free energy Eq. (2.37). However, when the pressure forces are oriented inwards ($p_0 > 0$) they tend to buckle the shell, with the shell eventually becoming unstable. Its stabilization can then only be realized through higher-order geometric nonlinearities. The resulting states are characterized by 'ruffled surfaces' with excess area available to compensate for surface tension.

To make those physical ideas precise, we integrate the RG flow equations Eqs. (2.43) and run numerical Langevin simulation for a range of different pressures (Fig. 2-2). In a low-deformation regime ($R_c = R$), simulation results agree with RG predictions (Fig. 2-2A,B): Negative pressure stabilizes the shell, while positive pressure leads to a resonant wavelength. Note, however, that larger positive pressures lead to divergent responses in the RG prediction: To 1-loop perturbative order, the RG flow equations diverge as nonlinear contributions to the free energy dominate the linear effects [29]. In a high-deformation regime ($R_c = 20R$), large negative pressure indeed leads to the expected l^{-2}, which corresponds to a tension-dominated regime. However, positive pressure always leads to divergences; the corresponding simulations show a qualitatively similar response between $p_0 = 0$ and $p_0 > 0$ curves, with a scaling exponent that corresponds to the effective bending response (Fig. 2-2C,D). It is interesting to note that even the $p_0 = 0$ response diverges at long-wavelength (not shown), which in the simulated system is limited by the infrared cutoff $1/R$.

Up to the limit where very large inward pressure forces lead to self-contact of shells, our results suggest that ruffled surfaces with wrinkles available to provide excess area have responses that are rather insensitive to pressure variation. This finding complements previous work that has experimentally found that the mean radius and volume of nuclear envelope in yeast cells are well-described by membranes with vanishing surface tension, which is explained by the presence of excess area buffering tension [69, 70]. This suggests that the dominant effect of osmotic pressure changes is an increase or decrease in the amount of excess area, while surface tension remains negligible. Therefore, we expect the $P_l \sim l^{-8/3}$ scaling result or its RG equivalent, which were obtained neglecting surface tension, still hold in our system even when osmotic pressure differences p_0 are non-zero.

To make the connection between p_0 introduced in Eq. (2.36) with the pressure p_{eff} appearing in Eq. (2.41) explicit, consider the scaling law obeyed by the deformed nucleus in Eq. (2.47),

$$P_l = \left(\frac{p' R^4}{Y \langle R \rangle^3} \right)^{2/3} l^{-8/3} \equiv \left(\frac{p_{\text{eff}} R}{Y} \right)^{2/3} l^{-8/3}, \tag{2.50}$$

where the effective pressure is given by

$$p_{\text{eff}} = p' \left(\frac{R}{\langle R \rangle} \right)^3, \tag{2.51}$$

with $\langle p_{\text{eff}} \rangle = 0$. This equation holds in our system, assuming that the crumpled surface leads to a vanishing surface tension. The effective pressure p_{eff} captures the effect of excess area in the power spectrum P_l, which in turn changes the mean radius $\langle R \rangle$. To connect the osmotic pressure difference p_0 to the crumpled shell's mean radius $\langle R \rangle$, we rewrite Eq. (2.35) in terms of the power spectrum P_l as

$$f_0 = \frac{p_0 R_c}{4(\lambda + \mu)} + \frac{R_c}{4} \sum_l P_l (2l+1) l (l+1), \tag{2.52}$$

where $\langle R\rangle = R - \langle f_0\rangle$ by construction of the Fourier transform in Sec. 2.4.1 (note that f_0 is distinct from the spherical harmonic f_{00}). Note that as $P_l \sim l^{-4}$ for large l, the sum is logarithmically divergent. However, for a stabilizing outward pressure $p_0 < 0$, a 1-loop perturbative RG expansion reveals a well-defined nonlinear relationship between $\langle R\rangle$ and p_0 [29]. For $p_0 > 0$, we can use a similar approach to the one in Ref. [56] to obtain an expression for the excess area by introducing a cut-off angular number $l_\xi < \gamma^{1/2} = R/h$. The resulting, cut-off-dependent estimate of $\langle R\rangle$ then follows from Eqs. (2.47) and (2.52) as the solution of

$$\langle R\rangle^3 + \left(\frac{p_0 R_c}{4(\lambda+\mu)} - R\right)\langle R\rangle^2 + \frac{R_c}{4}\left(\frac{p' R^4}{Y}\right)^{2/3}\xi = 0, \tag{2.53}$$

where $\xi = \sum_{l=1}^{l_\xi}(2l+1)l(l+1)l^{-8/3}$. Eq. (2.53) then leads to a nonlinear relationship between p_{eff} and p_0 in the presence of inhomogeneous loads p'. Our previous scaling results can thus be applied when $p_0 \neq 0$ by replacing p' with the effective load p_{eff} given in Eq. (2.51).

2.6 Conclusion

In this chapter, we have studied the statistical mechanics of an elastic shallow shell, which despite being made out of an isotropic linear elastic material, has a strongly nonlinear behavior owing to the geometric nonlinearities arising in the thin shell (large FvK number) limit. In chapter 3 we will find that the nuclear envelopes, the membranes defining cell nuclei, display a mechanical behavior that is well described by this nonlinear theory.

While the Föppl-von Kármán plate equation is valid even at large deformations, as long as the coordinate description is valid, the presence of a non-zero preferred curvature of the breaks down this validity by introducing metastable states that are not captured by the convex free energy Eq. (2.9). Effectively, by introducing $R_c \neq R$, we are using a ‘convex relaxation’ of the physical problem which ignores the non-convexity of the physical energy landscape. Rationalizing the construction of R_c and

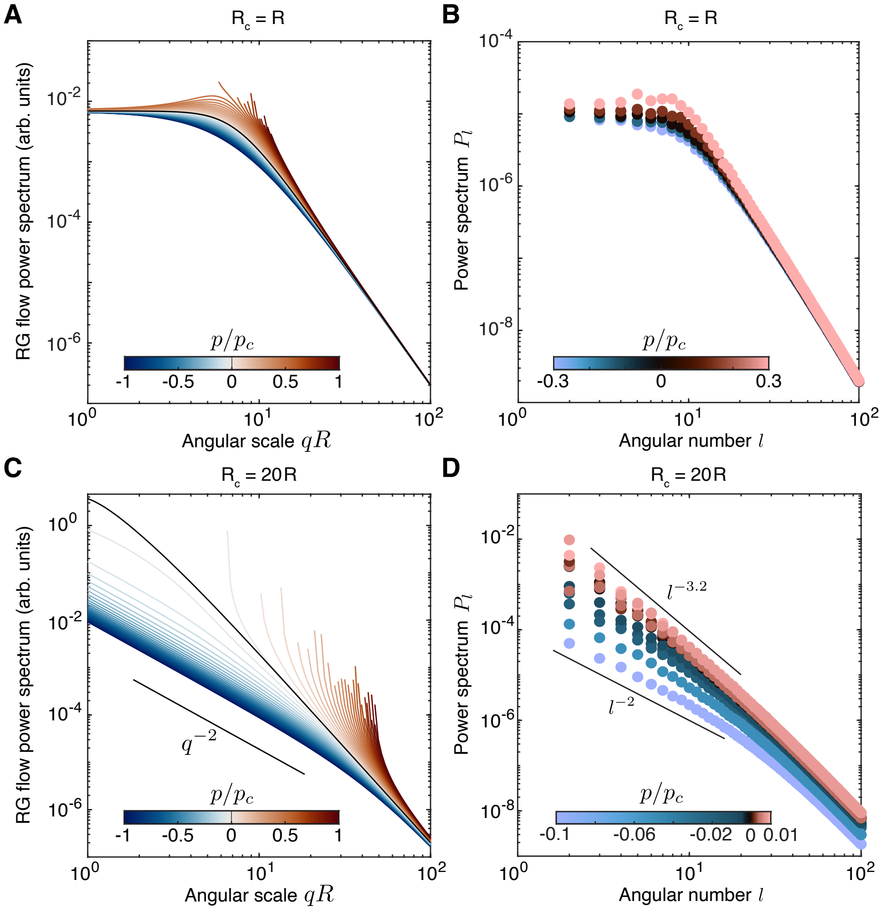

Figure 2-2 : The effects of non-zero pressure. **A,** Effective power spectrum obtained by integrating the renormalization group (RG) flow near the linear regime for varying pressure. High-enough positive pressures lead to a divergent RG flow, indicated by interrupted lines. In these cases, RG predictions are unreliable. **B,** Simulation data of a shell with $\gamma = 3 \cdot 10^4$, $\kappa = 5kT_{\text{eff}}$ and $R_c = R$ for varying pressure. In this smaller-deformation regime, data qualitatively agrees with RG. **C,** RG flow for varying pressure for $R_c = 20R$. Negative pressures lead to a q^{-2} scaling response at long-wavelengths, while even small positive pressures lead to divergent responses within 1-loop perturbative RG. **D,** Simulation data of a shell with $\gamma = 3 \cdot 10^4$, $\kappa = 5kT_{\text{eff}}$ and $R_c = 20R$ for varying pressure. Negative pressures, which stabilize the shell, lead to a l^{-2} response in accordance with RG. Positive pressures are stabilized by nonlinear effects.

deriving equivalent scaling results for more general shell models would be interesting problems in their own right.

Chapter 3

Geometry and mechanics of nuclear wrinkles

Parts of this chapter has been previously published as a preprint 'Dynamics, scaling behavior and control of nuclear envelope wrinkling', J. A. Jackson, N. Romeo, A. Mietke, K. J. Burns, J. F. Totz, A. C. Martin, J. Dunkel and J. Imran Alsous. (2023). Experimental data and figures are courtesy of Jonathan A. Jackson and Jasmin Imran Alsous.

Wrinkling and flickering of flexible sheet-like structures essentially determine mechanics and transport in a wide range of physical and biological systems, from graphene [71, 66] and DNA origami [72] to nuclear envelopes (NEs) [73, 74, 8, 75] and cell membranes [76, 77]. Over the last decade, much progress has been made through experimental and theoretical work in understanding the effects of environmental fluctuations on the bending behaviors of carbon-based monolayers [78] and the shape deformations of lipid bilayer membranes of vesicles [79, 80, 81] and cells [82, 57]. In contrast, the emergence and dynamical evolution of surface deformations in NEs [83, 8, 75] at different length- and timescales, to which we refer throughout this chapter simply as 'wrinkling', still pose fundamental open questions, as performing three-dimensional (3D) observations at high spatio-temporal resolution remains challenging, especially under natural physiological and developmental growth conditions. Specifically, it is unclear how NE wrinkle formation proceeds during cellular development, which biophysical processes govern wrinkle morphology, and whether there exist characteristic scaling laws for NE surface fluctuations [74, 84, 8]. Addressing these questions through quantitative measurements promises insights into the physics of complex membranes and can clarify the biological and biomedical implications of NE deformations that have been linked to gene expression [8], cellular aging [85], and disease like progeria syndrome [86, 73].

In this chapter, we combine 3D confocal microscopy, theoretical analysis, and simulations to characterize the wrinkling morphology and dynamics of nuclear surfaces in fruit fly egg chambers. A spectral analysis of over 300 nuclei provides evidence for an asymptotic power-law scaling of the surface fluctuations, consistent with predictions from renormalization calculations [46, 29] and scaling arguments based on a nonlinear elasticity model for thin shells. Although the scaling is found to be highly robust against physical and biological perturbations, its magnitude (prefactor) can be tuned via osmotic pressure variation and microtubule disruption. These two different control mechanisms enable the tuning and probing of the NE's spectral and mechanical properties, and provide biophysical strategies for suppressing and reversing nuclear wrinkling.

3.1 Characterizing the nuclear envelope geometry

The NE is a double membrane that separates the cell's nuclear interior from the surrounding cytoplasm. The two concentric ∼4 nm-thick lipid bilayers are ∼20-50 nm apart and are supported by the nuclear lamina, a non-contractile meshwork of intermediate filaments that lie adjacent to the inner nuclear membrane, conferring mechanical stability and affecting essential cellular processes through regulation of chromatin organization and gene expression [87, 88]. Among other proteins, the NE contains nuclear pore complexes, multi-protein channels that primarily regulate passage of macromolecules between the nucleus and the cytoplasm [89, 90]. Recent *in vitro* studies have provided key insights into the role of lamins, cytoplasmic structures, and the physical environment in affecting NE morphology, as well as evidence

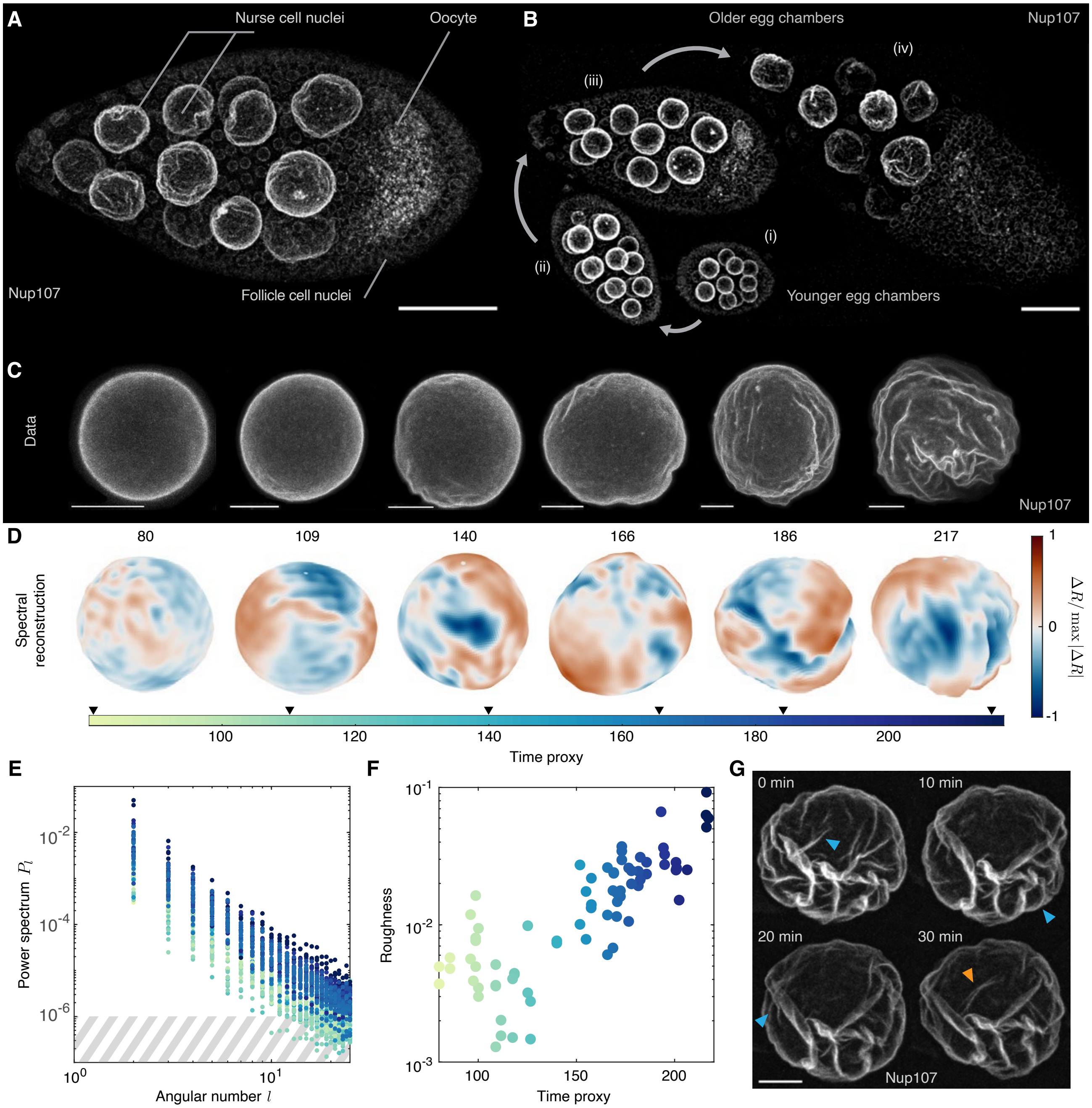

Figure 3-1 *(Caption next page)*

Figure 3-1 *(previous page)*: Dynamic wrinkling of nurse cell nuclear envelopes during *Drosophila* egg development. **A,** Maximum-intensity projection (MIP) of a 3D image of an egg chamber expressing GFP-labeled Nup107, a component of the nuclear pore complex. The wrinkled nuclei of the 15 nurse cells are substantially larger than those of the surrounding follicle cells. **B,** MIP of four egg chambers showing an increase in nurse cell nuclear size and nuclear surface deformation as egg chambers age. Curved arrows indicate developmental progression from youngest (i) to oldest (iv). **E,** MIPs of individual nurse cell nuclei from six egg chambers spanning all ages included in our dataset, showing an increase in nuclear radius and NE wrinkling with age. Note that scale bar is the same size for each image; oldest nucleus shown is about 2.3 times the diameter of youngest shown. **D,** Spectral reconstruction of NE surfaces shown in **C** from 3D microscopy data using spherical harmonics with an angular number up to $l_{\max} = 25$ (Eq. (3.1)). Time proxy values for each nucleus are included above the reconstructions. **E,** Power spectra normalized by average radius for $N = 78$ nuclei from 39 egg chambers in nurse cells directly connected to the oocyte (results are qualitatively similar for nuclei farther away from the oocyte; Fig. 3-2). Hashed area indicates approximate noise threshold for young nuclei; color indicates the time proxy (corresponding to the color bar in **D**). **F,** NE roughness $\mathcal{R} = \sum_{l \geq 3}(2l+1)P_l$ for the same nuclei as in **E** increases exponentially with time proxy (see also Fig. 3-2). **G,** Snapshots of the same nucleus at four different time points illustrate that NE wrinkling is a dynamic process. Blue and orange arrowheads point to wrinkles that disappear and appear, respectively, between subsequent frames. Scale bars: 50 μm (**A, B**), 10 μm (**C, G**).

for the critical importance of nuclear shape for many cellular and nuclear functions [84, 73], including transcriptional dynamics [8]. Despite notable progress, a quantitative understanding of how wrinkling phenomenology and 3D spectral properties of nuclear surfaces evolve in time and during cellular development has remained elusive.

To investigate the biophysical dynamics, scaling behaviors, and reversibility of nuclear wrinkling, we used the egg chamber of the fruit fly *Drosophila melanogaster*, a powerful system amenable to 3D high-resolution live imaging and targeted biological and physical perturbations [91]. The egg chamber contains 15 nurse cells and the oocyte (the immature egg cell), all connected via cytoplasmic bridges and enclosed by a thin layer of hundreds of follicle cells (Fig. 3-1A, [92]). For most of the ∼3 days of oogenesis, the nurse cells supply proteins, mRNAs, and organelles to the oocyte through diffusion and microtubule-mediated directed transport [93, 94, 30, 95]. To provide the prodigious amount of material and nutrients that the oocyte needs, each nurse cell replicates its DNA ∼10 times without undergoing cell division, thereby notably increasing its nuclear and cell sizes [96]. In the ∼30-hour window studied here, the diameter of nurse cell nuclei in cells directly connected to the oocyte increases from approximately 16 to about 40 micrometers [97, 96], accompanied by the progressive appearance of fold-like deformations in the NE, providing an ideal test bed for studying the onset and evolution of NE wrinkling (Fig. 3-1B,C).

To compare nurse cell nuclei within the same egg chamber and across different egg chambers, we defined a proxy measurement for developmental time (referred to here as the ‘time proxy’) based on the geometric average of the egg chamber’s length and width. Since egg chamber geometry correlates closely with developmental progression, adopting this continuous geometric characterization offers finer temporal resolution than the traditional approach of distinguishing 14 discrete morphological stages [93, 94] (for a comparison between the time proxy and developmental stage, see [1]). By time-ordering nuclei according to this metric, we could more accurately determine the time of emergence of nuclear wrinkling and reconstruct its evolution (Fig. 3-1B,C). To track the NEs of the nurse cells in space and time, we used a fluorescently-tagged version of the nuclear pore complex protein Nup107 that delineates the nucleus (qualitatively similar wrinkling patterns were observed using a different labeled protein in the NE and via label-free imaging, [1]); note that this label allows observation only of deformations that include both membranes of the nuclear envelope, but is unlikely to label deformations that include only the inner membrane, such as Type I nucleoplasmic reticula [98, 99]. Having acquired highly resolved 3D imaging data (Fig. 3-1C, Fig. 3-4), we reconstructed the nuclear surface radius $R(\theta, \phi)$ relative to the geometric center of the nucleus, where θ and ϕ are the spherical polar angles.

3.1.1 Using egg chamber geometry as proxy for developmental time

Egg chamber age, or progression through oogenesis, has traditionally been determined using broad morphological features, with chambers grouped into 14 stages, each of which encompasses several hours [94, 93, 96]. However, these stages provide a discrete time measurement with insufficient resolution for describing the continuous process of wrinkling progression, which occurs over much smaller time scales. Therefore, to determine if a readily-measurable and continuous-valued metric is suited for age comparisons and ranking egg chambers' progression through development, we plotted manually-determined egg chamber stages against several different size and morphological characteristics. One such metric, which we term the 'time proxy', is the geometric average of the egg chamber width and anterior-posterior axis length. This time proxy technically has units of distance (μm), but is left unitless on plots as the measure is used solely for arranging egg chambers in time relative to one another. When egg chambers were aligned with their long axis horizontal to the objective (their midplane aligned with the imaging plane), linear measurements were made using maximum intensity projections; when egg chambers were tilted, axis measurements were made in 3D space using the '3D_Distance_Tool' FIJI macro. Stages showed nearly monotonic increase with respect to the time proxy described above, unlike with other metrics such as follicle cell height, egg chamber length or width, or oocyte length [1]. Notably, this time proxy is similar to egg chamber cross-sectional area and to germline area, previously determined by others to be a good proxy for age [100, 101].

Nuclei in nurse cells directly connected to the oocyte are larger than those in the more anterior nurse cells during the egg chamber ages considered in this study [102]. Because of this size difference within a given egg chamber, plotting roughness against effective nucleus radius reveals separate trends for the two populations of nurse cell nuclei; nucleus radius is thus not an effective metric for comparing egg chambers across time [1]. This size difference also means nurse cells nearer the anterior have higher roughness values for the same nucleus radius than cells nearer the oocyte, suggesting that age increase alone is unlikely to explain the patterns of wrinkling observed in the data.

3.1.2 Spectral representation of nuclear envelope geometry

To obtain a compact 3D spectral representation of the nuclear surface deformations, in a similar manner as in Sec. 2.1.1 we computed the real spherical harmonic coefficients f_{lm} defined by

$$R(\theta, \phi) = \sum_{l=0}^{l_{\max}} \sum_{m=-l}^{l} f_{lm} Y_{lm}(\theta, \phi), \tag{3.1}$$

where Y_{lm} is the spherical harmonic with angular number l and order m (See Appendix A). Equation (3.1) allows for a continuous reconstruction of the NEs (Fig 3-1D, Fig. 3-4), with the mode-cutoff $l_{\max}$ setting the angular resolution of the spectral representation. The coefficient values $\{f_{lm}\}$ depend on the choice of coordinate system, that is, the orientation of the nuclei. To obtain a rotation-invariant characterization of the surface wrinkles, we consider the power spectrum of radial out-of-plane deformations

$$P_l = \frac{4\pi}{(2l+1) f_{00}^2} \sum_{m=-l}^{l} f_{lm}^2, \tag{3.2}$$

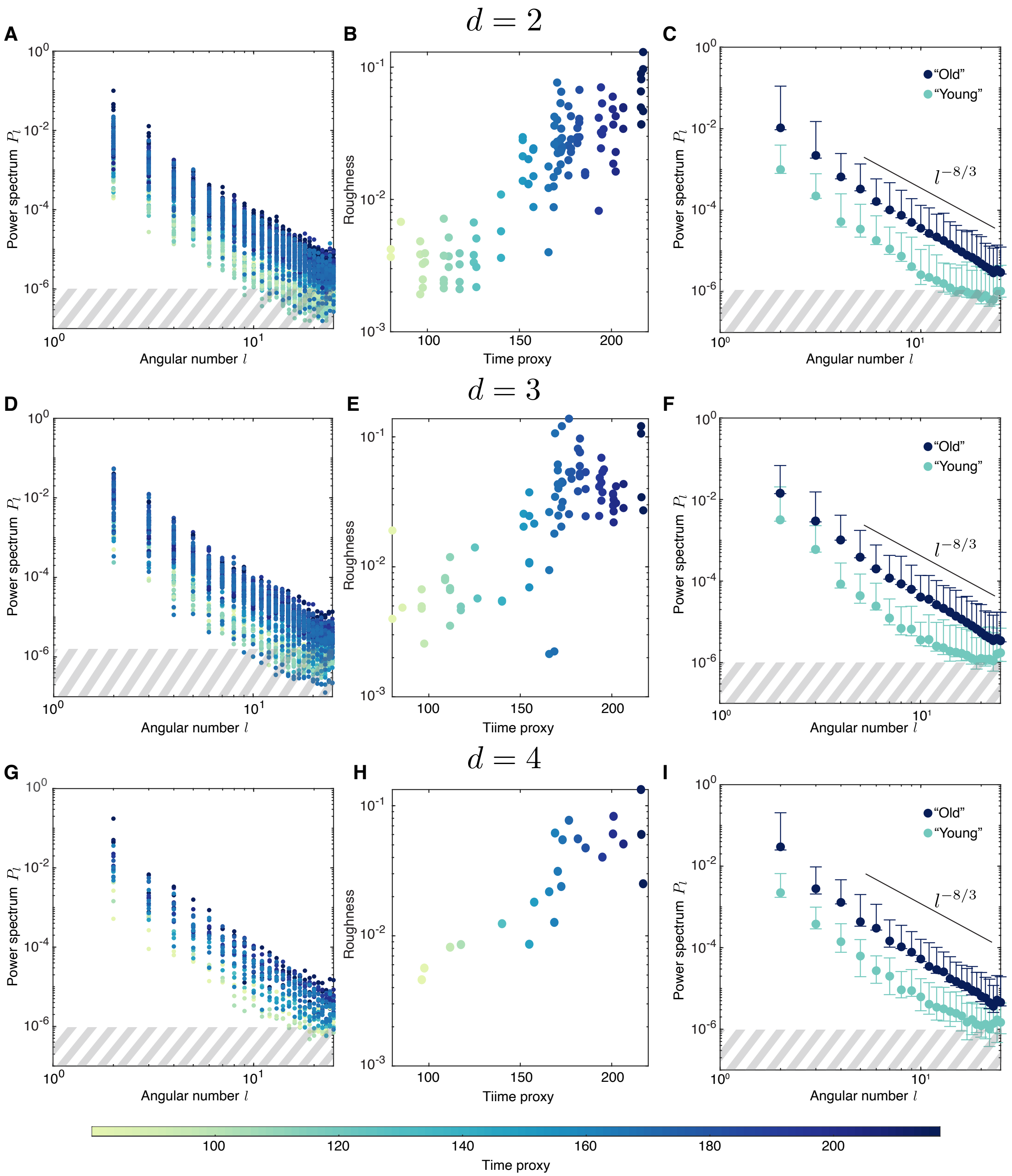

Figure 3-2 *(Caption next page)*

Figure 3-2 *(previous page)*: The analyses used for Fig. 3-1E,F and Fig. 3-5C for different sets of nurse cell nuclei yield qualitatively similar results. For nuclei d cells away from the oocyte, the same analysis as performed for cells directly connected to the oocyte is repeated with the same color bar throughout. **A,D,G** Power spectra P_l colored by time proxy, as in Fig. 3-1E. **B,E,H** Roughness as in Fig. 3-1F. **C,F,I** Binned average of "old" nuclei as in Fig. 3-5C reveals the same scaling behavior. "Young" nuclei have time proxy between $80 - 140$; "Old" nuclei have time proxy between $160 - 220$. Intervals in panels **C,F,I** represent extremal values. $N = 115$ nuclei for $d = 2$ (29 young and 72 old), from 41 egg chambers, $N = 86$ nuclei for $d = 3$ (17 young and 59 old), from 39 egg chambers, $N = 23$ nuclei for $d = 4$ (4 young and 16 old), from 23 egg chambers.

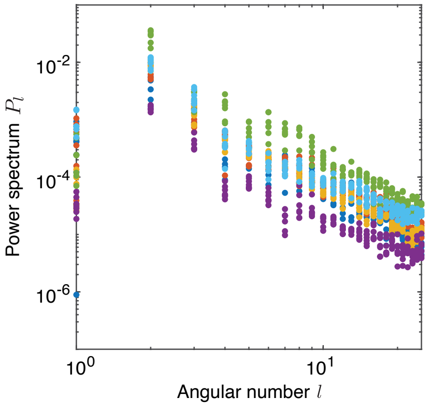

Figure 3-3 : 3D high-resolution imaging reveals the fluctuating nature of NE wrinkles. Power spectrum P_l of different frames of a time series of nuclei 3d snapshots do not overlap, indicating that NE morphology is fluctuating in time. Each color corresponds to a different nucleus, with identically-colored points corresponding to different frames.

normalized by the average radius of the shell $\langle R\rangle = f_{00}/\sqrt{4\pi}$ (note that this is a slightly different normalization than used in Sec. 2.1.1). The non-negative numbers P_l measure the average power in a mode of angular wavenumber l. A single-valued summary statistic of surface wrinkling can be given in terms of the 'roughness' parameter $\mathcal{R} = \sum_{l\geq 3}(2l+1)P_l$, the total power contained in angular numbers $l \geq 3$. By ignoring the long-wavelength modes $l < 3$, $\mathcal{R}$ measures the contribution of finer-scale wrinkles to NE deformations. Our analysis of over 300 nurse cell nuclei shows that the power spectrum of NEs maintains an approximately constant shape as development progresses, but with a steadily-increasing amplitude (Fig. 3-1E; Fig. 3-2), reflecting the fact that wrinkling becomes more pronounced as nuclei increase in size. $\mathcal{R}$ increases exponentially with the time proxy (Fig. 3-1F), suggesting that nurse cell nuclei transition smoothly from an unwrinkled to a wrinkled state.

Extraction of nuclear membrane coordinates

Nuclear envelopes were segmented and their coordinates extracted using FIJI and the MorphoLibJ plugin [103, 104]. Custom-built Matlab code [62] was used to perform least-square fits to determine spherical harmonic coefficients up-to the cutoff mode number $l_{\max} = 25$, which corresponds to an angular scale of roughly $7\,^{\circ}$, as well as to measure the LamC:Nup107 ratio over developmental time.

Images of Nup107::GFP nuclei were preprocessed using FIJI's built-in rolling-ball background subtraction method with a radius of 50 pixels, followed by applying a Gaussian blur with a width of 2 pixels. Segmentation was performed for still images using the 'Interactive Marker-controlled Watershed' algorithm of the MorphoLibJ library [104], and live images were segmented using the 'Marker-controlled Watershed' algorithm in a custom-built FIJI macro. In both cases, one seed point was used for each nucleus and another was used for the background. Individual nuclei were then isolated in FIJI, if necessary, and 3D coordinates saved for import to Matlab.

After segmentation, the NE surface has a multiple-pixel thickness that leads to an absolute standard deviation error of ∼200 nm on the membrane position. This noise appears in P_l as a constant value that can become dominant at high angular numbers l. For NEs of radius $5\,\mu$m, the absolute error translates to a $5\,\%$ relative standard deviation, which gives an error on P_l of about 10^{-6}, setting the approximate level of the noise floor shown in figures as a shaded gray area. For larger nuclei, the noise is less of a concern as the relative error diminishes; indeed, we do not observe a 'flattening' of power spectra for older nuclei at larger l.

3.1.3 Fluctuating wrinkles

Nuclear surface wrinkling is a highly dynamic process [8]. By imaging individual nurse cells at $\sim$40 s intervals, we observed that NE surface shapes fluctuate substantially, with smaller features appearing and disappearing faster than larger ones (Fig. 3-1G). Specifically, power spectra P_l of repeatedly imaged nuclei changed on timescales of minutes or faster (Fig. 3-2 and Fig. 3-3). The rotational invariance of spectra implies that these fluctuations are not the result of whole body rotations, but instead reflect a rapid shape dynamics of NE surfaces. Experimental limitations prevented quantification of timescales for the entire 3D surface, but our observations are qualitatively consistent with findings that smaller wrinkles typically decay faster [105, 57]. Furthermore, the fact that the deformation spectrum is monotonically decreasing (Fig. 3-1E) implies that there is no preferred wavelength, suggesting that the observed NE shapes do not correspond to fluctuations about the steady-states of buckled shells, but instead reflect dynamic wrinkling across all experimentally resolved angular scales.

3.2 Elastic modeling of the nuclear envelope

Both maximum-intensity projections and spectral reconstructions show that NE wrinkles and creases are sharp, with narrow bent regions separated by flatter areas (Fig. 3-1). This morphology is reminiscent of the nonlinear stress-focusing characteristic of crumpled elastic sheets and shells such as ordinary paper sheets, which are much more easily bent than stretched [106, 71, 107]. In particular, these geometric nonlinearities lead to anisotropic responses when point forces are applied to the shell [107].

To rationalize the experimentally observed wrinkle morphology, we will first detail

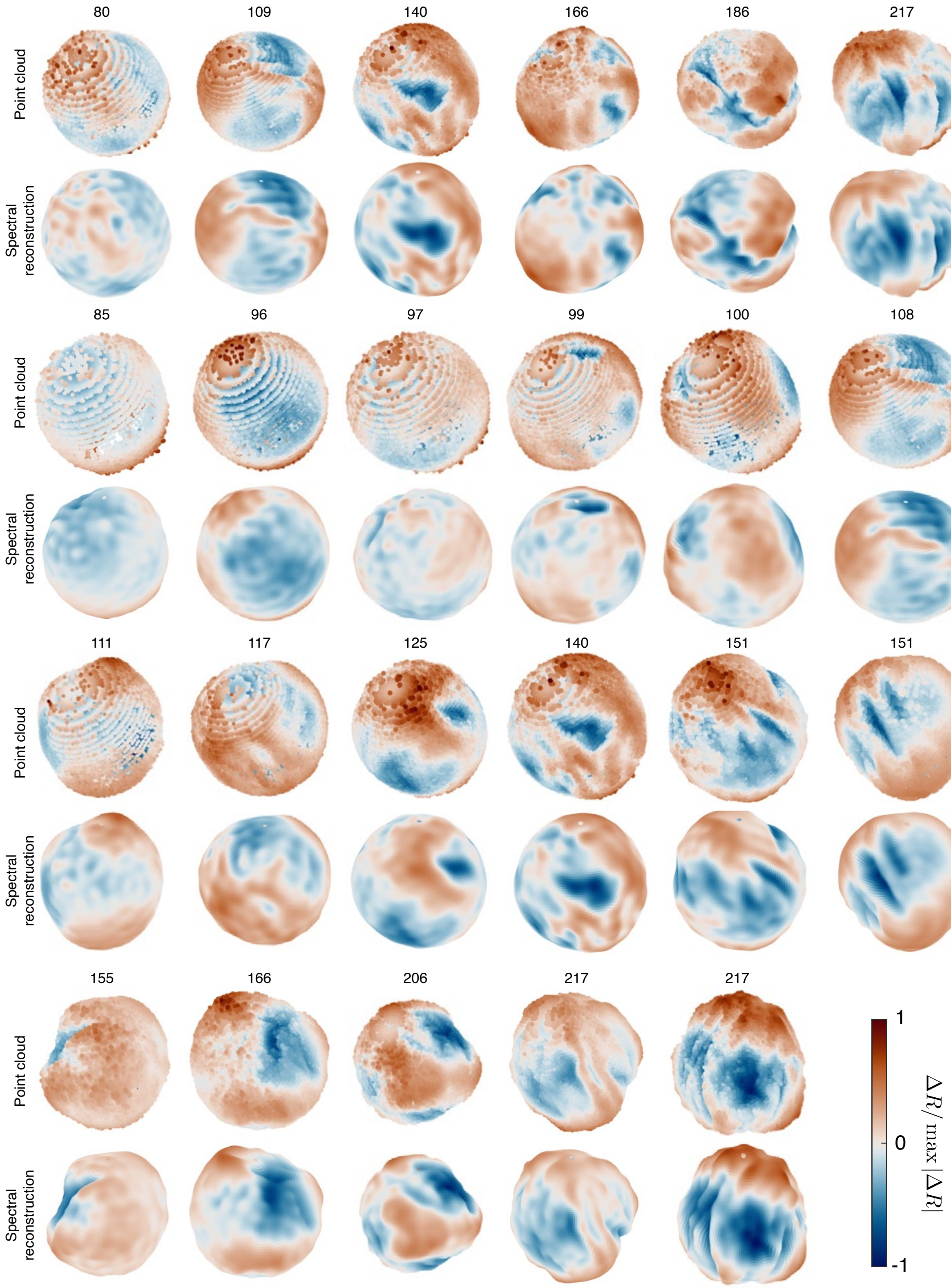

Figure 3-4 *(Caption next page)*

Figure 3-4 *(previous page)*: Additional examples of nurse cell NE segmentation and reconstructions. Representative examples of reconstructed surfaces (bottom row) from segmented point clouds (top row) obtained from 3D imaging. Numbers indicate time proxy, while color indicates deviation ΔR from the mean radius, normalized to maximum absolute value $\max|\Delta R|$. The first two rows of nuclei are those in Fig. 3-1C,D; other nuclei appear in order of ascending time proxy.

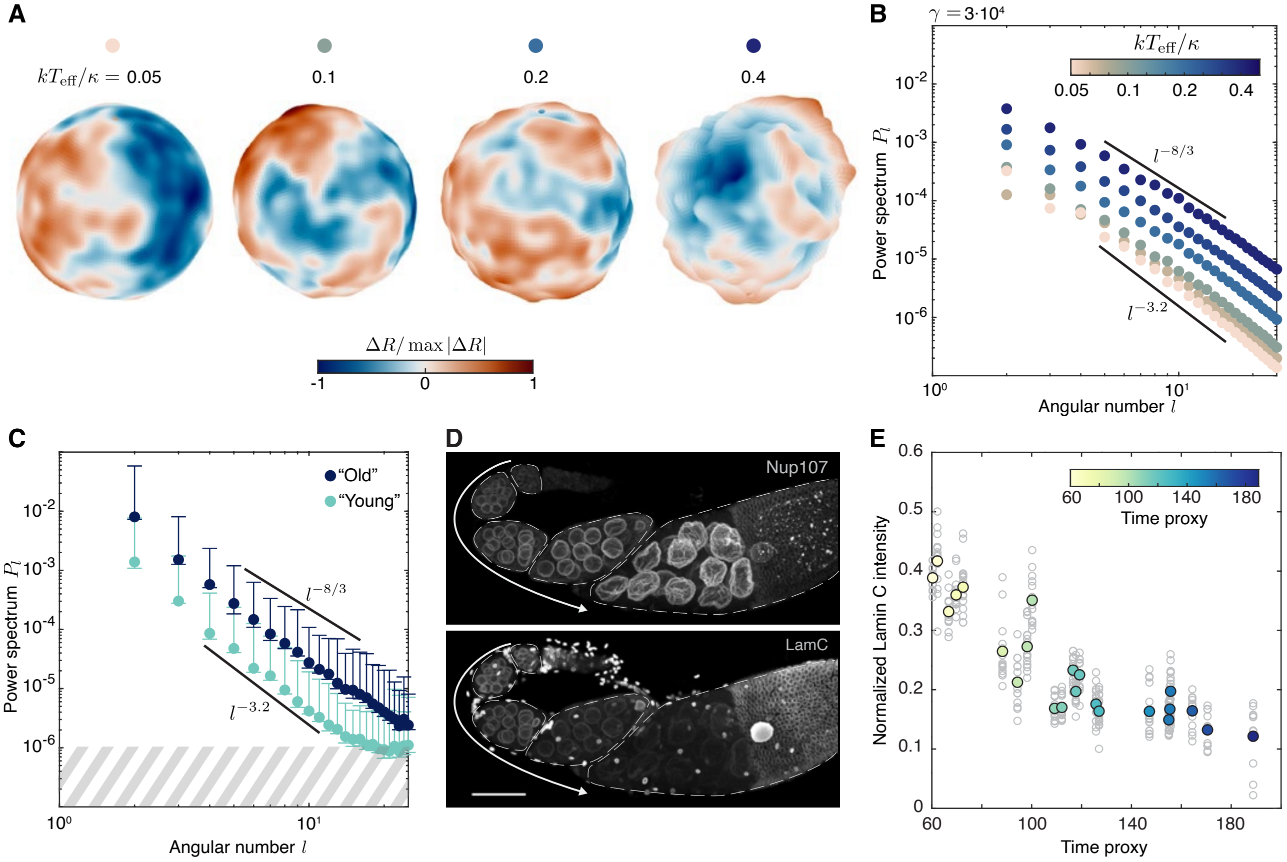

Figure 3-5 *(Caption next page)*

Figure 3-5 *(previous page)*: Fluctuating elastic shell theory predicts a scaling law with exponent ≈ 3 for the wrinkle power spectrum, in agreement with experiments. **A,** Equilibrium simulation snapshots of nuclei at temperature $T_{\text{eff}} = 10T_{eq}$, undeformed radius $R = 25$ μm and $R_c/R = 20$, at fixed FvK number $\gamma = 3 \times 10^4$ for varying elastic moduli controlled by kT_{eff}/κ. Color indicates the normalized deviation of the surface from the mean shell radius. **B,** Time-averaged spectra of simulated NEs of undeformed radius $R = 25$ μm, $R_c/R = 20$, $T_{\text{eff}} = 10T_{\text{eq}}$ for different moduli κ, Y at fixed $\gamma = 3\times10^4$, showing the transition from weak nonlinearity to strong nonlinearity as bending rigidity decreases. Color bar matches the dots from **A**. **C,** Binned averages of spectra from nuclei in nurse cells directly connected to the oocyte reveal that shape fluctuations follow a scaling law with an exponent between -3.2 and $-8/3$ that is obeyed throughout development. 'Young' nuclei have a time proxy between $80 - 140$, $N = 29$ nuclei, from 12 egg chambers; 'Old' nuclei have a time proxy between $160 - 220$, $N = 40$ nuclei, from 22 egg chambers. Bars show extremal values. Hashed area indicates approximate noise threshold for young nuclei. (See Fig. 3-2 for comparison between nuclei at different positions in the egg chamber) **D,** Fixed egg chambers expressing Nup107::RFP and stained for Lamin C, showing a decrease in Lamin C intensity in nurse cell nuclei as egg chambers increase in age. In contrast, Nup107::RFP intensity stays relatively constant. The same trend is observed in live imaging of *ex vivo* egg chambers expressing LamC::GFP and Nup107::RFP [1]. Wrinkling of nuclei in younger egg chambers (all but the rightmost) is a result of fixation and is not observed in live imaging until later stages. Arrows indicate increasing age; egg chamber boundaries are shown in dashed outlines. Scale bar: 50 μm. **E,** Normalized Lamin C fluorescence intensity decreases by approximately 5-fold over time. Normalization details are specified in [1]. $N = 337$ nuclei from 23 egg chambers.

in Sec. 3.2.1 the limitations of fluid membrane models that are commonly used to describe lipid bilayer membranes. We will then use the effective elastic model described and simulated in Chapter 2 to describe the NE as a deformed spherical shell (with undeformed radius R) parameterized by spherical coordinates $\mathbf{r} = (\theta, \phi)$. The shell has an isotropic elastic free energy [47, 29]

$$F_{\text{shell}} = \int \mathrm{d}^2\mathbf{r} \left[\frac{\kappa}{2} (\nabla^2 f)^2 + \frac{\lambda}{2} \epsilon_{ii}^2 + \mu \epsilon_{ij}^2 \right], \tag{3.3}$$

where $i, j \in \{\theta, \phi\}$ and using the Einstein summation convention. The energy functional (3.3) accounts for bending stiffness through a Helfrich-like bending term that penalizes out-of-plane deformation f (positive when pointing inwards), and the stretching of the membrane through the nonlinear strain tensor ϵ_{ij}. The 2D Lamé parameters λ, μ are proportional to the 2D Young's modulus Y. The strain combines contributions from f and from the in-plane deformation $\mathbf{u}(\mathbf{r})$. We will also allow for a preferred radius of curvature R_c of the shell mismatched with the radius R of the shell $R_c \geq R$, which in the large-Föppl-von Kármán (FvK) regime leads to a strain tensor $\epsilon_{ij} = \frac{1}{2} (\partial_i u_j + \partial_j u_i + \partial_i f \partial_j f) - \delta_{ij} f / R_c$.

3.2.1 Fluid membrane models are insufficient to describe nuclear envelopes

Fluid membrane models are commonly used to describe the mechanical behavior of biological membranes. In this section, we discuss the linear response behaviour of fluctuating fluid membranes. Specifically, we point out several discrepancies between our experiments, estimates of material parameters from the literature and fluid membrane theory. Together, these indicate the need for the more complex shell model introduced above and studied in chapter 2.

Biological membranes are often modeled as fluid membranes with properties described by the Helfrich-Canham Hamiltonian [39]

$$H = \int \mathrm{d}\mathbf{r}^2 \, \frac{\kappa}{2} (\nabla^2 f)^2 + \sigma A, \tag{3.4}$$

with bending modulus κ, effective surface tension σ [108] and total surface area A. Because under some small-deformations assumptions the Hamiltonian in Eq. (3.4) is quadratic in normal displacements f, the equipartition theorem can be readily applied to determine the linear response power-spectrum of radial out-of-plane deformations. For a fluctuating equilibrium steady state about a spherical surface, this well-known power spectrum is given by [56, 108]

$$P_l = \frac{kT}{(l-1)(l+2)[\kappa l(l+1) + \sigma R^2]}. \tag{3.5}$$

The behavior of P_l can be schematized as $P_l \sim l^{-2}$ for $l \ll l_c$, where $l_c = \sqrt{\sigma R^2/\kappa}$ is the critical wave number, and $P_l \sim l^{-4}$ for $l \gg l_c$. Using experimental measurements of mechanical nuclear membranes properties ($\kappa \approx 10^{-18}\,\mathrm{J}$ and $\sigma \approx 0.1 - 100\,\mathrm{mN/m}$, [109, 52, 51]), we can estimate for a nucleus of radius $R = 5\,\mu\mathrm{m}$ a *lower* bound $l_c^* \approx 50$ for the critical wave number. Under the reasonable assumption that the experimentally observed reduction of lamin concentration reduces the rigidity of the NE, the developmental progression of growing nuclei will most likely push l_c^* to even larger values. For the length scale and wave number regime $l \in [2, 25]$ to which we have experimental access, the fluid membrane model would therefore imply a dominant l^{-2} scaling of the power spectrum, in stark contrast to our observations (Fig. 3-5C, Fig. 3-2).

This contradiction, together with the experimental observation of sharp creases that suggest nonlinear stress focusing, lends further support for the nonlinear elastic surface model employed in this work.

The NE has been found to be stiffer than most biological membranes [109, 52, 51] and to be well described as a thin membrane of a 3D isotropic elastic material with an effective 3D Young's modulus $E \approx 1\,\mathrm{kPa}$ and thickness of $h \sim 10-100\,\mathrm{nm}$. With those parameters, the nuclear envelopes have a bending rigidity of $\kappa = 100 - 300\ kT_{\mathrm{eq}} \approx 10^{-18}\,\mathrm{J}$, where T_{eq} is the room temperature, and a stretching rigidity, captured by the 2D Young's modulus, of $Y \approx 10^{-4}\,\mathrm{N/m}$ [110]. Note that Y is a factor of 10^3 smaller than the stretching rigidity of a lipid bilayer, potentially explained by the presence of 'area reservoirs' in NEs and by transmembrane protein conformational changes [111]. For a shell of radius R, one can define the Föppl-von Kármán (FvK) number $\gamma = YR^2/\kappa$ which describes the relative propensity of the material to bend rather than to stretch; by construction, κ and Y are approximately related through the effective thickness $h \sim \sqrt{\kappa/Y}$, which implies that a large $\gamma \sim (R/h)^2$ corresponds to a thin-shell limit [29]. Using the above values, we find that the NE has a large FvK number $\gamma \sim 10^4 - 10^6$, comparable to that of a sheet of paper or graphene [71]. Accordingly, the NE is more amenable to bending than to stretching, and deformations are expected to appear as sharp wrinkles and creases, in agreement with our observations (Fig. 3-1).

3.2.2 Langevin simulations of fluctuating shells

To compare the surface shapes and fluctuations predicted by Eq. (3.3) with our experimental data, we simulated the equilibrium Langevin PDE derived from this free energy. The simulations account for hydrodynamic coupling and both passive and active fluctuations, which are modeled by an effective temperature kT_{eff}. Despite the model's minimal character, the numerically obtained shapes (Fig. 3-5A) are qualitatively similar to those in the experiments (Fig. 3-1D). In the experimentally accessible range of low-to-intermediate angular wave numbers $3 \lesssim l \lesssim 11$, the angular spectra extracted from the simulations at different ratios of $kT_{\text{eff}}/\kappa \in [0.05, 0.5]$ (Fig. 3-5B) and experimental data (Fig. 3-1E) also show an approximately similar decay, suggesting that the minimal elastic shell model in Eq. (3.3) captures relevant features of the NE, providing a basis for further analysis and predictions.

The fact that the power spectrum P_l does not change qualitatively when the nuclear radius R increases suggests that the preferred curvature radius R_c is rather large. In simulations, we thus set the preferred curvature radius to $R_c = 20R$ (Sec. 2.3). Consistent with experiments (Fig. 3-5C) and with Sec. 2.4.1, the appearance of a plateau region in the power spectrum P_l at small angular numbers is suppressed for this choice of R_c (Fig. 2-1). Indeed, the typical length scale above which finite-curvature effects become visible is $L_{\text{el}} = R\gamma^{-1/4}\sqrt{R_c/R}$, which is for FvK number

$\gamma = 10^4$ and $R_c = 20R$ approximately equal to $R/2$.

3.2.3 Scaling results for elastic thin shells

A main feature of the experimentally measured spectra is that both younger and older nuclei exhibit a similar asymptotic power law decay in the limit of small angular numbers $l \leq 10$ (Fig. 3-5C). To rationalize this observation, we first note that the scaling behavior in our experiments deviates from the basic linear response theory predictions, which is expected because, even for younger nuclei, the radial fluctuations f typically exceed the NE thickness $h \sim 10^{-3}R$ (Fig. 3-1C-F). As we will derive in Sec. 2.4, for small fluctuations $f \ll h \ll R$ and small thermodynamic pressure $p \ll p_c = 4\sqrt{\kappa Y}/R_c^2$, where p_c is the critical buckling pressure of the sphere, linear response theory predicts that the power spectrum P_l exhibits a plateau for $l \leq l_c$ and falls of as l^{-4} for $l \gg l_c$ with a crossover value $l_c \approx \gamma^{1/4}\sqrt{R/R_c}$ [29, 112], which is not seen in our experiments (Figs. 3-1E and 3-5C). Indeed, classical shell theory [66] states that nonlinear effects become important when the out-of-plane deformations f become comparable to or exceed the shell thickness h, which is generally the case in our data where $h \ll f \ll R$ (Fig. 3-1C,D,G). Nonlinear analysis of elastic plates and shells has a long history [41, 46] and has seen major advances in the last decade [47, 29], motivated in part by the discovery of graphene [113]. As demonstrated above, the FvK number of the NE is comparable to that of graphene, so we can borrow and apply recent theoretical results to understand the fluctuation spectra of the NE. Specifically, a detailed renormalization group (RG) analysis [29, 114] of Eq. (3.3) showed that, for sufficiently small plate fluctuations, elastic nonlinearities lead to a modified asymptotic decay of $P_l \propto l^{-3.2}$, consistent with our experimental and simulated data (Figs. 3-1E and 3-5B,C) and with previous experiments in red blood cell spectrin networks [115]. Notably, earlier studies [46, 29, 47] also predicted that the interplay of elastic nonlinearities and fluctuations can cause the spontaneous collapse of sufficiently large shells, suggesting a physical mechanism that could contribute to the eventual breakdown of the nurse cell NE when these cells donate their contents to the oocyte [116, 30].

As we showed in Sec. 2.5, the previously mentioned RG methods can give rise to divergences in large deformation regimes, where nonlinearities dominate the shell's response (Fig. 2-2). To obtain an analytical prediction for the scaling in the larger-deformation regime $h \ll f \ll R < R_c$, relevant to older nuclei in our experiments, we performed an asymptotic dimensional analysis on Eq. (2.38) that provides additional insight into how NE wrinkling can be controlled. To that end, we added to the elastic free energy F_{shell} an effective pressure term $F_p = -\int \mathrm{d}^2\mathbf{r}\, p_{\text{eff}} f$, where p_{eff} accounts for a normal load, which may arise from osmotic pressure differences or microtubule-induced local stresses. Denoting by L the characteristic surface variation length scale and omitting numerical prefactors that depend on details of the adopted thin-shell modeling approach (Sec. 2.4.1), one finds for shells of thickness $h \sim \sqrt{\kappa/Y}$ that the various free-energy components give scaling contributions of the form [29]

$$\frac{\delta F}{Y} \sim \left(\frac{h}{L}\right)^2 \left(\frac{f}{L}\right)^2 + \left(\frac{f}{R_c}\right)^2 + \frac{f}{R_c}\left(\frac{f}{L}\right)^2 + \left(\frac{f}{L}\right)^4 - \frac{p_{\text{eff}} f}{Y}. \tag{3.6}$$

The first term corresponds to bending, and the second and third terms arise from the non-zero curvature of the undeformed shell. The fourth term describes the nonlinear response associated with changes in the Gaussian curvature of the shells. For well-developed wrinkles with $f \gg h$, the first term can be neglected as it is smaller than the fourth term. Considering wrinkle amplitudes f_l at the spatial length scale $L \sim R/l$, where l is the angular wave number, the remaining terms can be recast as

$$\frac{\delta F_l}{Y} \sim \left(\frac{f_l}{R_c}\right)^2 + \frac{f_l}{R_c}\left(\frac{f_l}{R}\right)^2 l^2 + \left(\frac{f_l}{R}\right)^4 l^4 - \frac{p_{\text{eff}}}{Y} f_l. \tag{3.7}$$

Since $R_c > R$, the first two terms will be dominated by the l^4-term implying that, at steady-state, this quartic term and the pressure term must balance out, consistent with a corresponding earlier result for flat plates with $R_c = \infty$ [66]. We thus find $f_l \sim (p_{\text{eff}}/Y)^{1/3}(R/l)^{4/3}$, and hence for the angular power spectrum $P_l \sim (f_l/R)^2$ [see Eq. (3.2)] the scaling law

$$P_l \sim \left(\frac{p_{\text{eff}} R}{Y}\right)^{2/3} l^{-8/3}. \tag{3.8}$$

In this scaling regime, the surface deformation dynamics is dominated by the shell's resistance to stretching, which causes changes in its Gaussian curvature [67]. Both our experimental data (Fig. 3-5C, Fig. 3-2) and spherical shell simulations (Fig. 2-1) show an asymptotic spectral decay $P_l \propto l^{-\alpha}$ with an exponent α in the range $8/3 < \alpha < 3.2$, predicted by this scaling analysis and renormalization group calculations.

3.3 Experimental validation of the nonlinear thin-shell model

Both Eq. (2.41) and the robustness of the experimentally observed scaling behavior in time (Fig. 3-5C, Fig. 3-2), and under different chemical and physical perturbations (Fig. 3-6), suggests the emergence of NE wrinkling is primarily controlled by the material properties and the effective pressure p induced by thermal and by active fluctuations. For Gaussian fluctuations with effective temperature T_{eff}, previous theoretical work [47, 29] showed that $p_{\text{eff}} \sim p_c(kT_{\text{eff}})\sqrt{\gamma} \sim (Y/R)(kT_{\text{eff}}/\kappa)$, with $p_c = 4\sqrt{\kappa Y}/R^2$ the critical buckling pressure for a homogeneous spherical shell. If in addition to a fluctuating pressure p', there are uniform loads, such as those caused by osmotic pressure differences, we find $p_{\text{eff}} = p'(R/\langle R\rangle)^3$ accounts for excess area contributions to the amplitude (as long as the shell is not stretched taut; SI Sec. 2.5). Inserting these results into Eq. (2.41), our scaling analysis predicts that wrinkle formation can be tuned by changing the bending rigidity κ, the activity kT_{eff} and the osmotic pressure balance of the cell. To test these predictions, we performed three complementary types of experiments that explored the effects of material changes during nuclear development, as well as controlled perturbations.

To investigate the role of the NE's material structure during wrinkle formation, we performed live-imaging experiments in which we measured the concentration of structural components that determine nuclear stiffness. Elastic properties of the NE are known to depend strongly on the nuclear lamina [117], a roughly 10-100 nm thick meshwork of intermediate filaments that abuts the NE's inner membrane [87].

Drosophila have two lamin proteins, Lamin C (a developmentally-regulated A-type lamin similar to mammalian Lamin A/C, [118, 119]) and Lamin Dm0 (a B-type lamin present in most cell types). Both through live imaging of egg chambers simultaneously expressing a fluorescently-labeled nuclear pore complex protein (Nup107) and Lamin C, and through fixed imaging with an antibody against Lamin C, we found that, as egg chambers age and nurse cells grow in size, the ratio of Lamin C to Nup107 decreases (Fig. 3-5D,E;) while the intensity of Nup107 remains roughly constant . Nonetheless, Lamin C continues to appear alongside Nup107 at the sites of wrinkles [1]. These observations suggest that reduction in Lamin C concentration causes softening of the NE, and that reduced bending rigidity κ increases wrinkle amplitudes [117] as predicted by Eq. (2.41).

In addition to material properties, active fluctuations [120] or hydrodynamic effects [121, 79] can substantially affect buckling and pattern formation in shells and membranes [122, 123, 80]. To explore how changes in cytoskeleton-mediated intracellular activity [124] influence the spectrum of NE deformation, we performed additional perturbation experiments targeting the cytoplasmic microtubule and actin networks. Previous work showed that incoherent microtubule dynamics can cause fluctuations of the NE during cellularization of the *Drosophila* embryo [125]. Consistent with this earlier report and with the predictions of Eq. (2.41), we found that inhibition of microtubule polymerization by the small-molecule inhibitor colchicine notably reduces the amplitude of fluctuations (Fig. 3-6A). Colchicine treatment also decreased nucleus volume by 5%-20%; however, as a sudden volume decrease for a similar surface area would lead to a rougher NE in the absence of other factors rather than a smoother NE, it is unlikely that volume reduction explains the effects seen upon colchicine treatment. Furthermore, colchicine addition reduced the motion of cytoplasmic contents of the cells, suggesting microtubule-mediated active fluctuations contribute to NE wrinkling. In contrast, perturbation of actin by cytochalasin D did not unwrinkle the NE [1], suggesting cytoplasmic F-actin is not a major contributor to NE wrinkling during the developmental stages studied here. The observation that inhibition of microtubule polymerization reduces the wrinkle amplitude but does

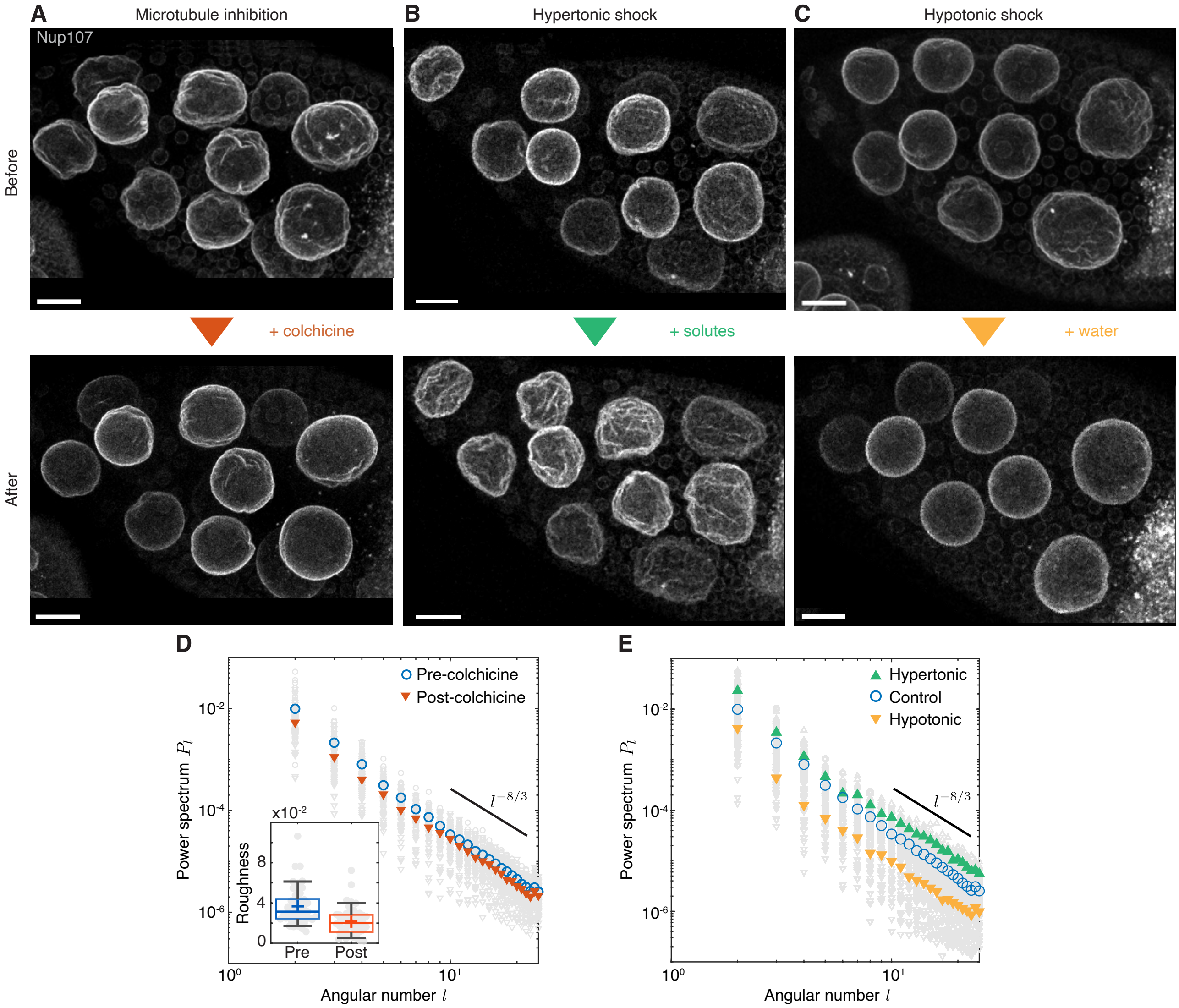

Figure 3-6 *(Caption next page)*

not change the spectral scaling behavior (Fig. 3-6D) suggests that, to leading order, non-equilibrium contributions to NE fluctuations arising from microtubule dynamics can be modeled through an effective temperature kT_{eff} [77, 57]. We also tested other mechanisms known to contribute to NE deformation, such as impingement by cytoskeletal filaments or changes to chromatin structure, but found Lamin C decrease to be the dominant factor correlating with NE wrinkle formation [1].

Eq. (2.41) also suggests that osmotic pressure variations, by tuning the available excess area [70, 69], can be used to enhance or reverse wrinkle formation by up- or

---

Figure 3-6 *(previous page)*: Perturbation experiments confirm robustness of observed scaling laws and reveal reversal mechanisms for NE wrinkling. **A,** MIP of one egg chamber before (top) and after (bottom) inhibition of microtubule polymerization by colchicine, showing that microtubule disruption can reverse wrinkling. **B,** MIPs before and after hypertonic shock using an external culture medium of 1.5x osmolarity, showing an increase in wrinkling. **C,** MIPs before and after hypotonic shock using an external culture medium of 0.5x osmolarity, showing a decrease in wrinkling. Egg chambers in **A**, **B**, and **C** have time proxies of 171, 174, and 171, respectively. **D,** The power spectrum after microtubule inhibition by colchicine still follows a power law with roughly the same exponent, with a reduction of roughness by a factor of 2 (inset). $N = 49$ pre-colchicine and post-colchicine nuclei, from 6 egg chambers. For box plots, plus signs denote mean, middle line is the median, top and bottom edges of the box are the upper and lower quartiles, and whiskers span from 9% to 91% of the data range. **E,** In the presence of increased inwards (hypertonic) or outwards (hypotonic) pressure, the overall shape of the power spectrum remains approximately conserved. Hypotonic shock treatment reduces the wrinkle amplitudes, providing a reversal mechanism for NE wrinkling. Spectra were computed using 49 control, 15 hypertonic, and 30 hypotonic nuclei in the time proxy range $165-185$, from 6, 3, and 6 egg chambers, respectively, using nuclei from all nurse cells rather than only those directly connected to the oocyte. Scale bars: 20 μm.

down-shifting the deformation spectrum without changing its characteristic decay. To test this prediction, we performed osmotic shock experiments. Adding salt to the ambient culture medium (hypertonic shock) increases the total external pressure on the NE, which drives fluid out of the nucleus and leads to visibly more wrinkled surfaces (Fig. 3-6B,E). Conversely, reducing the salt concentration in the culture medium (hypotonic shock) decreases the external pressure and leads to a substantial smoothening of wrinkled NE (Fig. 3-6C,E). In both cases, NEs maintained their altered morphology for 15-30 minutes before cell regulatory mechanisms began to compensate for the osmotic changes and nuclear shapes trended back towards their pre-shock state. In agreement with Eq. (2.41), the spectral slopes remain approximately preserved for both types of shocks. Taken together, these experimental results support the hypothesis that wrinkle morphology and dynamics of deformation of the nurse cells' NE are dominated by a nonlinear elastic response rather than liquid-like behavior.

NE wrinkles have been associated with biological processes including nuclear positioning [8], and as a mechano-sensitive element of the cell, the NE can regulate chromatin dynamics and force-induced transcription factor movement through nuclear pore complexes [126, 127, 128, 83]. Here we observed an increase in NE wrinkling during egg chamber growth that correlates with an increase in size of nuclei along with a decay in Lamin C concentrations. Although NE wrinkling may have consequences for the nurse cells' chromatin organization and transcriptional states, NE wrinkles could also simply result from concomitant nucleus growth and Lamin C density decrease in cells fated to die to enable egg development. It is however tempting to propose that NE wrinkles could play the role of a tension buffer: tension applied to the NE would initially unfold the wrinkles before leading to significant in-plane strain that might cause NE rupture. This two-stage response to tension has indeed been observed during cell spreading, in which a NE stretch-mediated response occurs only after the initially-wrinkled nucleus flattens by a certain amount [74, 84].

3.4 Conclusion

Prior work has shown that nurse cells in stage 5-9 egg chambers often have a high level of intranuclear actin and that this level is lower from stage 10 onwards (the wrinkles studied here become obvious partway through stage 9) [129]. Additionally, in other contexts such as the *Drosophila* larval muscle, Lamin C mutants can induce formation of intranuclear actin rods and potentially deform the nuclei [130], suggesting changes in intranuclear actin levels or organization may also play a role in wrinkling. However, whether they would increase or decrease wrinkling is not immediately clear; characterizing the role of intranuclear actin in the observed NE wrinkling is therefore a promising avenue of future research. Another future prospect is to perturb Lamin C levels to investigate how NE wrinkling changes when Lamin C density is exogenously modified, allowing further comparisons to theory and clarifying whether the wrinkles have biological function. Due to complications with existing fly reagents for perturbing Lamin C levels in the female germline, increasing or decreasing expression of Lamin C in the nurse cell NEs proved challenging [1]. We further note that our continuum model is by necessity a simplification of the complex NE biology and that our measurements cannot identify features that only include single NE membrane layers or are below the resolution of confocal light microscopy.

To conclude, our experimental and theoretical results suggest that essential qualitative aspects of NE wrinkling can be understood within the framework of nonlinear elastic thin-shell mechanics. As NEs have a Föppl-von Kármán number similar to both graphene and paper [71], we expect our theoretical observations to be relevant for these and other similar systems whenever fluctuations push membranes and shells into larger deformation regimes. With the power-law exponent set by the elastic behavior of the shell, the amplitude of wrinkles is controlled by the effective pressure, which we have manipulated here through osmotic shocks and microtubule inhibition. Our findings therefore raise the question of whether cellular control over pressure could be a generic biophysical mechanism for avoiding undesirable consequences of nuclear wrinkling [86, 84, 73].

Chapter 4

Hydraulic and active transport in *Drosophila* oogenesis

The contents of this chapter have been previously published as J. Imran Alsous, N. Romeo, J. A. Jackson, F. M. Mason, J. Dunkel and A. C. Martin, Proc. Natl. Acad. Sci. U.S.A. ***118*** *(10) e2019749118 (2021), Ref. [30]. Experimental data and figures are courtesy of Jasmin Imran Alsous and Jonathan A. Jackson.*

Fluid flows play an important role in biological development, from the definition of an organism's body plan [131] and vertebrate organogenesis [132] to cytoplasmic streaming [133] and tissue morphogenesis [134]. In this chapter, we investigate the dynamics of a robust fluid transport process which occurs during the development and growth of the egg cell, also known as an oocyte. Across diverse species, oocytes develop within germline cysts alongside nurse-like sister germ cells [135, 136]; a key juncture in oogenesis occurs when these sister cells transport their cytoplasm to the oocyte prior to fertilization. As a result, the oocyte grows as its sister cells regress and die [135, 136, 137, 138]. Although critical for fertility and early embryonic life, the biological and physical mechanisms underlying this transport process are poorly understood. We will find here that the geometry of the nurse cells is a key component of this important transport process.

In *Drosophila melanogaster*, the oocyte develops within an egg chamber, a multicellular structure comprising a germline cyst that is covered by an epithelium; the germline cyst itself comprises an oocyte and 15 nurse cells (NCs) that are interconnected through intercellular bridges called ring canals (Fig. 4-1A) [94, 139, 140]. Once the oocyte grows to $\sim$50% of the egg chamber's volume, the NCs transport their cytoplasm into the oocyte in a process called NC dumping; with a diameter of $\sim$10 μm, the ring canals are large enough to permit passage of most cytoplasmic contents (Fig. 4-1B) [141]. It has been proposed that NC dumping is driven by global cortical contractile forces generated through interactions of non-muscle myosin-II with actin filaments, which together form a complex known as actomyosin. According to this hypothesis, the increased contractility brings about an increase in pressure, causing cytoplasm to be 'squeezed' out of the NCs and into the oocyte [142, 143, 144]. Indeed, mutants in the myosin regulatory light chain (RLC), encoded for by the *spaghetti squash* (*sqh*) gene, do not complete NC dumping [145, 146], suggesting a critical role for actomyosin dynamics in this process. However, in the absence of time-resolved quantitative data, actomyosin's role in promoting the complete and directional transport of cytoplasm has remained unclear.

To investigate this process, we used live imaging of egg chambers to reconstruct the intercellular transport pattern within the 16-cell germline cluster and corresponding actomyosin activity during NC dumping. We found that our experimental observations, namely the intercellular directional transport pattern and time scale of this transport phenomenon, in both Wild-type (WT) and mutants, are best captured by a networked flow model inspired by the famous two-balloon problem. Our results also reveal a novel role for actomyosin dynamics during NC dumping: appearing as surface contraction waves, which have been prominently observed in a variety of biological systems [147, 148, 149], changes in actomyosin activity in the latter phase of NC dumping are required for enabling continuous, pressure-driven flow and complete transport. Combined with other recent studies [150], our results demonstrate the importance of both hydraulic transport and biological mechanisms in regulating multicellular collective behavior during oocyte development in higher organisms.

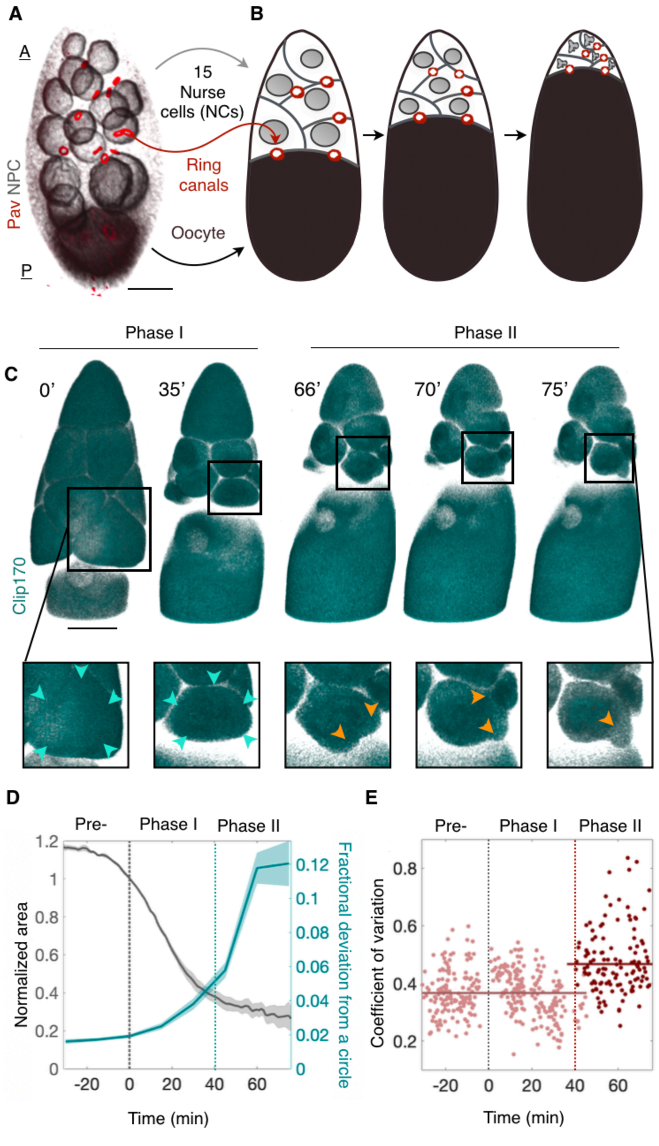

Figure 4-1 : Nurse cell (NC) dumping occurs in two phases. **A.** 3D-rendered confocal image of an egg chamber showing 15 anterior (A) NCs (gray: *Nuclear pore complex, NPC*) and one posterior (P) oocyte (black: *NPC*) connected through ring canals (red: *Pavarotti, Pav*). **B.** Schematic illustration of NC dumping: NCs shrink as their cytoplasm flows into the oocyte through ring canals. **C.** 3D-rendered time-lapse confocal images of an egg chamber expressing *Clip170::GFP* undergoing NC dumping. Blowups show a nurse cell first shrinking uniformly (cyan arrowheads; Phase I) before undergoing spatially nonuniform shape deformations and bleb-like protrusions (orange arrowheads; Phase II) that imply increased actomyosin contractility. Scale bar in **A** and **C**: 40 μm. **D.** Quantification of changes in cell size (gray) and shape (i.e. fractional deviation from a circle; Fig. S2, C and D) prior to NC dumping (Pre-), and during Phases I and II. Onset of non-uniform deformations (dashed cyan line) occurs $\sim$40 minutes into NC dumping ($N = 4$). **E.** Coefficient of variation of cortical Sqh intensity during NC dumping, showing a transition (dashed red line) from uniform ($N = 412$; Phase I) to non-uniform ($N = 122$; Phase II) distribution at $\sim$40 minutes, concomitant with the onset of dynamic cell shape deformations.

4.1 Nurse cell dumping proceeds in two distinct phase

Using *ex vivo* live imaging of egg chambers with simultaneously labeled membranes (*Ecad::GFP* or *Resille::GFP*), myosin-II (*sqh::mCh*), and cytoplasm (*Clip170::GFP*), we determined the dynamics of NC dumping and corresponding patterns of actomyosin activity. First, through size measurements of the oocyte and the 15 NCs [30], we found that NC dumping unfolds over the course of ∼100 minutes, a period ∼3-fold longer than previously reported through indirect estimates [151, 96]. We also found that NCs empty ∼75% of their volume into the oocyte through spatially uniform shrinkage of the cells, in the absence of nonuniform cell shape changes and membrane blebbing that imply contractile force generation (Phase I) [152, 153]. In contrast, transport of the remaining cytoplasm (Phase II) is accompanied by dynamic and persistent deformations of NC shape along with blebbing (Fig. 4-1, C and D).

Similarly, we found that NC dumping onset occurs without changes to the level and localization pattern of cortical myosin as compared to the previous developmental stage. NCs' cortical myosin reorganizes from a uniform to a nonuniform dynamic cortical pattern only ∼40 minutes into NC dumping, coincident with the onset of dynamic NC shape deformations (Fig. 4-1E). Importantly, no such changes in cortical distribution were observed in control membrane markers [30]. NC dumping therefore occurs in two distinct phases, only the latter of which coincides with changes in actomyosin distribution and hallmarks of increased contractility.

4.2 Phase I dynamics are captured by a flow-network model

We therefore explored mechanisms whereby directional intercellular fluid flow can occur in the absence of increased contractility and peristalsis-like cell deformations in the NCs. To that end, we first determined the spatiotemporal pattern of intercellular cytoplasmic transport in the 16-cell network. We found that NC dumping unfolds in a hierarchical manner that mirrors the cells' size and spatial arrangement. While the oocyte is the largest cell in the egg chamber, the NCs, which are arranged in four layers (L1-L4; Fig. 4-2A), also exhibit a descending cell size order according to their distance from the oocyte [154, 155, 156]. Our data show that NCs directly connected to the oocyte (L1 cells) are first to transport their contents into the oocyte, followed in order by smaller NCs in layers L2-L4 (Fig. 4-2, B and C). Therefore, smaller cells in the network empty their contents into larger ones prior to changes in myosin localization and corresponding cell shape deformations.

Driven by these experimental observations, we developed a networked fluid flow model that was inspired by the two-balloon problem: if two identical balloons inflated to different volumes are allowed to exchange air, the smaller balloon will empty its contents into the larger balloon (Fig. 4-2D). This seemingly counter-intuitive phenomenon can be explained by the Young-Laplace law, which states an inverse relationship between pressure p and radius R for a sufficiently large balloon. Taking into account the hyperelastic behavior of rubber, the pressure inside the inflated balloon is then given by:

$$p = \frac{2\gamma}{R}\left(1 - \left(\frac{R_0}{R}\right)^6\right) \tag{4.1}$$

where R_0 is the radius of the uninflated balloon and γ is its surface tension (Fig. 4-2D) [157, 158].

To investigate whether an analogous model can explain the hierarchical transport observed in Phase I, we approximated each cell by a sphere [159] with time-dependent radius $R_i(t)$. The actomyosin cortex was assumed to be incompressible and described as an effective neo-Hookean material under static loading. In this phenomenological description, the effective cell surface tension γ arises from the contributions of both in-plane tension of the plasma membrane and actomyosin cortical tension [160]. Extending the two-balloon model to the 16-cell network in the germline cyst (Fig. 4-2E), the pressure-driven flux J_{ij} from cell j to i through an approximately cylindrical ring canal with hydraulic conductance G_{ij} is

$$J_{ij} = G_{ij}(p_j - p_i). \tag{4.2}$$

Using experimentally determined cell sizes at onset of NC dumping as initial conditions [155], we numerically solved the transport equations for the evolution of cell volumes V_i in the 16-cell tree,

$$\frac{\mathrm{d}V_i}{\mathrm{d}t} = \sum_{\langle i,j \rangle} J_{ij} = \sum_{\langle i,j \rangle} G_{ij}(p_j - p_i) \tag{4.3}$$

where the sum runs over connected cell neighbors i and j. Before discussing the results of this model, we first detail the assumptions leading to the model defined by Eqs (4.1) and (4.2), and the protocol used to simulate these equations and adjust their parameters.

4.2.1 Details of the networked flow model

The *Drosophila* germline cyst forms a stereotypical 16-cell tree that are connected by circular openings that let cytoplasm flow during the dumping stage. We will approximate in first instance the ring canal connecting cells i and j by a small cylindrical pipe of radius r_{ij} and length L. We will take the viscosity of cytoplasm in *Drosophila* to be everywhere equal to its *in vivo* estimate as $\mu \approx 1$ Pa·s [161]. At the characteristic sizes of $a = 10^{-6}$ m and flow speeds $U = 10^{-6}$m/s of this flow, we are safely in a low Reynolds number regime $Re = (\rho_0 U a)/\mu \approx (10^3\text{kg})/\text{m}^3 \times (10^{-6}\text{m/s}) \times (10^{-6} m)/(1 Pa \cdot s) = 10^{-9} \ll 10^{-3}$, with ρ_0 the density of the cytoplasm. The fluid flow through the ring canals is hence assumed to be an incompressible Poiseuille flow. In this case, the volume flux J_{ij} from cell j to i is proportional to the difference in their respective pressures $(p_j - p_i)$, with the proportionality constant given by the hydraulic conductance G_{ij}.

The change in the volume of cell i is then determined by the total fluxes in and out of the cell:

$$\frac{\mathrm{d}V_i}{\mathrm{d}t} = \sum_{\langle i,j \rangle} J_{ij} = \sum_{\langle i,j \rangle} G_{ij}(p_j - p_i) \tag{4.4}$$

Here, the sum runs over the set of cells j connected to cell i by ring canals. Summing over all the cells, one can verify that the total cytoplasmic volume is conserved throughout the germline cyst, i.e. $\sum_i \frac{\mathrm{d}V_i}{\mathrm{d}t} = 0$ at all times.

As announced above, we model each cell i as a spherical 'balloon', with interior pressure p_i relative to the homogeneous pressure outside given by the modified Laplace pressure law due to Merritt and Weinhaus [157]:

$$p_i = \frac{2\gamma}{R_i}\left(1 - \left(\frac{R_{0,i}}{R_i}\right)^6\right) \tag{4.5}$$

Here, $R_i = 3V_i^{1/3}/4\pi$ is the radius of the i-th balloon, and γ is the surface tension of the shell. To gain intuition about the behavior of this pressure law, consider two balloons (or two cells) that are connected by an open canal. There are two possible equilibrium configurations for which the pressure in both balloons is equal. In the first case, both balloons are of equal size and the system does not deviate from its initial configuration. In the second case, the balloons assume unequal sizes; that is, an initial size imbalance will be amplified until the pressures balance out. For instance, assuming that initially both balloon radii are larger than R_0, the initially larger balloon will grow to a radius $R_{\text{large}} \gg R_p$, whereas the other will shrink down to a radius $R_{\text{small}} < R_p$ where $R_p = 7^{1/6}R_0 \approx 1.38R_0$ is the radius at maximum pressure. Note that as R_i grows relative to the zero-pressure radius $R_{0,i}$, one recovers the usual Laplace pressure law, $p_i = 2\gamma/R_i$.

Alternative pressure laws While the microscopic nature of a nurse cell is much more complex than a rubber balloon, cells can be considered effectively viscoelastic, with a filamentous cytoskeleton bearing similarities to crosslinked semiflexible polymer networks such as rubber [124]. Merritt and Weinhaus obtained the above pressure law for the case of an isothermal spherical rubber balloon, using a constitutive equation [157], first derived by James and Guth for rubber in 1943 [162]. In fact, as shown previously [158], one would obtain the same functional form for the pressure law for a neo-Hookean material, which itself is a particular case of a Mooney-Rivlin material for small enough extensions. Mooney-Rivlin materials are generally considered to be appropriate models of incompressible rubber-like materials and have been widely used to describe biological tissues, including the cellular cortex [163]. If we were to relax the assumption of incompressibility, another family of constitutive relations would follow the Blatz-Ko model [158] and more complex variants. Since cells are usually considered more fluid-like than solid [164], the assumption of incompressibility is reasonable, rendering the Merritt and Weinhaus law an appropriate framework for this problem.

From a more formal viewpoint, to illustrate how a different microscopic model would provide a different power law correction to Young-Laplace's law, consider for instance a spherical shell of radius R consisting of particles that interact according to an repulsive short-range pair potential $V(\mathbf{x}-\mathbf{y}) = -g\delta^2(\mathbf{x}-\mathbf{y})$. Assuming the particles' surface density is uniform $\rho(x) = \rho = N/(4\pi R^2)$, the energy contribution of this interaction is:

$$F = \frac{1}{2}\int \mathrm{d}^2\mathbf{x}\mathrm{d}^2\mathbf{y}\rho(\mathbf{x})\,\rho(\mathbf{y})V(\mathbf{x}-\mathbf{y}) = -\frac{g}{2}4\pi R^2\rho^2 \tag{4.6}$$

In the presence of a surface tension, the differential of free energy would be, at constant temperature,

$$\mathrm{d}F = -p\mathrm{d}V + \gamma\mathrm{d}A \tag{4.7}$$

where $\mathrm{d}A$ is the variation in area. The pressure as a function of radius would then be given by

$$p = -\frac{\partial F}{\partial V} + \gamma\frac{\mathrm{d}A}{\mathrm{d}V} = \frac{2\gamma}{R} - \frac{gN^2}{8\pi^2}\frac{1}{R^5} = \frac{2\gamma}{R}\left(1-\left(\frac{R_0}{R}\right)^4\right) \tag{4.8}$$

with $2\gamma R_0^4 = gN^2/(8\pi^2)$. Here we see that the repulsive interaction potential ends up contributing a $1/R^n$ correction to Laplace's law.

Different microscopic models thus lead to different regularizations of Young-Laplace's law at small sizes. To investigate whether different 'elastic' $1/R^n$ terms provide qualitative agreement with the data, we ran different simulations with varying integer values of n. While the slopes of curves varied, the directionality and layer-wise hierarchy of dumping order was preserved, and we settled for $n = 6$ corresponding to the ‘balloon’ law Fig. 4-3B.

Hydraulic conductance and surface tension-driven flow feasibility Nurse cells in the germline cyst are connected by ring canals. Assuming Poiseuille-type flow [163], the hydraulic conductance G of a cylinder of radius r and length L is given by:

$$G = \frac{\pi r^4}{8\mu L} \tag{4.9}$$

We use this formula as an initial guess for the hydraulic conductance G_{ij} between cells i and j at the onset of NC dumping, adopting typical parameters $r \approx 5$ μm and $L \approx 2$ μm inferred from our experimental imaging data. However, the Poiseuille approximation is only valid for $L \gg r$, and we expect the Poiseuille approximation to underestimate the actual conductance. In our simulations detailed in Sec. 4.2.2, we therefore scanned conductance values in the vicinity of the Poiseuille value.

To test whether such a surface tension-driven flow model could capture the observed dynamics of intercellular networked transport through ring canals, we first estimated the minimal effective surface tension required for Laplace pressure-driven flow at magnitudes comparable to those observed experimentally. The relative contributions of cortical cytoskeleton versus plasma membrane to cell surface tension are known to vary [164]. Here, we combine both contributions into a single effective surface tension parameter γ that can be estimated from measurable quantities as described below:

$$\gamma = \frac{4\mu LRJ}{\pi r^4} \tag{4.10}$$

To estimate an upper bound on J, the magnitude of flux through a single ring canal, we used the steepest rate of change in cell volume (Fig. 4-2C), multiplied it by the average volume of a layer 1 cell at NC dumping onset and obtained $J = 40$ μm^3/s.

Using $\mu \approx 1$ Pa·s, $L = 2$ μm, $R \approx 30$ μm, $J = 40$ μm^3/s, $r = 5$ μm, we find a value of approximately 4 pN/μm for γ. This estimate for γ is at the lower end of literature reported values [165], consistent with the known fact that the nurse cell cluster have a relatively low basement membrane stiffness [166]. We therefore contend that surface tension is sufficient for driving the observed transport dynamics.

In our subsequent calculations, we assumed that cell surface tension is constant in time for all cells as transport unfolds, which is supported by previous studies showing that plasma membrane tension is actively buffered, for instance through endocytosis [167, 168]. We also assume that cell surface tension is equal for all cells, justified by the fact that the cortical cytoskeletal network is invariant across cells within the germline cluster, and that it does not appear to be significantly altered during the first phase of NC dumping, that is during the phase of surface tension-driven flow.

Additionally, to account for cell-to-cell variability in effective cell surface tension, we explored the effects of fluctuations of surface tension between cells in the model. To this end, we first adjusted the model to the experimental data, and subsequently allowed for approximately 10% surface tension fluctuations to account for variations in shape, basement membrane stiffness and other factors of cell-to-cell variability (Sec. 4.2.2).

Dimensionless equations Writing out Eq. (4.4) in full yields:

$$\frac{\mathrm{d}V_i}{\mathrm{d}t} = \sum_{\langle i,j\rangle} \frac{\pi\gamma r_{ij}^4}{4\mu L}\left[\frac{1}{R_j}\left(1-\left(\frac{R_{0,j}}{R_j}\right)^6\right) - \frac{1}{R_i}\left(1-\left(\frac{R_{0,i}}{R_i}\right)^6\right)\right] \tag{4.11}$$

To rewrite this equation in nondimensionalized form we define the characteristic time-scale $\tau_0 = 4\mu L/(\pi\gamma)$ and length scale l_0 such that the initial oocyte volume is $100 l_0^3 = 10^6\ \mu\mathrm{m}^3$, yielding $l_0 \approx 20\ \mu\mathrm{m}$. Using our estimate for γ from above, we find $\tau_0 \approx 0.6$ s. Defining the dimensionless radius $\hat{R}_i = R_i/l_0$, time $\hat{t} = t/\tau_0$, and volume $\hat{V}_i = V_i/l_0^3$, the dynamical equation takes the dimensionless form

$$\frac{\mathrm{d}\hat{V}_i}{\mathrm{d}\hat{t}} = \sum_{\langle i,j\rangle} \left(\frac{r_{ij}}{l_0}\right)^4 \left[\frac{1}{\hat{R}_j}\left(1-\left(\frac{\hat{R}_{0,j}}{\hat{R}_j}\right)^6\right) - \frac{1}{\hat{R}_i}\left(1-\left(\frac{\hat{R}_{0,i}}{\hat{R}_i}\right)^6\right)\right] \tag{4.12}$$

where the dimensionless pressure is given by $\hat{p}_i = 1/\hat{R}_i(1-(\hat{R}_(0,i)/\hat{R}_i)^6)$. To generalize the model beyond the Poiseuille approximation, we introduced in equation

(4.12) the dimensionless conductances $\hat{G}_{ij} = (r_{ij}/l_0)^4$. Written in terms of $\hat{G}_{ij}$, the model does not depend on the precise scaling of G_{ij} with r_{ij}, and adjusting $\hat{G}_{ij}$ to achieve the best-fit of the model solution to the experimental data provides a way of measuring the hydraulic conductances.

Initial conditions and parameters. To simulate the model, one must provide initial conditions and parameter values for the zero-pressure radii $\hat{R}_{0,i}$ and conductances $\hat{G}_d$. At $t = 0$, the sixteen cells have a well-characterized cell size pattern, as nurse cells further from the oocyte are smaller than those that are closer. The initial size distribution is determined from empirical observatins as follows [155]:

1. the oocyte has a volume V_0 equal to the sum of all the nurse cells' volumes combined

2. nurse cells at same distance $d = 1, 2, 3, 4$ from the oocyte have the same cell volume V_d set by
$$\frac{V_{d+1}}{V_0} = \left(\frac{V_d}{V_0}\right)^{\nu} \tag{4.13}$$
with the exponent $\nu \approx 0.84$.

These properties completely determine the initial conditions. To fully determine our equations, we then finally need to fix the values of the following parameters:

1. Dimensionless conductances $\hat{G}_d$: To compensate for the inaccuracy of the Poiseuille formula, we adjusted the dimensionless conductance to obtain agreement with our experimental observations. Assuming that all ring canals at edge distance d from the oocyte have the same size r_d, all ring canals at edge distance d also have the same dimensionless conductance $\hat{G}_d$. We then allow for variations of $\hat{G}_d$ by allowing the effective ring canals radii $r_d := l_0 \hat{G}_d^{1/4}$ to vary from their corresponding average experimental values by up to plus or minus 60% as described in Sec. 4.2.2. As expected, the best-fit effective ring canal radii are larger than the directly measured ring canal radii, confirming that the Poiseuille formula Eq. (4.9) underestimates the actual hydraulic conductance. Test simu-

Fixed			**Optimized**		
Layer	**# of cells**	**Initial volume***	**Parameter**	**Parameter range**†	**Best fit**‡
Oocyte	1	100	ρ	$[0.22, 1]$	0.60
1	4	9.00	$\hat{G}_1$	$[1.5 \cdot 10^{-4}, 3.4 \cdot 10^{-2}]$	$1.7 \cdot 10^{-2}$
2	6	6.61	$\hat{G}_2$	$[1.5 \cdot 10^{-4}, 3.4 \cdot 10^{-2}]$	$2.3 \cdot 10^{-2}$
3	4	5.07	$\hat{G}_3$	$[2.9 \cdot 10^{-4}, 2.6 \cdot 10^{-2}]$	$8.1 \cdot 10^{-3}$
4	1	4.03	$\hat{G}_4$	$[1.0 \cdot 10^{-4}, 8.1 \cdot 10^{-3}]$	$4.6 \cdot 10^{-3}$

Table 4.1 : Summary of initial conditions and parameters used in the hydraulic model. *Given in units of $\ell_0^3 = 8 \cdot 10^3$ μm^3. †The scanned range of the dimensionless hydraulic conductances $\hat{G}_d$ corresponds to a range of effective ring canal radii $r_d := \ell_0 \hat{G}_d^{1/4}$ within ±60% of the experimentally measured average ring canal size for each layer. ‡Best fit parameters minimize the error as defined in Sec. 4.2.2.

lations with equal ring canal sizes do not reproduce the experimentally observed dumping hierarchy.

2. Zero-pressure radius: We assume all cells have a zero-pressure radius $R_(0, i) = \rho R_i(t = 0)$, where ρ is an adjustable parameter between 0 and 1.

Overall, this yields a total of five tunable parameters: the four hydraulic conductances $\hat{G}_d$ and the zero-pressure radius scale parameter ρ. A summary of the initial conditions and adjustable parameters is given in Table 4.1.

4.2.2 Simulations and optimization

In this section, we explain how we integrate the differential equations Eq. (4.12) and the procedure used to fit the model parameters.

Implementation. The simulations were implemented in Python 3 with the SciPy libraries. The standard `scipy.integrate.solve_ivp` routine was used to solve the system of ordinary differential equations defined by Eq. (4.12). Simulations were run until the system reached steady state, which always converged to a solution where all nurse cells have an equal small size and the oocyte is large. While we have not conducted a full analysis of the stability of the fixed points, since our initial conditions are hierarchical with the oocyte significantly larger than the next largest NCs, the dynamics for physically relevant parameters most likely lie in the basin of attraction of the '1 large; 15 small' solution. Furthermore, those dynamics do not lead to perfectly empty balloons at steady state; indeed, as our experimental data show, completion of the dumping process requires active contractions, which are not included in the network flow model; we can therefore only reliably compare our simulation results with experimental data before the effects of myosin activity become too important, and the simulated steady-state has no direct biological relevance.

Fitting procedure. Experimental measurements provided us with the relative cross-sectional areas of cells, which we averaged per layer of cells at distance d from the oocyte. We then estimated the relative experimental volumes

$$V_d^{\exp}(t)/V_d^{\exp}(t=0) = (A_d^{\exp}(t)/A_d^{\exp}(t=0))^{3/2}, \tag{4.14}$$

with time t expressed in units of $\tau_0 \approx 0.6$ s. Our simulations then yield a set of volume trajectories $V_d^{\text{sim}}(t)$ for the average volume of cells in layer d.

Since the model developed here describes the first phase of NC dumping, namely, surface tension-driven flow, and does not include the effect of the actomyosin contractility, we compared our trajectories to experimental data taken before onset of actomyosin contractility only. Experiments show that this occurs when cells reach a characteristic fraction of their initial volume $V_{\text{wave}} = 0.25V(t=0)$ [30]. The sum of squares error between the experimental and simulation data points was then computed for each of the layer-averaged cross-sectional areas of cells, with a set of weights $g_d = (4/15, 6/15, 4/15, 1/15)$ reflecting the number of nurse cells in each layer normalized such that $\sum_d g_d = 1$. The error is then given by:

$$E = \sum_i \sum_{\text{layers } d=1}^{4} g_d \left(V_d^{\exp} - V_d^{\text{sim}}\right)^2 (t_i) \tag{4.15}$$

This procedure was repeated as we searched through a grid of possible parameter values around their experimental averages, yielding the error plots shown in Fig. 4-3A (the final grid search was over 3.2 million simulations). The scanned parameter ranges and the best fit parameters that resulted in the smallest error E are summarized in Table 4.1.

Cell-to-cell variability. Once the parameters were determined through the method described above, we introduced fluctuations between individual cells in the effective surface tension. To that end, we sampled surface tension for each cell as $\gamma_i = \gamma_c(1 + \sigma\chi_i)$, where χ_i is a random variable sampled from the standard normal distribution with variance $\sigma = 0.1$. Results averaged over $N = 5000$ trials are presented Fig. 4-3C, where the envelope reflects one standard deviation of the fluctuation.

Ring canal fits. Measured ring canal diameters were averaged for each layer and each stage [30]. Exponential functions of the form $r(t) = r_0 e^{t/\tau}$ were then fit to the averages using the 'fit' function in Matlab. The fit parameters are as follows: r_0 =0.82, 0.55, 0.44, and 0.67 μm and τ = 34.8, 31.2, 29.1, and 38.0 hours for L1-L4, respectively. Values of R^2 are 0.93, 0.88, 0.85, and 0.83, respectively.

4.2.3 Model result interpretation

In the simulations, we used for all 16 cells the same effective tension value $\gamma = 4\,\text{pN}/\mu\text{m}$, estimated from earlier measurements of cytoplasmic viscosity [161] and our own measurements of ring canal radii and volume flux [30]. This estimate is consistent with previously reported cortical tension values [165]. The equilibrium radius R_0 in (4.1) was chosen proportional to the initial cell radius, $R_{0i} = \rho R_i(0)$, using the same proportionality constant ρ for all $i = 1, \ldots, 16$ cells. Since the initial NC volume is also approximately proportional to the NC nuclear volume [155], this choice is consistent with the fact that the nucleus sets a lower bound on the NC membrane area at the end of Phase I transport. By comparing simulations and experiment, we determined a best fit parameter $\rho \approx 0.60$; smaller values of ρ favor backflow between adjacent cell layers, in which more posterior NCs transport their cytoplasm into more anterior ones, whereas larger values suppress such backflow. The best fit value for

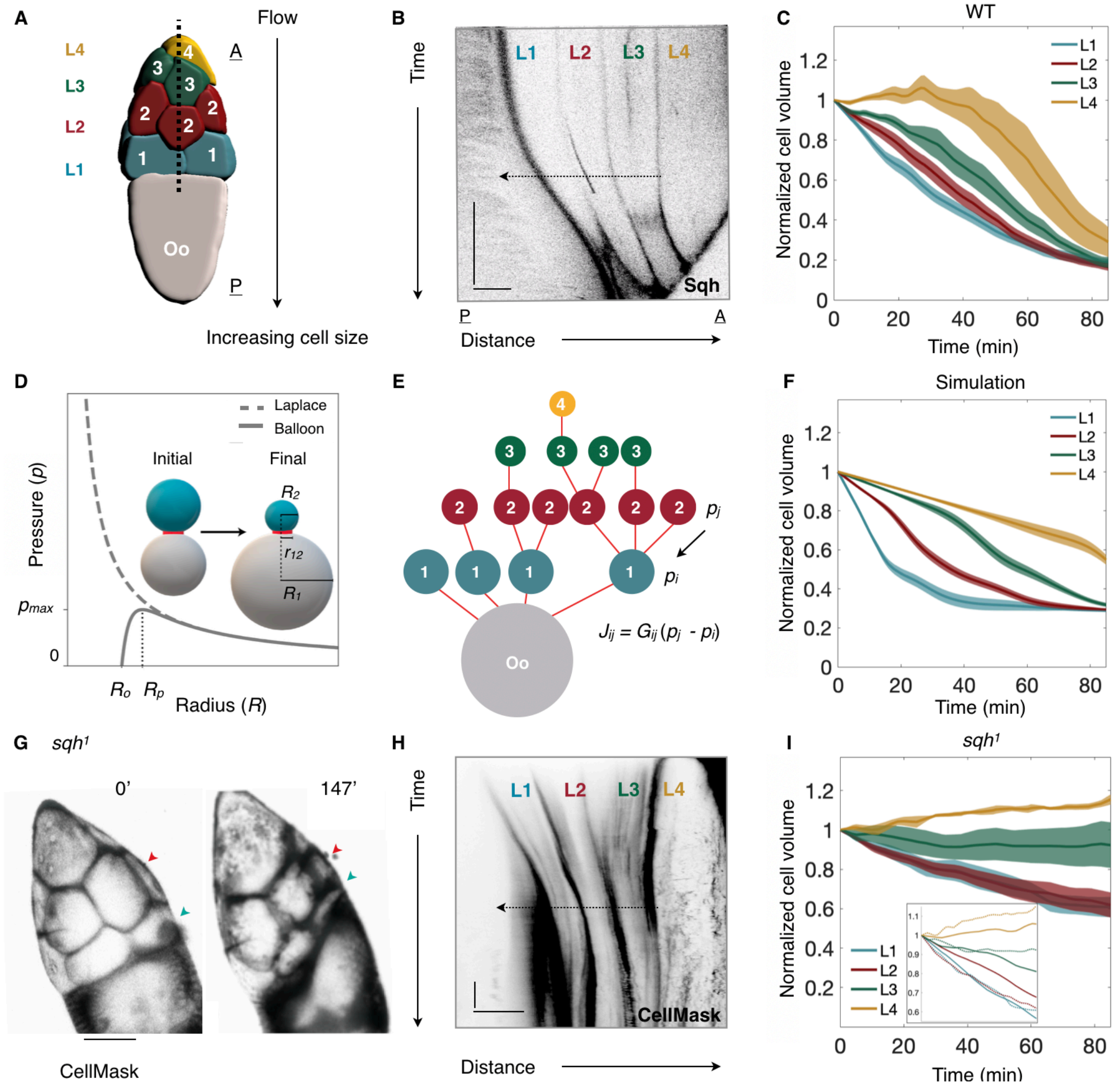

Figure 4-2 *(Caption next page)*

ρ yielded values R_{0i} no more than 10% larger than the directly measured nuclear radii (Table 4.1), suggesting that the presence of nuclei limits pressure-driven flow once NC volumes become comparable to nuclear volumes. Finally, an initial guess for the hydraulic conductances G_{ij} was obtained by assuming $G_{ij} = \pi r_{ij}^4/(8\mu L)$ for Poiseuille-type flow (Eq. (4.9), [169]), where r_{ij} and L are the measured ring canal diameters and their average length, respectively, and μ denotes the fluid viscosity. Since $r_{ij} \in [4, 10]\,\mu$m and $L \approx 2\,\mu$m are of the same order for the ring canals, the Poiseuille conductance provides only an approximation, and we therefore explored a range of values around the Poiseuille prediction in our simulations (Table 4.1).

Figure 4-2 *(previous page)*: NC dumping dynamics are explained by a pressure-driven networked-flow model. **A.** 3D-reconstruction of a germline cyst showing the NCs' arrangement into four layers relative to the oocyte (Oo). During NC dumping, cytoplasm flows in the direction of increasing cell size, from anterior (A) to posterior (P). **B.** Kymograph of Sqh intensity in WT along the dashed line shown in A, illustrating hierarchical onset of NC dumping across the 4 NC layers (L1-L4); arrow indicates direction of flow. Scale bars: 30 min, 50 μm; black indicates highest intensity. **C.** Plot of normalized NC volumes (V/V_0) during NC dumping for each layer from live imaging; $t = 0$ is onset of NC dumping; solid line indicates average; envelopes show standard error ($N = 15, 12, 9, 5$ cells for layers 1, 2, 3, and 4, respectively). **D.** Plots of Young-Laplace's law and the corrected pressure law for elastic balloons. Pressure is at its maximum, p_{max}, at radius R_p; R_0 is the uninflated balloon radius; r_{12} is the radius of the pipe connecting balloons 1 and 2. Schematic illustrates the two-balloon problem, where the smaller balloon (cyan) empties into the larger balloon (gray). **E.** Network representation of the germline cyst in **A** showing cells' relative sizes and connections; cells are shown as nodes and ring canals as edges. **F.** Plot of normalized NC volumes from simulations of fluid flow in the germline cyst using the best fit parameter set (solid line); envelopes show standard error constructed from the ten nearest sets in parameter space ($N = 11$). Time is scaled by the physical constants of the model. **G.** *sqh*^{1} germline mutant showing NCs in the first (blue arrowhead) and second (red arrowhead) layers emptying into the oocyte. **H.** Kymograph of intensity of CellMask (a membrane marker) in *sqh*^{1} mutants, showing transport of cytoplasm from the first two layers. Scale bars: 30 min; 70 μm. **I.** Plot as in C of normalized NC volumes over time in *sqh*^{1} germline clones; ($N = 14, 17, 7, 6$ cells for layers 1, 2, 3, and 4, respectively); inset shows WT cell volume trajectories from **C** (solid lines), re-scaled in time and overlaid with *sqh*^{1} mutant data (dashed lines), demonstrating slower yet hierarchical intercellular transport.

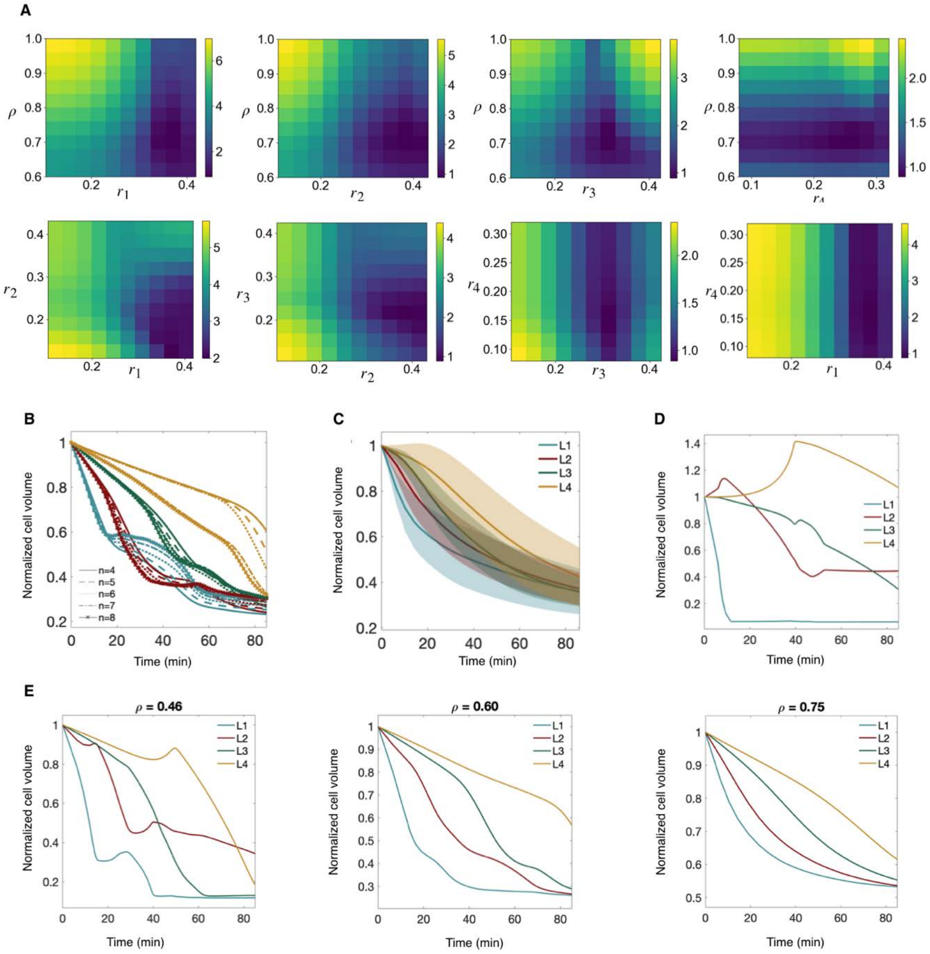

Figure 4-3 : Grid search through parameter space and effects of input parameters of the model. **A.** Two-dimensional slices of the simulation error as defined in Eq. (4.15) measured on the 5-dimensional grid space spanned by the sampled parameter ranges $(r_1, r_2, r_3, r_4, \rho)$. For a given pair of parameters, the remaining parameters are at their best-fit values. Color bar refers to simulation error ($\sigma = 0.1$). **B.** Normalized NC volume (V/V_o) from simulations for varying values of n, the exponent in the correction term to the Young-Laplace law, showing that intercellular transport hierarchy and qualitative behaviors are maintained for the values of n tested. **C.** Results from simulations averaged over 5,000 trials, where surface tension of each cell is sampled from a normal distribution; envelope reflects half a standard deviation of the fluctuations. As seen in the envelope for L4, in several of these simulations the L4 cell increases in size due to backflow from its downstream L3 cell - a feature of NC dumping that has been reported in previous studies [2]. **D.** Results from simulations showing layer-wise averaged cell volumes over time, in which all NCs and ring canal radii are equal for all cells, showing qualitative differences in the intercellular pattern and time scale of transport. **E.** Results from simulations for three values of ρ and all ring canal sizes at their best-fit values. Smaller values of ρ show transient increases in layer size indicative of backflow, while larger values result in less backflow and smoother curves.

Despite its minimal phenomenological character, the flow-network model captures qualitatively essential features of the experimentally observed transport dynamics (Fig. 4-3, A and C). Specifically, the best fit model correctly reproduces both the hierarchical pattern of intercellular transport and time scale of NC dumping (Fig. 4-2F). The model can be expanded to account for natural cell-to-cell variability in effective surface tension [170]; such extensions successfully capture experimentally observed complex transport dynamics along the 16-cell tree. For example, our data show the L4 NC transiently increasing in size during NC dumping, which can occur if the L3 cell to which it is connected shrinks sufficiently such that it becomes smaller than the L4 cell. Such transient backflow away from the oocyte is a feature of NC dumping that has been observed and documented before [2] and is predicted by our model (Fig. 4-3C). We also found that the gradient in NC and ring canal sizes, from smallest at the anterior to largest at the posterior end, is critical for the timely, directional, and hierarchical transport pattern observed experimentally; simulations in which these size gradients were ignored displayed aberrant intercellular transport patterns and dynamics (Fig. 4-3D).

An insight provided by the model is the high sensitivity of intercellular transport to changes in ring canal size through the approximately quartic scaling of the hydraulic conductances. During oogenesis, ring canal diameters increase in size by ∼10-fold [141]. However, ring canal diameter increases most rapidly in the stages of oogenesis prior to NC dumping [30], through the differential recruitment of F-actin towards expansion of the cytoskeletal ring rather than increasing the thickness of the ring canal [171]. Recent work has suggested a mechanosensory function for filamin in ring canal expansion, as rapid growth of the ring canal coincides with rapid growth of the egg chamber and increased tension on the cells' plasma membrane [172]. While onset of NC dumping is likely affected by factors such as interactions between the follicle cells and the germline, or by external cues, here we propose that the increase in ring canal size prior to NC dumping can also sharply accelerate cytoplasmic transport from NCs into the oocyte [30].

Our model predicts that lowering of the effective NC surface tension will slow down the rate of intercellular transport, as the parameter γ sets the overall time scale, but will not affect the hierarchical transport pattern. In a cell, surface tension is affected by the actomyosin cortex and can be reduced by inhibiting myosin [173]. Therefore, to test how transport is affected by reducing surface tension, we quantified the spatiotemporal pattern of NC dumping in a mutant in the myosin RLC, encoded by *spaghetti squash* (*sqh*). In sqh^1 mutant germline clones, *sqh* mRNA and protein levels are reduced by ∼90% [174, 175]. We found that while Sqh-depleted germline cysts are 'dumpless', i.e., do not complete NC dumping (Fig. 4-2G) [145], the hierarchical transport pattern observed in WT is largely maintained (Fig. 4-2, H and I). However, NC dumping in sqh^1 mutants proceeded more slowly (Fig. 4-2I, inset), which is consistent with myosin contributing to the baseline level of cortical tension required for Phase I, but not to the onset, direction or pattern of intercellular transport.

4.3 Phase II requires actomyosin contractile surface waves

Although transport of cytoplasm is initiated in sqh^1 mutant egg chambers, NC dumping is not completed in these mutants, suggesting that actomyosin activity and its regulation are important. Indeed, live imaging of egg chambers with labeled myosin (*sqh::mCh*) and actin (*F-tractin::TdTomato* and *Utr::GFP*) demonstrates that actomyosin is highly dynamic during Phase II of NC dumping. Myosin exhibits a diversity of spatiotemporally organized cortical waves, such as colliding myosin wave fronts, rotating cortical bands, and myosin rings travelling between the cell's poles, which lead to local and dynamic NC shape deformations, as opposed to isotropic contractions of the entire cell (Fig. 4-4, A to E). We also found that actomyosin waves in the NCs travel at ∼0.3 μm/s, a speed comparable to that of Rho-actin contraction waves observed in frog and starfish oocytes and embryos [147]. Notably, the intercellular pattern of actomyosin wave onset mirrors that of cytoplasmic transport, starting in

NCs closer to the oocyte, which shrink first, before appearing in NCs further away (Fig. 4-4F).

Dynamic actomyosin behaviors like those observed here are regulated through RhoA activation and inhibition [147, 176, 177]. RhoA is a small GTPase activated by guanine nucleotide exchange factors (GEFs) and inhibited by GTPase-activating proteins (GAPs) [178, 179]. Binding to downstream effectors, such as the Rho-associated and coiled-coil kinase (ROCK; Rok in *Drosophila*), results in increased contractility through myosin RLC phosphorylation (Fig. 4-4G) [180, 181, 182]. We found that while RhoGAP15B depletion in the germline cyst led to a 'dumpless' phenotype (Fig. 4-4H), onset of NC dumping and the time scale of Phase I transport were unaffected (Fig. 4-4I). The hierarchical pattern of Phase I transport was also largely unchanged, although there was greater variability between the timing of L1 and L2 in knockdown egg chambers (Fig. 4-4I). Instead, RhoGAP15B depletion disrupted myosin wave dynamics and concomitant cell-scale shape deformations otherwise observed during Phase II: cells displayed erratic myosin activity associated with smaller and more transient cell protrusions (Fig. 4-4, J and K). We confirmed that incomplete NC dumping in RhoGAP15B knockdowns is not attributable to obstructed or diminished ring canal sizes or disrupted actin cables that tether the NC nuclei [183, 144]. These data therefore suggest that incomplete cytoplasmic transport in RhoGAP15B knockdowns is due to disrupted actomyosin wave dynamics in Phase II of NC dumping.

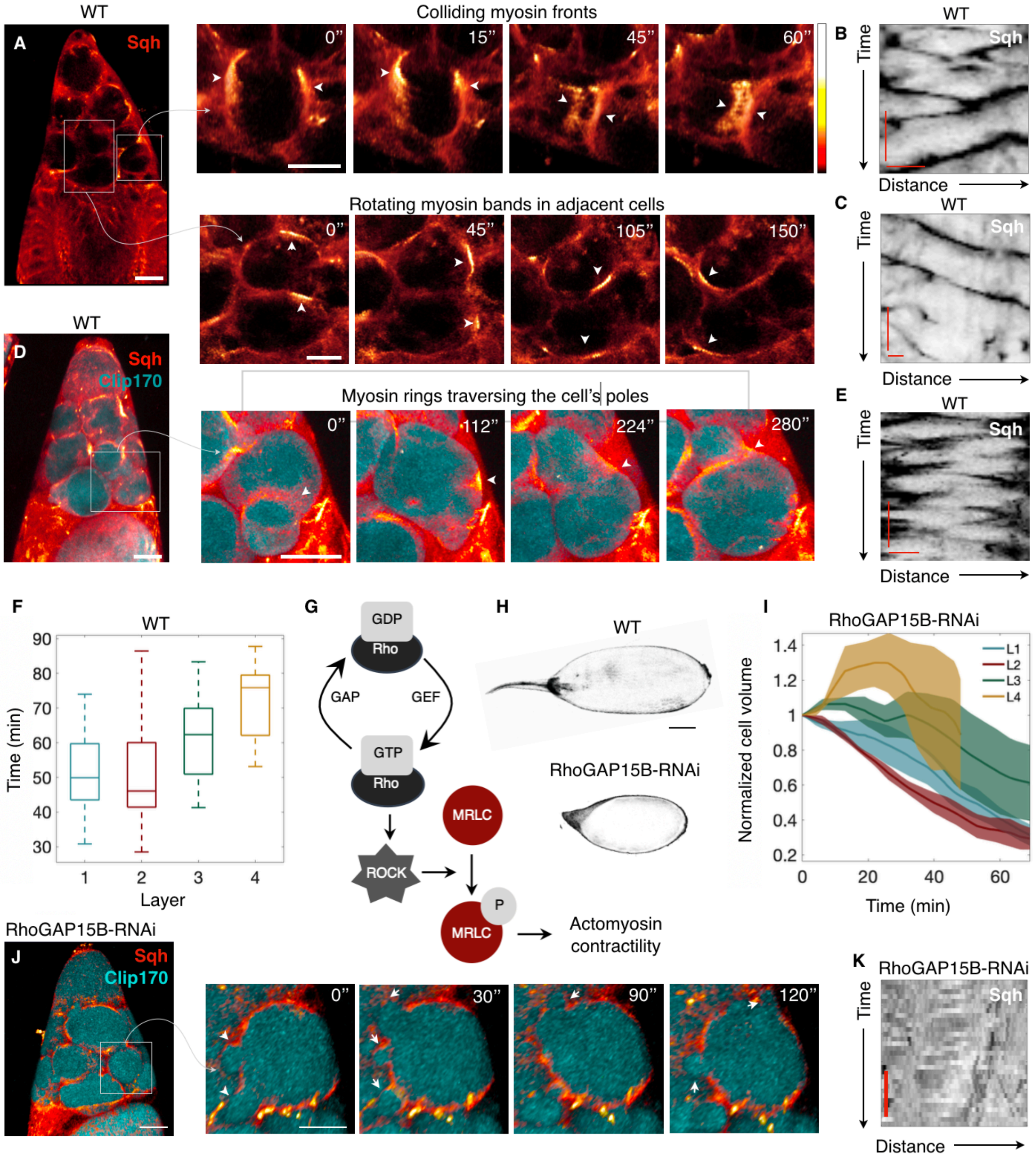

Figure 4-4 *(Caption next page)*

Figure 4-4 *(previous page)*: Complete NC dumping requires Rho-regulated wave-like actomyosin dynamics. **A.** Heat map of an egg chamber expressing *sqh::mCh*; blowups show NCs with dynamic actomyosin cortical waves as colliding fronts (top) and rotating bands (bottom) in adjacent NCs, with respective kymographs of Sqh intensity around NCs' perimeter (**B**, **C**). **D.** Heat map of an egg chamber expressing *sqh::mCh* and *Clip170::GFP* (cyan); blowups show a NC with an actomyosin ring (arrowhead) traversing the cell's opposing poles and deforming cell shape, with **E** showing a kymograph of Sqh intensity. **F.** Box-and-whisker plot of time at which nonuniform and persistent cell deformations are first observed following onset of NC dumping in each layer (center line = median; edges = upper and lower quartiles; whiskers extend to extrema; $N = 20, 22, 16, 5$ cells for layers 1, 2, 3, and 4). **G.** The Rho/ROCK signaling pathway regulates phosphorylation of the myosin regulatory light chain (MRLC) and actomyosin contractility. **H.** Comparison between wild-type (WT; top) and dumpless, RhoGAP15B-depleted (bottom) egg chambers. Scale bar: 50 μm. **I.** Plot of normalized NC volumes during NC dumping for each layer from live imaging of RhoGAP15B knockdowns; $t = 0$ is onset of NC dumping; solid line indicates average and envelopes show standard error ($N = 7, 6, 3, 2$ cells for layers 1, 2, 3, and 4, respectively). The trajectory for the L4 cells stops at $t \sim 50$ minutes due to membrane breakdown. **J.** RhoGAP15B-depleted germline expressing *sqh::mCh* and *Clip170::GFP*; blowup shows smaller short-lived cell protrusions as opposed to the cell-scale dynamic deformations observed in WT. **K.** Kymograph of Sqh intensity along the perimeter of a cell in a RhoGAP15B knockdown at a comparable time to **B**, **C**, and **E**, illustrating disrupted wave dynamics; black indicates highest intensity. The time scale bar is 5 minutes, while the horizontal axis represents fractional distance along cell perimeter. Scale bar in **A**, **D**, and **J**: 40 μm; scale bar in blowups: 20 μm; kymograph scale bars in **B**, **C**, and **E**: 5 min; 10 μm.

4.4 Physical and biochemical mechanisms are required for complete transport

A clue to how actomyosin surface waves enable complete NC dumping came from directly visualizing inter- and intracellular cytoplasmic flow using reflection-mode microscopy. Following actomyosin wave onset and concomitant NC shape deformations, cytoplasm was observed flowing through spaces between NC nuclei and membranes and completing multiple revolutions around the large polyploid nuclei as intercellular anterior-to-posterior transport continued (Fig. 4-5, A and B). In contrast, intracellular flow in RhoGAP15B knockdowns appeared erratic and lacked the persistent radial motions around NC nuclei necessary for bringing cytoplasm in contact with a ring canal (Fig. 4-5, C and D). As a result, RhoGAP15B knockdowns exhibited interrupted anterior-to-posterior intercellular flow, repetitive and more frequent transport of cytoplasm away from the oocyte (Fig. 4-5, E and F), a greater degree of layer 4 expansion (Fig. 4-4I), and incomplete NC dumping. Given that actomyosin waves first appear in a nurse cell once it has emptied most of its cytoplasmic contents, we propose that wave-mediated NC deformations enable continued pressure-driven transport by creating spaces between plasma membranes and nuclei in shrunken NCs. Because the oocyte is the largest cell in the germline cluster, it will always have the lowest pressure and will therefore set the directionality of flow. As a result, wave-mediated cell deformations could create a path that allows cytoplasm to flow past nuclei from anterior to posterior ring canals and transport into the oocyte to run to completion (Fig. 4-6).

4.5 Discussion and conclusion

The above analysis presents joint experimental and theoretical work that addresses a longstanding question concerning the origin and regulation of multicellular collective behavior during oocyte development: How do support sister cells in a germline cyst directionally transport the entirety of their cytoplasm into the future egg cell? Our

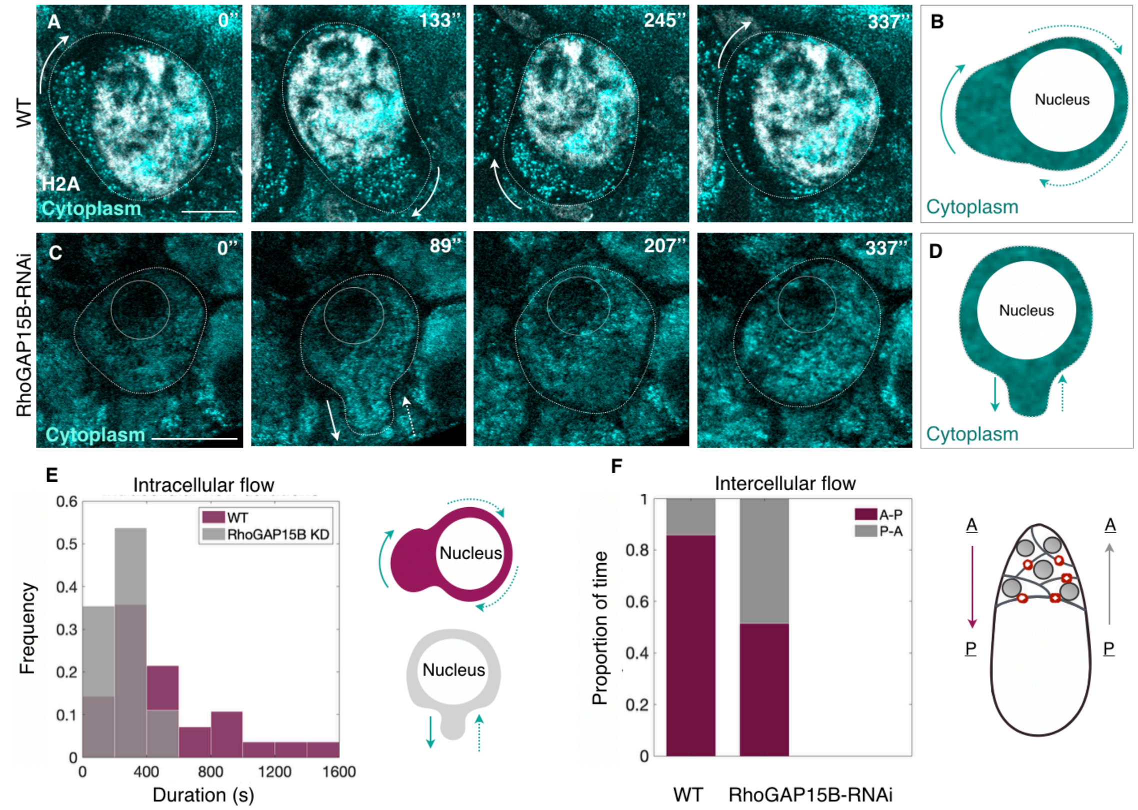

Figure 4-5 : Actomyosin contractions promote intracellular flow in shrunken NCs. **A.** Time-lapse images from reflection-mode microscopy showing cytoplasm (cyan) flowing around a NC nucleus (H2A, white) as persistent actomyosin waves deform cell shape. **B.** Illustration of cytoplasmic flow observed in **A**, where arrows point in the direction of flow. **C.** Erratic and transient intracellular cytoplasmic flow in a germline RhoGAP15B knockdown, illustrated in **D**, highlighting the lack of persistent revolutionary motions observed in WT. Scale bars in **A** and **C**: 20 μm. **E.** Histogram of the duration of observed intracellular cytoplasmic flow events in WT and RhoGAP15B knockdowns (WT: $N = 28$ events; RhoGAP15B-RNAi: $N = 82$). **F.** Bar plot of the proportion of time anterior-to-posterior (A-P) versus posterior-to-anterior (P-A) flows were observed through ring canals in WT and in RhoGAP15B-RNAi egg chambers (WT: 6 events of intercellular flow spanning 30 minutes total; RhoGAP15B knockdowns: 29 events spanning 54 minutes).

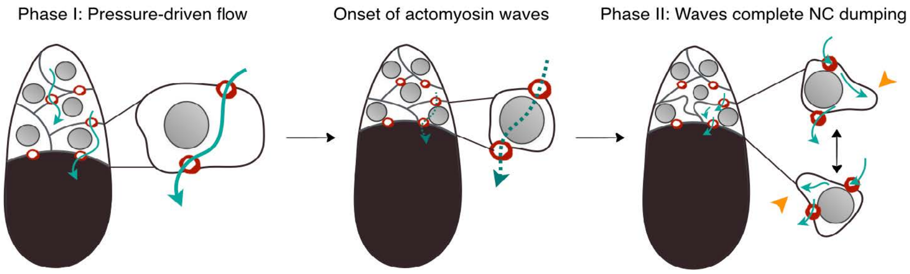

Figure 4-6 : Physical and biochemical mechanisms cooperate to enable NC dumping. Schematic of the proposed model for the contribution of pressure-driven flow with baseline cortical tension and actomyosin-dependent flows to directional and complete NC dumping. Arrows show direction of intercellular flow; dashed arrow indicates interrupted flow; arrowheads point to actomyosin-mediated cell deformations that permit continued intercellular flow in shrunken NCs.

experiments and theory show that baseline surface tension and differential cell size provide robust and highly tunable fluid-mechanical control over directional intercellular cytoplasmic flow, and that subsequent wave-like actomyosin contractions are essential to complete transport. These findings contrast with previous hypotheses for NC dumping, which suggested that cytoplasm is driven out of the NCs through a global increase in pressure mediated through upregulated cytoskeletal force generation, or squeezing [156, 144], requiring that actomyosin contractility increase at the onset of NC dumping [142]. Such a model however does not mechanistically explain the directionality and hierarchical flow pattern that is observed during NC dumping; importantly, our data show that changes in actomyosin localization and concomitant membrane blebbing do not occur until the NCs have emptied most of their cytoplasmic contents into the oocyte.

4.5.1 Model limitations

While the hydrodynamic model presented here faithfully reproduces the hierarchical dumping pattern, the interpretation of its parameters is limited by its partially phenomenological nature. The Young-Laplace term is biophysically motivated, with γ playing the role of an effective surface tension reflecting the energetic cost of having an interface of a certain area. However, the second term of Eq. (4.1) is a phenomenological correction to the Young-Laplace pressure. For a rubber balloon, R_0 is the radius at which the pressure difference across the balloon's surface is zero; however, cells do not have a well-defined 'empty' size. Indeed, a cell's cortex always generates some baseline tension, such that even as the cell decreases in size, the cortex is remodeled so that this baseline tension is maintained [184]. Another important difference between the classical balloon experiment and the NC tree is the presence of the cell nuclei, which can hinder intra- and intercellular fluid transport once the cell volume has become comparable to the nucleus size. Therefore, for a cell, the R_0 parameter can be thought of as an effective limiting radius below which cortical tension alone no longer suffices to drive flux through the ring canals, defining the end of Phase I. Identifying the biochemical and biophysical mechanisms that trigger the transition from the hydraulic Phase I to the contractile wave-mediated Phase II, which may be cell-size dependent or related to membrane-nucleus contact interactions, poses an interesting open question for future research.

4.5.2 Conclusion

The above analysis highlights the complementary importance of physical and biological mechanisms in achieving directed intercellular fluid transport during oogenesis and adds to the growing list of examples where hydrodynamics plays a critical role in development [131, 132, 133, 134]. This work has also revealed a diversity of myosin wave-like behaviors and a previously unknown function for excitable actomyosin dynamics. Indeed, as one of the final facilitators of material transfer between sister germ cells, this work expands the repertoire of roles played by surface cortical waves in development [147, 148, 149, 185].

Chapter 5

Characterizing developmental mode dynamics from single-cell trajectories

The contents of this chapter, and parts of chaps..., have been previously published as 'Learning developmental mode dynamics from single-cell trajectories', N. Romeo, A. D. Hastewell, A. Mietke, J.Dunkel,eLife 10:e68679 (2021)

Embryogenesis, the development of a multicellular organism from a single fertilized egg cell, requires coordinated collective motions of thousands of cells across a wide range of length and time scales [186, 187]. Understanding how a highly reproducible and robust tissue organization arises from the dynamics and interactions of individual cells presents a major interdisciplinary challenge [5]. Recent advances in high-resolution live imaging make it possible to track the internal biological states and physical movements of many individual cells on pan-embryonic scales throughout various stages of development [188, 189, 190, 4]. This unprecedented wealth of data poses two intertwined compression problems of equal practical and conceptual importance. The first concerns the efficient reduction of high-dimensional tracking data without loss of relevant information; the second relates to inferring predictive low-dimensional models for the developmental dynamics. Mathematical solutions to the first problem are aided by taking into account the geometry and symmetries of the developing embryo, which suggest suitable basis functions for a coarse-grained and sparse mode representation of raw data [191]. Efficient algorithmic approaches tackling the second problem appear within reach thanks to recent advances in the direct inference of dynamical systems equations from data [192, 193]. Building on these ideas, we construct and demonstrate here a computational framework that translates developmental single-cell trajectory data on curved surfaces into quantitative models for the dominant hydrodynamic modes.

Widely applied in physics [194, 195, 196, 197], engineering [198, 199] and spectral computing [200, 60, 201], mode representations [202, 203] provide a powerful tool to decompose and study system dynamics at and across different energetic, spatial and temporal scales. In quantum systems, for example, mode representations in the form of carefully constructed eigenstates are used to characterize essential energetic system properties [204, 205]. Similarly, turbulence theory has seen significant progress by studying the coupling between Fourier modes that represent dynamics at different length scales. This approach enabled a better understanding of energy cascades [206, 207] and provided insights into the nature of turbulence in non-living [208, 209] and in living [210, 211, 212, 213] systems. Additionally, the multi-scale nature of many biological processes make them particularly amenable to a representation in terms of spatial and temporal modes [214]. Despite this fact, however, mode representations are not yet widely used to characterize and compress cell tracking data, or to infer dynamic models from such data.

To demonstrate the practical potential of mode representations for the description of multicellular developmental processes, we develop here a computational framework that takes cell tracking data as inputs, translates these data into a sparse mode representation by exploiting symmetries of the biological system, and utilizes recently developed ODE inference techniques [193] to infer a predictive dynamical model. The model will be specified in terms of a learned Green's function that propagates initial cell density and flux data forward in time. To validate the approach, we demonstrate that it correctly recovers the hydrodynamic equations for active Brownian particle (ABP) dynamics on curved surfaces. Subsequently, as a first example application to experimental single-cell tracking data, we consider the pan-embryonic cell migration during early gastrulation in zebrafish [4], an important vertebrate model system for studying various morphogenetic events [187, 173, 215]. During gastrulation, complex migratory cell movements organize several thousand initially undifferentiated cells into different germlayers that lay out the primary body plan [216]. The underlying high-dimensional single-cell data make this process a prototypical test problem for illustrating how spatio-temporal information can be efficiently compressed to analyze and model biological structure formation.

Broadly, our goal is to translate experimentally measured single-cell trajectories on a curved surface into a quantitative model of collective cell migration dynamics. As a specific example, we consider recently published lightsheet microscopy data that captures the individual movements of thousands of cells during early zebrafish development from epiboly onset at 4 hours post-fertilization (hpf) to about 18 hpf [4]. This developmental period is characterized by a collective symmetry breaking event during which cells collectively migrate over the yolk cell surface [216]. Namely, they rearrange from an initial localization around the animal pole (AP) (Fig. 5-1A, left) into a more elongated configuration that already indicates the basic geometry of the fully developed zebrafish larva (Fig. 5-1A, right). Working with a two-dimensional (2D) sphere projection of the experimental data, we first describe a coarse-graining approach that faithfully captures cell-mass transport on a curved surface. We then construct a sparse mode representation of the resulting hydrodynamic fields in terms of scalar and vector spherical harmonic basis functions, discuss mode signatures of morphogenetic symmetry breaking events, and connect them to the dynamics of topological defects in the cellular flux. We validate this mode representation framework and the subsequent model inference using synthetic data of ABPs on a sphere, for which coarse-grained fields and learned models can be directly compared against analytical predictions. Finally, we infer a linear model for the mode dynamics of the experimental zebrafish data, which enables us to study the characteristics of cell interactions through kernels that couple cell density and flux and compare their features with the hydrodynamic mean-field signatures of ABPs on a sphere.

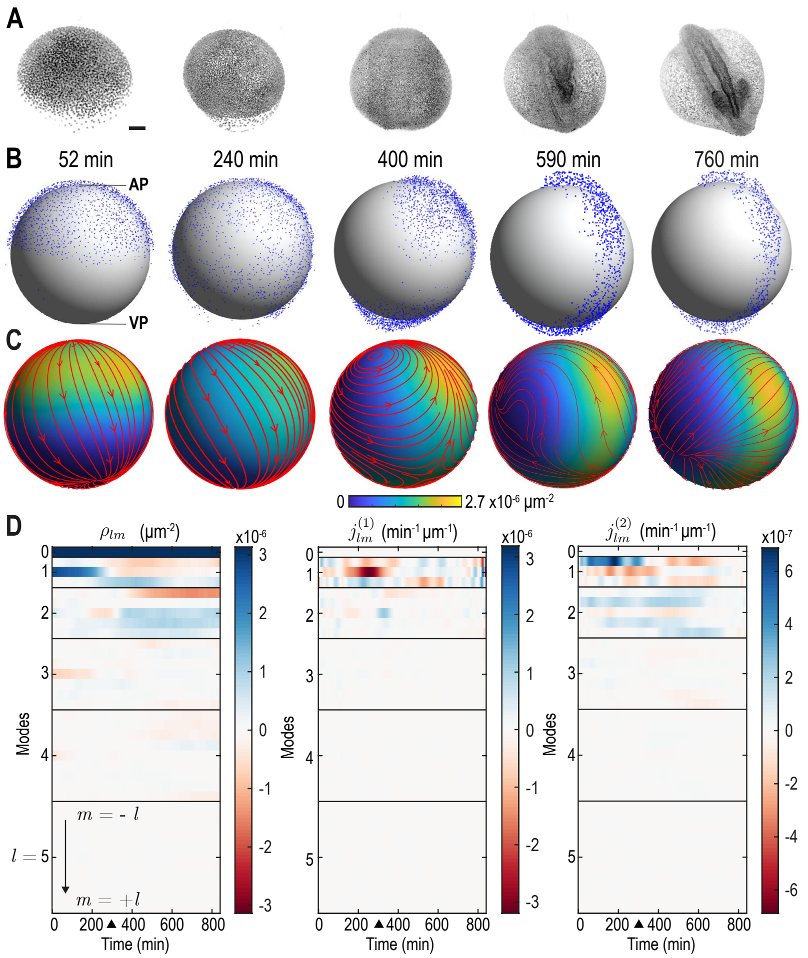

Figure 5-1 : From single-cell tracking data to sparse mode amplitude representations **A**: Microscopic imaging data of early zebrafish development (adapted from [3]) shows cell migration from an initially homogeneous pole of cells (left) towards an elongated structure that indicates the head-tail axis of the fully developed organism. Scale bar, $100\,\mu m$. **B**: Experimental single-cell tracking data from [4] (blue dots) during similar developmental time points (± 20 min) as in **A**. $t = 0$ min for the indicated time points in **B** corresponds to a developmental time of 4 hours post fertilization. The z-axis points from the ventral pole (VP) to the animal pole (AP). **C**: Coarse-grained relative cell density $\rho(\mathbf{r}, t)$ (color) and associated coarse-grained flux $\mathbf{J}(\mathbf{r}, t)$ (streamlines) determined from single cell positions and velocities from data in **B** via Eqs. (5.2). Thickness of streamlines is proportional to the logarithm of the spatial average of $|\mathbf{J}|$. **D**: Dynamic harmonic mode representation of the relative density $\rho(\mathbf{r}, t)$ (Eq. (5.4), left panel) and of the flux $\mathbf{J}(\mathbf{r}, t)$ (Eq. (5.5), middle and right panel) for fields shown in **C**. The modes $j^{(1)}_{lm}$ correspond to compressible, divergent cell motion, the modes $j^{(2)}_{lm}$ describe incompressible, rotational cell motion. Mode amplitudes become negligible for $l \geq 5$ (Fig. 5-2). For all panels, horizontal black lines delineate blocks of constant harmonic mode number l and black triangles denote the end of epiboly phase.

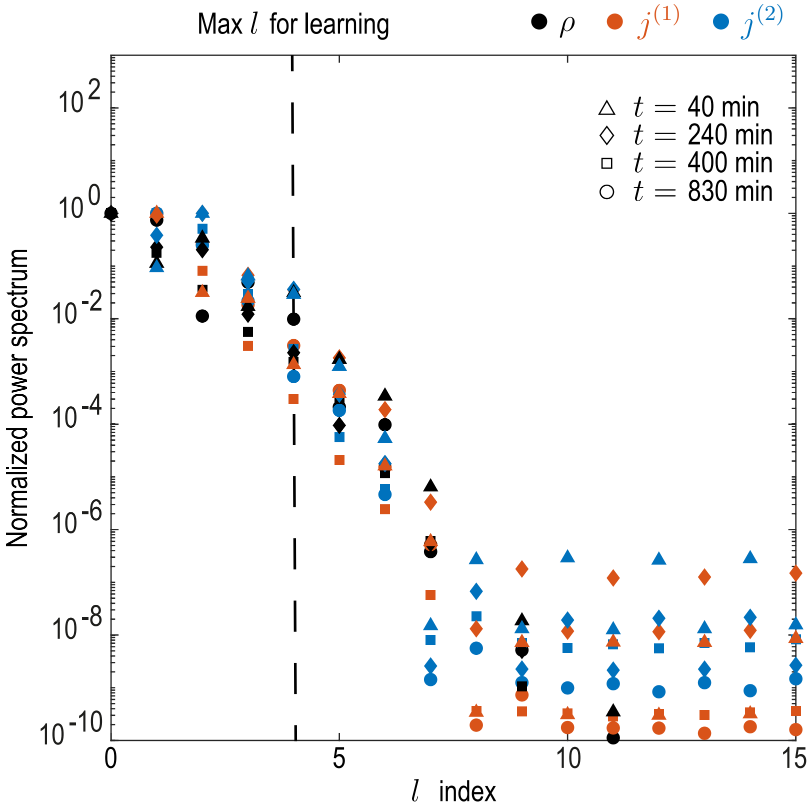

Figure 5-2 : Convergence of spectral representation. Rotationally invariant spatial power spectra as a function of the mode l index were computed for the density field ρ as $P_{\rho,l} = \sum_{m=-l}^{l} \rho_{lm}^2$ and for modes contributing to cell fluxes ($j^{(1)}$ and $j^{(2)}$) as $P_{jk,l} = \sum_{m=-l}^{l} [j_{lm}^{(k)}]^2$ for $k = 1, 2$. Spectra were computed at representative timepoints $t = 40\,, 240\,, 400\,, 830\,\mathrm{min}$ and normalized by their maximum value. The observed decay indicates that a spectral representations of the coarse-grained fields is meaningful, and shows that the mode cut-off chosen for the learning ($l \leq 4$) amounts to discarding approximately 1% of spectral power in each field.

5.1 Coarse-graining of cellular dynamics on a spherical surface

The experimentally observed cell motions are approximately two-dimensional (2D): The radius of the yolk cell surface on which the dynamics takes place is much larger than the average height changes of the evolving cell mass [4]. We therefore adopt a thin film approximation, in which the cellular motion is represented on an effective spherical mid-surface (gray surface in Fig. 5-1B); refined future models should aim to account for the full 3D dynamics. Focusing here on the in-plane dynamics, we project all cell positions and velocities onto a spherical mid-surface $\mathcal{S}$ of radius $R_s = 300\,\mu\mathrm{m}$. On this spherical surface, each cell $\alpha = 1, 2, ..., N$ has a position $\mathbf{r}_\alpha(t)$ and in-plane velocity $\mathbf{v}_\alpha(t) = \mathrm{d}\mathbf{r}_\alpha/\mathrm{d}t$.

As a second processing step, a coarse-grained representation of the single-cell dynamics on a spherical surface is determined. To facilitate the applicability of our framework to a wide range of experimental inputs, we propose a coarse-graining approach that can flexibly integrate cell number variations stemming from cell divisions, but also those from experimental uncertainties in cell imaging and tracking. Consequently, we first consider an idealized scenario in which the total cell number is approximately constant. In this case, mass conservation informs the construction of self-consistent coarse-graining kernels on a spherical surface. In a second step, we describe how this approach generalizes when there are variations in the total cell number.

5.1.1 Consistent coarse-graining of idealized microscopic data

Our specific aim is to translate microscopic cell positions $\mathbf{r}_\alpha(t)$ and velocities $\mathbf{v}_\alpha(t)$ into a continuous cell surface density $\rho(\mathbf{r}, t)$ and an associated flux $\mathbf{J}(\mathbf{r}, t)$ at any point $\mathbf{r}$ of the spherical mid-surface. For an approximately constant total number of cells, the fields ρ and $\mathbf{J}$ are related by the mass conservation equation

$$\frac{\partial \rho}{\partial t} + \nabla_{\mathcal{S}} \cdot \mathbf{J} = 0. \tag{5.1}$$

Here, $\nabla_{\mathcal{S}} \cdot \mathbf{J}$ denotes the in-plane divergence of the cell number flux. To convert cell position $\mathbf{r}_\alpha(t)$ and velocities $\mathbf{v}_\alpha(t)$ into a normalized cell surface density $\rho(\mathbf{r}, t)$ and an associated normalized flux $\mathbf{J}(\mathbf{r}, t)$, we consider a kernel coarse-graining of the form (Appendix B)

$$\rho(\mathbf{r}, t) = \frac{1}{N} \sum_{\alpha=1}^{N} K\left[\mathbf{r}, \mathbf{r}_\alpha(t)\right] \tag{5.2a}$$

$$\mathbf{J}(\mathbf{r}, t) = \frac{1}{N} \sum_{\alpha=1}^{N} \mathcal{K}\left[\mathbf{r}, \mathbf{r}_\alpha(t)\right] \cdot \bar{\mathbf{v}}_\alpha, \tag{5.2b}$$

where N is the total number of cells and $\bar{\mathbf{v}}_\alpha = \mathbf{v}_\alpha / |\mathbf{r}_\alpha|$ is the angular velocity of a given cell on a reference unit sphere (Appendix B). The kernels $K(\mathbf{r}, \mathbf{r}')$ and $\mathcal{K}(\mathbf{r}, \mathbf{r}')$ are given by a scalar and a matrix-valued function, respectively. The matrix kernel $\mathcal{K}(\mathbf{r}, \mathbf{r}')$ takes into account contributions of a particle with velocity $\mathbf{v}_\alpha$ at $\mathbf{r}' = \mathbf{r}_\alpha$ to nearby points $\mathbf{r}$ on the sphere, which involves an additional projection to ensure that $\mathbf{J}(\mathbf{r}, t)$ is everywhere tangent to the spherical surface (Appendix B). Importantly, the mass conservation Eq. (5.1) implies a non-trivial consistency relation between the kernels $K(\mathbf{r}, \mathbf{r}')$ and $\mathcal{K}(\mathbf{r}, \mathbf{r}')$ in Eqs. (5.2). The kernels that obey this condition represent different coarse-graining length scales (Appendix B–Fig. B-2). Throughout, we fix an intermediate coarse-graining length scale to enable a sparse representation of the experimental data, while ensuring that spatial details of the dynamics remain sufficiently well resolved. The final surface density $\rho(\mathbf{r}, t)$ and the associated normalized flux $\mathbf{J}(\mathbf{r}, t)$, computed from Eqs. (5.2) using a kernel with an effective great-circle coarse-graining width of $\sim 70\,\mu$m, are shown in Fig. 5-1C.

5.1.2 Consequences of cell number variations in experimental data

Because cell divisions are essential to most developmental processes, total cell numbers will in many cases – including early zebrafish gastrulation [3] – vary over time. True cell numbers and cell number changes are often difficult to measure due to experimental uncertainties arising from single-cell imaging and tracking within dense cellular aggregates. We therefore merely assume here that single cells are tracked in a representative fashion so that local relative surface densities found from Eq. (5.2a) reflect the probability that cells are present at a given point $\mathbf{r}$. In the absence of further information on cell deaths and cell divisions, we additionally make the more restrictive assumption that cell appearances or disappearances are everywhere proportional to the local cell density. With these assumptions, we can define a cell number surface density $\tilde{\rho}(\mathbf{r}, t) = N(t)\rho(\mathbf{r}, t)$, where $N(t)$ is the cell number at time t and $\rho(\mathbf{r}, t)$ is the normalized surface density given in Eq. (5.2a). Similarly, a cell number flux is given by $\tilde{\mathbf{J}}(\mathbf{r}, t) = N(t)\mathbf{J}(\mathbf{r}, t)$, where the flux $\mathbf{J}(\mathbf{r}, t)$ is computed from the data as described by Eq. (5.2b). Using these definitions in Eq. (5.1), we find that the fields $\tilde{\rho}(\mathbf{r}, t)$ and $\tilde{\mathbf{J}}(\mathbf{r}, t)$ obey a continuity equation

$$\frac{\partial \tilde{\rho}}{\partial t} + \nabla_{\mathcal{S}} \cdot \tilde{\mathbf{J}} = k(t)\tilde{\rho}, \tag{5.3}$$

where $k(t) = \dot{N}(t)/N(t)$ denotes a time-dependent effective growth rate. Importantly, under the two above assumptions, Eq. (5.3) encodes for any time-dependent total cell number $N(t) > 0$ the same information as Eq. (5.1) for coarse-grained normalized surface density $\rho(\mathbf{r}, t)$ and associated flux $\mathbf{J}(\mathbf{r}, t)$ given by Eq. (5.2a) and (5.2b), respectively. In the following analysis, we hence focus on these normalized fields.

5.2 Spatio-temporal mode decomposition

5.2.1 Spatial mode representation on a spherical surface

To obtain a sparse mode representation of the hydrodynamic fields $\rho(\mathbf{r}, t)$ and $\mathbf{J}(\mathbf{r}, t)$ on the spherical surface, we expand them in terms of scalar and vector spherical harmonics (SHs) [217, 218] (Appendix A). SHs are defined on points $\hat{\mathbf{r}} = \mathbf{r}/R_s$ of the unit sphere, where $R_s = 300\,\mu$m is the mid-surface radius. In this basis, the scalar density field is represented as

$$\rho(\mathbf{r}, t) = \sum_{l=0}^{l_{\max}} \sum_{m=-l}^{l} \rho_{lm}(t) Y_{lm}(\hat{\mathbf{r}}), \tag{5.4}$$

which conveniently separates the time- and space-dependence of $\rho(\mathbf{r}, t)$ into mode amplitudes $\rho_{lm}(t)$ and scalar harmonic functions $Y_{lm}(\hat{\mathbf{r}})$, respectively. The maximal mode number $l_{\max}$ is a proxy for the maximal spatial resolution at which $\rho(\mathbf{r}, t)$ is faithfully represented (Fig. 5-3). Similarly, the vector-valued flux $\mathbf{J}(\mathbf{r}, t)$ can be decomposed into time-dependent mode amplitudes $j_{lm}^{(1)}(t)$ and $j_{lm}^{(2)}(t)$, while its spatial dependence is described by vector SHs $\mathbf{\Psi}_{lm}(\hat{\mathbf{r}})$ and $\mathbf{\Phi}_{lm}(\hat{\mathbf{r}})$ [218] (Appendix A),

$$\mathbf{J}(\mathbf{r}, t) = \sum_{l=1}^{l_{\max}} \sum_{m=-l}^{l} \left(j_{lm}^{(1)}(t) \mathbf{\Psi}_{lm}(\hat{\mathbf{r}}) + j_{lm}^{(2)}(t) \mathbf{\Phi}_{lm}(\hat{\mathbf{r}}) \right). \tag{5.5}$$

Besides the in-plane divergence $\nabla_{\mathcal{S}} \cdot \mathbf{J}$ that leads to local density changes [see Eq. (5.1)], the cell number flux $\mathbf{J}(\mathbf{r}, t)$ also contains an in-plane curl component $\nabla_{\mathcal{S}} \times \mathbf{J}$ that is associated with locally rotational cell flux. The two sets of vector SHs $\{\mathbf{\Psi}_{lm}\}$ and $\{\mathbf{\Phi}_{lm}\}$ conveniently decompose the flux into these contributions: Because $\nabla_{\mathcal{S}} \cdot \mathbf{\Phi}_{lm} = \nabla_{\mathcal{S}} \times \mathbf{\Psi}_{lm} = 0$, and $\hat{\mathbf{r}} \cdot (\nabla_{\mathcal{S}} \times \mathbf{\Phi}_{lm}) = \nabla_{\mathcal{S}} \cdot \mathbf{\Psi}_{lm} = -l(l+1) Y_{lm}/R_s$ [218], we see from Eq. (5.5) that $j_{lm}^{(1)}(t)$ corresponds to modes that drive density changes and $j_{lm}^{(2)}(t)$ represents modes of local rotational cell motion that change relative cell positions but do not change local density. Indeed, using harmonic mode representations of the cell number density Eq. (5.4) and the cell number flux Eq. (5.5) directly in the continuity Eq. (5.1), we find a set of ordinary differential equation in mode space

$$\frac{\mathrm{d}}{\mathrm{d}t}\rho_{lm}(t) = \frac{l(l+1)}{R_s} j_{lm}^{(1)}(t), \tag{5.6}$$

where $l = 0, 1, ..., l_{\max}$ and for each value of l, $m = -l, -l+1, ..., l-1, l$. Equation (5.6) offers an alternative way of determining the modes $j_{lm}^{(1)}(t)$ directly from the modes $\rho_{lm}(t)$ of the coarse-grained cell number density [see Eqs. (5.2a) and (5.4)], while ensuring that the resulting fields obey mass conservation exactly. In practice, the modes $j_{lm}^{(1)}(t)$ found from a vector harmonic representation of the coarse-grained cell number flux Eq. (5.2b) will often deviate from modes $j_{lm}^{(1)}(t)$ determined from Eq. (5.6), even if cell numbers are expected to be conserved. This can be, for example, due to limited accuracy in determining velocities $\mathbf{v}_\alpha(t)$ from noisy single-cell trajectories $\mathbf{r}_\alpha(t)$, or due to spatially inhomogeneous appearances and disappearances of cells in tracking data. Consistent with our simplifying assumption that cell number changes in the data can be sufficiently well approximated by a globally homogeneous growth rate [compare Eqs. (5.1) and (5.3)], the subsequent analysis uses the modes $j_{lm}^{(1)}(t)$ as determined from the density modes $\rho_{lm}(t)$ via Eq. (5.6), together with modes $j_{lm}^{(2)}(t)$ from the explicit velocity coarse-graining Eq. (5.2b).

The representation of $\rho(\mathbf{r}, t)$ and $\mathbf{J}(\mathbf{r}, t)$ in terms of spherical harmonic modes with $l \leq l_{\max}$ leads in total to $3(l_{\max}+1)^2$ mode amplitude trajectories, displaying only a few dominant contributions (Fig. 5-1D) with almost no signal remaining for $l \geq 5$ (Fig. 5-2). This demonstrates that the underlying coarse-grained experimental data is sufficiently smooth and implies that a spectral representations is indeed meaningful. Thus, the coarse-graining approach outlined above provides a sparse spectral representation of high-dimensional microscopic single-cell data. The associated harmonic basis functions and vectors have an intuitive physical meaning, convenient algebraic properties and, as we will see, encode information about the length scales and symmetries of the collective dynamics.

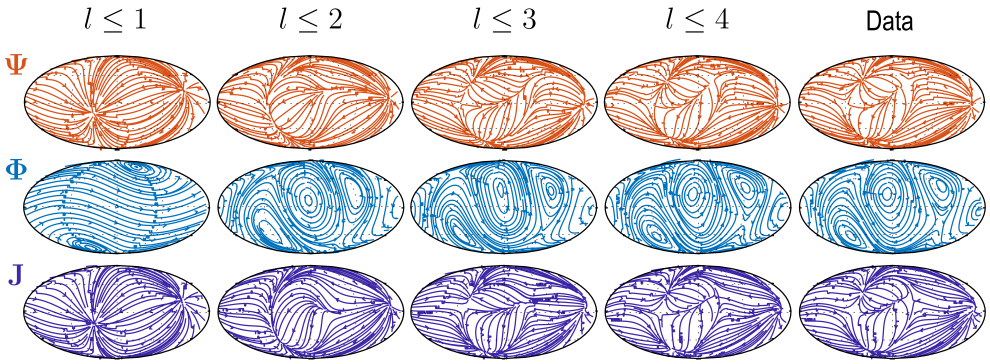

Figure 5-3 : Sequentially adding vector spherical harmonics $\mathbf{\Psi}_{lm}$ and $\mathbf{\Phi}_{lm}$ – equivalent to increasing $l_{\max}$ in Eq. (5.5) – resolves increasing levels of details present in experimental flux fields ("Data"). Main features of the data are captured already by a relatively small number of modes ($l_{\max} = 4$ used throughout this work).

5.2.2 Temporal mode representation

We further compress the dynamical information by representing the time series of the modes onto basis functions made out of the Chebushev polynomials of the first kind $T_n(t)$, which are defined by [217, 200, 219]

$$T_n(\cos x) = \cos(nx). \tag{5.7}$$

These polynomials form an orthogonal basis of continuous functions on the interval $[-1, 1]$, such that an expansion

$$f(t) = \sum_{n=0}^{n_{\max}} c_n T_n(t) \tag{5.8}$$

uniformly converges as $n_{\max} \to \infty$ [200]. This representation also allows computing derivatives spectrally from

$$f'(t) = \sum_{n=0}^{n_{\max}} c_n T'_n(t). \tag{5.9}$$

To simplify notation, we define a dynamic mode vector $\mathbf{a}(t) = [\rho_{lm}(t),\, j^{(1)}_{lm}(t),\, j^{(2)}_{lm}(t)]^\top$ that collects all the modes up to $l = l_{\max}$ determined in the previous section and consider an expansion

$$\mathbf{a}(t) = \sum_{n=0}^{n_{\max}} T_n(t)\, \hat{\mathbf{a}}_n \tag{5.10}$$

in terms of the spatio-temporal mode coefficients $\hat{\mathbf{a}}_n$ with temporal mode number n. This compression allows us to accurately evaluate time derivatives of the mode amplitudes [220], an important step when using Eq. (5.6) to determine flux modes $j_{lm}^{(1)}(t)$ directly from density modes ρ_{lm}. Fixing $l_{\max} = 4$ and $n_{\max} = 30$ in the remainder, the initial single-cell data set of about 1.4 million recorded cell position entries, or 4.2 million degrees of freedom, has thus been reduced to 2250 mode coefficients, corresponding to a compression ratio $\gtrsim 1800$.

5.2.3 Information loss through coarse-graining and spectral truncation

Coarse-graining microscopic data into smooth fields is an irreversible operation, during which some of the original particle information is irretrievably lost. The choice of coarse-graining scale is thus dictated by a trade-off between smoothness and information content - choosing larger coarse-graining scales leads to smoother fields but blurs finer scale structures which may be of interest. To inform our choice of coarse-graining scale, we quantify the loss of information incurred by the coarse-graining operation.

Additionally, spectral representations are exact in the limit of an infinite number of modes. In practice, we choose a maximal harmonic mode number $l_{\max}$ and maximal Chebyshev mode number $n_{\max}$. In Ref. [36], we additionally consider the tradeoff between compression and reconstruction accuracy as $l_{\max}$ and $n_{\max}$ are varied. In what follows, we only discuss the choice of coarse-graining length.

The measure we introduce to quantify information loss is based on the the well-known relationship between the smoothness of functions in real space and Fourier space [221]: A smooth function in real space should have a peaked, quickly decaying spectrum in Fourier space while a collection of point-like objects such as delta functions should have a uniform non-decaying spectrum. Specifically, we describe a uniformly sampled field as a $M \times N$ matrix with components being the field values

$X_{i,j} = X(\theta_i, \phi_j)$. In our case, $X_{i,j}$ represents either the density field ρ or any of the Cartesian components of the flux vector field $\mathbf{J}$ at a given time point. We find the complex discrete Fourier spectrum $\hat{X}_{i,j}$ of this matrix using the two-dimensional fast Fourier transform. We then calculate the power spectral density (PSD) of the Fourier spectrum as $R_{i,j} = |\hat{X}_{i,j}|^2$ and interpret the normalized PSD

$$P_{i,j} = \frac{R_{i,j}}{\sum_{a,b} R_{a,b}}$$

as a discrete probability distribution. The spectral entropy S characterizing the information content of the field X is then defined by

$$S(X) = -\frac{1}{\log_2 NM} \sum_{i,j} P_{i,j} \log_2 P_{i,j}. \tag{5.11}$$

Smooth fields are sharply peaked in Fourier space and have a low spectral entropy, whereas fields that resolve discrete single particle information are rather flat in Fourier space and have a large spectral entropy. The difference in entropy between particle data and smoothed fields then measures the information eliminated by the coarse-graining procedure. If we additionally normalize by the entropy of the spectral entropy $S_0(X)$ of the raw particle data, we finally obtain a relative measure of the information that is lost in the coarse-graining process. In general, a measure as given in Eq. (5.11) can be defined for any transform with the property that smoothness in real space leads to a fast decaying spectrum in transform space.

We compute the spectral entropy of density and flux component fields at a representative time point and for varying coarse-graining length scales (Fig. 5-4). Specifically, we coarse-grain density and flux through the procedure described above and in Appendix B for different values of the kernel parameter k [see Eqs. (B.12)]. Large values of k correspond to small coarse-graining length scales, with the effective half-width at half-maximum (HWHM) of the kernels Eqs. (B.8) with weight functions Eqs. (B.12) scaling as HWHM $= \arccos(2^{-1/k})$. Normalized spectral entropies $S(X)/S_0(X)$ with $X \in \{\rho, \mathbf{J}\}$ are then computed using Eq. (5.11). For the flux field, we define

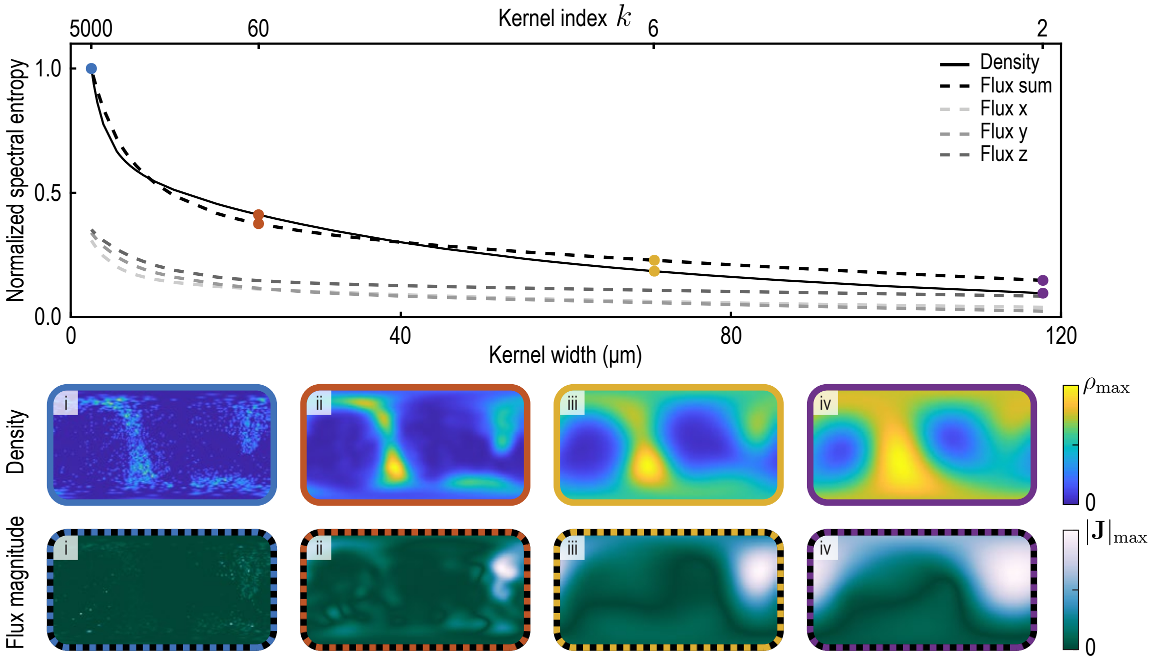

Figure 5-4 : Normalized spectral entropy as a function of the coarse-graining kernel width (top) computed for density ρ and flux field $\mathbf{J}$ using Eq. (5.11). To evaluate the spectral entropy for the vector-valued flux, we define $S(\mathbf{J}) := S(J_x) + S(J_y) + S(J_z)$ ("Flux sum"). The coarse-graining width – the half-width at half-maximum (HWHM) of the coarse-graining kernels Eqs. (B.8) with weight functions Eqs. (B.12) – is varied by varying the kernel index k, where HWHM $= \arccos(2^{-1/k})$ (see Appendix B–B-2). The fields ρ and $|\mathbf{J}|$ are shown in the two bottom rows for different values of k. i. $k = 5000$ (blue, data used to compute the reference spectral entropies $S_0(\rho)$ and $S_0(\mathbf{J})$) ii. $k = 60$ (brown) iii. $k = 6$ (yellow, and used for the main analysis) iv. $k = 2$ (purple).

$S(\mathbf{J}) := S(J_x) + S(J_y) + S(J_z)$ ("Flux sum" in Fig. 5-4) and interpret the sum of these three contributions ("Flux x", "Flux y", "Flux z" in Fig. 5-4) as the total information contained in the flux field. We find that the spectral entropies of all fields show similar features. In particular, an increasing coarse-graining width first results in a sharp loss of information as individual particle positions are blurred, followed by less steep information loss as continuous fields progressively lose details of finer structures. In this work, we use an intermediate value of the coarse-graining parameter $k = 6$ (yellow data in Fig. 5-4).

5.2.4 Characterization of the developmental mode dynamics

A harmonic mode decomposition naturally integrates the geometry of the underlying domain and simultaneously provides useful insights into spatial scales and symmetries of the dynamics. For each mode (lm) in the sets of SHs $\{Y_{lm}\}$, $\{\mathbf{\Psi}_{lm}\}$ and $\{\mathbf{\Phi}_{lm}\}$, the integer index l indicates the spatial scale of the harmonic, with $l = 0$ being a constant and larger l indicating progressively finer spatial scales. The second index $m \in \{-l, -l+1, \dots, l\}$ provides additional information about the orientation of the harmonic scalar function or vector field. The modes $l = 1$ and $l = 2$ are particularly useful for characterizing the symmetry of spatial patterns on a spherical surface [222, 223]: Modes with $l = 1$ indicate patterns with a global polar symmetry, whereas modes with $l = 2$ represent spatial patterns with a global nematic symmetry. We now exploit these features for a detailed characterization of the symmetry breaking that takes place during cellular rearrangements and to study the properties of the cellular flux in more detail. To this end, we discuss spatial averages

$$\langle O \rangle_s(t) = \frac{1}{A_s} \int_{\mathcal{S}} dA_s \, O(\mathbf{r}, t) \tag{5.12}$$

of different real-space observables $O(\mathbf{r}, t)$ over the mid-surface $\mathcal{S}$.

Mode signatures of developmental symmetry breaking

To study how different developmental stages and their associated symmetry breaking events are reflected in the mode representation, we first consider the average cell surface density fluctuations

$$\left\langle (\rho - \langle \rho \rangle_s)^2 \right\rangle_s = \sum_{l=1}^{l_{\max}} \sum_{m=-l}^{l} \rho_{lm}^2(t). \tag{5.13}$$

For each mode l, the power spectrum $P_{\rho,l}(t) = \sum_{m=-l}^{l} \rho_{lm}^2(t)$ in Eq. (5.13) provides a rotationally invariant quantity [224, 225] that can effectively serve as an order parameter to characterize the symmetry of cell density patterns on the spherical surface. The dynamics of the density fluctuations [Eq. (5.13)] broken down into contributions

$P_{\rho,l}(t)$ from each mode $l \leq l_{\max} = 4$ is shown in Fig. 5-5B. Several features of this representation are particularly striking and can be directly related to specific developmental stages. First, patterns of cell surface density fluctuations evolve from a dominantly polar symmetry ($l = 1$) into density patterns with a prominent nematic symmetry ($l = 2$). These mode signatures intuitively reflect the essential symmetry breaking that takes place when cells collectively reorganize from an initially localized cell dome (Fig. 5-1B, 52 min) into an elongated shape that wraps in an open ring-like pattern around the yolk cell (Fig. 5-1B, 760 min). Second, during this transition at around 300 min (9 hpf) (black triangle in Fig. 5-5B), the cell surface density is most homogeneous as fluctuations become minimal for all modes l. Interestingly, this time point approximately marks the completion of epiboly, when the different cell layers have fully engulfed the yolk. Finally, although in a less pronounced manner, the power spectrum of the mode $l = 4$ also exhibits an increased amplitude towards later times, indicating the formation of structures at finer spatial scales as development progresses. We find that mode signatures of the symmetry breaking and progression through developmental stages are robust (Fig. 5-6B,D), illustrating that mode-based analysis can provide a systematic and meaningful characterization of developmental symmetry breaking events.

Mode signatures of emergent topological defects in cellular flux

The vectorial nature of the cell number flux $\mathbf{J}(\mathbf{r}, t)$ on a spherical surface implies the presence of topological defects (colored circles in Fig. 5-5A, see Methods) [226]. Several recent experimental results pertaining to the self-organization of multicellular systems suggest an important role of such topological defects in organizing morphogenetic events [227, 228, 229, 230, 231, 232]. We therefore analyze how defects within the cell number flux $\mathbf{J}(\mathbf{r}, t)$ are dynamically organized during early zebrafish gastrulation and if signatures of defect formation and annihilation are present in the mode representation Eq. (5.5). We first consider the average squared divergence and curl

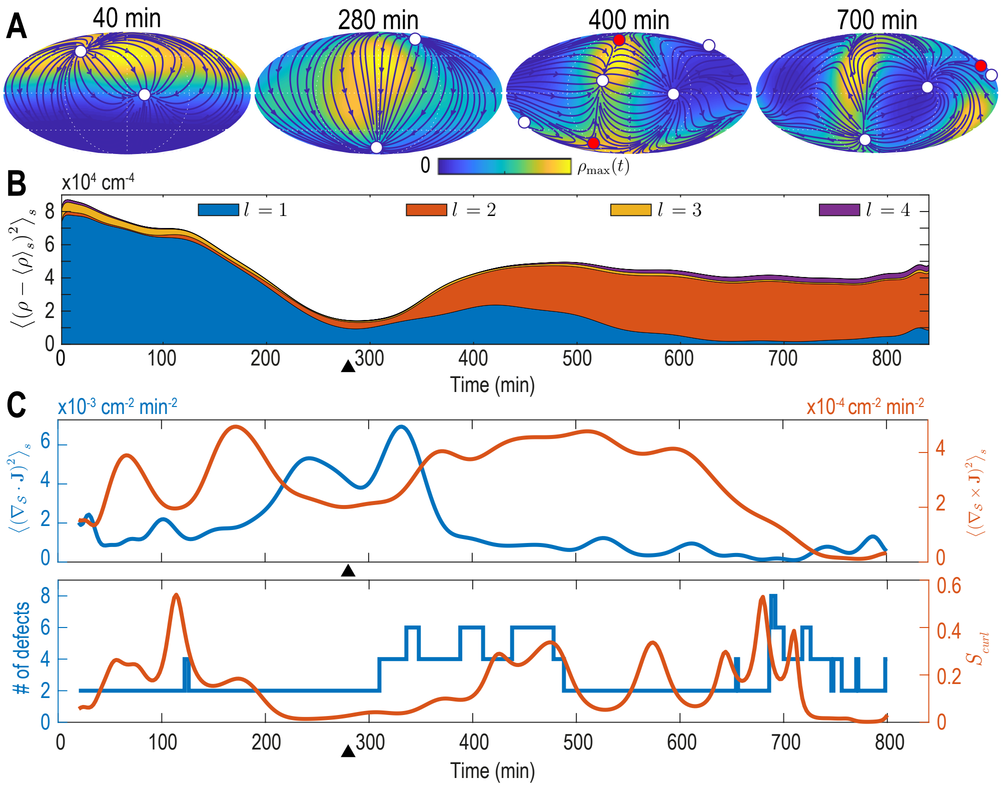

Figure 5-5 : Mode signatures of developmental symmetry breaking and topological defects in cellular flux **A**: Two-dimensional Mollweide projection of the compressed coarse-grained density field $\rho(\mathbf{r},t)$ (colormap) and of the coarse-grained cell flux $\mathbf{J}(\mathbf{r},t)$ (streamlines) at different time points of zebrafish gastrulation. White circles depict topological defects of charge $+1$ in the flux vector field, red circles depict defects with charge -1. The total defect charge is 2 at all times. Defects are seen to 'lead' the large-scale motion of cells and later localize mostly along the curve defined by the forming spine. Animal pole (AP) and ventral pole (VP) are located at top and bottom, respectively. **B**: Density fluctuations as a function of developmental time [see Eq. (5.13)], broken down in contributions from different harmonic modes l. The underlying symmetry breaking is highlighted prominently by this representation: During the first 75 % of epiboly (0–280 min) cells migrate away from, but are still mostly located near the animal pole, presenting a density pattern with polar symmetry ($l = 1$). During the following convergent extension phase cells converge towards a confined elongated region that is 'wrapped' around the yolk, corresponding to a density pattern with nematic symmetry ($l = 2$). Black triangles indicate transition from epiboly to convergent extension. **C**: Comparison of surface averaged divergence $\nabla_{\mathcal{S}}\cdot\mathbf{J}$ and curl $\nabla_{\mathcal{S}}\times\mathbf{J}$ of the cellular flux computed via Eqs. (5.14) (top). A relative curl amplitude S_{curl} computed from these quantities via Eq. (5.15) correlates with the appearance of an increased number of topological defects in the cell flux (bottom), suggesting that incompressible, rotational cell flux is associated with the formation of defects.

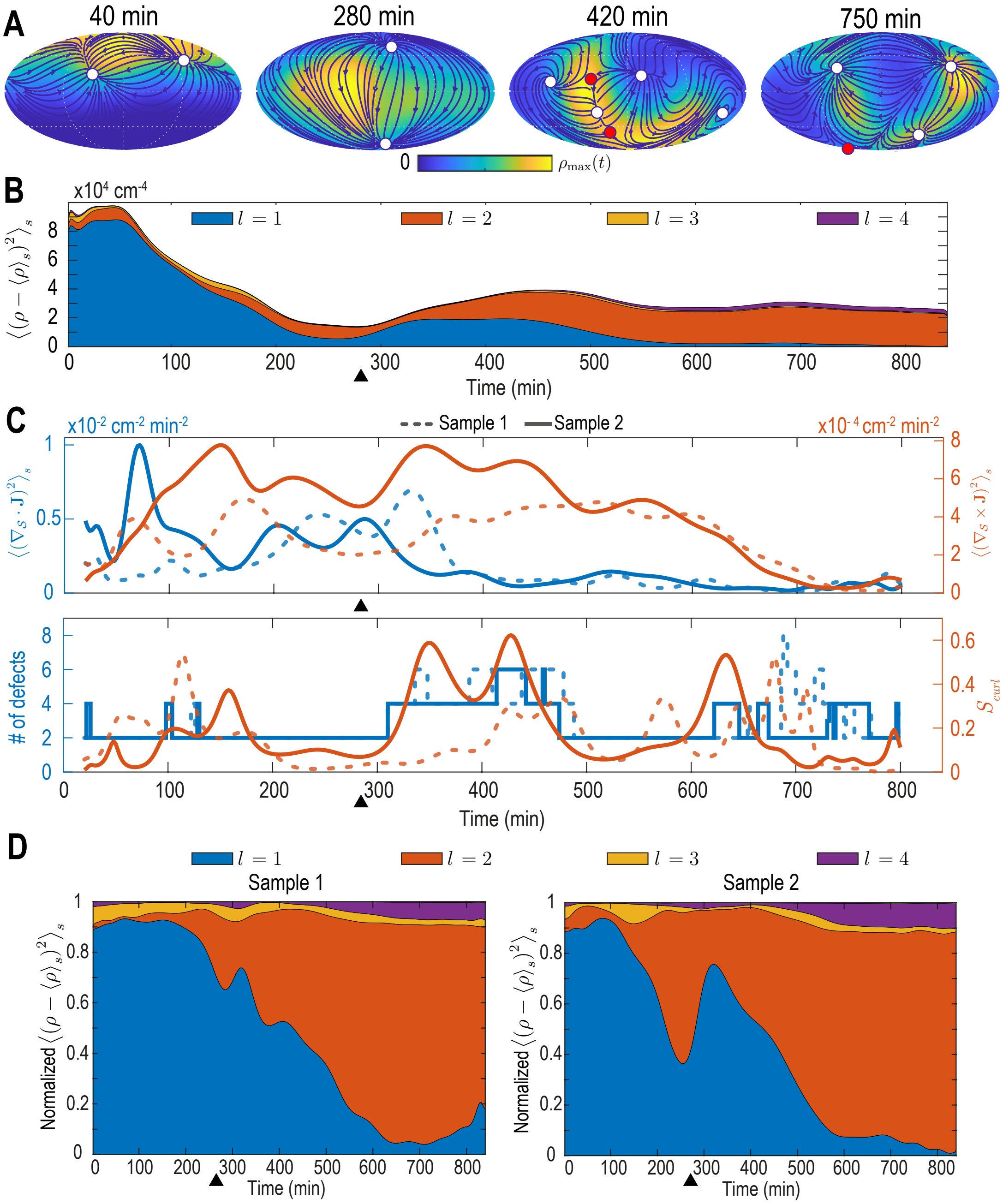

Figure 5-6 : Analysis of the harmonic mode representation for a second experimental dataset. **A–C**: Analysis presented in Fig. 5-5A–C of the main sample performed on a second cell-tracking dataset ('Sample 2'). In **C**, solid lines indicate results for Sample 2, dashed lines correspond to the results for the main dataset ('Sample 1'). **D:** Contributions to density fluctuations from both samples, broken down into contributions from different modes with harmonic mode number l and normalized at each time point by the total fluctuation intensity. Black triangles indicate the completion of epiboly.

of the cell number flux given by

$$\left\langle (\nabla_{\mathcal{S}} \cdot \mathbf{J})^2 \right\rangle_s = \sum_{l=1}^{l_{\max}} \sum_{m=-l}^{m} \left[\frac{l(l+1)}{R_s} j_{lm}^{(1)}(t) \right]^2 , \tag{5.14a}$$

$$\left\langle (\nabla_{\mathcal{S}} \times \mathbf{J})^2 \right\rangle_s = \sum_{l=1}^{l_{\max}} \sum_{m=-l}^{m} \left[\frac{l(l+1)}{R_s} j_{lm}^{(2)}(t) \right]^2 , \tag{5.14b}$$

which are shown in Fig. 5-5C (top). The two contributions to the collective cellular dynamics – locally compressible, divergent flux quantified by the divergence $\nabla_{\mathcal{S}} \cdot \mathbf{J}$ and locally incompressible, rotational cell motion characterized by the curl $\nabla_{\mathcal{S}} \times \mathbf{J}$ – are independently determined by the modes $j_{lm}^{(1)}(t)$ and $j_{lm}^{(2)}(t)$. Therefore, each contribution can be evaluated conveniently and with high accuracy from a representation of $\mathbf{J}(\mathbf{r}, t)$ in terms of vector SHs. From Fig. 5-5C (top), we see that the most significant divergent flux (blue curve) occurs around 300 min at the transition from epiboly towards the convergence and extension stage. A quantification of the incompressible rotational flux relative to the total cell number flux is shown in Fig. 5-5C (bottom), where we plotted the relative curl amplitude

$$S_{\text{curl}}(t) = \frac{\sum_{l,m} \left[j_{lm}^{(2)}(t) \right]^2}{\sum_{l,m} \left[j_{l,m}^{(1)}(t) \right]^2 + \sum_{l,m} \left[j_{l,m}^{(2)}(t) \right]^2}. \tag{5.15}$$

This measure suggests a correlation between incompressible rotational cell motion and the occurrence of topological defects (circles in Fig. 5-5A) in the cell flux $\mathbf{J}(\mathbf{r}, t)$. The total number of topological defects present at any time point is depicted in Fig. 5-5C (bottom, blue curve). Because the vector-valued flux is defined on a sphere, we observe that the total topological charge always sums to +2 [226], while additional defect pairs with opposite charge (red +1 and white −1 circles in Fig. 5-5A) can be created, resulting in total defect numbers greater than two (see Fig. 5-5C, bottom). Interestingly, the relative curl amplitude S_{curl} defined in Eq. (5.15) indicates that increased contributions from incompressible rotational flux are associated with the formation of topological defects in the cell number flux, a feature that is robustly identified by our framework (See additional samples in [36]). The appearance of additional defects at the end of epiboly, when the developing embryo begins to extrude more significantly in the radial direction, suggests that topological defects in the 2D projected cellular flux fields could signal the start of the formation of more complex structures in three dimensions.

5.3 Learning a linear hydrodynamic model of the developmental mode dynamics

The results in Fig. 5-5 confirm that a low-dimensional mode representation can capture essential characteristics of developmental symmetry breaking processes. The mode representation therefore provides a natural starting point for the inference of hydrodynamic models from coarse-grained cell-tracking data. For a given time-dependent mode vector $\mathbf{a}(t) = [\rho_{lm}(t), j^{(1)}_{lm}(t), j^{(2)}_{lm}(t)]^\top$ that contains all modes up to $l = l_{\max}$, the simplest hydrodynamic model corresponds to the linear dynamical equation

$$\frac{\mathrm{d}\mathbf{a}(t)}{\mathrm{d}t} = M \cdot \mathbf{a}(t), \tag{5.16}$$

where the *constant* coefficient matrix M encodes the couplings between different modes. Intuitively, Eq. (5.16) aims to describe an experimentally observed density and flux dynamics in terms of a relaxation process, starting from inhomogeneous initial conditions represented by $\mathbf{a}(0)$. The mathematical learning problem is then to find a coefficient matrix M such that the linear model Eq. (5.16) holds for the mode vector time series $\mathbf{a}(t)$ that was determined from the coarse-graining procedure described in the previous sections.

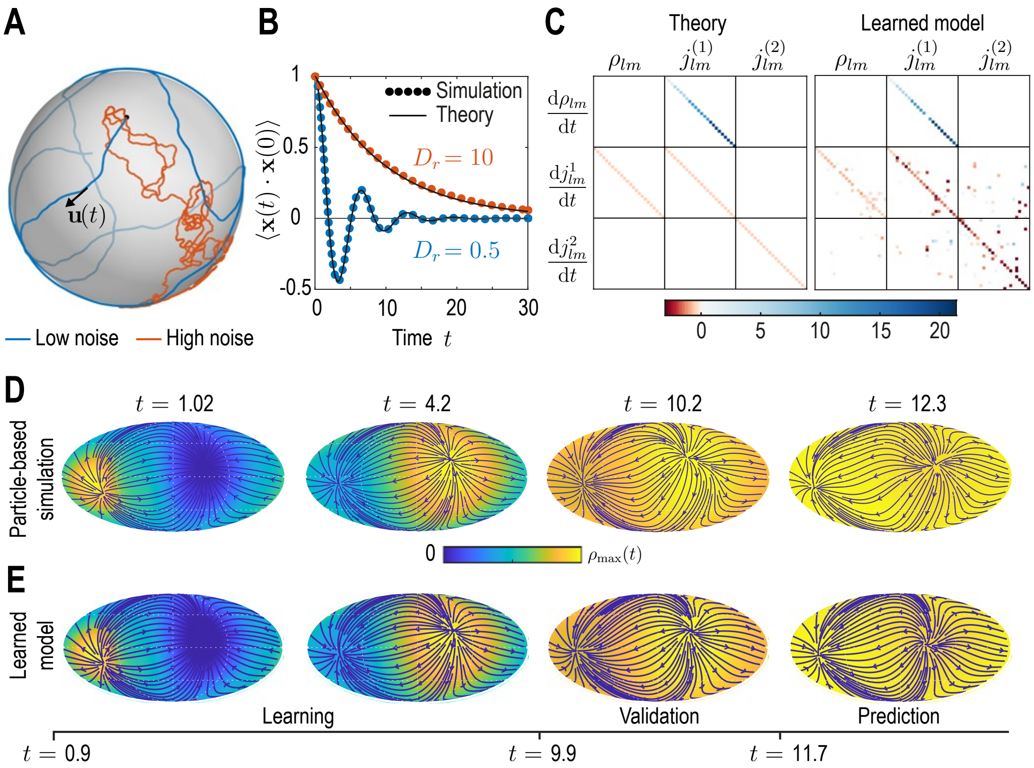

Figure 5-7 : Learning active Brownian particle (ABP) dynamics on a sphere. **A**: ABPs move on a unit sphere (radius $R_0 = 1$) with angular speed $v_0 = 1$ along a tangential unit vector $\mathbf{u}(t)$ that is subject to stochastic in-plane fluctuations (see Appendix C for further details). Example single-particle trajectories are shown in the high-noise (orange, $D_r = 10$ in units of $R_0 v_0$) and in the low-noise regime (blue, $D_r = 0.5$). Time t is measured in units of R_0/v_0 in all panels. **B**: Position correlation function $\langle \mathbf{x}(t) \cdot \mathbf{x}(0) \rangle$ averaged over 3×10^4 independent ABP trajectories show distinct oscillations of period $\approx 2\pi$ in the low-noise regime, as ABPs orbit the spherical surface more persistently. Standard error of the mean is smaller than symbol size. **C**: Analytically predicted (left) and inferred (right) dynamical matrices M [see Eq. (5.16)] describing the mean-field dynamics of a large collection of non-interacting ABPs (see Eqs. (5.17) and Appendix C) show good quantitative agreement. **D**: Mollweide projections of coarse-grained ABP simulations with $v_0 = 1$ and $D_r = 0.5$ using cell positions from the first time point in the zebrafish data (Fig. 5-1) as the initial condition: At each position 60 particles with random orientation were generated and their ABP dynamics simulated, amounting to approximately 1.2×10^5 particles in total. The density fields homogenize over time, where the maximum density at $t = 12.3$ has decayed to about 5 % of the maximum density at $t = 1.02$. Blue lines and arrows indicate streamlines of the cell flux $\mathbf{J}(\mathbf{r}, t)$. **E**: Simulation of the learned linear model, Eq. (5.16) with M shown in 5-7C (right), for the same initial condition as in **D**. Marked time points indicate intervals of learning, validation and prediction phases of the model inference.

5.3.1 Validation of the learning framework using active Brownian particle dynamics

Before applying the combined coarse-graining and inference framework to experimental data, we illustrate and validate the learning approach on synthetic data for which coarse-graining results and hydrodynamic mean-field equations are analytically tractable. To this end, we consider the stochastic dynamics of non-interacting active Brownian particles (ABPs) on the unit sphere of radius $R_0 = 1$ [233, 234, 235]. Similar to a migrating cell, an ABP at position $\mathbf{x}(t)$ moves across the unit sphere at constant speed v_0 in the direction of its fluctuating orientation unit vector $\mathbf{u}(t)$. The strength of the orientational Gaussian white noise is characterized by a rotational diffusion constant D_r (Fig. 5-7A, Appendix C).

Compared with conventional passive Brownian motion, self-propulsion of an ABP along its orientation direction $\mathbf{u}$ introduces a persistence to the particle's motion that is reduced as rotational noise D_r is increased. Additionally, the topology of the spherical surface implies that in the low-noise regime, $R_0 D_r / v_0 < 1$, particles are expected to return to the vicinity of their starting points after a duration $\Delta t \approx 2\pi R_0 / v_0$. The conjunction of persistent motion and topology then leads to oscillatory dynamics in the positional correlation $\langle \mathbf{x}(t) \cdot \mathbf{x}(0) \rangle$ (blue dots in Fig. 5-7B, Appendix C). Comparing correlations from stochastic ABP simulations in different noise regimes with theoretical predictions (solid lines in Fig. 5-7B) validates our numerical ABP simulation scheme.

To generate a test data set for our coarse-graining and inference framework, we simulated non-interacting ABPs in both the low-noise ($R_0 D_r / v_0 < 1$) and the high-noise ($R_0 D_r / v_0 > 1$) regime with initial positions drawn from the experimental data shown in Fig. 5-1. Specifically, at each cell position present in the data, we generated 60 particles with random orientation, amounting to approximately 1.2×10^5 particles in total, and simulated their dynamics on a unit sphere. The resulting trajectory data were coarse-grained following the procedure outlined in the previous sections, yielding dynamic density fields $\rho(\mathbf{r}, t)$ and fluxes $\mathbf{J}(\mathbf{r}, t)$, together with their mode representations $\rho_{lm}(t), j^{(1)}_{lm}(t)$ and $j^{(2)}_{lm}(t)$.

In the second 'learning' step, we infer a sparse mode coupling matrix M that approximates the dynamics Eq. (5.16) for the dynamical mode vectors $\mathbf{a}(t) = [\rho_{lm},\, j^{(1)}_{lm},\, j^{(2)}_{lm}]^\top$ obtained from the coarse-grained simulated ABP data. Our inference algorithm combines adjoint techniques [193] and a multi-step sequential thresholding approach inspired by the Sparse Identification of Nonlinear Dynamics (SINDy) algorithm introduced by [192]. The full algorithm is detailed in [36].Importantly, we perform the sparse regression using dynamical mode vectors $\mathbf{a}(t)$ rescaled by their median absolute deviation (MAD) to compensate for substantial scale variations between different modes. The final output matrix M of this learning algorithm is shown in the right panel of Fig. 5-7C and can be compared against the analytically coarse-grained dynamics of ABPs on curved surfaces [234, 235]. Under suitable closure assumptions (Appendix C), the mean-field dynamics of ABPs on a unit sphere is given in harmonic mode space by

$$\frac{\mathrm{d}\rho_{lm}}{\mathrm{d}t} = \frac{l(l+1)}{R_0} j^{(1)}_{lm} \tag{5.17a}$$

$$\frac{\mathrm{d}j^{(1)}_{lm}}{\mathrm{d}t} = -\frac{v_0^2}{2R_0}\rho_{lm} - D_r j^{(1)}_{lm} \tag{5.17b}$$

$$\frac{\mathrm{d}j^{(2)}_{lm}}{\mathrm{d}t} = -D_r j^{(2)}_{lm}, \tag{5.17c}$$

from which we can read off the mode coupling matrix M shown in the left panel of Fig. 5-7C. A direct comparison between the theoretical and the inferred matrices shows that our framework recovers both the structure and the quantitative values of M with good accuracy. Due to the finite number of ABPs used to determine the coarse-grained fields, we do not expect that the theoretically predicted coupling matrix is recovered perfectly from the data. Instead, some mode couplings suggested by Eqs. (5.17) may not be present or modified in the particular realization of the ABP dynamics that was coarse-grained. Indeed, direct simulation of the learned model projected in real space (Fig. 5-7E) reveals a density and flux dynamics that agrees very well with the dynamics of the the coarse-grained input data (Fig. 5-7D).

Altogether, these results demonstrate that the proposed inference framework enables us to to faithfully recover expected mean-field dynamics from coarse-grained fields of noisy particle-based data.

5.3.2 Learning developmental mode dynamics from experimental data

The same inference framework can now be directly applied to the coarse-grained experimental zebrafish embryo data shown in Fig. 5-1C and D, yielding a sparse coefficient matrix M (Fig. 5-8A,B) that encodes the dynamics of the developmental mode vector $\mathbf{a}(t) = [\rho_{lm}(t),\, j^{(1)}_{lm}(t),\, j^{(2)}_{lm}(t)]^\top$ according to Eq. (5.16). The inferred coupling between the time derivative of density modes ρ_{lm} and flux modes $j^{(1)}_{lm}$ faithfully recovers mass conservation [Fig. 5-8C; see Eq. (5.6)]. Overall, the learned matrix M has 395 non-zero elements, effectively providing further compression of the experimental data, which required 2250 spatio-temporal mode coefficients collected in $\hat{\mathbf{a}}_n$ [see Eq. (5.10)] for its representation. Using the mode vector $\mathbf{a}(t = 0)$ of the first experimental time point as the initial condition, the inferred minimal model Eq. (5.16) with M shown in (Fig. 5-8A,B) faithfully recovers both the mode and real-space dynamics seen in the coarse-grained fields of the experimental input data (Fig. 5-8E–G).

It is instructive to analyze the inferred matrix M and the linear model it encodes in more detail. Comparing the MAD-rescaled matrix learned for the experimental zebrafish data (Fig. 5-8B) with the non-dimensionalized matrix learned for the active Brownian particle dynamics (Fig. 5-7C), we find similar patterns of prominent diagonal and block-diagonal couplings. Consistent with the analysis of single cell trajectories [4], this suggests that a random, but persistent movement of cells akin to ABPs moving on a sphere partially contributes to the early gastrulation process in zebrafish. This is complemented in the minimal model of the experimental dynamics by significant off-diagonal contributions (Fig. 5-8B), which are absent in the non-interacting ABP model. Such off-diagonal contributions represent effective linear approximations of cell-cell interactions, environmental influences or other external stimuli reflected in the experimental time-series data. Ultimately, such contributions to the mode coupling matrix M help realize the symmetry breaking process observed in the underlying experimental data (Fig. 5-5).

The inferred mode coupling matrix M shown in Fig. 5-8B together with Eq. (5.16) provides a highly robust minimal model. Specifically, despite being linear, it is numerically stable over a period approximately four times as long as the input data from which the matrix M was learned. Furthermore, simulations with modified initial conditions [36] still exhibit a characteristic symmetry breaking and lead to the emergence of density and flux patterns similar to those seen in Fig. 5-8F,G. For example, simulating Eq. (5.16) using the initial condition of a different experimental data set [36]leads to final patterns with the same symmetry as in the original training data, further corroborating that the observed symmetry breaking is directly encoded in the interactions represented by the matrix M. A similar robustness is observed under moderate perturbations of the initial condition, such as a rotation of initial cell density patterns relative to the coordinate system in which M was inferred, or a local depletion of the initial density, emulating a partial removal of cells as experimentally realized in [215]. Taken together, these numerical experiments demonstrate that the inferred mode coupling matrix M meaningfully captures the dynamics and interactions of cells that facilitate the symmetry breaking observed during early zebrafish development.

5.3.3 Green's function representation of learned models in real space

To characterize the inferred spatial interactions in more detail, we can analyze the real-space representation of the learned mode coupling matrix M. While the density dynamics represented by M (the first row in Fig. 5-8AB) simply reflects mass conservation Eq. (5.1) in real space, the dynamics of the flux (the second and third row

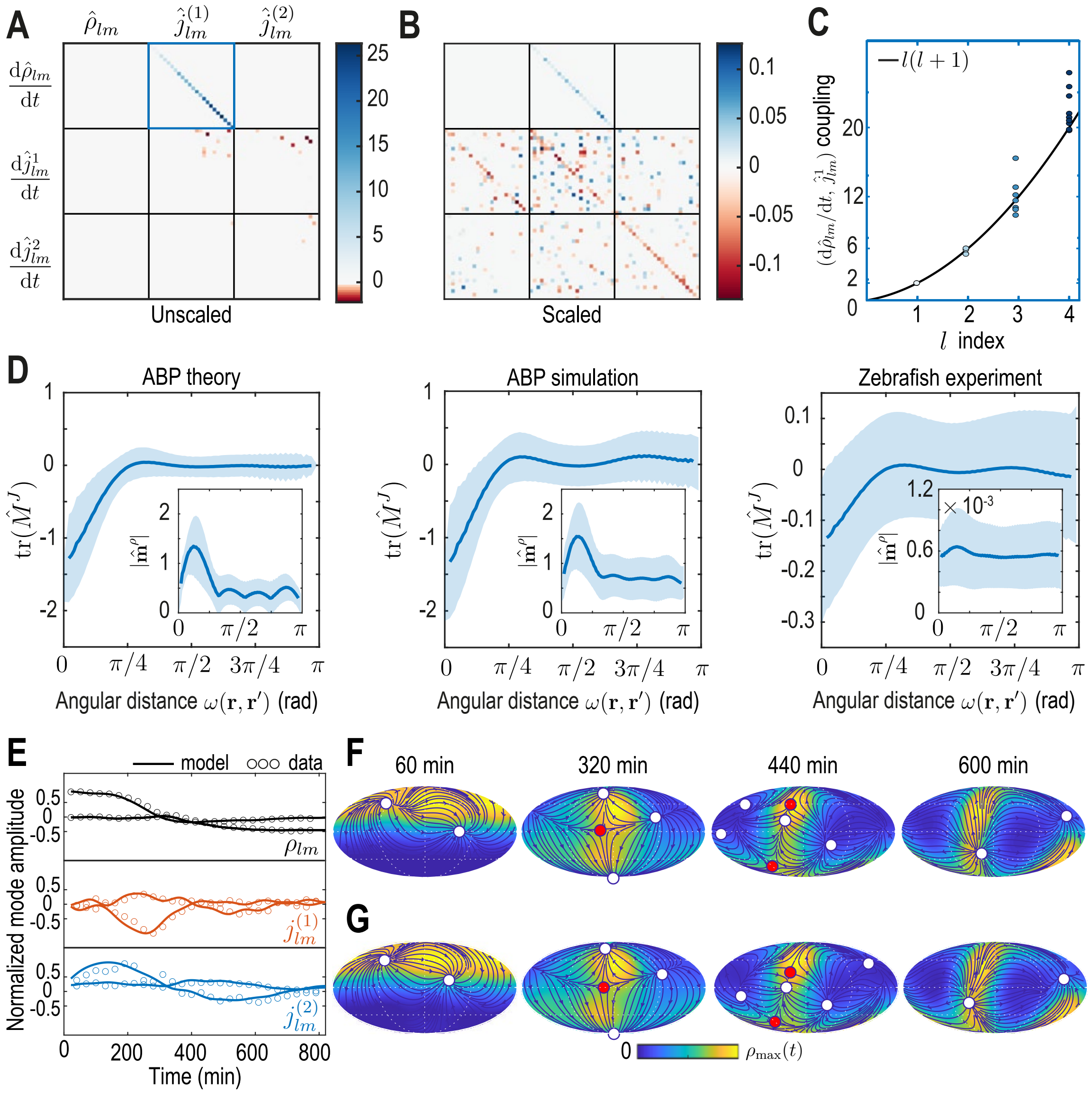

Figure 5-8 *(Caption next page)*

Figure 5-8 *(previous page)*: Model learning for experimental data of collective cell motion during early zebrafish development. **A**: Visualization of the constant mode coupling matrix M that was learned from experimental data and describes the dynamics of the mode vector $\mathbf{a} = [\rho_{lm}(t),\, j^{(1)}_{lm}(t),\, j^{(2)}_{lm}(t)]^T$ via Eq. (5.16). Dimensionless fields are defined by $\hat{\rho}_{lm} = R_s^2 \rho_{lm}$ and $\hat{j}^{(i)}_{lm} = R_s \Delta t j^{(i)}_{lm}$ $(i = 1, 2)$ with $R_s = 300\,\mu\text{m}$ and $\Delta t = 2\,\text{min}$. **B**: Scaling the learned matrix M by the Mean Absolute Deviation (MAD) of the modes reveals structures reminiscent of the mode coupling matrix learned for ABPs (Fig. 5-7C). **C**: The learned model recovers mass conservation in mode space [Eq. (5.6)]. **D**: Comparison of theoretical and inferred real-space kernels (see Eq. (5.18)) for the ABP dynamics and for the experimental data of collective cell motion. The trace of the non-dimensional kernel $\hat{M}^J(\mathbf{r}, \mathbf{r}')$ (the only non-zero eigenvalue) indicates a localized flux-flux coupling with a similar profile among both systems. The oscillating magnitude of the non-dimensionalized density-flux kernel $|\hat{\mathbf{m}}^\rho(\mathbf{r}, \mathbf{r}')|$ (insets) in the ABP system indicates a gradient-like coupling and is consequence of the persistent ABP motion. In the experimental data, a first peak around $\omega = \pi/4$ is also visible, but less pronounced. All kernel properties were computed by averaging over pairs of positions $\mathbf{r}, \mathbf{r}'$ that are separated by the same angular distance $\omega = \arccos(\mathbf{r} \cdot \mathbf{r}') \in [0, \pi]$. Solid lines indicate mean, shaded areas indicate standard deviation. **E**: Comparison of experimental mode dynamics (circles) with numerical solution (solid line) of the minimal model Eq. (5.16) for learned matrix M visualized in Fig. 5-8A. For clarity, the comparison is shown for the two dominant modes of each set of harmonic modes ρ_{lm}, $j^{(1)}_{lm}$ and $j^{(2)}_{lm}$. **F, G**: Mollweide projections of the experimental data (**F**) and of the numerical solution of the learned model (**F**) show very good agreement. Blue lines and arrows illustrate streamlines defined by the cell flux $\mathbf{J}(\mathbf{r}, t)$, circles depict defects with topological charge $+1$ (white) and -1 (red).

in Fig. 5-8A,B) corresponds in real space to the integral equation [36]

$$\frac{\partial}{\partial t}\mathbf{J}(\mathbf{r},t) = \int \mathrm{d}\Omega' \left[\mathbf{m}^{\rho}(\mathbf{r},\mathbf{r}')\rho(\mathbf{r}',t) + M^{J}(\mathbf{r},\mathbf{r}')\cdot\mathbf{J}(\mathbf{r}',t)\right], \tag{5.18}$$

where $d\Omega' = \sin\theta' d\theta' d\phi'$ is the spherical surface area element. The vector-valued kernel $\mathbf{m}^{\rho}(\mathbf{r},\mathbf{r}')$ in Eq. (5.18) connects the distribution of cell density ρ across the surface to dynamic changes of the flux $\mathbf{J}$ at a given point $\mathbf{r}$. Similarly, the matrix-valued kernel $M^{J}(\mathbf{r},\mathbf{r}')$ describes how the distribution of cell fluxes at $\mathbf{r}'$ affects temporal changes of the flux at $\mathbf{r}$.

To analyze the spatial range of interactions between points $\mathbf{r}$ and $\mathbf{r}'$, we use the fact that the matrix-valued kernel $M^{J}(\mathbf{r},\mathbf{r}')$ has only one non-zero eigenvalue [36]. Consequently, the trace $\mathrm{tr}(M^{J})$ serves as a proxy for the distance-dependent interaction strength mediated by M^{J}. Averages of $\mathrm{tr}(M^{J})$ over point-pairs with the same angular distance $\omega = \mathrm{acos}(\mathbf{r}\cdot\mathbf{r}')$ are shown for the ABP dynamics and for the minimal model inferred from experimental data in Fig. 5-8D. Note that to make the models amenable to comparison, we compute $M^{J}(\mathbf{r},\mathbf{r}')$ from the known mean-field model of ABPs Eqs. (5.17) using the same *finite* number of modes as used to represent the ABP and the zebrafish data ($l_{\max} = 4$). In theory, one expects for the ABP dynamics a highly localized, homogeneous kernel $\mathrm{tr}(M^{J}) \sim \delta(\mathbf{r}-\mathbf{r}')$, so that an exact spectral representation would require an infinite number of modes [36]. In practice, using a finite number of modes leads to a wider kernel range (Fig. 5-8D 'ABP theory') and introduces an apparent spatial inhomogeneity, as indicated by the non-zero standard deviation of $\mathrm{tr}(M^{J})$ at fixed distance ω (blue shades). Both the quantitative profile of $\mathrm{tr}(M^{J})$ and its variation are successfully recovered by applying the inference framework to stochastic simulations of ABPs (Fig. 5-8D 'ABP simulation') where $M^{J}(\mathbf{r},\mathbf{r}')$ was computed from the learned mode coupling matrix M shown in Fig. 5-7C. For the inferred minimal model of the cell dynamics (Fig. 5-8D 'Zebrafish experiment'), we find a similar short-ranged flux-flux coupling mediated by M^{J}. However, the increased variability of $\mathrm{tr}(M^{J})$ at fixed distances ω indicates more substantial spatial inhomogeneities of the corresponding interactions. These inhomogeneities are absent in a non-interacting system of ABPs and represent an interpretable real-space signature of the symmetry-breaking mechanisms built into the underlying mode coupling matrix M.

A similar analysis can be performed for the kernel $\mathbf{m}^{\rho}(\mathbf{r}, \mathbf{r}')$ that couples the density at position $\mathbf{r}'$ to dynamics of fluxes at position $\mathbf{r}$ [see Eq. (5.18)], where we average the magnitude $|\mathbf{m}^{\rho}(\mathbf{r}, \mathbf{r}')|$ over pairs $(\mathbf{r}, \mathbf{r}')$ with the same angular distance ω (Fig. 5-8D insets). Using a finite number of modes to compute this kernel in the different scenarios again introduces apparent spatial inhomogeneities in all cases. Additionally, all kernel profiles exhibit a distinct maximum at short range, indicating a coupling between density gradients and the flux dynamics that emerges microscopically from a persistent ABP and cell motion (see Appendix C – an observations that is consistent with the similar block-diagonal structure of both inferred matrices M (compare Fig. 5-7C and Fig. 5-8B).

In conclusion, the real-space analysis and comparison of inferred interaction kernels further highlights potential ABP-like contributions to the collective cellular organization during early zebrafish development and reveals an effectively non-local coupling between density and flux dynamics. The latter could result, for example, from unresolved fast-evolving morphogens [236], through mechanical interactions with the surrounding material [237] or due to other relevant degrees of freedom that are not explicitly captured in this linear hydrodynamic model. More generally, a real-space representation of kernels provides an alternative interpretable way to study the interactions and symmetry-breaking mechanisms encoded by models directly learned in mode space.

5.4 Conclusion

Leveraging a sparse mode representation of collective cellular dynamics on a curved surface, we have presented a learning framework that translates single-cell trajectories into quantitative hydrodynamic models. This work complements traditional approaches to find quantitative continuum models of complex multicellular processes [238, 239, 215, 240, 237] that match problem-specific constitutive relations of active materials in real-space with experimental observations. We have demonstrated here that length scales and symmetries associated with a mode representation can directly inform about the character of symmetry breaking transitions and topological features of collective cellular motion even before a model is specified. The successful applications to synthetic ABP simulation data and experimental zebrafish embryo data show that model learning in mode space provides a promising and computationally feasible approach to infer quantitative interpretable models in complex geometries.

The learned linear minimal model for cell migration during early zebrafish morphogenesis quantitatively recapitulates the spatiotemporal dynamics of a complex developmental process (Fig. 5-8F,G), and highlights similarities between collective cell migration and analytically tractable ABP dynamics on a curved surface. An extension to nonlinear mode-coupling models or an integration of additional, experimentally measured degrees of freedom, such as concentration fields of morphogens involved in mechanochemical feedbacks [236], is in principle straightforward by including nonlinear terms in Eq. (5.16). Furthermore, the above framework could be generalized to describe the dynamics within a spherical shell of finite height by complementing the surface vector SHs used in this work by their radial counterpart [241].

To provide a concrete example, we focused here on applying the model learning framework to single-cell tracking data of early zebrafish morphogenesis. However, the essentially spherical organization of cells during gastrulation observed in zebrafish is shared by many species whose early development occurs through a similar discoidal cleavage [186], and the framework introduced here is directly applicable once tracking data becomes available for these systems. More generally, as novel imaging technologies are being developed [242, 243, 4], we expect that even larger and more detailed imaging data will further facilitate the exploration of finer scales and length-scale bridging processes [244] through learning approaches that directly built on mode-based data representations.

Chapter 6

Conclusions and outlook

Towards the goal of understanding the respective roles of physical and biological processes during development, we strove in this thesis to bridge soft matter physics and developmental biology by directly connecting biological data to physical descriptions. Together, this work provides examples of the complex interplay between the geometry of biological objects and their function. Geometric nonlinearities lead to robustness in the response of elastic membranes to fluctuations and robust intercellular transport, while transport by collective cell migration reshapes the emerging embryo.

In chapters 2 and 3, we show the importance of geometric nonlinearities in the response of the nuclear envelope, the membrane which surrounds the cell nucleus. However, between analytical and experimental challenges, our description is necessarily incomplete: a better understanding of the interplay between geometry, material laws and phenomenology could take on many forms:

- The free energy we used only has a limited applicable range as the amplitude of deformations become comparable to the radius and the shallow-shell assumption breaks down. Those effects would especially matter at long wavelengths; would using different, more complex shell descriptions that better support large deformations lead to qualitatively different results? Are such shell models still amenable to analytical insights in fluctuating regimes?

- Our analysis pointed out a limiting regime where nonlinearities suppressing changes in Gaussian curvature are dominant. A canonical physical system that is strongly nonlinear and spatially-extended is a fluid governed the Navier-Stokes equations at large Reynolds number; can we adapt tools developed for the study of turbulent fluid, such as triad expansions, to understand the nonlinear cascades at play in fluctuating elastic plates and shells [67]?

- Experimental insights would also motivate a different viewpoint from the statistical ensemble averaging. With progress in biological imaging techniques or novel artificial systems, it could be possible to characterize the dynamics and structure of fluctuating shells at shorter timescales. This would require a dynamical description that would go beyond our statistical description. In this dynamical regime, what are the effects of viscosity, plasticity, or surrounding fluid medium on the observed patterns?

In chapter 4, we proposed a minimal model of intercellular transport mediated by cell deformations in *Drosophila* oogenesis. We found that Phase I of intercellular transport could be explained by simple hydraulic arguments. However, this description was purposefully minimal, neglecting for instance any mechanical or chemical coupling between nurse cells, or did not provide any explanation of tension regulation by endocytosis. Other effects that could contribute to cytoplasm transport would be internal coherent flows, which lead to a phenomenon known as 'cytoplasmic streaming' [245, 246]. Streaming has mostly been studied as a mechanism of intracellular transport; what role it could play in intercellular transport is still unresolved. We also did not provide a physical model of Phase II. Notably, how are the actomyosin contractility waves initiated? What are the chemical interactions responsible for these waves, and what are the mechanisms coupling those mechanical waves back to the surface chemistry [247]?

In the second part of this thesis, we developed a symmetry-based framework to characterize the emergent body structures and their time-evolution in zebrafish gastrulation. Because the approach described in chapter 5 relies on very general physical mechanisms and is close to theoretical descriptions, we expect it to provide a way to meaningfully characterize the complex dynamics of spatially-extended systems by providing effective linear models as a novel class of observables [248]. In the same vein as the first half of the thesis, one could hope to uncover geometric effects in the self-organization of collective cell migration. Applying our framework to understand and discriminate between minimal symmetry breaking mechanisms such as aligning interactions [233, 249] at play in zebrafish gastrulation would shed light on the relative importance of biological and physical regulation for the robustness of developmental processes. Extending this framework to arbitrary complex surfaces by leveraging modern geometry processing tools [34, 250] could extend the reach of this method to lower-symmetry systems such as later-stage embryos and organisms. Such developments would be key to broadening the practical applicability of our ideas.

Appendix A

Scalar and vector spherical harmonics

In this appendix, we present definitions and general properties of scalar and vector spherical harmonics that are used extensively in Chapters 3 and 5. We then provide for the reader's reference a series of identities providing coupling integrals for possible cross terms involving scalar and vector spherical harmonics and their gradients, relating them to canonical integrals that are expressible in terms of Wigner's 3-j symbols.

A.1 Basic properties

A.1.1 Scalar spherical harmonics

We will define scalar spherical harmonics as eigenfunctions of the Laplace-Beltrami operator on the unit sphere [217]

$$\Delta Y_{lm} = -l(l+1)Y_{lm}. \tag{A.1}$$

Spherical harmonics are important objects in the mathematical study of rotations, as they form irreducible representations of SO(3). The spherical harmonics can be represented in terms of complex functions, which is common in quantum mechanics, or equivalently in terms of purely real functions, which are convenient for numerical purposes and are the form used throughout this work. For completeness, and to help navigate formulas written in terms of either representation, we will define both representations in this appendix. In what follows, we will use a standard spherical coordinate representation of the sphere (θ, ϕ) where $\theta \in [0, \pi]$ and $\phi \in [0, 2\pi[$.

The complex spherical harmonics $\mathcal{Y}_{lm}$ are explicitly written in terms of associated Legendre polynomials as

$$\mathcal{Y}_{lm}(\theta, \phi) = \sqrt{\frac{(2l+1)}{4\pi} \frac{(l-m)!}{(l+m)!}} P_l^m(\cos\theta) e^{im\phi} \tag{A.2}$$

where the associated Legendre polynomials $P_l^m(x)$ are related to $P_l(x)$ the standard Legendre polynomials of degree l by $P_l^m(x) = (1-x^2)^{m/2} \mathrm{d}^m P_l(x)/\mathrm{d}x^m$ for $m \leq 0$, and $P_l^{-m}(x) = (-1)^m (l-m)!/(l+m)! P_l^m(x)$. With this normalization choice, we do not account for the Condon-Shortley phase.

In chapters 2, 3 and 5 we use the real spherical harmonics defined in spherical coordinates (θ, ϕ) by [217]

$$Y_{lm}(\theta, \phi) = \sqrt{\frac{2l+1}{4\pi} \frac{(l-|m|)!}{(l+|m|)!}} P_l^{|m|}(\cos\theta) N_m(\phi) \tag{A.3}$$

where $P_l^{|m|}(x)$ is the associated Legendre polynomial of degree l and order $|m|$, and

$$N_m(\phi) = \begin{cases} \sqrt{2}\cos(m\phi) & \text{if } m > 0 \\ 1 & \text{if } m = 0 \\ \sqrt{2}\sin(|m|\phi) & \text{if } m < 0 \end{cases} . \tag{A.4}$$

Since $N_m = 0$ for $|m| > l$, there are $2l+1$ harmonics for each $l = 0, 1, 2 \ldots$, and there are thus $(l_{\max}+1)^2$ modes with $l \leq l\mathrm{max}$. Example scalar spherical harmonics are illustrated in Fig. A-1.

Orthogonality relations

Complex spherical harmonics are orthonormal under the hermitian inner product

$$\int \mathrm{d}\Omega\, \mathcal{Y}^*_{lm}\mathcal{Y}_{l'm'} = \delta_{ll'}\delta_{mm'}, \tag{A.5}$$

where $\mathrm{d}\Omega = \sin\theta\, \mathrm{d}\theta \mathrm{d}\phi$ while real spherical harmonics are orthonormal under the standard L^2 scalar product on S^2

$$\int \mathrm{d}\Omega\, Y_{lm}Y_{l'm'} = \delta_{ll'}\delta_{mm'}. \tag{A.6}$$

This orthonormality property, along with the completeness of the basis formed by Y_{lm} for functions in L^2 allows scalar functions $f(\theta,\phi)$ to be represented as

$$f(\theta,\phi) = \sum_{l=0}^{\infty}\sum_{m=-l}^{l} f_{lm}Y_{lm}(\theta,\phi) \tag{A.7}$$

with coefficients f_{lm} given by the projections

$$f_{lm} = \int \mathrm{d}\Omega\, fY_{lm}. \tag{A.8}$$

Converting between representations

One can switch between the real and complex representations by the unitary transformations $U^{(l)}_{m\mu}$ [251], which in our phase convention is given by

$$U^{(l)}_{m\mu} = \frac{1}{\sqrt{2}}\begin{pmatrix} -i & & & & & & (-1)^l i \\ & \ddots & & & & \iddots & \\ & & -i & & (-1)^1 i & & \\ & & & \sqrt{2} & & & \\ & & 1 & & (-1)^1 & & \\ & \iddots & & & & \ddots & \\ 1 & & & & & & (-1)^l \end{pmatrix} \tag{A.9}$$

where $m, \mu \in (-l, -l+1, \ldots, l)$, such that $Y_{lm} = \sum_{\mu=-l}^{l} U_{m\mu}^{(l)} \mathcal{Y}_{l\mu}$. For the correct transformation with the Condon-Shortley phase convention, see Ref. [251].

A.1.2 Vector spherical harmonics

Real vector spherical harmonics can be defined and expressed as vector fields in 3D or covariantly as [218, 222]

$$\boldsymbol{\Psi}_{lm} = \nabla_S Y_{lm} \Leftrightarrow \Psi^i_{(lm)} = g^{ij}\partial_j Y_{lm} \tag{A.10a}$$

$$\boldsymbol{\Phi}_{lm} = \hat{\mathbf{r}} \times \boldsymbol{\Psi}_{lm} \Leftrightarrow \Phi^i_{(lm)} = \epsilon^{ji}\partial_j Y_{lm} \tag{A.10b}$$

where $\nabla_S = \mathbf{e}_\theta \partial_\theta + \mathbf{e}_\phi \sin^{-1}\theta \partial_\phi$ denotes the gradient operator on the unit sphere, ϵ_{ij} is the covariant Levi-Civita tensor, and g_{ij} the metric tensor. Note that since $Y_{00} = 1/\sqrt{4\pi}$, $\Psi_{00} = \Phi_{00} = 0$. Projecting a vector field onto $\Psi^i_{(lm)}$ and $\Phi^i_{(lm)}$ realizes the Helmoltz-Hodge decomposition of the vector field, as

$$\nabla_S \cdot \boldsymbol{\Psi}_{lm} = -l(l+1)Y_{lm}, \qquad \nabla_S \cdot \boldsymbol{\Phi}_{lm} = 0, \tag{A.11a}$$

$$\epsilon_{ji}\nabla^i \Phi^j_{(lm)} = -l(l+1)Y_{lm}, \qquad \epsilon_{ji}\nabla^i \Psi^j_{(lm)} = 0. \tag{A.11b}$$

Finally, the vector spherical harmonics are, similarly to their scalar counterpart, eigenfunctions of the Laplace-Beltrami operator, with

$$\nabla_k \nabla^k \Psi^i_{(lm)} = \left(1 - l(l+1)\right) \Psi^i_{(lm)} \tag{A.12a}$$

$$\nabla_k \nabla^k \Phi^i_{(lm)} = \left(1 - l(l+1)\right) \Phi^i_{(lm)}. \tag{A.12b}$$

$$\tag{A.12c}$$

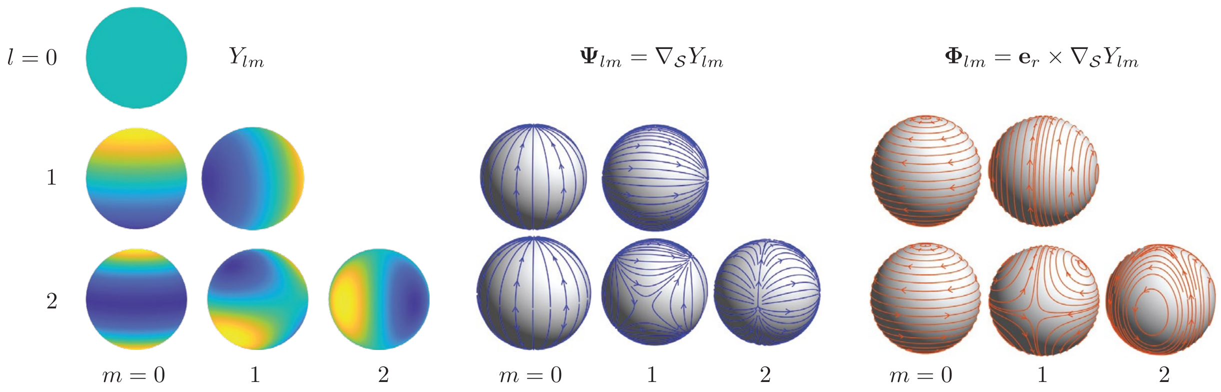

Figure A-1 : Scalar (Y_{lm}) and vector $\mathbf{\Psi}_{lm}$, $\mathbf{\Phi}_{lm}$ real spherical harmonics for $l = 0, 1, 2$ and $m \geq 0$. Functions with $m < 0$ are found by rotating the pattern around the vertical axis by $\pi/2$.

Orthogonality

Without further normalization, the vector harmonics are orthogonal within and between the Ψ and Φ families:

$$\int \mathrm{d}\Omega\, \mathbf{\Psi}_{lm} \cdot \mathbf{\Psi}_{l'm'} = l(l+1)\delta_{ll'}\delta_{mm'}, \tag{A.13a}$$

$$\int \mathrm{d}\Omega\, \mathbf{\Phi}_{lm} \cdot \mathbf{\Phi}_{l'm'} = l(l+1)\delta_{ll'}\delta_{mm'}, \tag{A.13b}$$

$$\int \mathrm{d}\Omega\, \mathbf{\Psi}_{lm} \cdot \mathbf{\Phi}_{l'm'} = 0. \tag{A.13c}$$

The increasing complexity of patterns with larger l is illustrated in Fig. A-1. In a similar fashion as Eq. (A.7), any vector field $v^i(\theta, \phi)$ tangent to the sphere can be written as

$$v^i(\theta,\phi) = \sum_{l\geq 1} \sum_{m=-l}^{l} v_{lm}^{(1)} \Psi^i_{(lm)}(\theta,\phi) + v_{lm}^{(2)} \Phi^i_{(lm)}(\theta,\phi) \tag{A.14}$$

with coefficients obtained by projections

$$v_{lm}^{(1)} = \frac{1}{l(l+1)} \int \mathrm{d}\Omega\, g_{ij} v^i \Psi^j_{(lm)}, \tag{A.15a}$$

$$v_{lm}^{(2)} = \frac{1}{l(l+1)} \int \mathrm{d}\Omega\, g_{ij} v^i \Phi^j_{(lm)}. \tag{A.15b}$$

A.2 Coupling integrals

In this section, we derive a series of identities relating coupling integrals projecting nonlinear combinations of (vector) spherical harmonics onto single harmonic subspaces. These identities appear in the construction of fully-spectral PDE solvers, and can be used for analytic purposes, for instance in perturbative schemes for interacting scalar and vector fields on the sphere to extend results such as ref. [252] to vector fields living on a sphere.

These coupling integrals are reducible to combinations of selected integrals, the Adams-Gaunt and Elsasser dynamo integrals which are known functions in the form of Wigner 3-j symbols [253]. To lighten notation, we use greek letters to denote multi-indices defining spherical harmonic degree l and order m as in $\alpha = (l, m)$, and we use latin letters for co- and contra-variant coordinate indices.

The (real) Adams-Gaunt integrals are defined by

$$Y_{\alpha,\beta,\gamma} = \int \mathrm{d}\Omega \, Y_\alpha Y_\beta Y_\gamma \tag{A.16}$$

which satisfies $Y_\alpha Y_\beta = \sum_\nu Y_{\alpha,\beta,\nu} Y_\nu$, and thus are the Clebsch-Gordan coefficients associated with the algebra formed by the scalar spherical harmonics Y_{lm}.

The (real) Elsasser dynamo integrals are defined by

$$E_{\alpha\beta\gamma} = \int \mathrm{d}^2\Omega \, Y_\alpha \Psi^i_\beta \Phi_{i,\gamma} = \int \mathrm{d}\Omega \frac{Y_\alpha}{\sin\theta} (\partial_\theta Y_\gamma \partial_\phi Y_\beta - \partial_\phi Y_\gamma \partial_\theta Y_\beta). \tag{A.17}$$

Note the order of the indices α, β, γ in the integrand.

Computing the Adams-Gaunt and Elsasser integrals

The complex Adams-Gaunt and Elsasser integrals are defined as

$$\mathcal{Y}_{\alpha\beta\gamma} = \int \mathrm{d}\Omega \, \mathcal{Y}_\alpha \mathcal{Y}_\beta \mathcal{Y}_\gamma \tag{A.18}$$

$$\mathcal{E}_{\alpha\beta\gamma} = \int \mathrm{d}\Omega \, \frac{\mathcal{Y}_\alpha}{\sin\theta} \left(\partial_\theta \mathcal{Y}_\gamma \partial_\phi \mathcal{Y}_\beta - \partial_\phi \mathcal{Y}_\gamma \partial_\theta \mathcal{Y}_\beta\right) \tag{A.19}$$

The complex integrals have closed forms in terms of the Wigner 3-j symbols [253], for which fast computational methods are available [254].

$$\begin{aligned}
\mathcal{Y}_{\alpha\beta\gamma} =& \sqrt{\frac{(2l_\alpha+1)(2l_\beta+1)(2l_\gamma+1)}{4\pi}} \begin{pmatrix} 2l_\alpha & 2l_\beta & 2l_\gamma \\ 2m_\alpha & 2m_\beta & 2m_\gamma \end{pmatrix} \begin{pmatrix} 2l_\alpha & 2l_\beta & 2l_\gamma \\ 0 & 0 & 0 \end{pmatrix}, \quad \text{(A.20)} \\
\mathcal{E}_{\alpha\beta\gamma} =& - i\sqrt{\frac{(2l_\alpha+1)(2l_\beta+1)(2l_\gamma+1)}{4\pi}} \sqrt{\frac{(l_\alpha+l_\beta+l_\gamma+2)(l_\alpha+l_\beta+l_\gamma+4)}{4(l_\alpha+l_\beta+l_\gamma+3)}} \\
&\times \sqrt{(l_\alpha-l_\beta+l_\gamma+1)(-l_\alpha+l_\beta+l_\gamma+1)} \\
&\times \begin{pmatrix} 2l_\alpha & 2l_\beta & 2l_\gamma \\ 2m_\alpha & 2m_\beta & 2m_\gamma \end{pmatrix} \begin{pmatrix} 2(l_\alpha+1) & 2(l_\beta+1) & 2(l_\gamma+1) \\ 0 & 0 & 0 \end{pmatrix}. \quad \text{(A.21)}
\end{aligned}$$

It is important to note that only few terms in are non-zero: notably, the 3-j symbols

$$\begin{pmatrix} l & l' & l'' \\ m & m' & m'' \end{pmatrix} \quad \text{(A.22)}$$

are zero unless a variety of selection rules are obeyed, which include $m+m'+m''=0$, $|l-l'|<l''<l+l'$ and even permutations between columns.

The complex and real Adams-Gaunt integrals are related by the linear transformation

$$Y_{lm,l'm',\bar{l}\bar{m}} = \sum_{\mu=-l}^{l} \sum_{\mu'=-l'}^{l'} \sum_{\bar{\mu}=-\bar{l}}^{\bar{l}} U^{(l)}_{m\mu} U^{(l')}_{m'\mu'} U^{(\bar{l})}_{\bar{m}\bar{\mu}} \mathcal{Y}_{l\mu,l'\mu',\bar{l}\bar{\mu}} \quad \text{(A.23)}$$

and similarly for the Elasser integrals. Faster multiplication methods leveraging the sparsity patterns of the matrices $U^{(l)}_{m\mu}$ are listed in [251].

A.2.1 Cubic terms

We consider the possible integrals obtained by combining scalar and vector spherical harmonics that would appear for instance in deriving dynamical equations involving quadratic nonlinearities.

Psi-Psi-Y Integrating by parts [62]

$$\begin{aligned}\int \mathrm{d}\Omega\, \Psi^{\alpha}_{k}\Psi^{k,\beta}Y_\gamma =& \int \mathrm{d}\Omega(\nabla_k Y_\alpha)(\nabla^k Y_\beta)Y_\gamma\\ =& -\int Y_\alpha \nabla_k\left((\nabla^k Y_\beta)Y_\gamma\right)\\ =& l_\beta(l_\beta+1)\int \mathrm{d}\Omega\, Y_\alpha Y_\beta Y_\gamma - \int \mathrm{d}\Omega\, Y_\alpha(\nabla_k Y_\beta)(\nabla^k Y_\gamma)\\ =& [l_\beta(l_\beta+1) - l_\gamma(l_\gamma+1)]\int \mathrm{d}\Omega\, Y_\alpha Y_\beta Y_\gamma + \int \mathrm{d}^2\mathbf{x}(\nabla^k Y_\alpha)Y_\beta(\nabla^k Y_\gamma)\\ =& [l_\alpha(l_\alpha+1) + l_\beta(l_\beta+1) - l_\gamma(l_\gamma+1)]\int \mathrm{d}\Omega\, Y_\alpha Y_\beta Y_\gamma - \int \mathrm{d}\Omega \Psi^{\alpha}_{k}\Psi^{k,\beta}Y_\gamma\end{aligned} \tag{A.24}$$

to finally obtain

$$\int \mathrm{d}\Omega\, \Psi^{\alpha}_{k}\Psi^{k,\beta}Y_\gamma = \frac{1}{2}(l_\alpha(l_\alpha+1) + l_\beta(l_\beta+1) - l_\gamma(l_\gamma+1))Y_{\alpha,\beta,\gamma} \tag{A.25}$$

Phi-Phi-Y We have by the identity $\epsilon_{ij}\epsilon^{mn} = \delta^m_i\delta^n_j - \delta^n_i\delta^m_j$ that

$$\begin{aligned}\int \mathrm{d}\Omega\, \Phi^{\alpha}_{k}\Phi^{k,\beta}Y_\gamma =& \int \mathrm{d}\Omega\, \epsilon_{ki}\epsilon^{kj}(\nabla^i Y_\alpha)(\nabla_j Y_\beta)Y_\gamma\\ =& \int \mathrm{d}\Omega(\nabla_k Y_\alpha)(\nabla^k Y_\beta)Y_\gamma\end{aligned} \tag{A.26}$$

which is precisely the Psi-Psi-Y integral, which gives

$$\int \mathrm{d}\Omega\, \Phi^{\alpha}_{k}\Phi^{k,\beta}Y_\gamma = \frac{1}{2}(l_\alpha(l_\alpha+1) + l_\beta(l_\beta+1) - l_\gamma(l_\gamma+1))Y_{\alpha,\beta,\gamma} \tag{A.27}$$

Psi-Psi-grad Psi We can again integrate by part

$$\begin{aligned}
\int \mathrm{d}\Omega\, \Psi_i^{\alpha}\Psi_{j,\beta}\nabla^i\Psi_\gamma^j =& \int \mathrm{d}\Omega\, \nabla_i Y_\alpha \nabla_j Y_\beta \nabla^i\nabla^j Y_\gamma \\
&= l_\alpha(l_\alpha+1)\int \mathrm{d}\Omega\, \Psi_k^{\beta}\Psi^{k,\gamma}Y_\alpha - \int \mathrm{d}\Omega\, \nabla_i Y_\alpha \nabla^i\nabla_j Y_\beta \nabla^j Y_\gamma \\
&= \frac{1}{2}\left[l_\alpha(l_\alpha+1)\int \mathrm{d}\Omega\, \Psi_k^{\beta}\Psi^{k,\gamma}Y_\alpha \right. \\
&\qquad + l_\beta(l_\beta+1)\int \mathrm{d}\Omega\, \Psi_k^{\alpha}\Psi^{k,\gamma}Y_\beta \\
&\qquad \left. - l_\gamma(l_\gamma+1)\int \mathrm{d}\Omega\, \Psi_k^{\alpha}\Psi^{k,\beta}Y_\gamma \right]
\end{aligned} \tag{A.28}$$

which finally leads to

$$\int \mathrm{d}\Omega\, \Psi_i^{\alpha}\Psi_{j,\beta}\nabla^i\Psi_\gamma^j = \frac{1}{4}\left[2l_\alpha(l_\alpha+1)l_\beta(l_\beta+1) - l_\alpha^2(l_\alpha+1)^2 - l_\beta^2(l_\beta+1)^2 + l_\gamma^2(l_\gamma+1)^2\right] Y_{\alpha\beta\gamma} \tag{A.29}$$

Psi-Psi- tensor Phi Defining $\Phi_{ij}^{(lm)} = \frac{1}{2}(\nabla_i\Phi_j^{(lm)} + \nabla_j\Phi_i i^{(lm)})$, we consider the integral

$$\int \mathrm{d}\Omega\, \Psi_i^{\alpha}\Psi_{j,\beta}\nabla^i\Phi_\gamma^j. \tag{A.30}$$

To reduce this integral to Elsasser and Gaunt integrals, note that by integrating by part and using that $\nabla_i\Phi_\gamma^i = 0$, $E_{\alpha\beta\gamma} = -E_{\beta\alpha\gamma}$. We also have $E_{\alpha\beta\gamma} = -E_{\alpha\gamma\beta}$. Integrating by part and using that $\nabla_j\Phi_\gamma^j = 0$,

$$\begin{aligned}
\int \mathrm{d}\Omega\, \Psi_i^{\alpha}\Psi_{j,\beta}\nabla^i\Phi_\gamma^j =& l_\alpha(l_\alpha+1)E_{\alpha\beta\gamma} - \int \mathrm{d}\Omega\, \nabla_i Y_\alpha \nabla^i\nabla_j Y_\beta \epsilon^{j}{}_{k}\nabla^k Y_\gamma \\
=& l_\alpha(l_\alpha+1)E_{\alpha\beta\gamma} + l_\beta(l_\beta+1)E_{\beta\alpha\gamma} - \int \mathrm{d}\Omega\, \Psi_i^{\alpha}\Psi_{j,\beta}\nabla^j\Phi_\gamma^i
\end{aligned} \tag{A.31}$$

which implies

$$\int \mathrm{d}\Omega\, \Psi_i^{\alpha}\Psi_{j,\beta}\Phi_\gamma^{ij} = \frac{1}{2}\left[l_\alpha(l_\alpha+1)E_{\alpha\beta\gamma} + l_\beta(l_\beta+1)E_{\beta\alpha\gamma}\right] \tag{A.32}$$

A.2.2 Selected quartic integrals

Y-Y-Y-Y We consider the integral

$$\int \mathrm{d}\Omega\, Y_\alpha Y_\beta Y_\gamma Y_\delta \tag{A.33}$$

which appears for instance in ϕ^4 theory for fields on S^2 [252]. By expanding the products $Y_\alpha Y_\beta = \sum_\nu Y_{\alpha\beta\nu} Y_\nu$ and $Y_\gamma Y_\delta = \sum_\mu Y_{\gamma\delta\mu} Y_\mu$, one finds

$$\begin{aligned}\int \mathrm{d}\Omega\, Y_\alpha Y_\beta Y_\gamma Y_\delta =& \sum_\nu \sum_\mu \int \mathrm{d}\Omega\, Y_{\alpha\beta\nu} Y_\nu Y_{\gamma\delta\mu} Y_\mu \\ =& \sum_\nu \sum_\mu Y_{\alpha\beta\nu} Y_{\gamma\delta\mu} \int \mathrm{d}\Omega\, Y_\nu Y_\mu \\ =& \sum_\nu \sum_\mu Y_{\alpha\beta\nu} Y_{\gamma\delta\mu} \delta_{\mu,\nu} \\ =& \sum_\nu Y_{\alpha\beta\nu} Y_{\gamma\delta\nu}\end{aligned} \tag{A.34}$$

where ν covers all multi-indices, but since $Y_{\alpha\beta\nu} = 0$ if $l_\nu > l_\alpha + l_\beta$, ν only needs to cover indices such that $l_\nu \leq 2l_{\max}$.

Psi-Psi-Psi-Psi The last identity involves the quartic integral

$$\int \mathrm{d}\Omega\, \Psi_k^\alpha \Psi^{k,\beta} \Psi_j^\gamma \Psi^{j,\delta} \tag{A.35}$$

which arises for example in the dynamics of free energies involving terms such as $\int \mathrm{d}\Omega\ (\nabla f)^4$, where f is a scalar field.

$$\begin{aligned}\int \mathrm{d}\Omega\, \Psi^{\alpha}_{k}\Psi^{k,\beta}\Psi^{\gamma}_{j}\Psi^{j,\delta} =& \sum_{\nu} l_{\beta}(l_{\beta}+1)\left(\int \mathrm{d}\Omega\, \Psi^{\gamma}_{j}\Psi^{j,\delta}Y_{\nu}\right)\\ &-\int \mathrm{d}\Omega\, Y_{\alpha}\nabla_{j}Y_{\beta}\nabla^{j}(\Psi^{\gamma}_{k}\Psi^{k,\delta})\\ =&\sum_{\nu}(l_{\beta}(l_{\beta}+1)+l_{\alpha}(l_{\alpha}+1))Y_{\alpha\beta\nu}\left(\int \mathrm{d}\Omega\, \Psi^{\gamma}_{j}\Psi^{j,\delta}Y_{\nu}\right)\\ &-\int \mathrm{d}\Omega\, Y_{\alpha}Y_{\beta}\nabla_{j}\nabla^{j}(\Psi^{\gamma}_{k}\Psi^{k,\delta})-\int \mathrm{d}\Omega\, \Psi^{\alpha}_{k}\Psi^{k,\beta}\Psi^{\gamma}_{j}\Psi^{j,\delta}\\ =&\sum_{\nu}\frac{1}{2}(l_{\beta}(l_{\beta}+1)+l_{\alpha}(l_{\alpha}+1))Y_{\alpha\beta\nu}\left(\int \mathrm{d}\Omega\, \Psi^{\gamma}_{j}\Psi^{j,\delta}Y_{\nu}\right)\\ &-\sum_{\nu}\frac{1}{2}Y_{\alpha\beta\nu}\int \mathrm{d}\Omega\, Y_{\nu}\nabla_{j}\nabla^{j}(\Psi^{\gamma}_{k}\Psi^{k,\delta}) \qquad \text{(A.36)}\end{aligned}$$

To deal with the last term, we use $\nabla_i\nabla^i\Psi^{\alpha}_{j} = (1-l_{\alpha}(l_{\alpha}+1))\Psi^{\alpha}_{j}$, and we can find a nicer symmetric formula by summing the results of the integrations by parts with respect to γ and δ terms respectively

$$\begin{aligned}\int \mathrm{d}\Omega\, \nabla_{i}\Psi^{\gamma}_{k}\nabla^{i}\Psi^{k,\delta}Y_{\nu} =& -\frac{1}{2}\Bigg[(2-(l_{\gamma}(l_{\gamma}+1)-l_{\delta}(l_{\delta}+1))\int \mathrm{d}\Omega\, \Psi^{\gamma}_{j}\Psi^{j,\delta}Y_{\nu}\\ &+\int \mathrm{d}\Omega\, \nabla_{i}\Psi^{\gamma}_{k}\Psi^{k,\delta}\Psi^{\nu}_{i}+\int \mathrm{d}\Omega\, \Psi^{\gamma}_{k}\nabla_{i}\Psi^{k,\delta}\Psi^{\nu}_{i}\Bigg]\\ =& -\frac{1}{2}\left[2-(l_{\gamma}(l_{\gamma}+1)-l_{\delta}(l_{\delta}+1)+l_{\nu}(l_{\nu}+1)\right]\int \mathrm{d}\Omega\, \Psi^{\gamma}_{j}\Psi^{j,\delta}Y_{\nu}\end{aligned} \qquad \text{(A.37)}$$

The final result is the compact formula

$$\int \mathrm{d}\Omega\, \Psi^{\alpha}_{k}\Psi^{k,\beta}\Psi^{\gamma}_{j}\Psi^{j,\delta} = \sum_{\nu=0}^{2l_{\max}}\left(\int \mathrm{d}\Omega\, \Psi^{\alpha}_{k}\Psi^{k,\beta}Y_{\nu}\right)\left(\int \mathrm{d}\Omega\, \Psi^{\gamma}_{j}\Psi^{j,\delta}Y_{\nu}\right) \qquad \text{(A.38)}$$

which explicitly connects the quartic integral to the previous coupling integrals.

Appendix B

Consistent coarse-graining on curved surfaces

In this appendix, we describe the derivation of self-consistent coarse-graining kernels that are used in Chapter 5 to convert single cell information into a continuous density field and its associated fluxes on a spherical surface. We first motivate this problem for a flat surface and then proceed with a detailed derivation for the case of a spherical surface.

B.1 Kernel consistency in Euclidean space

It is instructive to first consider a set of particles $\alpha = 1, 2, 3, ...$ at positions $\mathbf{X}_\alpha(t)$ moving with velocities $\mathbf{V}_\alpha(t) = \mathrm{d}\mathbf{X}_\alpha/\mathrm{d}t$, where capitalized vectors indicate position and velocity in *Euclidean* space, e.g. particles move on a flat surface or within some three-dimensional volume. A coarse-grained density $\rho(\mathbf{X}, t)$ and a mass flux $\mathbf{J}(\mathbf{X}, t)$ can be defined from this microscopic information by

$$\rho(\mathbf{X}, t) = \sum_\alpha K_e \left[\mathbf{X}, \mathbf{X}_\alpha(t)\right], \tag{B.1a}$$

$$\mathbf{J}(\mathbf{X}, t) = \sum_\alpha \mathcal{K}_e \left[\mathbf{X}, \mathbf{X}_\alpha(t)\right] \cdot \mathbf{V}_\alpha(t), \tag{B.1b}$$

where $K_e(\mathbf{X}, \mathbf{X}')$ and $\mathcal{K}_e(\mathbf{X}, \mathbf{X}')$ represent a scalar-valued and a matrix-valued kernel function, respectively. At the same time, in a system with a constant number of particles, mass conservation implies, in general,

$$\partial_t \rho(\mathbf{X}, t) + \nabla_{\mathbf{X}} \cdot \mathbf{J}(\mathbf{X}, t) = 0, \tag{B.2}$$

relating the density $\rho(\mathbf{X}, t)$ and the mass flux $\mathbf{J}(\mathbf{X}, t)$ of particles. Using the coarse-graining prescriptions Eqs. (B.1) directly in Eq. (B.2) and assuming the resulting relation must hold for any set of particle trajectories, one finds a general kernel consistency relation

$$\nabla_{\mathbf{X}'} K_e(\mathbf{X}, \mathbf{X}') + \nabla_{\mathbf{X}} \cdot \mathcal{K}_e(\mathbf{X}, \mathbf{X}') = 0. \tag{B.3}$$

This condition is automatically satisfied for any translationally invariant and isotropic pair of kernels $K_e(\mathbf{X}, \mathbf{X}') = K_e(\mathbf{X} - \mathbf{X}')$ and $\mathcal{K}_e(\mathbf{X}, \mathbf{X}') = K_e(\mathbf{X} - \mathbf{X}')\mathbb{I}$, where $\mathbb{I}$ is the unit matrix. Coarse-graining with such kernels is frequently employed in practice: Positions and velocities can be, for example, simply convolved with a Gaussian function of mean zero [220].

B.2 Kernel consistency on a curved surface

For a surface parameterized by $\mathbf{r}(s^1, s^2) \in \mathbb{R}^3$ with generalized coordinates s^1, s^2, two tangential basis vectors are defined by $\mathbf{e}_i = \partial \mathbf{r}/\partial s^i$ $(i = 1, 2)$. Partial derivatives are, in the following, denoted $\partial_i := \partial/\partial s^i$. The metric tensor is given by $g_{ij} = \mathbf{e}_i \cdot \mathbf{e}_j$. The mean curvature is defined by $H\mathbf{n} = -\nabla_i \mathbf{e}^i/2$, where $\mathbf{n} = \mathbf{e}_1 \times \mathbf{e}_2/|\mathbf{e}_1 \times \mathbf{e}_2|$ denotes the unit surface normal and the Einstein summation convention is used. The covariant form of mass conservation Eq. 5.1 (main text) on a curved surface reads

$$\partial_t \rho + \nabla_i J^i = 0, \tag{B.4}$$

with $J^i = \mathbf{e}^i \cdot \mathbf{J}$ and ∇_i denotes the covariant derivative. In general, we are interested in describing an effective dynamics for cell positions and velocities that are projected onto a common reference sphere of radius R_s. Such a description can be found by first formulating the coarse-graining approach for a unit sphere, on which particle positions and velocities are fully determined by angular coordinates and corresponding angular velocities, and finally rescaling the density and flux fields by suitable factors of R_s. The corresponding coarse-graining Eq. (5.2b) (main text) of in-plane angular velocities $\bar{\mathbf{v}}_\alpha(t) = \mathbf{v}_\alpha(t)/|\mathbf{r}_\alpha(t)|$ for particles α on a unit sphere reads covariantly

$$J^i = \sum_\alpha \mathcal{K}\left(\mathbf{r}, \mathbf{r}_\alpha\right)^i{}_{j'}\, \bar{v}_\alpha^{j'}, \tag{B.5}$$

where $\bar{v}_\alpha^i = \mathbf{e}^i \cdot \bar{\mathbf{v}}_\alpha$ and we drop the dependence on time to simplify the notation. The two-point kernel tensor $\mathcal{K}\left(\mathbf{r}, \mathbf{r}'\right)_{ij'}$ (a ‘bitensor’) is evaluated in the tangent space of $\mathbf{r}$ for its first index and in the tangent space of $\mathbf{r}'$ at the second, primed index (Appendix 1–Fig. B-1). Mass conservation on a curved surface, Eq. (B.4), together with the coarse-graining prescriptions Eqs. (5.2a) (main text) and (B.5) then implies a covariant kernel consistency relation

$$\partial_{j'} K(\mathbf{r}, \mathbf{r}') + \nabla_i \mathcal{K}(\mathbf{r}, \mathbf{r}')^i{}_{j'} = 0. \tag{B.6}$$

B.3 Solving the kernel consistency relation on a sphere

We solve Eq. (B.6) in the following on the unit sphere, such that $\mathbf{r} = \mathbf{n}$ corresponds to the surface normal. The final result can simply be rescaled to any spherical surface of radius R_s. Furthermore, we note that the parameter

$$x = \mathbf{r} \cdot \mathbf{r}' \tag{B.7}$$

provides a measure for the great circle distance $\omega(x) = \mathrm{acos}(x)$ between two points on a sphere. Hence, we consider an ansatz for the kernels in Eq. (B.6) of the form

$$K(\mathbf{r}, \mathbf{r}') = f(x) \tag{B.8a}$$

$$\mathcal{K}(\mathbf{r}, \mathbf{r}')_{ij'} = g(x)\mathbf{e}_i \cdot \mathbf{e}_{j'}, \tag{B.8b}$$

with two unknown scalar functions $f(x)$ and $g(x)$. The relevant derivatives of the ansatz Eqs. (B.8) can readily be evaluated to

$$\partial_{j'} K(\mathbf{r}, \mathbf{r}') = \frac{\mathrm{d}f(x)}{\mathrm{d}x}\mathbf{r} \cdot \mathbf{e}_{j'} \tag{B.9a}$$

$$\nabla_i \mathcal{K}(\mathbf{r}, \mathbf{r}')^i_{\ j'} = \frac{\mathrm{d}g(x)}{\mathrm{d}x}\mathbf{r}' \cdot \big(\mathbf{e}_i \otimes \mathbf{e}^i\big) \cdot \mathbf{e}_{j'} - 2g(x)\, \mathbf{r} \cdot \mathbf{e}_{j'}. \tag{B.9b}$$

Here, $\otimes$ denotes a dyadic product and we use $\partial_i x = \mathbf{r}' \cdot \mathbf{e}_i$ and $\partial_{i'} x = \mathbf{r} \cdot \mathbf{e}_{i'}$, which follows from Eq. (B.7), as well as $\nabla_i \mathbf{e}^i = -2\mathbf{r}$ in the second equation, which holds on a unit sphere and follows from the definition of the mean curvature. We then use the expansion of the identity matrix in $\mathbb{R}^3$ on the spherical basis $\mathbb{I} = \mathbf{e}_i \otimes \mathbf{e}^i + \mathbf{n} \otimes \mathbf{n}$, such that in our case with $\mathbf{r} = \mathbf{n}$ we have $\mathbf{e}_i \otimes \mathbf{e}^i = \mathbb{I} - \mathbf{r} \otimes \mathbf{r}$. Hence, Eq. (B.9b) becomes

$$\nabla_i \mathcal{K}(\mathbf{r}, \mathbf{r}')^i_{\ j'} = -\frac{\mathrm{d}g(x)}{\mathrm{d}x}(\mathbf{r}' \cdot \mathbf{r})(\mathbf{r} \cdot \mathbf{e}_{j'}) - 2g(x)\, \mathbf{r} \cdot \mathbf{e}_{j'}. \tag{B.10}$$

Using Eqs. (B.9a) and (B.10) in the kernel consistency relation Eq. (B.6) and dividing by $\mathbf{r} \cdot \mathbf{e}_{j'}$ (at $\mathbf{r} = \mathbf{r}'$, for which $\mathbf{r} \cdot \mathbf{e}_{j'} = 0$, Eq. (B.6) is obeyed for any $f(x)$, $g(x)$), we find that the scalar functions in the kernel ansatz Eqs. (B.8) have to obey

$$x\frac{\mathrm{d}g(x)}{\mathrm{d}x} + 2g(x) = \frac{\mathrm{d}f(x)}{\mathrm{d}x}.$$

Hence, the general covariant consistency relation Eq. (B.6) implies for the kernel ansatz Eqs. (B.8) that the weighting functions $g(x)$ and $f(x)$ must be related by

$$g(x) = \frac{1}{x^2}\int_0^x \mathrm{d}u\, u\frac{\mathrm{d}f(u)}{\mathrm{d}u}. \tag{B.11}$$

B.4 Kernel functions with compact support

In the last step, we determine a family of kernel functions $g(x)$ and $f(x)$ defined on the interval $x \in [-1, 1]$ that satisfy (B.11), along with the requirements:

1. $f(x)$ and $g(x)$ must be C^1 regular on $[-1, 1]$
2. $f \geq 0$ on $[-1, 1]$
3. f is normalized to 1 on the unit sphere.

Recalling $x = \cos[\omega(\mathbf{r}, \mathbf{r}')]$ with angular distance ω between $\mathbf{r}$ and $\mathbf{r}'$, a family of functions fulfilling these conditions is given by

$$f_k(\omega) = \frac{k+1}{2\pi}(\cos\omega)^k \mathbf{1}_{\{\cos\omega > 0\}} \tag{B.12a}$$

$$g_k(\omega) = \frac{k}{2\pi}(\cos\omega)^{k-1} \mathbf{1}_{\{\cos\omega > 0\}}, \tag{B.12b}$$

where $\mathbf{1}_{\{\cos\omega>0\}}$ is an indicator function that is 1 if $\cos\omega > 0$ and vanishes otherwise (Appendix 1–Fig. B-2). In this work, we have chosen the kernels Eqs. (B.8) with $f = f_k$ and $g = g_k$ for $k = 6$. For these kernels derived here, densities $\rho(\mathbf{r}, t)$ and associated fluxes $\mathbf{J}(\mathbf{r}, t)$ that are coarse-grained on a unit sphere can be converted into effective densities and fluxes on a spherical surface of radius R_s through the rescaling $\rho \to \rho/R_s^2$ and $\mathbf{J} \to \mathbf{J}/R_s$. Equivalently, rescaled kernels $K(\mathbf{r}, \mathbf{r}') \to K(\mathbf{r}, \mathbf{r}')/R_s^2$ and $\mathcal{K}(\mathbf{r}, \mathbf{r}')_{ij'} \to \mathcal{K}(\mathbf{r}, \mathbf{r}')_{ij'}/R_s$ can be used directly, as was done in Eqs. (5.2) of the main text to generate the data shown in Fig. 5-1 (main text).

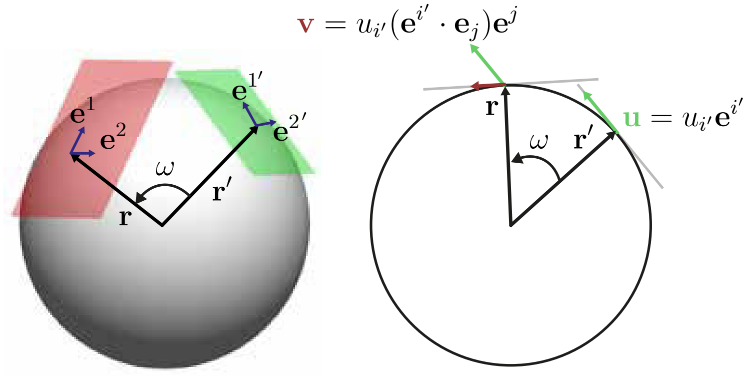

Figure B-1 : Illustration of the action of the coarse-graining tensor kernel $\mathcal{K}(\mathbf{r}, \mathbf{r}')_{ij'}$ [Eq. (B.5)]. Left: $\mathcal{K}_{ij'}$ acts in the two tangent space at points $\mathbf{r}$ and $\mathbf{r}'$ that are separated by an angular distance $\omega = \mathrm{acos}(\mathbf{r} \cdot \mathbf{r}')$. Each tangent plane has corresponding basis vectors $\mathbf{e}_i$, $\mathbf{e}_{i'}$ for $i = 1, 2$. Right: The tensor kernel $\mathcal{K}_{ij'} \sim \mathbf{e}_i \cdot \mathbf{e}_{j'}$ projects vectors $\mathbf{u}$ in the tangent space of $\mathbf{r}'$ and generates a vector $\mathbf{v}$ tangent at $\mathbf{r}$.

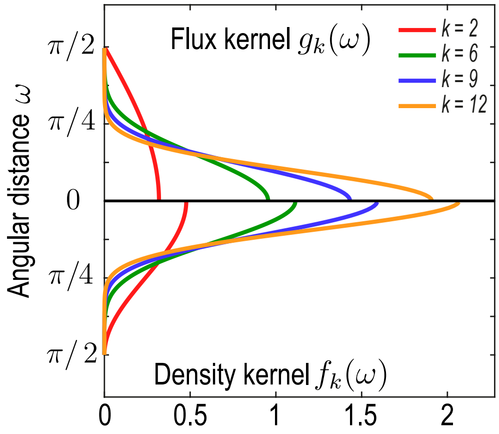

Figure B-2 : Family of kernel functions $f_k(\omega)$ and $g_k(\omega)$ given in Eqs. (B.12). These functions represent weights of the coarse-graining kernels defined in Eqs. (B.8) and are defined such that the kernels satisfy the consistency relation Eq. (B.5). $\omega = \mathrm{acos}(\mathbf{r} \cdot \mathbf{r}')$ denotes angular distances between $\mathbf{r}$ and $\mathbf{r}'$. Coarse-graining of a conserved number of particles on a sphere to determine a density field ρ (Eq. (2a), main text) requires a different weighting – $f_k(\omega)$ – than the coarse-graining of an associated flux $\mathbf{J}$ (Eq. (2b), main text), which requires a weighting $g_k(\omega)$ instead to ensure that coarse-grained fields obey mass conservation Eq. (B.4). A characteristic coarse-graining length scale associated with these kernels is the half-width at half-maximum (HWHM), which is related to k by HWHM $= \arccos(2^{-1/k})$.

Appendix C

Active Brownian Particles on the sphere

In this appendix, we describe the stochastic dynamics of non-interacting, active Brownian particles (ABPs) [255] on curved surfaces and derive analytically coarse-grained mean-field equations, as well as a kernel representation of ABP dynamics. These results are used in chapter 5 to validate our coarse-graining and inference framework.

We consider active Brownian particles at position $\mathbf{x} \in \mathbb{R}^3$ that move with speed v_0 on the surface of a unit sphere (radius $R_0 = 1$) in the direction of their unit orientation vector $\mathbf{u} \in \mathbb{R}^3$. Since $|\mathbf{x}| = 1$ at all times, we can interpret v_0 as the particle's angular speed on the unit sphere. The orientation vector is at all times tangential to the surface, but is subject to random in-plane fluctuations characterized by a rotational diffusion coefficient D_r. The corresponding dynamics of $\mathbf{x}(t)$ and $\mathbf{u}(t)$ is given by the stochastic differential equations (in units $R_0 = 1$)

$$\mathrm{d}\mathbf{x} = v_0 \mathbf{u}\, \mathrm{d}t \tag{C.1a}$$

$$\mathrm{d}\mathbf{u} = -v_0 \mathbf{x} \mathrm{d}t + (\mathbf{x} \times \mathbf{u})\, \sqrt{2D_r} \circ \mathrm{d}\xi, \tag{C.1b}$$

where the stochastic differential equation (C.1b) is interpreted in the Stratonovich sense, as denoted by the symbol "$\circ$" [256]. It follows from Eqs. (C.1) that $\mathbf{x}(t)$ and $\mathbf{u}(t)$ are normalized at all times. In the absence of rotational diffusion ($D_r = 0$), the vectors $\mathbf{x}$ and $\mathbf{u}$ rotate over time by an angle $v_0 t$ around the axis $\mathbf{u}\times\mathbf{x}$. Consequently, particle trajectories in the absence of noise trace out great circles in the plane defined by $(\mathbf{u}\times\mathbf{x})$.

C.1 Spatial correlation of APBs on a sphere

To illustrate how ABPs on a sphere differ from ABPs in Euclidean space, we study first the correlation function $C(t) = \langle \mathbf{x}(t)\cdot\mathbf{x}(0)\rangle$, where the angled brackets denote a Gaussian white-noise average. To this end, we rewrite the ABP dynamics Eqs. (C.1) in their equivalent Itô form given by

$$\mathrm{d}\mathbf{x} = v_0 \mathbf{u}\,\mathrm{d}t \tag{C.2a}$$

$$\mathrm{d}\mathbf{u} = -\left(v_0\mathbf{x} + D_r\mathbf{u}\right)\mathrm{d}t + \sqrt{2D_r}\,(\mathbf{x}\times\mathbf{u})\;\mathrm{d}\xi. \tag{C.2b}$$

In the Itô formulation any smooth function $f(\mathbf{x},\mathbf{u})$ obeys $\langle f(\mathbf{x},\mathbf{u})\mathrm{d}\xi\rangle = 0$, such that [257]

$$\frac{\mathrm{d}}{\mathrm{d}t}\langle \mathbf{x}(t)\cdot\mathbf{x}(0)\rangle = v_0\langle \mathbf{u}(t)\cdot\mathbf{x}(0)\rangle$$

and

$$\frac{\mathrm{d}}{\mathrm{d}t}\langle \mathbf{u}(t)\cdot\mathbf{x}(0)\rangle = -v_0\langle \mathbf{x}(t)\cdot\mathbf{x}(0)\rangle - D_r\langle \mathbf{u}(t)\cdot\mathbf{x}(0)\rangle,$$

which yields a damped harmonic oscillator equation for the correlation function

$$\frac{\mathrm{d}^2}{\mathrm{d}t^2}C(t) + D_r\frac{\mathrm{d}}{\mathrm{d}t}C(t) + v_0^2 C(t) = 0. \tag{C.3}$$

Normalization and orthogonality of $\mathbf{x}(t)$ and $\mathbf{u}(t)$ imply the initial conditions $C = 1$ and $\mathrm{d}C/\mathrm{d}t = 0$ at $t = 0$. The behavior of solutions of Eq. (C.3) is a function of the rotational Péclet number $\mathrm{Pe}_r := v_0/D_r$ that quantifies the ratio between active motion and orientational diffusion. For $\mathrm{Pe}_r < 1$, ('high-noise regime'), the position correlation function $C(t) = \langle \mathbf{x}(t) \cdot \mathbf{x}(0) \rangle$ decays according to Eq. (C.3) monotonically to zero. For $\mathrm{Pe}_r > 1$, ('low-noise regime') position correlations exhibit damped oscillations. To validate our simulation method (described in the following section), analytic predictions for $C(t)$ are in Fig. 5-7B (main text) compared against the ensemble average $\langle \mathbf{x}(t) \cdot \mathbf{x}(0) \rangle$ over 3×10^4 simulated ABPs.

C.2 Stochastic simulation of active Brownian particles on the sphere

To ensure a numerically exact normalization of the particle's position and orientation vectors on the unit sphere, we simulated the dynamics

$$\mathrm{d}\mathbf{x} = \frac{v_0}{|\mathbf{u}|} \left(\mathbf{u} - \frac{\mathbf{u} \cdot \mathbf{x}}{|\mathbf{x}|^2} \mathbf{x} \right) \mathrm{d}t \tag{C.4a}$$

$$\mathrm{d}\mathbf{u} = -v_0 \frac{\mathbf{x}}{|\mathbf{x}|} \mathrm{d}t + \frac{(\mathbf{x} \times \mathbf{u})}{|\mathbf{x} \times \mathbf{u}|} \sqrt{2D_r} \circ \mathrm{d}\xi. \tag{C.4b}$$

We numerically solve the Itô formulation of this system using the Euler-Mayurama scheme [258], and confirm that this system reproduces the correlation dynamics predicted by Eq. (C.3) (Fig. 5-7B).

C.3 Fokker-Planck equation

To study the continuum dynamics of a large number of non-interacting ABPs on a sphere, we determine the dynamics of the probability density $p(\mathbf{x}, \mathbf{u}, t)$ of particle positions $\mathbf{x}$ and orientations $\mathbf{u}$ at time t. To do so, it is convenient to express particle positions in terms of a parameterisation $\mathbf{x}(t) = \mathbf{x}[x^1(t), x^2(t)]$ that defines tangential basis vectors by $\mathbf{e}_i = \partial \mathbf{x} / \partial x^i$ $(i = 1, 2)$ and a metric tensor $g_{ij} = \mathbf{e}_i \cdot \mathbf{e}_j$. By definition, we have $\mathrm{d}\mathbf{x} = \mathbf{e}_i \mathrm{d}x^i$ and Eq. (C.1a) can be rewritten as

$$\mathrm{d}x^i = v_0 u^i \mathrm{d}t. \tag{C.5}$$

General tangential vectors on the surface can be written as $\mathbf{u} = u^i \mathbf{e}_i$ and on a unit sphere the surface normal can be identified with particle positions $\mathbf{n} = \mathbf{e}_1 \times \mathbf{e}_2 / |\mathbf{e}_1 \times \mathbf{e}_2| = \mathbf{x}$. Hence, on the unit sphere the Gauss-Weingarten relation reads $\partial_i \mathbf{e}_j = -C_{ij}\mathbf{x} + \Gamma^k_{ij}\mathbf{e}_k$, where Γ^k_{ij} denote Christoffel symbols and C_{ij} is the curvature tensor. This implies together with Eq. (C.5) the geometric relation

$$\begin{aligned} \mathrm{d}\mathbf{u} &= \mathbf{e}_i \mathrm{d}u^i + u^i(\partial_j \mathbf{e}_i)\mathrm{d}x^j \\ &= \mathbf{e}_i \mathrm{d}u^i - C_{ij}u^i u^j v_0 \mathbf{x}\mathrm{d}t + v_0 u^i u^j \Gamma^k_{ij}\mathbf{e}_k \mathrm{d}t. \end{aligned}$$

Comparing this identity with the stochastic dynamics $\mathrm{d}\mathbf{u}$ in Eq. (C.1b) and using that $C_{ij}u^i u^j = g_{ij}u^i u^j = |\mathbf{u}|^2 = 1$ for unit vectors $\mathbf{u}$ on the unit sphere, we find the covariant stochastic differential equation

$$\mathrm{d}u^i = -v_0 u^j u^k \Gamma^i_{jk}\mathrm{d}t + \epsilon^i{}_k u^k \sqrt{2D_r} \circ \mathrm{d}\xi. \tag{C.6}$$

In Eq. (C.6), $\epsilon_{ij} = \mathbf{x} \cdot (\mathbf{e}_i \times \mathbf{e}_j)$ denotes the Levi-Civita tensor on the unit sphere.

In this covariant basis, we define the scalar probability density

$$p(\mathbf{x}, \mathbf{u}, t) = \left\langle \frac{1}{\sqrt{g(\mathbf{x})}} \prod_i \delta[x^i - x^i(t)]\delta[u^i - u^i(t)] \right\rangle, \tag{C.7}$$

where $\delta(x)$ denotes a Dirac function. Combining Eqs. (C.5) and (C.6), standard methods [234, 235] allow us to obtain the Fokker-Planck equation for $p(\mathbf{x}, \mathbf{u}, t)$ as

$$\frac{\partial}{\partial t}p(\mathbf{x}, \mathbf{u}, t) = D_r \frac{\partial}{\partial u^i}\left[\epsilon^i{}_k u^k \frac{\partial}{\partial u^j}\left(\epsilon^j{}_l u^l p\right)\right] - \nabla_i(v_0 u^i p) + \frac{\partial}{\partial u^i}\left(v_0 u^j u^k \Gamma^i_{jk} p\right) \tag{C.8}$$

Using the identity $\epsilon^i{}_k \epsilon^j{}_l = g^{ij}g_{kl} - \delta^i_l \delta^j_k$, the dynamics of the probability density is finally given by

$$\frac{\partial}{\partial t}p(\mathbf{x}, \mathbf{u}, t) = D_r \frac{\partial}{\partial u^i}\left[(g^{ij} - u^i u^j)\frac{\partial p}{\partial u^j}\right] - v_0 u^i \nabla_i p + \frac{\partial}{\partial u^i}\left(v_0 u^j u^k \Gamma^i_{jk} p\right), \tag{C.9}$$

which agrees with the result in [235].

C.4 Hydrodynamic expansion

To connect the Fokker-Planck dynamics given in Eq. (C.9) to hydrodynamic fields, we define (probability) density and fluxes by $\rho(\mathbf{x},t) = \int \mathrm{d}^2\mathbf{u}\, p(\mathbf{x},\mathbf{u},t)$, and $J^i(\mathbf{x},t) = v_0 \int \mathrm{d}^2\mathbf{u}\, u^i p(\mathbf{x},\mathbf{u},t)$. Their dynamics on the unit sphere is given by [235]

$$\frac{\partial \rho}{\partial t} = -\nabla_i J^i \tag{C.10a}$$

$$\frac{\partial J^i}{\partial t} = -\frac{v_0^2}{2}\nabla^i \rho - D_r J^i, \tag{C.10b}$$

where couplings to higher order fields are neglected, as they vanish at shorter timescales due to the presence of rotational noise. Expressing Eqs. (C.10) in terms of scalar and vector spherical harmonics (see Appendix A) for an arbitrary sphere radius R_0 yields the mode dynamics given in Eqs. (5.17) of the main text.

C.5 Coarse-graining non-interacting ABPs on the sphere

In this section, we show that the kernel-based coarse-graining approach introduced in Appendix B is compatible with the hydrodynamic expansion of the probability density obtained by the Fokker-Planck equation. We again consider N Active Brownian particles on a sphere, with trajectories $\{\mathbf{x}_\mu(t)\mathbf{v}_\mu(t)\}_{\mu=1,\ldots,N}$. Let us also consider two spherical coarse-graining kernels $K_0(\mathbf{x},\mathbf{x}')$ and $[K_1(\mathbf{x},\mathbf{x}')]^i{}_{j'}$ such that $\nabla_{j'}K_0 + \nabla_i[K_1]^i{}_{j'} = 0$.

In terms of these kernels, we define the density and flux

$$\rho(\mathbf{x},t) = \left\langle \sum_\mu K_0(\mathbf{x},\mathbf{x}_\mu(t)) \right\rangle \tag{C.11a}$$

$$J^k(\mathbf{x},t) = \left\langle \sum_\mu [K_1(\mathbf{x},\mathbf{x}_\mu(t))]^k{}_{j'} v_0 u_\mu^{j'}(t) \right\rangle \tag{C.11b}$$

then we have

$$\begin{aligned}
\partial_t \rho(\mathbf{x}, t) &= \left\langle \sum_\mu \nabla_{j'} K_0(\mathbf{x}, \mathbf{x}_\mu(t)) v_0 u_\mu^{j'}(t) \right\rangle \\
&= - \left\langle \sum_\mu \nabla_k [K_1(\mathbf{x}, \mathbf{x}_\mu(t))]^k_{\ j'} v_0 u_\mu^{j'}(t) \right\rangle \\
&= -\nabla_k J^k
\end{aligned}$$

since the spatial derivative on unprimed coordinates commute with the averaging over particle positions. Hence, by construction of our kernels we recover exactly mass conservation $\partial_t \rho + \nabla_k J^k = 0$ with no further assumptions. What about the dynamical equation for $\mathbf{J}$? Averaging over the possible realizations of the ABP trajectories (denoted by $\langle . \rangle$), we have

$$\begin{aligned}
\partial_t J^k(\mathbf{x}, t) &= \left\langle v_0 \sum_\mu \partial_t \left([K_1(\mathbf{x}, \mathbf{x}'_\mu)]^k_{\ j'} u_\mu^{j'}(t) \right) \right\rangle \\
&= \left\langle v_0 \sum_\mu \partial_{a'} [K_1(\mathbf{x}, \mathbf{x}'_\mu)]^k_{\ j'} u_\mu^{a'} u_\mu^{j'} + [K_1(\mathbf{x}, \mathbf{x}'_\mu)]^k_{\ j'} \mathrm{d}_t u_\mu^{j'}(t) \right\rangle .
\end{aligned}$$

Moreover ABPs satisfy in the Itô calculus

$$\mathrm{d}_t u_\mu^{j'}(t) = -v_0 u_\mu^{a'} u_\mu^{b'} \Gamma^{j'}_{\ a'b'} - D u_\mu^{j'} + \sqrt{2D} g^{j'a'} \epsilon_{a'b'} u_\mu^{b'} \frac{\mathrm{d}\xi}{\mathrm{d}t}.$$

Now, by the property that the multiplicative noise term averages out to zero in the Itô calculus, we have

$$\begin{aligned}
\partial_t J^k(\mathbf{x}, t) &= \left\langle v_0 \sum_\mu \partial_{a'} [K_1(\mathbf{x}, \mathbf{x}'_\mu)]^k_{\ j'} v_0 u_\mu^{a'} u_\mu^{j'} - [K_1(\mathbf{x}, \mathbf{x}'_\mu)]^k_{\ j'} v_0^2 u_\mu^{a'} u_\mu^{b'} \Gamma^{j'}_{\ a'b'} - D [K_1(\mathbf{x}, \mathbf{x}'_\mu)]^k_{\ j'} u_\mu^{j'} \right\rangle \\
&= \left\langle v_0^2 \sum_\mu \nabla_{a'} [K_1(\mathbf{x}, \mathbf{x}'_\mu)]^k_{\ b'} u_\mu^{a'} u_\mu^{b'} \right\rangle - D J^k
\end{aligned}$$

where we used the definition of the covariant derivative at point $\mathbf{x}'$ $\nabla_{a'} F_{b'} = \partial_{a'} F_{b'} - \Gamma^{c'}_{\ a'b'} F_{c'}$ and some index relabeling.

Define now the microscopic nematic tensor of particle μ by $n_\mu^{a'b'} = u_\mu^{a'} u_\mu^{b'} - \frac{1}{2}\delta^{a'b'}$. Then

$$\begin{aligned}
\partial_t J^k(\mathbf{x},t) &= \left\langle v_0^2 \sum_\mu \nabla_{a'} [K_1(\mathbf{x},\mathbf{x}')]^k_{\ b'} \left(n_\mu^{a'b'} + \frac{1}{2}\delta^{a'b'} \right) \right\rangle - DJ^k \\
&= \left\langle v_0^2 \sum_\mu \nabla_{a'} [K_1(\mathbf{x},\mathbf{x}'_\mu)]^k_{\ b'} n_\mu^{a'b'} \right\rangle + \left\langle \frac{v_0^2}{2} \sum_\mu \nabla^{b'} [K_1(\mathbf{x},\mathbf{x}'_\mu)]^k_{\ b'} \right\rangle - DJ^k
\end{aligned}$$

To proceed, notice that our kernels satisfy $K_0(\mathbf{x},\mathbf{x}') = f(\mathbf{x}\cdot\mathbf{x}')$ and $[K_1(\mathbf{x},\mathbf{x}')]^i_{\ j'} = g(\mathbf{x}\cdot\mathbf{x}')(e^i \cdot e_{j'})$ - given that $\nabla_{j'} K_0 + \nabla_i [K_1]^i_{\ j'} = 0$, by symmetry between primed and unprimed indices, we also have that $\nabla^k K_0 + \nabla^{j'} [K_1]^k_{\ j'} = 0$. Hence now we have

$$\begin{aligned}
\partial_t J^k(\mathbf{x},t) &= \left\langle v_0^2 \sum_\mu \nabla_{a'} [K_1(\mathbf{x},\mathbf{x}'_\mu)]^k_{\ b'} n_\mu^{a'b'} \right\rangle - \nabla^k \left\langle \frac{v_0^2}{2} \sum_\mu [K_0(\mathbf{x},\mathbf{x}'_\mu)] \right\rangle - DJ^k \\
&= \left\langle v_0^2 \sum_\mu \nabla_{a'} [K_1(\mathbf{x},\mathbf{x}'_\mu)]^k_{\ b'} n_\mu^{a'b'} \right\rangle - \frac{v_0^2}{2} \nabla^k \rho - DJ^k \\
&= -v_0^2 \nabla_i Q^{ik} - \frac{v_0^2}{2} \nabla^k \rho - DJ^k \qquad \text{(C.12a)}
\end{aligned}$$

where we defined a macroscopic nematic tensor $Q^{ik} = \left\langle \sum_\mu [K_2(\mathbf{x},\mathbf{x}'_\mu)]^{ik}_{\ \ a'b'} n_\mu^{a'b'} \right\rangle$, with the kernel K_2 chosen such that $[K_2]^{ik}_{\ \ a'b'} = [K_2]^{ki}_{\ \ a'b'}$, which by symmetry on primed indices also satisfies $\nabla_{a'} [K_1]^i_{\ b'} + \nabla_k [K_2]^{ik}_{\ \ a'b'} = 0$. Eq. (C.12a) is the same as the one obtained through the Fokker-Planck approach in [235], and reduces to Eq. C.10b under the same closure assumption that $Q^{ij} = 0$.

Appendix D

Tracking topological defects on a sphere

In this appendix, we detail the geometric construction employed to numerically identify topological defects in vector fields on the sphere S^2 embedded in $\mathbb{R}^3$, which is used in chapter 5.

D.1 Topological charge

We consider a vector field $\mathbf{v}$ on the sphere S^2. Let us consider a small Burgers circuit Γ, an oriented closed curve circling point $\mathbf{r}$.

Then the topological charge contained at point $\mathbf{r}$ is given by [259]

$$q = \oint_{\Gamma} \mathrm{d}\theta \tag{D.1}$$

where θ is the angle formed by the vector field with an arbitrary direction. On a sphere, one cannot simply use a fixed direction to define the angle θ, and the evaluation of the integral Eq. (D.1) requires a careful geometric construction. For our application purposes, we consider a vector field defined on a discrete quasi-regular grid on the sphere.

D.2 Geometrical construction

Basis definition

We consider a quasi-regular grid on the unit sphere of points $\{\mathbf{r}^j\}_{j=1,\dots,N} \in \mathbb{R}^3$. Let us focus on a point $\mathbf{r}^i$ on the sphere, with first neighbors $\{\mathbf{r}_s^i\}_{s=1,\dots,n}$. For each neighbor, we define unit vectors $\mathbf{n}_s \propto \mathbf{r}_s^i - (\mathbf{r}_s^i \cdot \mathbf{r}^i)\mathbf{r}^i$ and $\mathbf{t}_s^i = \mathbf{r}^i \times \mathbf{n}_s^i$ such that $(\mathbf{n}_s^i, \mathbf{t}_s^i, \mathbf{r}^i)$ is orthonormal direct. Note that since we consider points on the unit sphere, the vectors $\mathbf{r}^i$ are all unitary. In what follows, we will drop the superscript i for compactness.

Choosing a point at random in the neighborhood of $\mathbf{r}^i$ and labeling it $s = 1$, we order the points $\{\mathbf{r}_s^i\}_\{s = 1, \dots, n\}$ in the neighborhood of i such as the angle $\alpha_s = \text{atan2}(\mathbf{n}_s \cdot \mathbf{t}_1, \mathbf{n}_s \cdot \mathbf{n}_1) + \pi \in [0, 2\pi[$ is increasing with s.

Computing the topological charge around a point r_i

Once the neighborhood of each point is identified and ordered, we create the tangent vectors to the closed curve going through the neighbor points in order. We choose the curve to be composed of the piece-wise geodesics $\{\gamma_s\}_{s=1,\dots,n}$ connecting points $\mathbf{r}_s$ and $\mathbf{r}_{s+1}$. To close the curve, we define $\mathbf{r}_{n+1} = \mathbf{r}_1$. Defining the unit vector $\mathbf{k}_s \propto (\mathbf{r}_s \times \mathbf{r}_{s+1})$, the tangents to γ_s are $t_s^0 = \mathbf{r}_s \times \mathbf{k}_s$ and $t_s^1 = \mathbf{r}_{s+1} \times \mathbf{k}_s$ at points $\mathbf{r}_s$ and $\mathbf{r}_{s+1}$ respectively, and are in the plane defined by $\mathbf{k}_s$. We can then compute the change in the angle of the vector field $\mathbf{v}_s \in \mathbb{R}^3$ with respect to the geodesic tangent $\Delta\theta_s$. Defining $v_{t,s}^{(j)} = \mathbf{v}_{s+j} \cdot \mathbf{t}_s^{(j)}$ and $v_{n,s}^{(j)} = \mathbf{v}_{s+j} \cdot \mathbf{k}_s$ for $j = 0, 1$, the change in angle $\Delta\theta_s$ then comes out as

$$\Delta\theta_s = \text{diff}(\theta_s^{(1)}, \theta_s^{(0)}) \tag{D.2}$$

where we define $\text{diff}(y, x) = \text{mod}(y - x + \pi, 2\pi) - \pi$ the function that takes two angles in $]-\pi, \pi]$ and return the difference of their angles in $]-\pi, \pi]$, and

$$\theta_s^{(j)} = \text{atan2}\left(\frac{v_{t,s}^{(j)}}{\sqrt{[v_{t,s}^{(j)}]^2 + [v_{n,s}^{(j)}]^2}}, \frac{v_{n,s}^{(j)}}{\sqrt{[v_{t,s}^{(j)}]^2 + [v_{n,s}^{(j)}]^2}} \right). \tag{D.3}$$

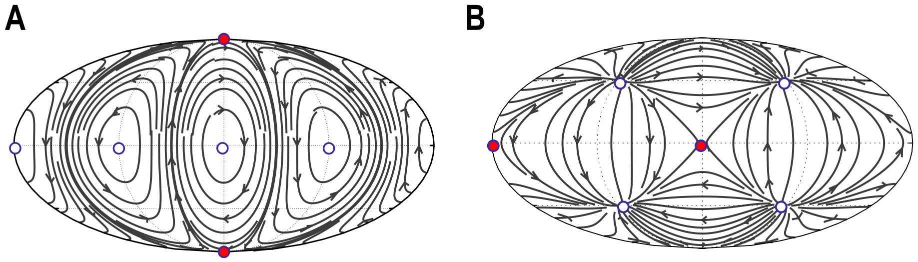

Figure D-1 : Demonstration of the defect tracking on two example tangential vector fields on a spherical surface. **A**: Vector field defined by $\mathbf{J} = \mathbf{\Phi}_{(2,2)}$. **B**: Vector field defined by $\mathbf{J} = \mathbf{\Psi}_{(2,-1)} + 0.1\mathbf{\Phi}_{(2,2)}$. Black lines depict the streamlines defined by these vector fields. White circles depict topological defects of charge +1, red circles depict defects with charge −1.

We finally evaluate q as

$$q = \frac{1}{2\pi} \sum_{s=1}^{n} \Delta\theta_s \tag{D.4}$$

If $|q| > .1$, we then count the center point as topological defect and record its charge and position. For the polar vector fields that we consider, our flux vector field must complete an integer number of turns around a Burgers circuit and thus all defects must be integer-charged. We hence round q to the nearest signed integer.

Additional processing

We use a hierarchical clustering method using a distance cutoff of the order of the grid spacing to identify spurious clusters of defects arising from misalignment of the grid points with the location of the continuous field singular points (MATLAB 2020b). We then pick a single representative from each cluster as final result. Example results are shown in Fig. D-1.

After locating defects at all time points, it is possible to additionally reconstruct the defect tracks by using the Munkres (Hungarian) algorithm [260] to match defects at times t and $t + 1$, distinguishing between defects of different charges.

Bibliography

[1] Jonathan A Jackson, Nicolas Romeo, Alexander Mietke, Keaton J. Burns, Jan F. Totz, Adam C. Martin, Jörn Dunkel, and Jasmin Imran Alsous. Dynamics, scaling behavior, and control of nuclear wrinkling. *arXiv*, 2210:11581, 2022.

[2] H. O. Gutzeit. The role of microfilaments in cytoplasmic streaming in Drosophila follicles. *Journal of Cell Science*, 80(1):159–169, February 1986. Publisher: The Company of Biologists Ltd Section: Journal Articles.

[3] Andrei Y. Kobitski, Jens C. Otte, Masanari Takamiya, Benjamin Schäfer, Jonas Mertes, Johannes Stegmaier, Sepand Rastegar, Francesca Rindone, Volker Hartmann, Rainer Stotzka, Ariel García, Jos van Wezel, Ralf Mikut, Uwe Strähle, and G. Ulrich Nienhaus. An ensemble-averaged, cell density-based digital model of zebrafish embryo development derived from light-sheet microscopy data with single-cell resolution. *Sci. Rep.*, 5(1):8601, 2015.

[4] Gopi Shah, Konstantin Thierbach, Benjamin Schmid, Johannes Waschke, Anna Reade, Mario Hlawitschka, Ingo Roeder, Nico Scherf, and Jan Huisken. Multi-scale imaging and analysis identify pan-embryo cell dynamics of germlayer formation in zebrafish. *Nature Communications*, 10(1):5753, December 2019.

[5] Claudio Collinet and Thomas Lecuit. Programmed and self-organized flow of information during morphogenesis. *Nat. Rev. Mol. Cell Biol.*, 22:245—-265, 2021.

[6] Jan Brugués, Valeria Nuzzo, Eric Mazur, and Daniel J. Needleman. Nucleation and Transport Organize Microtubules in Metaphase Spindles. *Cell*, 149(3):554–564, April 2012.

[7] J H. C. Wang and B P. Thampatty. An Introductory Review of Cell Mechanobiology. *Biomechanics and Modeling in Mechanobiology*, 5(1):1–16, March 2006.

[8] Maria Almonacid, Adel Al Jord, Stephany El-Hayek, Alice Othmani, Fanny Coulpier, Sophie Lemoine, Kei Miyamoto, Robert Grosse, Christophe Klein, Tristan Piolot, Philippe Mailly, Raphaël Voituriez, Auguste Genovesio, and Marie-Hélène Verlhac. Active Fluctuations of the Nuclear Envelope Shape the Transcriptional Dynamics in Oocytes. *Developmental Cell*, 51(2):145–157.e10, October 2019.

[9] Chenyi Fei, Alexandra T. Wilson, Niall M. Mangan, Ned S. Wingreen, and Martin C. Jonikas. Modelling the pyrenoid-based CO2-concentrating mechanism provides insights into its operating principles and a roadmap for its engineering into crops. *Nature Plants*, 8(5):583–595, May 2022.

[10] Peter Friedl and Darren Gilmour. Collective cell migration in morphogenesis, regeneration and cancer. *Nature Reviews Molecular Cell Biology*, 10(7):445–457, July 2009.

[11] Sebastian J Streichan, Matthew F Lefebvre, Nicholas Noll, Eric F Wieschaus, and Boris I Shraiman. Global morphogenetic flow is accurately predicted by the spatial distribution of myosin motors. *eLife*, 7:e27454, February 2018.

[12] Morgan Huse. Mechanical forces in the immune system. *Nature Reviews Immunology*, 17(11):679–690, November 2017.

[13] Sui Huang and Donald E. Ingber. Cell tension, matrix mechanics, and cancer development. *Cancer Cell*, 8(3):175–176, September 2005.

[14] Florence Broders-Bondon, Thanh Huong Nguyen Ho-Bouldoires, Maria-Elena Fernandez-Sanchez, and Emmanuel Farge. Mechanotransduction in tumor progression: The dark side of the force. *Journal of Cell Biology*, 217(5):1571–1587, May 2018.

[15] Udo Seifert. Stochastic thermodynamics, fluctuation theorems and molecular machines. *Reports on Progress in Physics*, 75(12):126001, December 2012.

[16] D. Collin, F. Ritort, C. Jarzynski, S. B. Smith, I. Tinoco, and C. Bustamante. Verification of the Crooks fluctuation theorem and recovery of RNA folding free energies. *Nature*, 437(7056):231–234, September 2005.

[17] Dillon J. Cislo, Fengshuo Yang, Haodong Qin, Anastasios Pavlopoulos, Mark J. Bowick, and Sebastian J. Streichan. Active cell divisions generate fourfold orientationally ordered phase in living tissue. *Nature Physics*, May 2023.

[18] Josep-Maria Armengol-Collado, Livio Nicola Carenza, Julia Eckert, Dimitrios Krommydas, and Luca Giomi. Epithelia are multiscale active liquid crystals. preprint, Biophysics, February 2022.

[19] Nicholas Noll, Madhav Mani, Idse Heemskerk, Sebastian J. Streichan, and Boris I. Shraiman. Active tension network model suggests an exotic mechanical state realized in epithelial tissues. *Nature Physics*, 13(12):1221–1226, December 2017.

[20] Tzer Han Tan, Alexander Mietke, Junang Li, Yuchao Chen, Hugh Higinbotham, Peter J. Foster, Shreyas Gokhale, Jörn Dunkel, and Nikta Fakhri. Odd dynamics of living chiral crystals. *Nature*, 607(7918):287–293, July 2022.

[21] Daniel Needleman and Zvonimir Dogic. Active matter at the interface between materials science and cell biology. *Nature Reviews Materials*, 2(9):17048, July 2017.

[22] Gerhard Gompper, Roland G Winkler, Thomas Speck, Alexandre Solon, Cesare Nardini, Fernando Peruani, Hartmut Löwen, Ramin Golestanian, U Benjamin Kaupp, Luis Alvarez, Thomas Kiørboe, Eric Lauga, Wilson C K Poon, Antonio DeSimone, Santiago Muiños-Landin, Alexander Fischer, Nicola A Söker, Frank Cichos, Raymond Kapral, Pierre Gaspard, Marisol Ripoll, Francesc Sagues, Amin Doostmohammadi, Julia M Yeomans, Igor S Aranson, Clemens Bechinger, Holger Stark, Charlotte K Hemelrijk, François J Nedelec, Trinish Sarkar, Thibault Aryaksama, Mathilde Lacroix, Guillaume Duclos, Victor Yashunsky, Pascal Silberzan, Marino Arroyo, and Sohan Kale. The 2020 motile active matter roadmap. *Journal of Physics: Condensed Matter*, 32(19):193001, May 2020.

[23] Sriram Ramaswamy. The Mechanics and Statistics of Active Matter. *Annual Review of Condensed Matter Physics*, 1(1):323–345, August 2010.

[24] M. C. Marchetti, J. F. Joanny, S. Ramaswamy, T. B. Liverpool, J. Prost, Madan Rao, and R. Aditi Simha. Hydrodynamics of soft active matter. *Reviews of Modern Physics*, 85(3):1143–1189, July 2013.

[25] D'Arcy Wentworth Thompson. *On growth and form.* Dover, New York, 1992.

[26] Ibrahim I. Cisse, Ignacio Izeddin, Sebastien Z. Causse, Lydia Boudarene, Adrien Senecal, Leila Muresan, Claire Dugast-Darzacq, Bassam Hajj, Maxime Dahan, and Xavier Darzacq. Real-Time Dynamics of RNA Polymerase II Clustering in Live Human Cells. *Science*, 341(6146):664–667, August 2013.

[27] Gopi Shah, Konstantin Thierbach, Benjamin Schmid, Johannes Waschke, Anna Reade, Mario Hlawitschka, Ingo Roeder, Nico Scherf, and Jan Huisken. Multiscale imaging and analysis identify pan-embryo cell dynamics of germlayer formation in zebrafish. *Nat. Commun.*, 10:5753, 2019.

[28] Louis H. Sullivan. *The tall office building artistically considered.* J.B. Lippincott Co., Philadelphia, 1896.

[29] Andrej Košmrlj and David R. Nelson. Statistical Mechanics of Thin Spherical Shells. *Physical Review X*, 7(1):011002, January 2017.

[30] Jasmin Imran Alsous, Nicolas Romeo, Jonathan A. Jackson, Frank M. Mason, Jörn Dunkel, and Adam C. Martin. Dynamics of hydraulic and contractile wave-mediated fluid transport during *Drosophila* oogenesis. *Proceedings of the National Academy of Sciences*, 118(10):e2019749118, March 2021.

[31] Philipp J. Keller, Annette D. Schmidt, Joachim Wittbrodt, and Ernst H.K. Stelzer. Reconstruction of Zebrafish Early Embryonic Development by Scanned Light Sheet Microscopy. *Science*, 322(5904):1065–1069, November 2008.

[32] Vincent F. Fiore, Matej Krajnc, Felipe Garcia Quiroz, John Levorse, H. Amalia Pasolli, Stanislav Y. Shvartsman, and Elaine Fuchs. Mechanics of a multilayer epithelium instruct tumour architecture and function. *Nature*, 585(7825):433–439, September 2020.

[33] Shannon E. Keenan, Maria Avdeeva, Liu Yang, Daniel S. Alber, Eric F. Wieschaus, and Stanislav Y. Shvartsman. Dynamics of *Drosophila* endoderm specification. *Proceedings of the National Academy of Sciences*, 119(15):e2112892119, April 2022.

[34] Idse Heemskerk and Sebastian J Streichan. Tissue cartography: compressing bio-image data by dimensional reduction. *Nature Methods*, 12(12):1139–1142, December 2015.

[35] Daniel S. W. Lee, Ned S. Wingreen, and Clifford P. Brangwynne. Chromatin mechanics dictates subdiffusion and coarsening dynamics of embedded condensates. *Nature Physics*, 17(4):531–538, April 2021.

[36] Nicolas Romeo, Alasdair Hastewell, Alexander Mietke, and Jörn Dunkel. Learning developmental mode dynamics from single-cell trajectories. *eLife*, 10:e68679, December 2021.

[37] Amita Gorur, Lin Yuan, Samuel J. Kenny, Satoshi Baba, Ke Xu, and Randy Schekman. COPII-coated membranes function as transport carriers of intracellular procollagen I. *Journal of Cell Biology*, 216(6):1745–1759, June 2017.

[38] Bruce Alberts. *Molecular biology of the cell*. W. W. Norton & Company, New York, seventh edition edition, 2022.

[39] Ou-Yang Zhong-can and W. Helfrich. Instability and Deformation of a Spherical Vesicle by Pressure. *Physical Review Letters*, 59(21):2486–2488, November 1987.

[40] Chase P. Broedersz and Fred C. MacKintosh. Modeling semiflexible polymer networks. *Reviews of Modern Physics*, 86(3):995–1036, July 2014.

[41] Lev Davidovitch Landau, Evgenij M. Lifshitz, Lev Davidovitch Landau, and Lev Davidovitch Landau. *Theory of elasticity*. Number 7 in Course of theoretical physics / L. D. Landau and E. M. Lifshitz. Elsevier, Butterworth-Heinemann, Amsterdam Heidelberg, 3. engl. ed., rev. and enlarged, [nachdr.] edition, 2009.

[42] Douglas P. Holmes and A. J. Crosby. Snapping Surfaces. *Advanced Materials*, 19(21):3589–3593, November 2007.

[43] Yael Klein, Efi Efrati, and Eran Sharon. Shaping of Elastic Sheets by Prescription of Non-Euclidean Metrics. *Science*, 315(5815):1116–1120, February 2007.

[44] Yohai Bar-Sinai, Gabriele Librandi, Katia Bertoldi, and Michael Moshe. Geometric charges and nonlinear elasticity of two-dimensional elastic metamaterials. *Proceedings of the National Academy of Sciences*, 117(19):10195–10202, May 2020.

[45] Jeong-Ho Lee, Harold S. Park, and Douglas P. Holmes. Elastic Instabilities Govern the Morphogenesis of the Optic Cup. *Physical Review Letters*, 127(13):138102, September 2021.

[46] D. Nelson, T. Piran, and S. Weinberg. *Statistical Mechanics of Membranes and Surfaces: Proceedings of the Jerusalem Winter School for Theoretical Physics*. World Scientific, Jerusalem, Israel, April 1989.

[47] J. Paulose, G. A. Vliegenthart, G. Gompper, and D. R. Nelson. Fluctuating shells under pressure. *Proceedings of the National Academy of Sciences*, 109(48):19551–19556, November 2012.

[48] Guillaume Salbreux and Frank Jülicher. Mechanics of active surfaces. *Phys. Rev. E*, 96:032404, Sep 2017.

[49] B. Audoly and Yves Pomeau. *Elasticity and geometry: from hair curls to the non-linear response of shells*. Oxford University Press, Oxford ; New York, 2010.

[50] A. van der Heijden. *W.T. Koiter's Elastic Stability of Solids and Structures*. Cambridge University Press, 2009.

[51] Dong-Hwee Kim, Bo Li, Fangwei Si, Jude M. Phillip, Denis Wirtz, and Sean X. Sun. Volume regulation and shape bifurcation in the cell nucleus. *Journal of Cell Science*, 128(18):3375–3385, September 2015.

[52] Chloe M. Funkhouser, Rastko Sknepnek, Takeshi Shimi, Anne E. Goldman, Robert D. Goldman, and Monica Olvera de la Cruz. Mechanical model of blebbing in nuclear lamin meshworks. *Proceedings of the National Academy of Sciences*, 110(9):3248–3253, February 2013.

[53] E. Efrati, E. Sharon, and R. Kupferman. Elastic theory of unconstrained non-euclidean plates. *J. Phys. Chem. Solids*, 57(4):762–775, 2009.

[54] Matteo Pezzulla, Norbert Stoop, Xin Jiang, and D. P. Holmes. Curvature-driven morphing of non-Euclidean shells. *Proceedings of the Royal Society A: Mathematical, Physical and Engineering Sciences*, 473(2201):20170087, May 2017.

[55] Lawrence C.-L. Lin and Frank L. H. Brown. Brownian Dynamics in Fourier Space: Membrane Simulations over Long Length and Time Scales. *Physical Review Letters*, 93(25):256001, December 2004.

[56] Scott T. Milner and S. A. Safran. Dynamical fluctuations of droplet microemulsions and vesicles. *Physical Review A*, 36(9):4371–4379, November 1987.

[57] H. Turlier, D. A. Fedosov, B. Audoly, T. Auth, N. S. Gov, C. Sykes, J.-F. Joanny, G. Gompper, and T. Betz. Equilibrium physics breakdown reveals the active nature of red blood cell flickering. *Nature Physics*, 12(5):513–519, May 2016.

[58] Horace Lamb. *Hydrodynamics*. Cambridge University Press, 1932.

[59] M F. Thorpe and I Jasiuk. New results in the theory of elasticity for two-dimensional composites. *Proceedings of the Royal Society of London. Series A: Mathematical and Physical Sciences*, 438(1904):531–544, September 1992.

[60] Keaton J. Burns, Geoffrey M. Vasil, Jeffrey S. Oishi, Daniel Lecoanet, and Benjamin P. Brown. Dedalus: A flexible framework for numerical simulations with spectral methods. *Phys. Rev. Res.*, 2(2):023068, 2020.

[61] Albert Reuther, Jeremy Kepner, Chansup Byun, Siddharth Samsi, William Arcand, David Bestor, Bill Bergeron, Vijay Gadepally, Michael Houle, Matthew Hubbell, Michael Jones, Anna Klein, Lauren Milechin, Julia Mullen, Andrew Prout, Antonio Rosa, Charles Yee, and Peter Michaleas. Interactive supercomputing on 40,000 cores for machine learning and data analysis. In *2018 IEEE High Performance extreme Computing Conference (HPEC)*, pages 1–6. IEEE, 2018.

[62] Alexander Mietke. *Dynamics of active surfaces*. PhD thesis, Technische Universität Dresden, 2018.

[63] S Sachdev and D R Nelson. Crystalline and fluid order on a random topography. *Journal of Physics C: Solid State Physics*, 17(30):5473–5489, October 1984.

[64] Mehran Kardar. *Statistical Physics of Fields*. Cambridge University Press, 1 edition, June 2007.

[65] Noah P. Mitchell, Vinzenz Koning, Vincenzo Vitelli, and William T. M. Irvine. Fracture in sheets draped on curved surfaces. *Nature Materials*, 16(1):89–93, January 2017.

[66] J. H. Los, A. Fasolino, and M. I. Katsnelson. Mechanics of thermally fluctuating membranes. *npj 2D Materials and Applications*, 1(1):9, December 2017.

[67] Gustavo Düring, Christophe Josserand, Giorgio Krstulovic, and Sergio Rica. Strong turbulence for vibrating plates: Emergence of a Kolmogorov spectrum. *Physical Review Fluids*, 4(6):064804, June 2019.

[68] Nigel Goldenfeld, Olivier Martin, and Y. Oono. Intermediate asymptotics and renormalization group theory. *Journal of Scientific Computing*, 4(4):355–372, December 1989.

[69] Joël Lemière, Paula Real-Calderon, Liam J Holt, Thomas G Fai, and Fred Chang. Control of nuclear size by osmotic forces in Schizosaccharomyces pombe. *eLife*, 11:e76075, July 2022.

[70] Dan Deviri and Samuel A. Safran. Balance of osmotic pressures determines the nuclear-to-cytoplasmic volume ratio of the cell. *Proceedings of the National Academy of Sciences*, 119(21):e2118301119, May 2022.

[71] Melina K. Blees, Arthur W. Barnard, Peter A. Rose, Samantha P. Roberts, Kathryn L. McGill, Pinshane Y. Huang, Alexander R. Ruyack, Joshua W. Kevek, Bryce Kobrin, David A. Muller, and Paul L. McEuen. Graphene kirigami. *Nature*, 524(7564):204–207, August 2015.

[72] Jejoong Yoo and Aleksei Aksimentiev. In situ structure and dynamics of DNA origami determined through molecular dynamics simulations. *Proceedings of the National Academy of Sciences*, 110(50):20099–20104, December 2013.

[73] Yohalie Kalukula, Andrew D. Stephens, Jan Lammerding, and Sylvain Gabriele. Mechanics and functional consequences of nuclear deformations. *Nature Reviews Molecular Cell Biology*, 23(9):583–602, September 2022.

[74] A. J. Lomakin, C. J. Cattin, D. Cuvelier, Z. Alraies, M. Molina, G. P. F. Nader, N. Srivastava, P. J. Sáez, J. M. Garcia-Arcos, I. Y. Zhitnyak, A. Bhargava, M. K. Driscoll, E. S. Welf, R. Fiolka, R. J. Petrie, N. S. De Silva, J. M. González-Granado, N. Manel, A. M. Lennon-Duménil, D. J. Müller, and M. Piel. The nucleus acts as a ruler tailoring cell responses to spatial constraints. *Science*, 370(6514):eaba2894, October 2020.

[75] Stefan Biedzinski, Gökçe Agsu, Benoit Vianay, Marc Delord, Laurent Blanchoin, Jerome Larghero, Lionel Faivre, Manuel Théry, and Stéphane Brunet. Microtubules control nuclear shape and gene expression during early stages of hematopoietic differentiation. *The EMBO Journal*, 39(23):e103957, 2020.

[76] F. Brochard and J.F. Lennon. Frequency spectrum of the flicker phenomenon in erythrocytes. *Journal de Physique*, 36(11):1035–1047, 1975.

[77] Timo Betz, Martin Lenz, Jean-François Joanny, and Cécile Sykes. ATP-dependent mechanics of red blood cells. *Proceedings of the National Academy of Sciences*, 106(36):15320–15325, September 2009.

[78] Mark J. Bowick, Andrej Košmrlj, David R. Nelson, and Rastko Sknepnek. Non-Hookean statistical mechanics of clamped graphene ribbons. *Physical Review B*, 95(10):104109, March 2017.

[79] Vasiliy Kantsler, Enrico Segre, and Victor Steinberg. Vesicle Dynamics in Time-Dependent Elongation Flow: Wrinkling Instability. *Physical Review Letters*, 99(17):178102, October 2007.

[80] Gašper Kokot, Hammad A. Faizi, Gerardo E. Pradillo, Alexey Snezhko, and Petia M. Vlahovska. Spontaneous self-propulsion and nonequilibrium shape fluctuations of a droplet enclosing active particles. *Communications Physics*, 5(1):91, December 2022.

[81] Aurelia R. Honerkamp-Smith, Francis G. Woodhouse, Vasily Kantsler, and Raymond E. Goldstein. Membrane viscosity determined from shear-driven flow in giant vesicles. *Phys. Rev. Lett.*, 111:038103, Jul 2013.

[82] Eyal Ben-Isaac, YongKeun Park, Gabriel Popescu, Frank L. H. Brown, Nir S. Gov, and Yair Shokef. Effective Temperature of Red-Blood-Cell Membrane Fluctuations. *Physical Review Letters*, 106(23):238103, June 2011.

[83] Fang-Yi Chu, Shannon C. Haley, and Alexandra Zidovska. On the origin of shape fluctuations of the cell nucleus. *Proceedings of the National Academy of Sciences*, 114(39):10338–10343, September 2017.

[84] Valeria Venturini, Fabio Pezzano, Frederic Català Castro, Hanna-Maria Häkkinen, Senda Jiménez-Delgado, Mariona Colomer-Rosell, Monica Marro, Queralt Tolosa-Ramon, Sonia Paz-López, Miguel A. Valverde, Julian Weghuber, Pablo Loza-Alvarez, Michael Krieg, Stefan Wieser, and Verena Ruprecht. The nucleus measures shape changes for cellular proprioception to control dynamic cell behavior. *Science*, 370(6514):eaba2644, October 2020.

[85] Paola Scaffidi and Tom Misteli. Lamin A-Dependent Nuclear Defects in Human Aging. *Science*, 312(5776):1059–1063, May 2006.

[86] Leslie C. Mounkes, Serguei Kozlov, Lidia Hernandez, Teresa Sullivan, and Colin L. Stewart. A progeroid syndrome in mice is caused by defects in A-type lamins. *Nature*, 423(6937):298–301, May 2003.

[87] Ueli Aebi, Julie Cohn, Loren Buhle, and Larry Gerace. The nuclear lamina is a meshwork of intermediate-type filaments. *Nature*, 323(6088):560–564, October 1986.

[88] Jan Lammerding, P. Christian Schulze, Tomosaburo Takahashi, Serguei Kozlov, Teresa Sullivan, Roger D. Kamm, Colin L. Stewart, and Richard T. Lee. Lamin A/C deficiency causes defective nuclear mechanics and mechanotransduction. *Journal of Clinical Investigation*, 113(3):370–378, February 2004.

[89] Caterina Strambio-De-Castillia, Mario Niepel, and Michael P. Rout. The nuclear pore complex: bridging nuclear transport and gene regulation. *Nature Reviews Molecular Cell Biology*, 11(7):490–501, July 2010.

[90] Kevin E. Knockenhauer and Thomas U. Schwartz. The Nuclear Pore Complex as a Flexible and Dynamic Gate. *Cell*, 164(6):1162–1171, March 2016.

[91] Andrew M. Hudson and Lynn Cooley. Methods for studying oogenesis. *Methods*, 68(1):207–217, June 2014.

[92] R. C. King, A. C. Rubinson, and R. F. Smith. Oogenesis in adult Drosophila melanogaster. *Growth*, 20(2):121–157, June 1956.

[93] John M. McLaughlin and Diana P. Bratu. Drosophila melanogaster Oogenesis: An Overview. In Diana P. Bratu and Gerard P. McNeil, editors, *Drosophila Oogenesis*, volume 1328, pages 1–20. Springer New York, New York, NY, 2015. Series Title: Methods in Molecular Biology.

[94] Rebecca Bastock and Daniel St Johnston. Drosophila oogenesis. *Current biology: CB*, 18(23):R1082–1087, dec 2008.

[95] Shalina Mahajan-Miklos and Lynn Cooley. Intercellular Cytoplasm Transport during Drosophila Oogenesis. *Developmental Biology*, 165(2):336–351, October 1994.

[96] H. Lin and A. C. Spradling. Germline stem cell division and egg chamber development in transplanted Drosophila germaria. *Developmental Biology*, 159(1):140–152, September 1993.

[97] Amit Tzur, Ran Kafri, Valerie S. LeBleu, Galit Lahav, and Marc W. Kirschner. Cell Growth and Size Homeostasis in Proliferating Animal Cells. *Science*, 325(5937):167–171, July 2009.

[98] Ashraf N. Malhas and David J. Vaux. Nuclear Envelope Invaginations and Cancer. In Eric C. Schirmer and Jose I. De Las Heras, editors, *Cancer Biology and the Nuclear Envelope*, volume 773, pages 523–535. Springer New York, New York, NY, 2014.

[99] Mark Fricker, Michael Hollinshead, Nick White, and David Vaux. Interphase Nuclei of Many Mammalian Cell Types Contain Deep, Dynamic, Tubular Membrane-bound Invaginations of the Nuclear Envelope. *Journal of Cell Biology*, 136(3):531–544, February 1997.

[100] Dongyu Jia, Qiuping Xu, Qian Xie, Washington Mio, and Wu-Min Deng. Automatic stage identification of Drosophila egg chamber based on DAPI images. *Scientific Reports*, 6(1):18850, May 2016.

[101] Vanessa Weichselberger, Patrick Dondl, and Anne-Kathrin Classen. Eya-controlled affinity between cell lineages drives tissue self-organization during *Drosophila* oogenesis. preprint, Developmental Biology, July 2022.

[102] Jasmin Imran Alsous, Paul Villoutreix, Alexander M. Berezhkovskii, and Stanislav Y. Shvartsman. Collective Growth in a Small Cell Network. *Current Biology*, 27(17):2670–2676.e4, September 2017.

[103] Johannes Schindelin, Ignacio Arganda-Carreras, Erwin Frise, Verena Kaynig, Mark Longair, Tobias Pietzsch, Stephan Preibisch, Curtis Rueden, Stephan Saalfeld, Benjamin Schmid, Jean-Yves Tinevez, Daniel James White, Volker

Hartenstein, Kevin Eliceiri, Pavel Tomancak, and Albert Cardona. Fiji: an open-source platform for biological-image analysis. *Nature Methods*, 9(7):676–682, July 2012.

[104] David Legland, Ignacio Arganda-Carreras, and Philippe Andrey. MorphoLibJ: integrated library and plugins for mathematical morphology with ImageJ. *Bioinformatics*, 32(22):3532–3534, July 2016.

[105] A. G. Zilman and R. Granek. Undulations and Dynamic Structure Factor of Membranes. *Physical Review Letters*, 77(23):4788–4791, December 1996.

[106] Jovana Andrejevic, Lisa M. Lee, Shmuel M. Rubinstein, and Chris H. Rycroft. A model for the fragmentation kinetics of crumpled thin sheets. *Nature Communications*, 12(1):1470, December 2021.

[107] T. A. Witten. Stress focusing in elastic sheets. *Reviews of Modern Physics*, 79(2):643–675, April 2007.

[108] Guillaume Gueguen, Nicolas Destainville, and Manoel Manghi. Fluctuation tension and shape transition of vesicles: renormalisation calculations and Monte Carlo simulations. *Soft Matter*, 13(36):6100–6117, 2017.

[109] Farshid Guilak, John R. Tedrow, and Rainer Burgkart. Viscoelastic Properties of the Cell Nucleus. *Biochemical and Biophysical Research Communications*, 269(3):781–786, March 2000.

[110] Kris Noel Dahl, Samuel M. Kahn, Katherine L. Wilson, and Dennis E. Discher. The nuclear envelope lamina network has elasticity and a compressibility limit suggestive of a molecular shock absorber. *Journal of Cell Science*, 117(20):4779–4786, September 2004.

[111] Balázs Enyedi and Philipp Niethammer. Nuclear membrane stretch and its role in mechanotransduction. *Nucleus*, 8(2):156–161, March 2017.

[112] J. Pécréaux, H.-G. Döbereiner, J. Prost, J.-F. Joanny, and P. Bassereau. Refined contour analysis of giant unilamellar vesicles. *The European Physical Journal E*, 13(3):277–290, March 2004.

[113] K. S. Novoselov, A. K. Geim, S. V. Morozov, D. Jiang, Y. Zhang, S. V. Dubonos, I. V. Grigorieva, and A. A. Firsov. Electric Field Effect in Atomically Thin Carbon Films. *Science*, 306(5696):666–669, October 2004.

[114] Lorenz Baumgarten and Jan Kierfeld. Buckling of thermally fluctuating spherical shells: Parameter renormalization and thermally activated barrier crossing. *Physical Review E*, 97(5):052801, May 2018.

[115] Christoph F. Schmidt, Karel Svoboda, Ning Lei, Irena B. Petsche, Lonny E. Berman, Cyrus R. Safinya, and Gary S. Grest. Existence of a Flat Phase in Red Cell Membrane Skeletons. *Science*, 259(5097):952–955, February 1993.

[116] Alla Yalonetskaya, Albert A. Mondragon, Zackary J. Hintze, Susan Holmes, and Kimberly McCall. Nuclear degradation dynamics in a nonapoptotic programmed cell death. *Cell Death & Differentiation*, 27(2):711–724, February 2020.

[117] Joe Swift, Irena L. Ivanovska, Amnon Buxboim, Takamasa Harada, P. C. Dave P. Dingal, Joel Pinter, J. David Pajerowski, Kyle R. Spinler, Jae-Won Shin, Manorama Tewari, Florian Rehfeldt, David W. Speicher, and Dennis E. Discher. Nuclear Lamin-A Scales with Tissue Stiffness and Enhances Matrix-Directed Differentiation. *Science*, 341(6149):1240104, August 2013.

[118] Sandra R Schulze, Beatrice Curio-Penny, Yuhong Li, Reza A Imani, Lena Rydberg, Pamela K Geyer, and Lori L Wallrath. Molecular Genetic Analysis of the Nested *Drosophila melanogaster* Lamin C Gene. *Genetics*, 171(1):185–196, September 2005.

[119] D. Riemer, N. Stuurman, M. Berrios, C. Hunter, P.A. Fisher, and K. Weber. Expression of Drosophila lamin C is developmentally regulated: analogies with vertebrate A-type lamins. *Journal of Cell Science*, 108(10):3189–3198, October 1995.

[120] Vipin Agrawal, Vikash Pandey, and Dhrubaditya Mitra. Active buckling of pressurized spherical shells : Monte carlo simulation. *arXiv*, 2206:14172, 2022.

[121] Brato Chakrabarti, Yanan Liu, John LaGrone, Ricardo Cortez, Lisa Fauci, Olivia du Roure, David Saintillan, and Anke Lindner. Flexible filaments buckle into helicoidal shapes in strong compressional flows. *Nature Physics*, 16(6):689–694, June 2020.

[122] Bastien Loubet, Udo Seifert, and Michael Andersen Lomholt. Effective tension and fluctuations in active membranes. *Physical Review E*, 85(3):031913, March 2012.

[123] Hanumantha Rao Vutukuri, Masoud Hoore, Clara Abaurrea-Velasco, Lennard van Buren, Alessandro Dutto, Thorsten Auth, Dmitry A. Fedosov, Gerhard Gompper, and Jan Vermant. Active particles induce large shape deformations in giant lipid vesicles. *Nature*, 586(7827):52–56, October 2020.

[124] A. R. Bausch and K. Kroy. A bottom-up approach to cell mechanics. *Nature Physics*, 2(4):231–238, April 2006.

[125] Bernhard Hampoelz, Yannick Azou-Gros, Roxane Fabre, Olga Markova, Pierre-Henri Puech, and Thomas Lecuit. Microtubule-induced nuclear envelope fluctuations control chromatin dynamics in *Drosophila* embryos. *Development*, 138(16):3377–3386, August 2011.

[126] Brian D. Cosgrove, Claudia Loebel, Tristan P. Driscoll, Tonia K. Tsinman, Eric N. Dai, Su-Jin Heo, Nathaniel A. Dyment, Jason A. Burdick, and Robert L.

Mauck. Nuclear envelope wrinkling predicts mesenchymal progenitor cell mechano-response in 2D and 3D microenvironments. *Biomaterials*, 270:120662, March 2021.

[127] Alberto Elosegui-Artola, Ion Andreu, Amy E.M. Beedle, Ainhoa Lezamiz, Marina Uroz, Anita J. Kosmalska, Roger Oria, Jenny Z. Kechagia, Palma Rico-Lastres, Anabel-Lise Le Roux, Catherine M. Shanahan, Xavier Trepat, Daniel Navajas, Sergi Garcia-Manyes, and Pere Roca-Cusachs. Force Triggers YAP Nuclear Entry by Regulating Transport across Nuclear Pores. *Cell*, 171(6):1397–1410.e14, November 2017.

[128] Ekta Makhija, D. S. Jokhun, and G. V. Shivashankar. Nuclear deformability and telomere dynamics are regulated by cell geometric constraints. *Proceedings of the National Academy of Sciences*, 113(1):E32–E40, 2016.

[129] Daniel J. Kelpsch, Christopher M. Groen, Tiffany N. Fagan, Sweta Sudhir, and Tina L. Tootle. Fascin regulates nuclear actin during *Drosophila* oogenesis. *Molecular Biology of the Cell*, 27(19):2965–2979, October 2016.

[130] George Dialynas, Sean Speese, Vivian Budnik, Pamela K. Geyer, and Lori L. Wallrath. The role of *Drosophila* Lamin C in muscle function and gene expression. *Development*, 137(18):3067–3077, September 2010.

[131] Shigenori Nonaka, Hidetaka Shiratori, Yukio Saijoh, and Hiroshi Hamada. Determination of left–right patterning of the mouse embryo by artificial nodal flow. *Nature*, 418(6893):96–99, 2002.

[132] Albrecht G. Kramer-Zucker, Felix Olale, Courtney J. Haycraft, Bradley K. Yoder, Alexander F. Schier, and Iain A. Drummond. Cilia-driven fluid flow in the zebrafish pronephros, brain and Kupffer's vesicle is required for normal organogenesis. *Development*, 132(8):1907–1921, apr 2005. Publisher: The Company of Biologists Ltd Section: Research Article.

[133] Sujoy Ganguly, Lucy S. Williams, Isabel M. Palacios, and Raymond E. Goldstein. Cytoplasmic streaming in Drosophila oocytes varies with kinesin activity and correlates with the microtubule cytoskeleton architecture. *Proceedings of the National Academy of Sciences of the United States of America*, 109(38):15109, sep 2012.

[134] Bing He, Konstantin Doubrovinski, Oleg Polyakov, and Eric Wieschaus. Apical constriction drives tissue-scale hydrodynamic flow to mediate cell elongation. *Nature*, 508(7496):392–396, apr 2014.

[135] Melissa E. Pepling, Margaret de Cuevas, and Allan C. Spradling. Germline cysts: a conserved phase of germ cell development? *Trends in Cell Biology*, 9(7):257–262, jul 1999. Publisher: Elsevier.

[136] William H. Telfer. Development and Physiology of the Oöcyte-Nurse Cell Syncytium. In J. E. Treherne, M. J. Berridge, and V. B. Wigglesworth, editors, *Advances in Insect Physiology*, volume 11, pages 223–319. Academic Press, jan 1975.

[137] Victoria K. Jenkins, Allison K. Timmons, and Kimberly McCall. Diversity of cell death pathways: insight from the fly ovary. *Trends in Cell Biology*, 23(11):567–574, nov 2013.

[138] Lei Lei and Allan C. Spradling. Mouse oocytes differentiate through organelle enrichment from sister cyst germ cells. *Science (New York, N.Y.)*, 352(6281):95–99, apr 2016.

[139] Robert C. King. *Ovarian development in Drosophila melanogaster*. Academic Press, New York, 1970.

[140] Allan Spradling. Developmental genetics of oogenesis. *The Development of Drosophila Melanogaster*, 1993. Publisher: Cold Spring Harbor Laboratory Press.

[141] W. E. Theurkauf and T. I. Hazelrigg. In vivo analyses of cytoplasmic transport and cytoskeletal organization during Drosophila oogenesis: characterization of a multi-step anterior localization pathway. *Development*, 125(18):3655–3666, September 1998.

[142] P. Jordan and R. Karess. Myosin light chain-activating phosphorylation sites are required for oogenesis in Drosophila. *The Journal of Cell Biology*, 139(7):1805–1819, December 1997.

[143] Herwigo Gutzeit and Roswitha Koppa. Time-lapse film analysis of cytoplasmic streaming during late oogenesis of Drosophila. *Development*, 67(1):101–111, February 1982.

[144] Shalina Mahajan-Miklos and Lynn Cooley. Intercellular cytoplasm transport during drosophila oogenesis. *Developmental biology*, 165(2):336–351, 1994.

[145] S. Wheatley, S. Kulkarni, and R. Karess. Drosophila nonmuscle myosin II is required for rapid cytoplasmic transport during oogenesis and for axial nuclear migration in early embryos. *Development*, 121(6):1937–1946, June 1995.

[146] K. A. Edwards and D. P. Kiehart. Drosophila nonmuscle myosin II has multiple essential roles in imaginal disc and egg chamber morphogenesis. *Development*, 122(5):1499–1511, May 1996.

[147] William M. Bement, Marcin Leda, Alison M. Moe, Angela M. Kita, Matthew E. Larson, Adriana E. Golding, Courtney Pfeuti, Kuan-Chung Su, Ann L. Miller, Andrew B. Goryachev, and George von Dassow. Activator–inhibitor coupling between Rho signalling and actin assembly makes the cell cortex an excitable medium. *Nature Cell Biology*, 17(11):1471–1483, November 2015.

[148] Victoria E. Deneke, Alberto Puliafito, Daniel Krueger, Avaneesh V. Narla, Alessandro De Simone, Luca Primo, Massimo Vergassola, Stefano De Renzis, and Stefano Di Talia. Self-Organized Nuclear Positioning Synchronizes the Cell Cycle in Drosophila Embryos. *Cell*, 177(4):925–941.e17, 2019.

[149] Johanna Bischof, Christoph A. Brand, Kálmán Somogyi, Imre Májer, Sarah Thome, Masashi Mori, Ulrich S. Schwarz, and Péter Lénárt. A cdk1 gradient guides surface contraction waves in oocytes. *Nature Communications*, 8(1):849, October 2017.

[150] N. T. Chartier, A. Mukherjee, J. Pfanzelter, S. Fürthauer, B. T. Larson, A. W. Fritsch, M. Kreysing, F. Jülicher, and S. W. Grill. A hydraulic instability drives the cell death decision in the nematode germline. *bioRxiv*, page 2020.05.30.125864, June 2020.

[151] J. David and J. Merle. A re-evaluation of the duration of egg chamber stages in oogenesis of drosophila melanogaster. *Dros. Inf. Serv.*, 1968.

[152] G. T. Charras. A short history of blebbing. *Journal of Microscopy*, 231(3):466–478, 2008.

[153] Guillaume T. Charras, Margaret Coughlin, Timothy J. Mitchison, and L. Mahadevan. Life and times of a cellular bleb. *Biophysical Journal*, 94(5):1836–1853, March 2008.

[154] Jasmin Imran Alsous, Paul Villoutreix, Norbert Stoop, Stanislav Y. Shvartsman, and Jörn Dunkel. Entropic effects in cell lineage tree packings. *Nature physics*, 14(10):1016–1021, October 2018.

[155] Jasmin Imran Alsous, Paul Villoutreix, Alexander M. Berezhkovskii, and Stanislav Y. Shvartsman. Collective Growth in a Small Cell Network. *Current Biology*, 27(17):2670–2676.e4, September 2017.

[156] E. H. Brown and R. C. King. Studies on the Events Resulting in the Formation of an Egg Chamber in Drosophila Melanogaster. *Growth*, 28:41–81, March 1964.

[157] D. R. Merritt and F. Weinhaus. The pressure curve for a rubber balloon. *American Journal of Physics*, 46(10):976–977, October 1978.

[158] E. Verron, R. E. Khayat, A. Derdouri, and B. Peseux. Dynamic inflation of hyperelastic spherical membranes. *Journal of Rheology*, 43(5):1083–1097, August 1999.

[159] N. K. Tu and A. M. Gusak. Appendix a: Laplace pressure in nonspherical nanoparticle. In *Kinetics in Nanoscale Materials*, pages 280–281. Wiley, New Jersey, 2 edition, 2014.

[160] Jinrong Hu, Shenbao Chen, Wenhui Hu, Shouqin Lü, and Mian Long. Mechanical Point Loading Induces Cortex Stiffening and Actin Reorganization. *Biophysical Journal*, 117(8):1405–1418, October 2019.

[161] Konstantin Doubrovinski, Michael Swan, Oleg Polyakov, and Eric F. Wieschaus. Measurement of cortical elasticity in Drosophila melanogaster embryos using ferrofluids. *Proceedings of the National Academy of Sciences*, 114(5):1051–1056, January 2017.

[162] Hubert M. James and Eugene Guth. Theory of the Elastic Properties of Rubber. *The Journal of Chemical Physics*, 11(10):455–481, October 1943.

[163] R. Vargas-Pinto, H. Gong, A. Vahabikashi, and M. Johnson. The Effect of the Endothelial Cell Cortex on Atomic Force Microscopy Measurements. *Biophysical Journal*, 105(2):300–309, July 2013.

[164] Thomas Lecuit and Pierre-François Lenne. Cell surface mechanics and the control of cell shape, tissue patterns and morphogenesis. *Nature Reviews Molecular Cell Biology*, 8(8):633–644, August 2007.

[165] C. E. Morris and U. Homann. Cell surface area regulation and membrane tension. *The Journal of Membrane Biology*, 179(2):79–102, January 2001.

[166] Julien Chlasta, Pascale Milani, Gaël Runel, Jean-Luc Duteyrat, Leticia Arias, Laurie-Anne Lamiré, Arezki Boudaoud, and Muriel Grammont. Variations in basement membrane mechanics are linked to epithelial morphogenesis. *Development*, page dev.152652, January 2017.

[167] Joseph Jose Thottacherry, Anita Joanna Kosmalska, Amit Kumar, Amit Singh Vishen, Alberto Elosegui-Artola, Susav Pradhan, Sumit Sharma, Parvinder P. Singh, Marta C. Guadamillas, Natasha Chaudhary, Ram Vishwakarma, Xavier Trepat, Miguel A. Del Pozo, Robert G. Parton, Madan Rao, Pramod Pullarkat, Pere Roca-Cusachs, and Satyajit Mayor. Mechanochemical feedback control of dynamin independent endocytosis modulates membrane tension in adherent cells. *Nature Communications*, 9(1):4217, October 2018.

[168] Nicolas Perez Gonzalez, Jiaxiang Tao, Nash D. Rochman, Dhruv Vig, Evelyn Chiu, Denis Wirtz, and Sean X. Sun. Cell tension and mechanical regulation of cell volume. *Molecular Biology of the Cell*, 29(21):0–0, October 2018.

[169] David J Acheson. *Elementary fluid dynamics*. Clarendon Press, Oxford, 1990.

[170] Laurie-Anne Lamiré, Pascale Milani, Gaël Runel, Annamaria Kiss, Leticia Arias, Blandine Vergier, Stève de Bossoreille, Pradeep Das, David Cluet, Arezki Boudaoud, and Muriel Grammont. Gradient in cytoplasmic pressure in germline cells controls overlying epithelial cell morphogenesis. *PLOS Biology*, 18(11):e3000940, November 2020.

[171] L. G. Tilney, M. S. Tilney, and G. M. Guild. Formation of actin filament bundles in the ring canals of developing Drosophila follicles. *The Journal of Cell Biology*, 133(1):61–74, April 1996.

[172] Sven Huelsmann, Nina Rintanen, Ritika Sethi, Nicholas H. Brown, and Jari Ylänne. Evidence for the mechanosensor function of filamin in tissue development. *Scientific Reports*, 6(1):32798, September 2016.

[173] M. Krieg, Y. Arboleda-Estudillo, P.-H. Puech, J. Käfer, F. Graner, D. J. Müller, and C.-P. Heisenberg. Tensile forces govern germ-layer organization in zebrafish. *Nature Cell Biology*, 10(4):429–436, April 2008.

[174] R. E. Karess, X. J. Chang, K. A. Edwards, S. Kulkarni, I. Aguilera, and D. P. Kiehart. The regulatory light chain of nonmuscle myosin is encoded by spaghetti-squash, a gene required for cytokinesis in Drosophila. *Cell*, 65(7):1177–1189, June 1991.

[175] Claudia G. Vasquez, Mike Tworoger, and Adam C. Martin. Dynamic myosin phosphorylation regulates contractile pulses and tissue integrity during epithelial morphogenesis. *Journal of Cell Biology*, 206(3):435–450, August 2014.

[176] Frank M. Mason, Shicong Xie, Claudia G. Vasquez, Michael Tworoger, and Adam C. Martin. RhoA GTPase inhibition organizes contraction during epithelial morphogenesis. *Journal of Cell Biology*, 214(5):603–617, August 2016.

[177] Jonathan B. Michaux, François B. Robin, William M. McFadden, and Edwin M. Munro. Excitable RhoA dynamics drive pulsed contractions in the early C. elegans embryo. *Journal of Cell Biology*, 217(12):4230–4252, October 2018.

[178] Johannes L. Bos, Holger Rehmann, and Alfred Wittinghofer. GEFs and GAPs: critical elements in the control of small G proteins. *Cell*, 129(5):865–877, June 2007.

[179] D. R. Cook, K. L. Rossman, and C. J. Der. Rho guanine nucleotide exchange factors: regulators of Rho GTPase activity in development and disease. *Oncogene*, 33(31):4021–4035, July 2014.

[180] K. Kimura, M. Ito, M. Amano, K. Chihara, Y. Fukata, M. Nakafuku, B. Yamamori, J. Feng, T. Nakano, K. Okawa, A. Iwamatsu, and K. Kaibuchi. Regulation of myosin phosphatase by Rho and Rho-associated kinase (Rho-kinase). *Science (New York, N.Y.)*, 273(5272):245–248, July 1996.

[181] C. G. Winter, B. Wang, A. Ballew, A. Royou, R. Karess, J. D. Axelrod, and L. Luo. Drosophila Rho-associated kinase (Drok) links Frizzled-mediated planar cell polarity signaling to the actin cytoskeleton. *Cell*, 105(1):81–91, April 2001.

[182] M. Amano, M. Ito, K. Kimura, Y. Fukata, K. Chihara, T. Nakano, Y. Matsuura, and K. Kaibuchi. Phosphorylation and activation of myosin by Rho-associated

kinase (Rho-kinase). *The Journal of Biological Chemistry*, 271(34):20246–20249, August 1996.

[183] Sven Huelsmann, Jari Ylänne, and Nicholas H. Brown. Filopodia-like Actin Cables Position Nuclei in Association with Perinuclear Actin in Drosophila Nurse Cells. *Developmental Cell*, 26(6):604–615, September 2013.

[184] Guillaume Salbreux, Guillaume Charras, and Ewa Paluch. Actin cortex mechanics and cellular morphogenesis. *Trends in Cell Biology*, 22(10):536–545, oct 2012.

[185] Adam C. Martin, Matthias Kaschube, and Eric F. Wieschaus. Pulsed contractions of an actin–myosin network drive apical constriction. *Nature*, 457(7228):495–499, January 2009.

[186] Scott F Gilbert and Michael J. F Barresi. *Developmental biology.* Oxford University Press, Oxford, 2016.

[187] Lilianna Solnica-Krezel. Conserved patterns of cell movements during vertebrate gastrulation. *Current Biology*, 15(6):R213–R228, 2005.

[188] Ernst H K Stelzer. Light-sheet fluorescence microscopy for quantitative biology. *Nat. Meth.*, 12(1):23–26, 2015.

[189] Rory M Power and Jan Huisken. A guide to light-sheet fluorescence microscopy for multiscale imaging. *Nat Meth*, 14(4):360–373, 2017.

[190] Raimo Hartmann, Praveen K. Singh, Philip Pearce, Rachel Mok, Boya Song, Francisco Díaz-Pascual, Jörn Dunkel, and Knut Drescher. Emergence of three-dimensional order and structure in growing biofilms. *Nat. Phys.*, 15:251–256, 2019.

[191] B. Levy. Laplace-beltrami eigenfunctions towards an algorithm that "understands" geometry. In *IEEE International Conference on Shape Modeling and Applications 2006 (SMI'06)*, pages 13–13, 2006.

[192] S. L. Brunton, J. L. Proctor, and J. N. Kutz. Discovering governing equations from data by sparse identification of nonlinear dynamical systems. *Proc. Natl. Acad. Sci. U.S.A.*, 113(15):3932–3937, 2016.

[193] Christopher Rackauckas, Yingbo Ma, Julius Martensen, Collin Warner, Kirill Zubov, Rohit Supekar, Dominic Skinner, Ali Ramadhan, and Alan Edelman. Universal differential equations for scientific machine learning, 2021.

[194] Mark Kac. Can one hear the shape of a drum? *Am. Math. Mon.*, 73(4):1–23, 1966.

[195] Nigel Goldenfeld and Carl Woese. Life is physics: Evolution as a collective phenomenon far from equilibrium. *Annu. Rev. Condens. Matter Phys.*, 2(1):375–399, 2011.

[196] Vasily Kantsler and Raymond E. Goldstein. Fluctuations, dynamics, and the stretch-coil transition of single actin filaments in extensional flows. *Phys. Rev. Lett.*, 108(3):038103, 2012.

[197] Basanta Bhaduri, Murat Yessenov, and Ayman F. Abouraddy. Anomalous refraction of optical spacetime wave packets. *Nat. Photonics*, 14(7):416–421, 2020.

[198] T. T. Soong and Mircea Grigoriu. Random vibration of mechanical and structural systems. *NASA STI/Recon Technical Report A*, 93:14690, 1993.

[199] Nasser Heydari, Panayiotis Diplas, J. Nathan Kutz, and Soheil Sadeghi Eshkevari. Modal analysis of turbulent flow near an inclined bank–longitudinal structure junction. *J. Hydraul. Eng.*, 147(3):04020100, 2021.

[200] T A. Driscoll, N Hale, and L N. Trefethen, editors. *Chebfun Guide.* Pafnuty Publications, Oxford, 2014.

[201] Daniel Fortunato, Nicholas Hale, and Alex Townsend. The ultraspherical spectral element method. *J. Comp. Phys.*, 436:110087, 2021.

[202] Peter J. Schmid. Dynamic mode decomposition of numerical and experimental data. *J. Fluid Mech.*, 656:5–28, 2010.

[203] Jonathan H Tu, Clarence W Rowley, Dirk M Luchtenburg, Steven L Brunton, and J Nathan Kutz. On dynamic mode decomposition: Theory and applications. *J Comput. Dyn.*, 1(2):391, 2014.

[204] J. C. Slater and G. F. Koster. Simplified lcao method for the periodic potential problem. *Phys. Rev.*, 94(6):1498–1524, 1954.

[205] E. T. Jaynes and F. W. Cummings. Comparison of quantum and semiclassical radiation theories with application to the beam maser. *Proc. IEEE*, 51(1):89–109, 1963.

[206] Andrey N. Kolmogorov. The local structure of turbulence in incompressible viscous fluid for very large Reynolds numbers. *C. R. (Dokl.) Acad. sci. URSS*, 30:301–305, 1941.

[207] Xueying Wang, Hong-Yan Shih, and Nigel Goldenfeld. Emergence of puffs, weak and strong slugs from a stochastic predator-prey model for transitional turbulence with stream-wise shear interactions. In *Bulletin of the American Physical Society.* American Physical Society, 2021.

[208] R. H. Kraichnan and D. Montgomery. Two-dimensional turbulence. *Rep. Progr. Phys.*, 43(5):547–619, 1980.

[209] Stephen B. Pope. *The scales of turbulent motion*, page 182–263. Cambridge University Press, 2000.

[210] J. Dunkel, S. Heidenreich, K. Drescher, H. H. Wensink, M. Bär, and R. E. Goldstein. Fluid dynamics of bacterial turbulence. *Phys. Rev. Lett.*, 110:228102, 2013.

[211] V. Bratanov, F. Jenko, and Erwin Frey. New class of turbulence in active fluids. *Proc. Natl. Acad. Sci. U.S.A.*, 112(49):15048–15053, 2015.

[212] Rajesh Ramaswamy and Frank Jülicher. Activity induces traveling waves, vortices and spatiotemporal chaos in a model actomyosin layer. *Sci. Rep.*, 6(1):20838, 2016.

[213] Ricard Alert, Jean-François Joanny, and Jaume Casademunt. Universal scaling of active nematic turbulence. *Nat. Phys.*, 16(6):682–688, 2020.

[214] M. C. Marchetti, J. F. Joanny, S. Ramaswamy, T. B. Liverpool, J. Prost, Madan Rao, and R. Aditi Simha. Hydrodynamics of soft active matter. *Rev Mod Phys*, 85:1143–1189, 2013.

[215] Hitoshi Morita, Silvia Grigolon, Martin Bock, S. F. Gabriel Krens, Guillaume Salbreux, and Carl-Philipp Heisenberg. The physical basis of coordinated tissue spreading in zebrafish gastrulation. *Dev. Cell*, 40(4):354–366.e4, 2017.

[216] Laurel A. Rohde and Carl-Philipp Heisenberg. Zebrafish gastrulation: Cell movements, signals, and mechanisms. In *International Review of Cytology*, volume 261, pages 159–192. Academic Press, 2007.

[217] G.B. Arfken, H.J. Weber, and F.E. Harris. *Mathematical Methods for Physicists: A Comprehensive Guide.* Elsevier Science, 2013.

[218] Vernon D. Sandberg. Tensor spherical harmonics on S2 and S3 as eigenvalue problems. *J. Math. Phys.*, 19(12):2441–2446, 1978.

[219] John C Mason and David C Handscomb. *Chebyshev polynomials.* CRC press, 2002.

[220] Rohit Supekar, Boya Song, Alasdair Hastewell, Gary P. T. Choi, Alexander Mietke, and Jörn Dunkel. Learning hydrodynamic equations for active matter from particle simulations and experiments, 2021.

[221] Elias M. Stein and Rami Shakarchi. *Fourier Analysis: An Introduction.* Princeton University Press, 2011.

[222] Alexander Mietke, V. Jemseena, K. Vijay Kumar, Ivo F. Sbalzarini, and Frank Jülicher. Minimal model of cellular symmetry breaking. *Phys. Rev. Lett.*, 123:188101, 2019.

[223] André Scholich, Simon Syga, Hernán Morales-Navarrete, Fabián Segovia-Miranda, Hidenori Nonaka, Kirstin Meyer, Walter de Back, Lutz Brusch, Yannis

Kalaidzidis, Marino Zerial, Frank Jülicher, and Benjamin M. Friedrich. Quantification of nematic cell polarity in three-dimensional tissues. *PLOS Computational Biology*, 16(12):1–22, 2020.

[224] H. E. Çetingül, B. Afsari, and R. Vidal. An algebraic solution to rotation recovery in hardi from correspondences of orientation distribution functions. In *2012 9th IEEE International Symposium on Biomedical Imaging (ISBI)*, pages 38–41, 2012.

[225] Evan Schwab, H. Ertan Çetingül, Bijan Afsari, Michael A. Yassa, and René Vidal. Rotation invariant features for hardi. In James C. Gee, Sarang Joshi, Kilian M. Pohl, William M. Wells, and Lilla Zöllei, editors, *Information Processing in Medical Imaging*, pages 705–717, Berlin, Heidelberg, 2013. Springer Berlin Heidelberg.

[226] Randall D. Kamien. The geometry of soft materials: a primer. *Rev. Mod. Phys.*, 74:953–971, 2002.

[227] Amin Doostmohammadi, Sumesh P. Thampi, and Julia M. Yeomans. Defect-mediated morphologies in growing cell colonies. *Phys. Rev. Lett.*, 117(4):048102, 2016.

[228] Thuan Beng Saw, Amin Doostmohammadi, Vincent Nier, Leyla Kocgozlu, Sumesh Thampi, Yusuke Toyama, Philippe Marcq, Chwee Teck Lim, Julia M. Yeomans, and Benoit Ladoux. Topological defects in epithelia govern cell death and extrusion. *Nature*, 544(7649):212–216, 2017.

[229] Pau Guillamat, Carles Blanch-Mercader, Karsten Kruse, and Aurélien Roux. Integer topological defects organize stresses driving tissue morphogenesis. *bioRxiv*, 2020.

[230] Katherine Copenhagen, Ricard Alert, Ned S Wingreen, and Joshua W Shaevitz. Topological defects promote layer formation in Myxococcus xanthus colonies. *Nat. Phys.*, 17(2):211–215, 2021.

[231] O. J. Meacock, A. Doostmohammadi, K. R. Foster, J. M. Yeomans, and W. M. Durham. Bacteria solve the problem of crowding by moving slowly. *Nat. Phys.*, 17(2):205–210, 2021.

[232] Yonit Maroudas-Sacks, Liora Garion, Lital Shani-Zerbib, Anton Livshits, Erez Braun, and Kinneret Keren. Topological defects in the nematic order of actin fibres as organization centres of Hydra morphogenesis. *Nat. Phys.*, 17(2):251–259, 2021.

[233] Rastko Sknepnek and Silke Henkes. Active swarms on a sphere. *Phys. Rev. E*, 91:022306, 2015.

[234] Yaouen Fily, Aparna Baskaran, and Michael F. Hagan. Active particles on curved surfaces, 2016.

[235] Pavel Castro-Villarreal and Francisco J. Sevilla. Active motion on curved surfaces. *Phys. Rev. E*, 97:052605, 2018.

[236] Edouard Hannezo and Carl-Philipp Heisenberg. Mechanochemical feedback loops in development and disease. *Cell*, 178(1):12–25, 2019.

[237] Stefan Münster, Akanksha Jain, Alexander Mietke, Anastasios Pavlopoulos, Stephan W Grill, and Pavel Tomancak. Attachment of the blastoderm to the vitelline envelope affects gastrulation of insects. *Nature*, 568(7752):395–399, 2019.

[238] Raphaël Etournay, Marko Popović, Matthias Merkel, Amitabha Nandi, Corinna Blasse, Benoît Aigouy, Holger Brandl, Gene Myers, Guillaume Salbreux, Frank Jülicher, and Suzanne Eaton. Interplay of cell dynamics and epithelial tension during morphogenesis of the *Drosophila* pupal wing. *eLife*, 4:e07090, 2015.

[239] Edouard Hannezo, Bo Dong, Pierre Recho, Jean-François Joanny, and Shigeo Hayashi. Cortical instability drives periodic supracellular actin pattern formation in epithelial tubes. *Proc. Natl. Acad. Sci. U.S.A.*, 112(28):8620–8625, 2015.

[240] Sebastian J Streichan, Matthew F Lefebvre, Nicholas Noll, Eric F Wieschaus, and Boris I Shraiman. Global morphogenetic flow is accurately predicted by the spatial distribution of myosin motors. *eLife*, 7:e27454, 2018.

[241] R G Barrera, G A Estevez, and J Giraldo. Vector spherical harmonics and their application to magnetostatics. *Eur. J. Phys.*, 6(4):287–294, 1985.

[242] Philipp J Keller, Annette D Schmidt, Anthony Santella, Khaled Khairy, Zhirong Bao, Joachim Wittbrodt, and Ernst H K Stelzer. Fast, high-contrast imaging of animal development with scanned light sheet–based structured-illumination microscopy. *Nat. Methods*, 7(8):637–642, 2010.

[243] Loïc A Royer, William C Lemon, Raghav K Chhetri, Yinan Wan, Michael Coleman, Eugene W Myers, and Philipp J Keller. Adaptive light-sheet microscopy for long-term, high-resolution imaging in living organisms. *Nat. Biotechnol.*, 34(12):1267–1278, 2016.

[244] Pierre François Lenne, Ed Munro, Idse Heemskerk, Aryeh Warmflash, Laura Bocanegra-Moreno, Kasumi Kishi, Anna Kicheva, Yuchen Long, Antoine Fruleux, Arezki Boudaoud, Timothy E Saunders, Paolo Caldarelli, Arthur Michaut, Jerome Gros, Yonit Maroudas-Sacks, Kinneret Keren, Edouard Hannezo, Zev J Gartner, Benjamin Stormo Stormo, Amy Gladfelter Gladfelter, Alan Rodrigues, Amy Shyer, Nicolas Minc, Jean-Léon Maître, Stefano Di Talia, Bassma Khamaisi, David Sprinzak, and Sham Tlili. Roadmap on multiscale coupling of biochemical and mechanical signals during development. *Phys. Biol.*, 2020.

[245] Raymond E. Goldstein and Jan-Willem Van De Meent. A physical perspective on cytoplasmic streaming. *Interface Focus*, 5(4):20150030, August 2015.

[246] Brato Chakrabarti, Michael J. Shelley, and Sebastian Fürthauer. Collective Motion and Pattern Formation in Phase-Synchronizing Active Fluids. *Physical Review Letters*, 130(12):128202, March 2023.

[247] Manon C. Wigbers, Tzer Han Tan, Fridtjof Brauns, Jinghui Liu, S. Zachary Swartz, Erwin Frey, and Nikta Fakhri. A hierarchy of protein patterns robustly decodes cell shape information. *Nature Physics*, 17(5):578–584, May 2021.

[248] Alexander E. Cohen, Alasdair D. Hastewell, Sreeparna Pradhan, Steven W. Flavell, and Jorn Dunkel. Schrodinger dynamics and berry phase of undulatory locomotion, 2023.

[249] Suraj Shankar, Mark J. Bowick, and M. Cristina Marchetti. Topological Sound and Flocking on Curved Surfaces. *Physical Review X*, 7(3):031039, September 2017.

[250] Noah P. Mitchell and Dillon J. Cislo. TubULAR: Tracking *in toto* deformations of dynamic tissues via constrained maps. preprint, Developmental Biology, April 2022.

[251] Herbert H.H. Homeier and E.Otto Steinborn. Some properties of the coupling coefficients of real spherical harmonics and their relation to Gaunt coefficients. *Journal of Molecular Structure: THEOCHEM*, 368:31–37, September 1996.

[252] Maxim O. Lavrentovich, Eric M. Horsley, Asja Radja, Alison M. Sweeney, and Randall D. Kamien. First-order patterning transitions on a sphere as a route to cell morphology. *Proceedings of the National Academy of Sciences*, 113(19):5189–5194, May 2016.

[253] Reginald W. James. The Adams and Elsasser dynamo integrals. *Proceedings of the Royal Society of London. A. Mathematical and Physical Sciences*, 331(1587):469–478, January 1973.

[254] H. T. Johansson and C. Forssén. Fast and Accurate Evaluation of Wigner 3j, 6j, and 9j Symbols Using Prime Factorization and Multiword Integer Arithmetic. *SIAM Journal on Scientific Computing*, 38(1):A376–A384, January 2016.

[255] Pawel Romanczuk, Markus Bär, Werner Ebeling, Benjamin Lindner, and Lutz Schimansky-Geier. Active brownian particles. *Eur Phys J Spec Top*, 202(1):1–162, 2012.

[256] Carlos A. Braumann. Itô versus Stratonovich calculus in random population growth. *Math. Biosci.*, 206(1):81–107, 2007.

[257] Roland G. Winkler, Adam Wysocki, and Gerhard Gompper. Virial pressure in systems of spherical active Brownian particles. *Soft Matter*, 11(33):6680–6691, 2015.

[258] Desmond Higham. An algorithmic introduction to numerical simulation of stochastic differential equations. *SIAM Rev.*, 43(3):525–546, 2001.

[259] Anand U. Oza and Jörn Dunkel. Antipolar ordering of topological defects in active liquid crystals. *New Journal of Physics*, 18(9):093006, September 2016.

[260] H. W. Kuhn. The Hungarian method for the assignment problem. *Naval Research Logistics Quarterly*, 2(1-2):83–97, March 1955.